Numerical simulation of selected geologic processes based on Discrete Element Method

To the Faculty of Geosciences, Geoengineering and Mining
of the Technische Universität Bergakademie Freiberg
approved

THESIS

to attain the academic degree of
Doctor of Engineering
Dr.-Ing.
submitted

by M. Sc. Yuan, Liu

born on the May 19, 1989 in Hubei, China

Reviewers: Prof. Dr.-Ing. habil. Heinz Konietzky, Freiberg, Germany
Prof. Dr. Kamil Ustaszewski, Jena, Germany
Prof. Dr. Jianmin Hu, Beijing, China

Date of the award: 18.04.2018

Acknowledgements

I really appreciate the precious and wonderful four years during my Ph.D. study at the Geotechnical Institute of TU Bergakademie Freiberg, Germany. This thesis represents not only my work at the institute, but it is also the result of many experiences and support I have got from the individuals who I wish to acknowledge.

First and foremost, I would like to express my sincere and deepest gratitude to my advisor, Professor Heinz Konietzky, Head of the Geotechnical Institute, TU Bergakadamie Freiberg. I appreciate his guidance, motivation, enthusiasm, immense knowledge, understanding, patience, encouragement, and continuous support all these years. I will always remember and cherish his quick feedbacks and fruitful suggestions.

I am grateful to Prof. Paul Mann for his constructive comments and suggestions which have significantly improved the work. Prof. Jianmin Hu, Prof. Wei Shi, Prof. Jiaxi Yang, Prof. Thomas Monecke are thanked for useful discussions.

My sincere thanks go to all of my colleagues at the Geotechnical Institute for their kind support. I would like to thank Mrs. Angela Griebsch for her kind help whenever needed. I also thank Dr. Martin Herbst for solving my software problems and providing a very good work environment.

I wish to express my special thanks to all my Chinese colleagues and friends for their kind support and happy time during the study in Germany. I also owe deepest gratitude to my family in China for their unconditional love and support all these years.

Finally, I would like to thank the Chinese Scholarship Council (CSC) and TU Bergakademie Freiberg for the financial support during my Ph.D. study in Germany.

Abstract

This study presents numerical modeling of geologic processes based on Discrete Element Method (DEM), including modeling of pull-apart basin development based on Particle Flow Code (PFC) and simulation of deformation and earthquake potential of Ordos Block (China) under present tectonic stress regime based on Universal Distinct Element Code (UDEC).

A scale-independent modeling approach based on PFC^{2D} has been established to simulate the development of pull-apart basins. The micro-scale PFC models are used to investigate crack propagation and basin development in releasing sidestep systems with pure strike-slip, transtensional, and transpressional master faults, respectively. In each system, three typical models including 30° underlapping, 90° non-overlapping, and 150° overlapping releasing sidesteps are chosen. The modeling results are compared with pull-apart basins in nature. The geometric differences of pull-apart basins result from both the initial strike-slip fault geometries and its various evolution stages. Rhomboidal basins which have larger basin length than the amount of motion form in overlapping systems and do not progress through the spindle-shaped and lazy-Z-shaped stages such as the Dead Sea basin. Rhomboidal basins with cross-basin faults tend to form in underlapping systems. Finally, the origin of rhomboidal pull-apart basins, depocenters of pull-apart basins, cross-basin faults and their significances, models for pull-apart basin development, and minimum displacements and ages to form pull-apart basins are discussed.

A two-dimensional UDEC model involving Ordos Block and adjacent areas is set up. Boundary conditions based on present tectonic regime are assumed. Block rotations, shear stress and displacement on faults, ratio of shear to normal force are simulated. Slip tendency which represents the assessment of the potential for causing slip on individual faults and earthquake-prone of the faults is predicted. Modeling results are compared with geologic evidences.

Table of Contents

List of Figures

List of Tables

Notation

c	Cohesion
d	Fault separation
d_{max}	Maximum ball size
d_{min}	Minimum ball size
E	Young's modulus
F	Resultant force
G	Shear modulus
Jk_n	Normal stiffness for joint
Jk_s	Shear stiffness for joint
K	Bulk modulus
k_n	Particle normal stiffness
k_n	Particle shear stiffness
m	Mass
n-bond	Normal contact bond strength
R	Particle radius
s-bond	Shear contact bond strength
S_n	Normal strength of the contact bond (n-bond)
t	Time
T_c	Time needed to form the first cracks
T_{min}	Minimum age of a pull-apart basin
T_s	Slip tendency
u_x	Horizontal displacement of ball D
u'	Velocity of the block centroid
u''	Acceleration of the block centroid
U_x	Displacement
U_x^c	Displacement needed to form the first cracks
U_x^{min}	Minimum displacement to form the first depression area
γ	Poisson's ratio

δ_{ij}	Kronecker symbol
Δt	Time step
Δu_n	Normal displacement increment
Δu_s	Shear displacement increment
$\Delta \varepsilon_\gamma$	Increment of volumetric strain
$\Delta \sigma_{ij}$	Stress increment
$\Delta \varepsilon_{ij}$	Strain increment
$\Delta \sigma_n$	Normal stress increment
$\Delta \sigma_s$	Shear stress increment
ε	Strain
ε_x^*	Relative extension
$\varepsilon_{x\,max}^*$	Relative extension when the peak stress is reached
η	Viscosity
μ	Frictional coefficient
ν	Fault slip rate
ρ	Density
σ_1	Major principle stress in circle C
σ_{11}	Horizontal normal stress in circle C
σ_{22}	Vertical normal stress in circle C
σ_{12}	Shear stress in circle C
σ_t	Tensile strength
σ_n	Normal stress
σ_s	Shear stress
σ	Stress
Φ	Angle of friction

1 Introduction

1.1 Objective and scope

Geologic processes are complex. Geologic models range from micro-scale, for example dealing with deformations at the grain size level, to macro-scale such as the movement of blocks and orogenic belts or deformation of the entire lithosphere. Numerical simulation of geologic processes has become simpler with the access to significantly increased computational power and development of new numerical simulation techniques. Complex modeling needs sophisticated simulation techniques, including continuum-based methods such as Finite Element Method (FEM) and Finite Difference Method (FDM), or even better discontinuum based methods such as Discrete Element Method (DEM).

Rock fractures and big faults in crust largely control many of the Earth's dynamic processes such as plate-boundary formation and evolution, tectonic earthquakes, volcanic eruptions, and fluid transport in the crust. How rock fractures and faults in the crust form and develop are of great importance in many fields of earth sciences and engineering. Compared with continuum-based methods, DEM is better suited to simulate geologic processes considering the propagation and coalescence of fractures and faults [*Finch et al*., 2003; *Cardozo et al*., 2005; *Naylor et al*., 2005; *Benesh et al*., 2007; *Liu and Konietzky*, 2018]. This study presents numerical modeling results of geologic processes based on DEM, including modeling of pull-apart basin development based on Particle Flow Code (PFC) and simulation of tectonic deformation of Ordos Block (China) under present tectonic regime based on Universal Distinct Element Code (UDEC).

All the presented simulations are two-dimensional. The author is aware that this implies several restrictions. If not explicitly mentioned all the presentations are top (plane) views. It has to be distinguished between physical justified conclusions and geologic interpretations of the modelling results. Especially the statements for the vertical direction (perpendicular to the model plane) are more speculative although supported by other studies.

Additionally, the author does not distinguish the minor differences of the components of the Riedel-shears because of the limitation of the two-dimensional modeling. The term "Riedel-shears" in this thesis is a general description of the new cracks, which are also called the "first cracks" in this study.

1.1.1 Development of pull-apart basins

Pull-apart basins form in extensional structures or releasing sidesteps and bends where a left-lateral strike-slip fault steps to the left or a right-lateral fault steps to the right [*Fossen,* 2016]. The term "pull-apart basin" was first introduced by *Burchfiel and Stewart* [1966] in their work at Death Valley, California. Since that time, numerous studies of pull-apart basins have been conducted by geologists, seismologists and theoreticians [e.g. *Wright et al*., 1974; *Aydin and Nur*, 1982; *Mann et al*., 1983; *Woodcock and Fischer*, 1986; *IG and SBNHAP*, 1990; *Ben-Avraham and Zoback*, 1992; *Kim et al*., 2004; *Wu et al*., 2009; *Corti and Dooley*, 2005; *van Wijk et al*., 2017; *Liu and Konietzky*, 2018]. For geologists, pull-apart basins can provide more information than the strike-slip belts themselves and the pressure ridges where little rock record is preserved. Moreover, a surficial depression of an active basin is easily to be recognized and mapped in field investigation. Well mapped pull-apart basins can reveal a tectonic environment of strike-slipping and provide useful information of the strike-slip faults about the direction, sense, timing, and minimum amount of offset along the master faults. For seismologists, volcanism and earthquake swarms tend to occur at pull-apart basins [*Segall and Pollard*, 1980; *Mann et al*., 1983]. For geologists, it is interesting to produce both, pull-apart basin physical models and numerical models. Therefore, understanding pull-apart basins along strike-slip faults is of great academic as well as practical interest.

Although field investigations, physical modeling studies, and continuum methods have already contributed a lot to the understanding of pull-apart basin development, DEM based models concentrating on crack propagation and coalescence, and pull-apart basin development are lacking. Previous numerical studies of pull-apart basins [e.g., *Rogers*, 1980; *Gölke et al*., 1994; *Katzmann et al*., 1995 *Bertoluzza and Perotti*, 1997; *Petrunin and Sobolev*, 2006; *van Wijk et al*., 2017] based on continuum mechanical approaches like the FEM have

certain limitations. One major purpose of this study is to simulate crack propagation and coalescence during pull-apart basin formation and development. Compared with continuum methods, the advantage of DEM modeling is that we can intuitively see the crack propagation and coalescence during the pull-apart basin development based on fracture mechanical theory with explicit consideration of material separation. This study presents numerical modeling results including crack propagation and coalescence, pull-apart basin development, stress-deformation pattern in releasing sidesteps where right-lateral strike-slip faults step to the right with several different initial strike-slip fault kinematics (pure strike-slip, transtension, transpression, and pure strike-slip of several fault strands). Modeling results are compared with both, experimental studies and natural basins. Finally, the origin of rhomboidal pull-apart basins, depocenters of pull-apart basins, basin-cross faults and their significances, models for pull-apart basin development, and the minimum displacement and time to form a pull-apart basin are discussed.

1.1.2 Tectonic deformation of Ordos Block under present tectonic regime

Ordos Block is a large and stable crustal segment in the western NCC. The deformation inside of the Ordos Block is small while the movement of the Ordos Block with respect to the adjacent blocks is relatively large based on GPS measurements [*Fan et al*., 2003]. The surrounding areas of Ordos Block are intensively active because of the coupled influences of the Indian, Eurasian, and Pacific Oceanic plates in Cenozoic [e.g., *Deng et al*., 1989; *IG and SBNHAP*, 1990; *Burchfiel et al*., 1991]. Devastating and large historical earthquakes were located at the study area. Therefore, numerical models based on UDEC have been built to simulate the deformation features, block rotations, and shear stress and shear displacement on the major faults. In addition, slip tendency (Ts), which represents the assessment of the potential for causing slip on individual faults and earthquake-prone of the faults, is predicted under the present tectonic regime.

1.2 Research strategy and structure of thesis

Figure 1.1 illustrates the research strategy and structure of the thesis. Objective and literature review are presented in chapter 1 and chapter 2, respectively. Particle based modeling of

pull-apart basin development is included in chapter 3 and chapter 4. Pre-investigations which include scale-independency and parameter study are shown in chapter 3. Numerical simulation of pull-apart basin development including different initial fault kinematics such as pure strike-slip, transtension, transpression, and pure strike-slip of several fault strands is included in Chapter 4. Chapter 5 compares the modeling results with natural examples and discusses the main concerns of pull-apart basin study based on the modeling results, such as origin of rhomboidal basin, depocenters of pull-apart basin, cross-basin faults and their significances, models for pull-apart basin development, and the minimum displacement and time to form a pull-apart basin. Chapter 6 presents numerical simulation of deformation and earthquake potential of Ordos Block and adjacent areas under present tectonic regime. Finally, a summary of this thesis and an outlook are given in chapter 7.

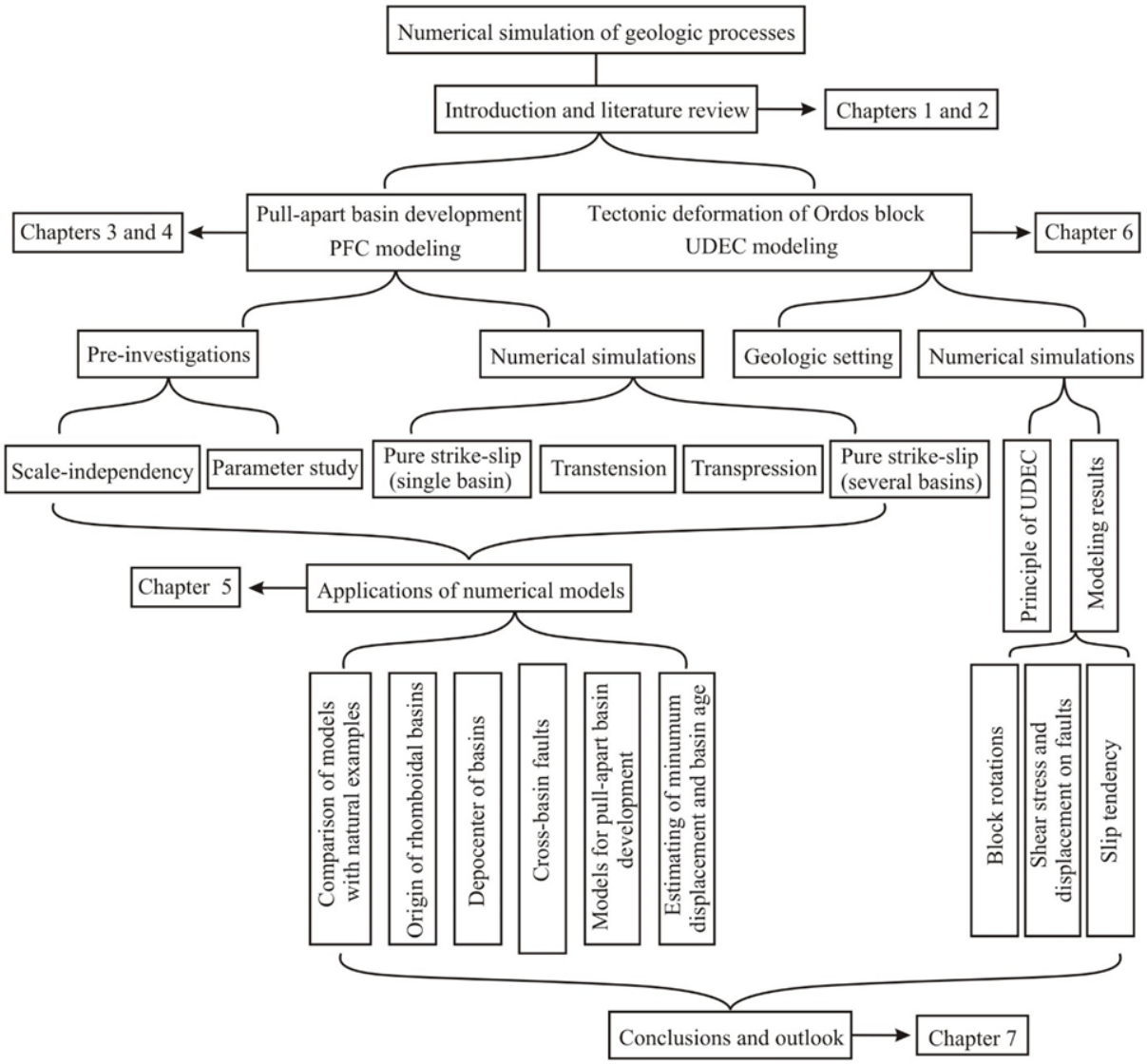

Figure 1.1 Research strategy and structure of thesis

2 State of the art

2.1 Numerical methods

2.1.1 Continuum-based methods

Continuum-based methods are classic and one of the most widely used approaches of numerical mesh-based modeling. They are often used by geologists to model displacement, velocity or stress fields during fault interaction and fracture formation in rock masses or fold formation and development under different conditions, microscale diffusion processes during plastic deformation and other geologic processes [e.g., *Rogers*, 1980; *Zhao and Morgan, 1987; Katzmann et al*., 1995; *Bertoluzza and Perotti*, 1997; *Liu and Yang*, 2003; *Petrunin and Sobolev*, 2008; *Gerya et al*., 2015; *van Wijk et al*., 2017].

However, continuum mechanical approaches have several disadvantages including numerical instabilities in case of physical instabilities during geologic processes. In addition, models based on continuum mechanics have problems to simulate crack initiation, propagation and interaction. Also, remeshing might be necessary in case of large deformations and simulation of processes such as mass movement (avalanches, landslides, erosion processes etc.). Simulation of rockfall might be even impossible.

2.1.2 Discontinuum-based methods

Discontinuum-based methods on the basis of DEM are relatively new. Although there is still limited experience, and compared to continuum-based methods, larger computational power is needed, it became more and more attractive in the last two decades because of the ability to consider rotations, fracturing, separation and structure. Rock fractures and big faults in the crust largely control many of the earth's dynamic processes such as plate boundary formation and evolution, tectonic earthquakes, volcanic eruptions, and fluid transport. How rock fractures and faults in the crust form and develop is of great importance in earth sciences and geo-engineering.

The DEM allows to simulate the initiation, propagation and interaction as well as any kind of separation of any kind of discontinuities (faults, fractures, cracks, layer boundaries etc.) without the limitations of continuum mechanics. The basic elements of the DEM can be of arbitrary shape, but the most common shapes are polyhedra and spheres (Figure 2.1). The elements interact with each other via a force displacement law.

The two-dimensional Particle Flow Code (PFC^{2D}) [*Itasca*, 2004] based on DEM has been widely used in many fields such as engineering [e.g., *Theuerkauf et al*, 2003], soil and rock mechanics [e.g., *Ting et al*., 1989; *Wang et al*., 2003; *Potyondy and Cundall*, 2004; *Groh et al*., 2011; *Stahl and Konietzky*, 2011; *Ding et al*., 2014; *Sarfarazi et al*., 2014]. The DEM has also been successfully used to simulate geologic problems [e.g. *Burbidge and Braun*, 2002; *Lee et al*., 2004; *Naylor et al*., 2005; *Hardy*, 2008; *Dean et al*., 2013; *Chu et al*., 2015] and tectonic processes such as the growth and interaction of faults and the formation of related structures [e.g. *Peacock and Xing*, 1994; *Finch et al*., 2003; *Imber et al*., 2004; *Cardozo et al*., 2005; *Schöpfer et al.,* 2006, 2007a, 2007b*; Benesh et al*., 2007; *Liu and Konietzky*, 2018].

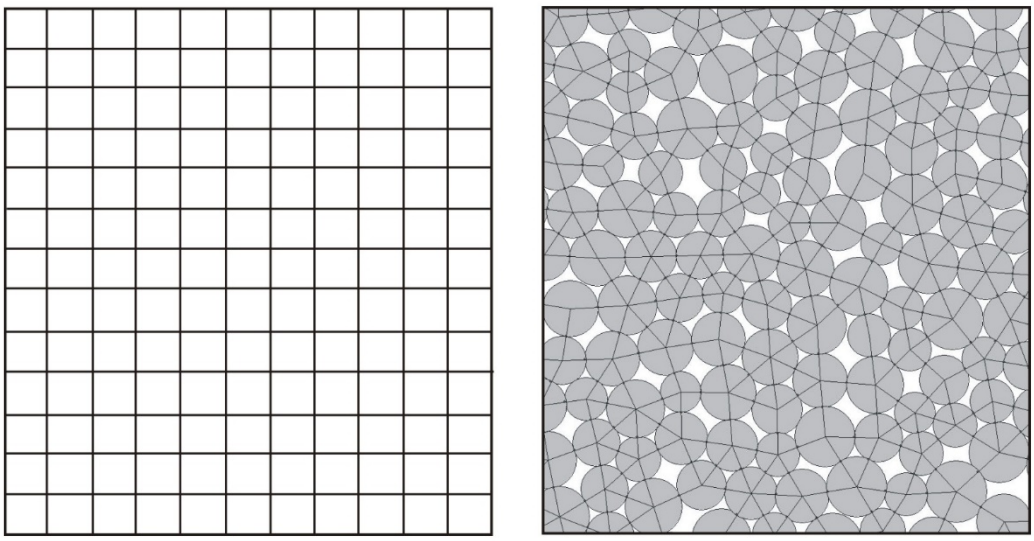

Figure 2.1 Model examples for continuum (left: mesh) and discontinuum (right: sphere assembly) methods

2.2 Research status of pull-apart basins

2.2.1 Pull-apart basin definition and related terms used in this thesis

Strike-slip faults are those faults where the displacement vector is parallel to the strike of the fault and thus parallel to the surface of the earth [*Sylvester*, 1988; *Fossen*, 2016]. Some long and large strike-slip faults can form plate boundaries and some are long-existing and long-living basement faults. Strike-slip faults on a regional scale might produce areas of transtension or transpression. On a local scale, when strike-slip fault segments overlap and link, contractional structures and extensional structures form. Contractional structures or restraining sidesteps such as pressure ridges are related to right lateral strike-slip faults with left sidestep (Figure 2.2d) or left lateral strike-slip faults with right sidestep (Figure 2.2b). Extensional structures or releasing sidesteps form where a right-lateral strike-slip fault steps to the right (Figure 2.2a) or a left-lateral fault steps to the left (Figure 2.2c). These extensional basins along strike-slip faults are called pull-apart basins.

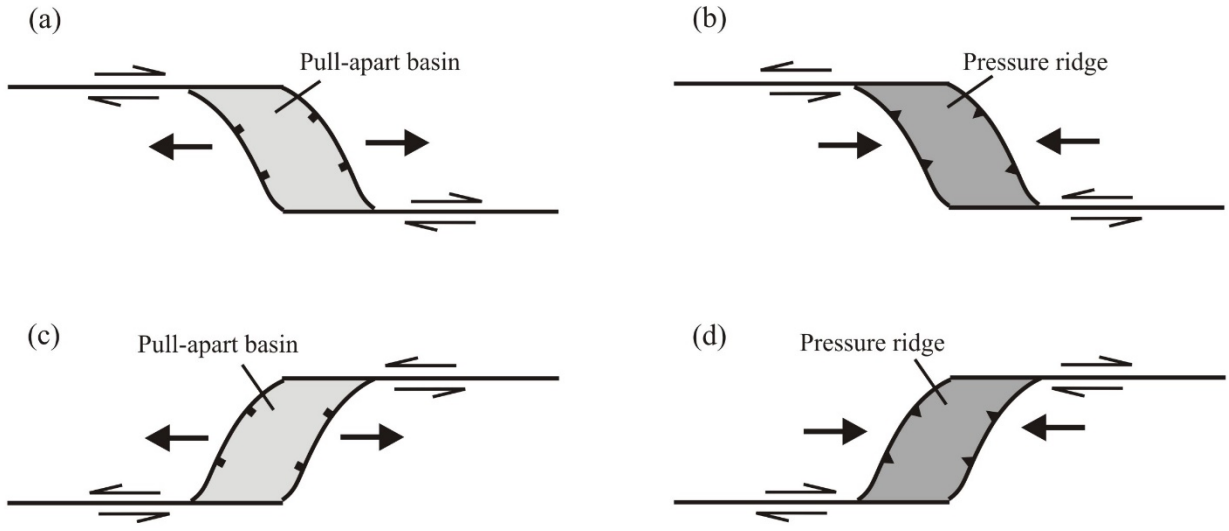

Figure 2.2 General features of pure strike-slip fault systems. (a) releasing sidestep, (b) restraining sidestep, (c) releasing sidestep, (d) restraining sidestep.

The term “pull-apart basin” was first introduced by *Burchfiel and Stewart* [1966] in their work at Death Valley, California. Many descriptions and terms of strike-slips and pull-apart basins have been proposed over the past five decades. *Mann* [2007] summarized and

classified the usage of these terms. Following *Mann* [2007], this thesis use the term "strike-slip fault" for subaerial strike-slip faults in continental settings whose slip vectors are roughly parallel to their strike [*Sylvester*, 1988; *Mann*, 2007]. Two generally used terms are "transtension" and "transpression" (Figure 2.3) which refer to strike-slip deformation zones that deviate from simple shear by a component of extension (transtension) or shortening (transpression) across the zone [*Sanderson and Marchini*, 1984; *Fossen and Tikoff*, 1998; *Dewey et al*., 1998].

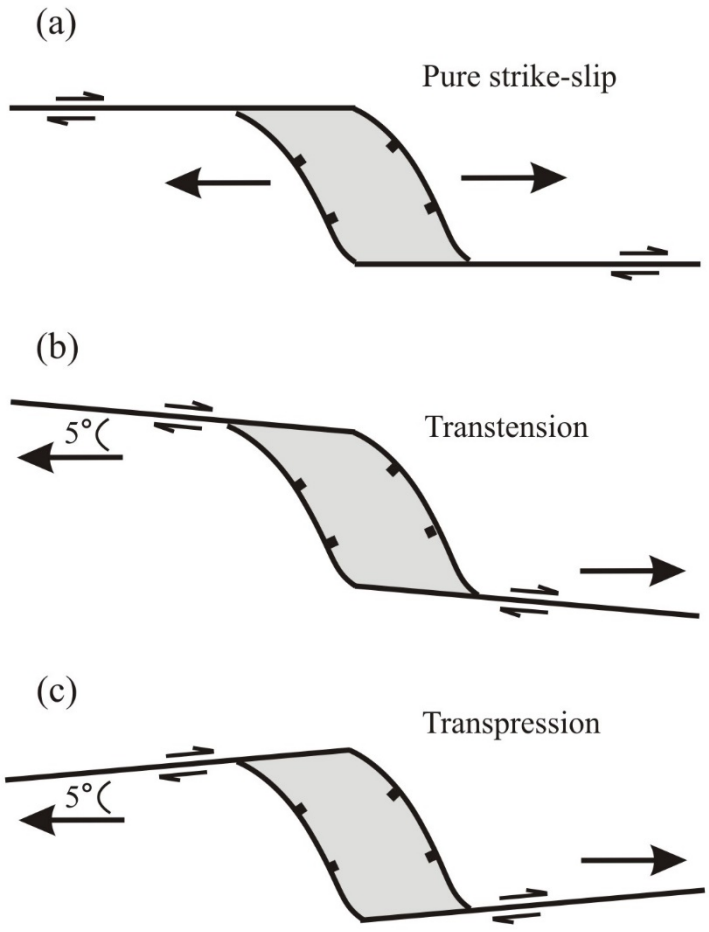

Figure 2.3 General features of a pull-apart basin in a right-lateral sidestep. The pull-apart basin is defined to form in (a) pure strike-slip, (b) transtension, and (c) transpression.

The term "pull-apart basin" or "releasing sidestep" is used for extensional structures where a left-lateral strike-slip fault steps to the left or a right-lateral fault steps to the right. The two roughly parallel strike-slip faults bounding pull-aparts or push-ups are called "master faults"

[*Rodgers*, 1980]. The fault distance between the master faults is "fault separation" or pull-apart basin width. The overlap between the overlapping master faults is the so-called "fault overlap" and roughly defines the pull-apart basin length (Figure 2.4). The basin is bounded by a transverse system of oblique extensional faults which are called "basin sidewall faults" [*Burchfiel and Stewart*, 1966; *Mann et al*., 1983; *Woodcock and Fische*r, 1986; *Mann*, 2007; *Wu et al*., 2009].

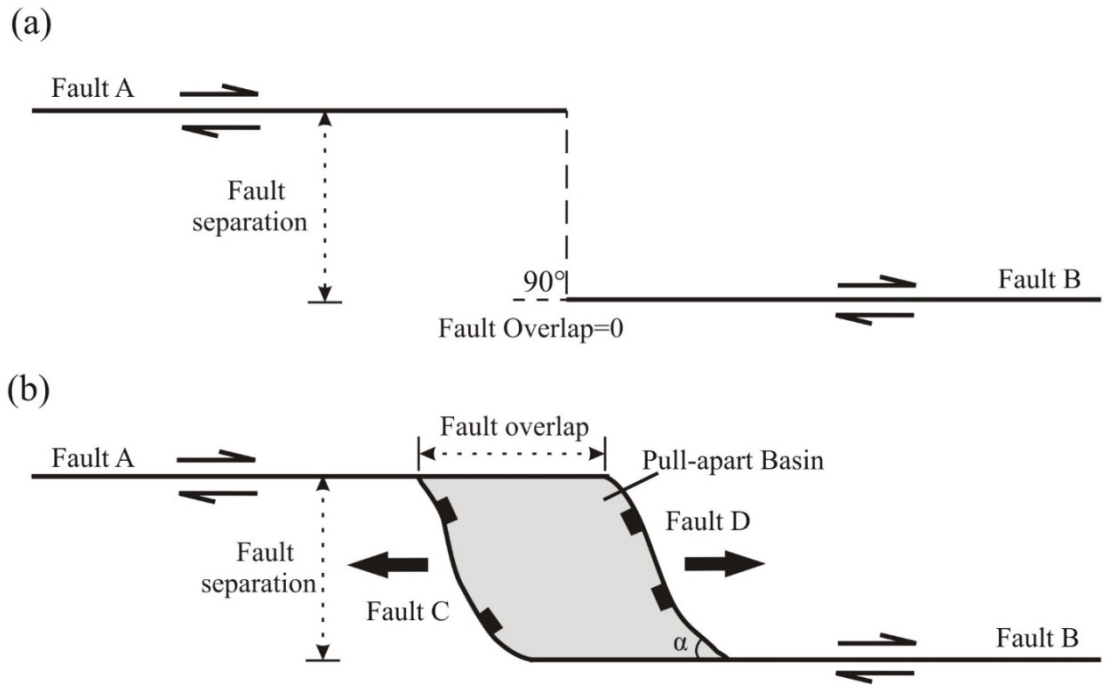

Figure 2.4 Terms related to pull-apart basins used in this study. Fault A and Fault B: master faults, Fault C and Fault D: basin sidewall faults, α is defined as the angel between the master faults and the basin sidewall faults.

2.2.2 Different approaches and observations on pull-apart basins

After the first introduction of the term "pull-apart basin" by *Burchfiel and Stewart* [1966], numerous studies of pull-apart basins including worldwide compilation of published information on pull-apart basins [e.g., *Aydin and Nur*, 1982; *Mann et al*., 1983; *Mann*, 2007], experimental studies [e.g., *Koide and Bhattacharji*, 1977; *McClay and Dooley*, 1995; *Dooley and McClay*, 1997; *Rahe et al*., 1998; *Sims et al*., 1999; *Wu et al*., 2009; *Dooley and Schreurs,* 2012], numerical simulations [e.g., *Rogers*, 1980; *Segall and Pollard*, 1980; *Petrunin and*

Sobolev, 2006; *van Wijk et al*., 2017; *Liu and Konietzky*, 2018], and also specific case studies [e.g., *Wright et al*., 1974; *Deng et al*., 1986; *Lallemand and Jolivet*, 1986; *Zhang et al*., 1989; *Deng et al*., 1989; *IG and SBNHAP*, 1990; *Burchfiel et al*., 1991; *Okay et al*., 2000; *Itoh*, 2001; *Hurwitz et al*., 2002; *Shi et al*., 2015] have been conducted because of its important tectonic meaning and the possible association with earthquakes.

Published data compilation

Previous studies of published data compilation mainly concentrated on pull-apart basins' length to width ratio, development of pull-apart basins, and the angles between master faults and basin sidewall faults.

After a compilation of the shapes of 62 well-defined pull-apart basins of different sizes worldwide, *Aydin and Nur* [1982] drew the conclusion that rhombic pull-apart basins' length to width ratio is approximately three. The basins become wider with increasing fault offset. Two possible mechanisms are proposed: (1) coalescence of neighboring pull-apart basins; and (2) formation of new fault strands parallel to the existing faults.

A comparative study of well-mapped active and ancient pull-apart basins in northern Caribbean and Turkey [*Mann et al*., 1983] showed that pull-apart basins evolve through time starting with spindle-shaped and proceeding through the lazy-Z-shaped to the rhomboid and extreme rhomboid. They suggested that the basin width remains fixed by the separation between the strike-slip faults and does not increase significantly as the basin grows further. Most pull-apart basins have low length to width ratios. This is a result of their short live time in fast changing strike-slip areas. *Mann* [2007] compiled published data on the strike-slip tectonic setting, size, basin and bend type, age and models for active and ancient releasing and restraining bends. Examples of bends on strike-slip faults were compiled and explained on the basis of five various active strike-slip settings. Global classification and tectonic origins of these releasing and restraining bends were proposed.

Bahat [1983] compared the geometric features of 48 grabens, horsts and upthrusts with

rhombic, triangular and trapezoidal shapes all over the world. The results showed that the angles (α) between master faults and basin sidewall faults change from 7° to 73° (Figure 2.5). The acute angles are independent from the basin scale, and the two acute angles differ considerably in most structures. *Gürbüz* [2010] compiled the geometric results of the 11 pull-apart basins along the North Anatolian fault zone in Turkey, and found that the acute angles spread in the 28° - 44° range, with a mean angle of 33° (Figure 2.5).

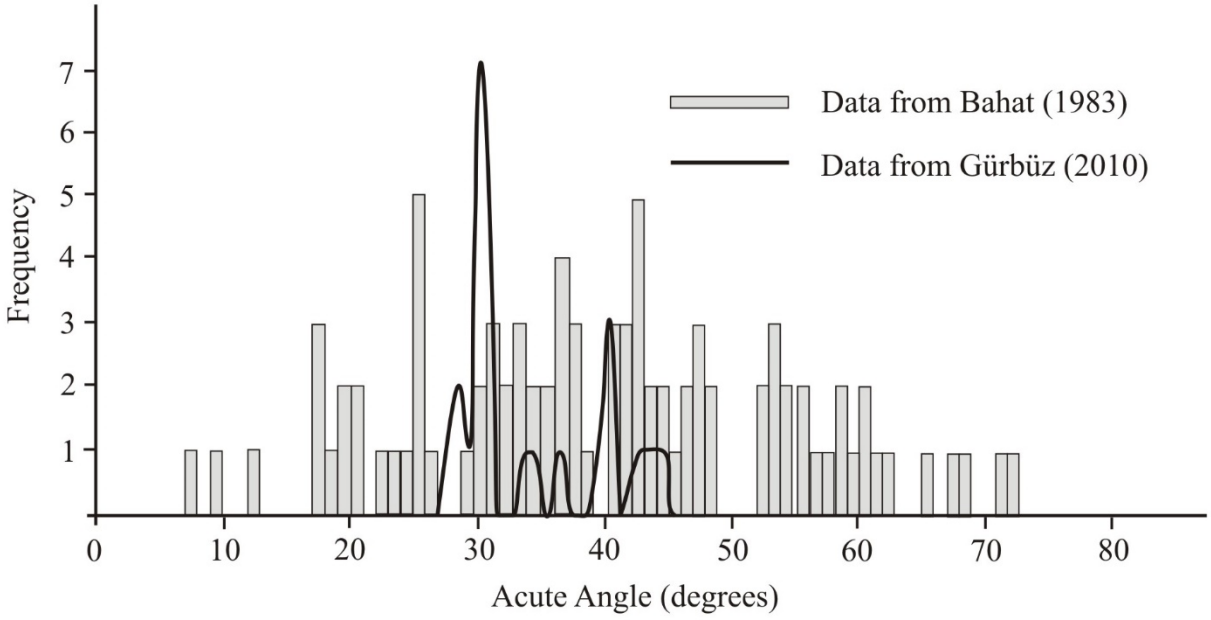

Figure 2.5 Frequency of acute angles (α) between master faults and basin sidewall faults in pull-apart basins (data come from *Bahat* [1983] and *Gürbüz* [2010]).

Experimental studies

Experimental studies have also been used to simulate the geometry and evolution of pull-apart basins in a sedimentary cover above rigid basement with strike-slip. Scaled sandbox models built by *McClay and Dooley* [1995] and *Dooley and McClay* [1997] have simulated the basin shapes and further evolution of pull-apart basins developed in a weak sedimentary cover above rigid basement where right-lateral strike-slip faults step to the right (Figure 2.6). The pull-apart basins evolve progressively from a narrow graben bounded by the oblique-slip link faults to wider rhombic basins flanked by terraced basin sidewall fault systems. The geometries of the pull-apart basins are dependent on the architecture of the

underlying basement strike-slip fault systems. *Rahe et al*. [1998] considered that the evolution of a pull-apart basin is separated into three stages: incipient, early and mature. Asymmetric, symmetric and hybrid pull-apart basins all follow the same evolution sequence. *Basile and Brun* [1999] conducted 17 small-scale experiments to study the deformation between two transform faults and transform and divergent plate boundaries. The results showed that the basin length-to-width ratio remains between 2.2 and 3.8, indicating that scale independence of pull-apart basins is related to the geometric shape of bounding strike-slip faults. *Wu et al*. [2009] conducted scaled sandbox tests to simulate the evolution of pull-apart basins formed above underlapping releasing sidesteps in both pure strike-slip and transtensional basement fault systems. Their results showed that the geometry of the basin is a consequence of its evolution through various basin types.

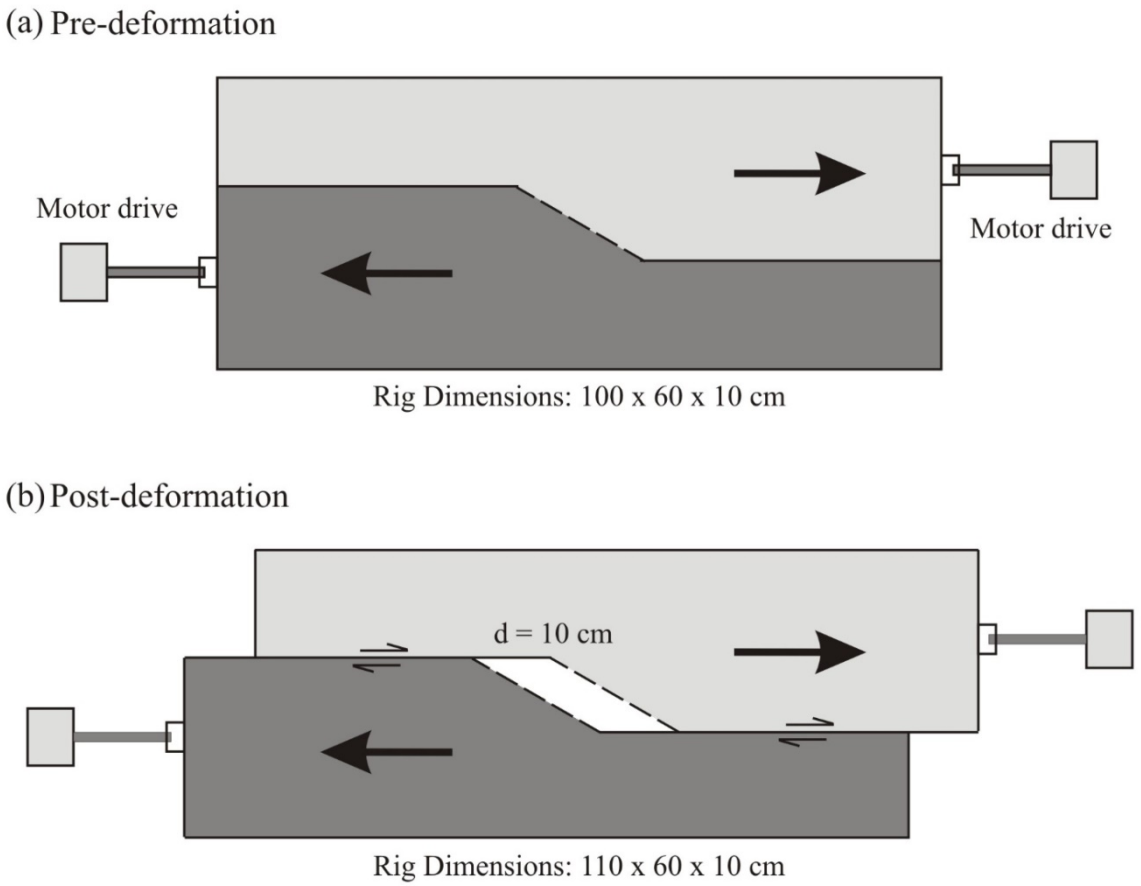

Figure 2.6 Simplified plan view of sandbox experimental apparatus and baseplate geometries used by *Dooley and McClay* [1997].

Numerical studies

Structural development of pull-apart basins was studied by *Rogers* [1980] based on mathematical models using elastic dislocation theory. The results indicated that secondary normal faults develop at the ends of the master faults. As pull-apart basins evolve, two distinct areas of normal faulting at the distal ends of the basin form. *Gölke et al*. [1994] built 2D finite element models (Figure 2.7), where the master faults are pre-defined and the growth of the faults is not considered because of the limitations of continuum mechanics. They mainly focused on the relationship between fault geometry (i.e., fault overlap and separation) and sedimentary depocenters of pull-apart basins. 3D elastic modeling was conducted by *Katzman et al*. [1995], and the results showed that the shape of pull-apart basins depend mainly on the width of the shear zone and the amount of fault overlap. Based on finite element modeling, *Bertoluzza and Perotti* [1997] concluded that the angle between the potential normal fault and the strike-slip faults is strongly dependent on the model boundary conditions (pure strike-slip, transtension and transpression) and only slightly on the elastic rock properties and the ratio between fault overlap and fault separation. *Petrunin and Sobolev* [2006] have built 3D thermo-mechanical models and paid more attentions to the deep, they found that the major effect on basin length, sediment thickness and deformation pattern beneath the basin is the thickness of the crust brittle layer. Elastic models based on finite element software built by *van Wijk et al*. [2017] was used to simulate the development of pull-apart basins. They thought that the shape of a pull-apart basin is inherited from the initial geometry of the master strike-slip faults. They also concluded that pull-apart basins become extinct when active cross-basin faults form because a zone of compressional stress concentration in their elastic models forms that connects the master faults.

However, these numerical studies of pull-apart basins based on continuum mechanical approaches [e.g., *Rogers*, 1980; *Gölke et al*., 1994; *Katzmann et al*., 1995; *Bertoluzza and Perotti*, 1997; *Petrunin and Sobolev*, 2006; *van Wijk et al*., 2017] have certain limitations. New crack formation and propagation cannot be seen in these models. Although field investigations, physical modeling studies, and continuum methods have already contributed a lot to the understanding of pull-apart basin development, DEM models concentrating on

crack propagation and coalescence, and pull-apart basin development are lacking.

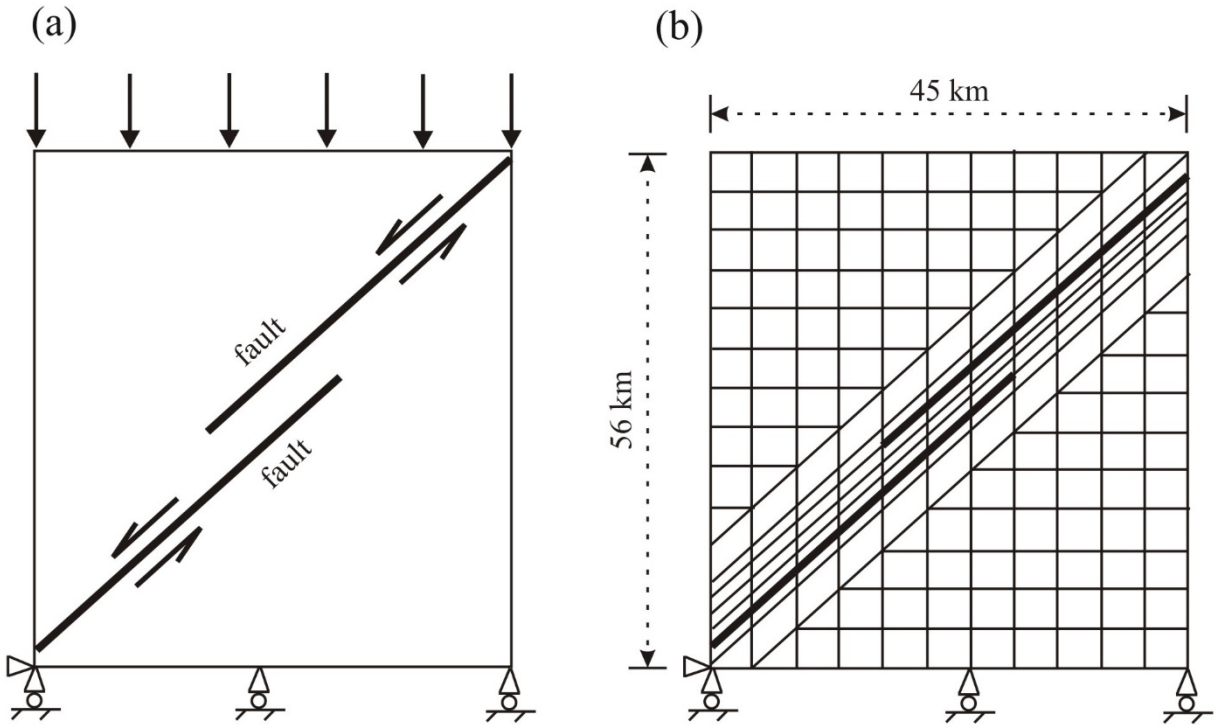

Figure 2.7 Continuum-based modeling (2D finite element model) of pull-apart basin formation by *Gölke et al*. [1994]. (a) Initial and boundary conditions for left-lateral left-stepping sidestep model. (b) Finite element mesh.

2.2.3 Origin and development of pull-apart basins

Pure strike-slip and basins

A lot of models for pull-apart basin development have been proposed. The simplest evolution model was that a depression nucleates between two parallel strike-slip faults and evolves into a "sharp pull-apart" [*Quennell*, 1958; *Crowell*, 1974]. Basin width is determined by the master fault separation and remains fixed. The basin lengthens as displacement of strike-slip faults increases (see Figure 2.8a: master fault overlap is "O" and master fault separation is "S"). Model (a) according to Figure 2.8a was widely applied to basin development along the Dead Sea fault system [e.g., *Garfunkel et al*., 1981].

On the basis of shear box experiments, *Koide and Bhattacharji* [1977] suggested that

pull-apart basins nucleate on en-echelon faults (Figure 2.8b). *Dewey* [1978] proposed a similar model where pull-apart basins tend to form at large-scale rotated tension gashes or Riedel-shears generate during the initial stages of basin formation.

Rogers [1980] studied pull-apart basin development between two parallel master strike-slip faults based on mathematical models using elastic dislocation theory (Figure 2.8c). Their results showed that master fault overlap, master fault separation, and whether the faults intersect the surface or not play most important role in pull-apart basin development. They thought that secondary normal faults develop at the ends of the master faults. As pull-apart basins evolve, two distinct areas of normal faulting at the distal ends of the basin form.

Aydin and Nur [1982] proposed a new model that pull-apart basins could become wider with increasing fault offset after compilation of well-studied pull-apart basins worldwide (Figure 2.8d). Two possible mechanisms are proposed: (1) coalescence of neighboring pull-apart basins; and (2) formation of new fault strands parallel to the existing faults.

Mann et al. [1983] summarized the previous models of pull-apart basin development [e.g., *Freund*, 1971; *Koide and Bhattacharji*, 1977; *Rogers*, 1980; *Aydin and Nur*, 1982] and pointed out both, the advantages and limitations of each model. Meanwhile, *Mann et al*. [1983] and *Mann et al*. [2007] proposed the process that pull-apart basins evolve through a sequence of closely related states, from spindle-shaped through lazy-Z-shaped to the rhomboidal and extreme basin based on a comparative study of well-mapped active and ancient pull-apart basins worldwide (Figure 2.8e). They also thought that most pull-apart basins in nature have low ratios of length to width because of the short live time in rapid changing strike-slip regimes.

This study summarizes the development of pull-apart basins in pure strike-slip systems with different initial fault geometries based on the discontinuum method.

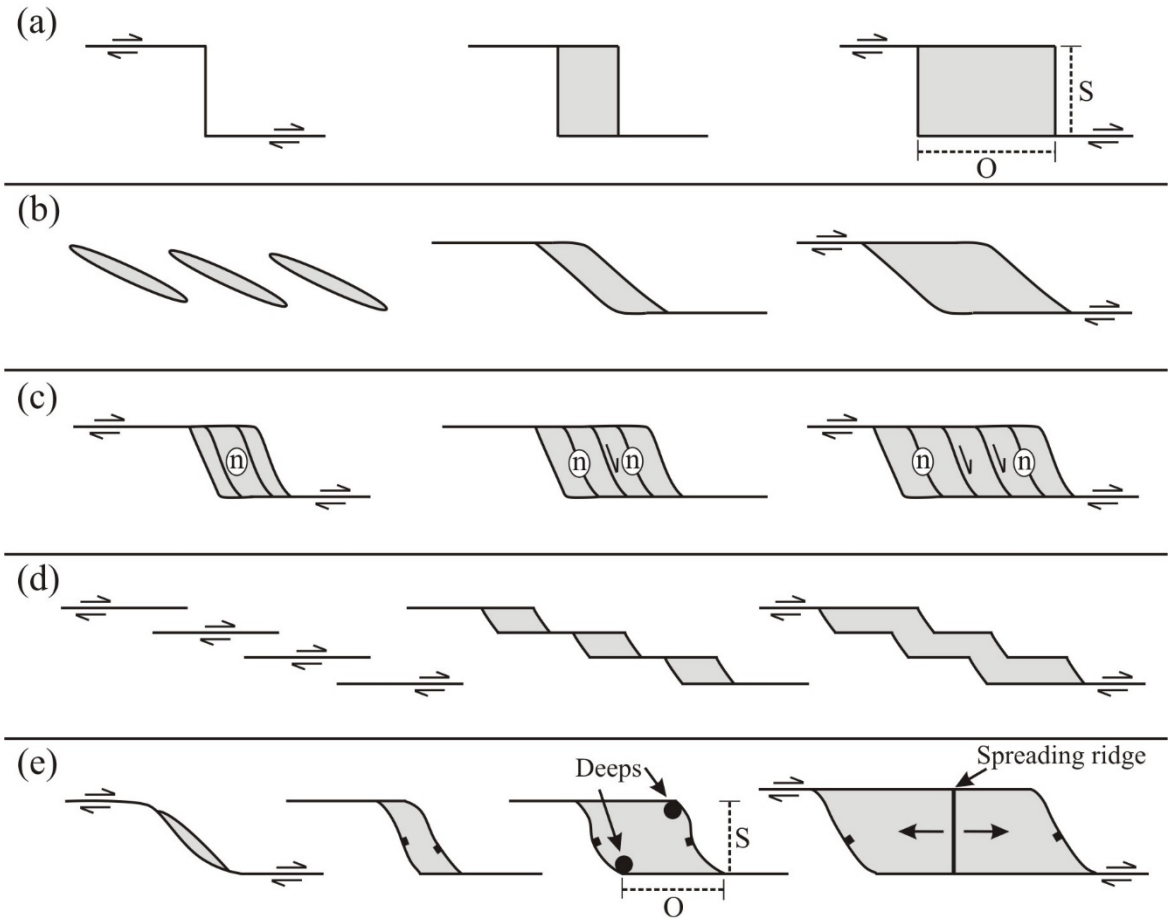

Figure 2.8 Summary of previous models for pull-apart basin development. (a) Simple model of pull-apart formation between right-lateral right-stepping master strike-slip faults. Master fault separation (S) or basin width remains constant while master fault overlap (O) increases with strike-slip displacement. (b) Pull-apart basin formation and evolution suggested by *Koide and Bhattacharji* [1977] based on shear box experiments. (c) Model proposed by *Rodgers* [1980] using elastic dislocation theory. "n" donates areas of predicted normal faulting. (d) Coalescence of neighboring pull-apart basins suggested by *Aydin and Nur* [1982]. (e) *Mann et al.* [1983] and *Man*n [2007] proposed the process that pull-apart basins evolve through a sequence of closely related states, from spindle-shaped through lazy-Z-shaped to the rhomboidal and extreme basin.

Transform-normal extension and asymmetric basins

Nature is complex. Pull-apart basins in nature developed not only in pure strike-slip fault systems, but also formed in transform-normal extension settings, transtensionl systems, and transpressional systems. However, traditional models of pull-apart basin development generally only consider the situation of pure strike-slip motion [e.g., *Mann et al*., 1983].

Ben-Avraham and Zoback [1992] pointed out that although lots of small-scale pull-apart basins exist and confirm the traditional development sequence, much larger scale basins are usually not consistent with the traditional pull-apart models. Large-scale basins are conspicuous asymmetric, bounded by linear strike-slip faults on one side of the basin and subparallel normal faults on the other, indicating strike-slip movement and transform-normal extension at the same time [*Ben-Avraham*, 1985; *Ben-Avraham and Zoback*, 1992]. They compared their results to pull-apart basin in the Gulf of Aqaba (Elat) in the southern segment of the Dead Sea fault system.

Transtensional master faults and wider basins

Based on three-dimensional elastic modeling, *ten Brink et al.* [1996] concluded that master faults with a small component (5°) of transtension generate a depression area 2-3 times wider compared to pure strike-slip. Physical modeling conducted by *Wu el al*. [2009] showed that quite different pull-apart basins are developed in transtension compared to pure strike-slip. They found that the basin geometries of each system were similar, both types produced elongated, sigmoidal to rhomboidal pull-apart basins, but two opposing depocenters formed in the transtensional system whereas a single, central depocenter formed in pure strike-slip. Moreover, the basins forming in transtensional systems were much wider than the basins in pure strike-slip. Two pull-apart basins in the southern end of the well-studied left-lateral Dead Sea fault system including the Dead Sea basin and the Gulf of Aqaba (Elat) have been compared with the modeling results and lead to this conclusion.

Transpression master faults and basins

According to detailed investigation of deformed Quaternary terraces in Hanmer pull-apart basin along the Hope fault in New Zealand, *Freund* [1971] found that the two master strike-slip faults are not parallel but converge across the basin. In addition, the master faults are not overlapping but connected by a short oblique-slip fault. Accordingly, *Freund* [1971] modified the simple model of rhomboidal basin forming between parallel strike-slip faults. Seismic reflection data and geological mapping by *Wood et al.* [1994] showed a continuous lateral and longitudinal asymmetry of Hanmer basin, suggesting that the structural geometry

and evolution of Hanmer basin do not fit the traditional pull-apart basin models well. *Wood et al.* [1994] proposed a hybrid model for Hanmer basin that basin was initiated with the first graben as the two master faults propagated and became indirectly linked by the oblique-slip fault at the southwest margin. As a result, basin depocenter is located at the adjacent area of the southwest margin, which leads to further asymmetric subsidence of the basin. The east part of the basin is under transpression while the west part is under transtension.

2.2.4 Extinction of pull-apart basin

Zhang et al. [1989] first proposed the extinction model of pull-apart basins in their work at Haiyuan fault in northwestern China. They have studied the geometric pattern and deformational style of pull-apart basins along the Haiyuan fault zone through detailed large-scale mapping to understand the extinction of pull-apart basins. They suggested that the extinction of pull-apart basins appears to be the development of new strike-slip faults diagonally across the basin. They thought that the formation of new cross-basin faults play an important role in causing a cessation in the evolution process of pull-apart basins. Based on analog modeling, *Rahe et al*. [1998] stated that the formation of cross-basin faults appears to be a contributing factor of pull-apart basin extinction. At the incipient stage of pull-apart basin development, cross-basin faults have similar sense of slip to the Riedel-shears in strike-slip settings. *Van Wijk et al*. [2017] also thought that the formation of an active cross-basin fault during pull-apart basin development is the reason of basin extinction. They concluded that larger ratios of basin length to width with master fault overlapping do not tend to form cross-basin faults.

2.3 Research status of Ordos Block neotectonics

The North China Craton (NCC) is made up of two major parts (the eastern NCC and western NCC), separated by the Trans-North China Orogen [*Tian et al*., 2011]. Ordos Block is a large and stable crustal segment in the western NCC. The deformation inside of the Ordos Block is small while the movement of the Ordos Block with respect to the adjacent blocks is relatively large based on GPS measurements [*Fan et al*., 2003]. The Ordos Block is surrounded by several grabens which include the Yinchuan-Hetao graben in the northwest and the

Shanxi-Shaanxi graben in the southeast. Several convex-to-the-northeast oroclinal structures with strike of NW-SE (the Haiyuan, Xiang Shan - Tianjin Shan, Yantong Shan, and Luo Shan - Niushou Shan faults from southwest to northeast) are situated in the southwest region of the Ordos Block. This region is located at the northeasternmost margin of the Tibetan Plateau and has gone through a complex intracontinental deformation during the Cenozoic because of the uplift of the Tibetan Plateau, and today is still a really active region driven by the coupled influences of the Indian, Eurasian, and Pacific Oceanic plates [e.g., *Deng et al*., 1989; *IG and SBNHAP*, 1990; *Burchfiel et al*., 1991; *Shi et al*., 2015]. The present tectonic regime of Ordos Block and adjacent basins was inferred from the focal solutions of earthquakes [*He et al*., 2003; *IG and SBNHAP*, 1990], GPS measurements [*Wang et al*., 2001; *Zheng et al*., 2013], geo-stresses [*Xie et al*., 2004], and fault kinematic analyses [*Shi et al*. 2015]. According to the present tectonic stress regime, numerical modeling based on UDEC has been performed to simulate the deformation features, block rotations, and shear stress and shear displacement on faults, and slip tendency.

3 Pre-investigations

3.1 Introduction

Geologic situations can cover quite different scales ranging from micro-scale to macro-scale. The dimensions which have to be considered in-situ are often several orders of magnitudes bigger than physical models, which can be used to validate numerical models. Also, the basic elements in DEM simulations have a certain size and the corresponding strength and stiffness parameters have to be adjusted to that size. Consequently, the scaling of numerical models is an important issue. This chapter is dedicated towards the set-up of scale-independent models including the corresponding scaling of properties. Then, a parameter study is conducted. This subchapter includes the effect of parameters on modeling results and explanation of low Young's modulus.

3.2 Principle of PFC

PFC is widely used to simulate tectonic processes such as the formation of shear zones and deformation bands [*Morgan and Boettcher*, 1999], normal faulting in layered strata [*Schöpfer et al*., 2006; *Schöpfer et al*., 2007a; *Schöpfer et al*., 2007b], and fold and thrust belts [*Burbidge and Braun*, 2002]. In contrast to continuum mechanics, some of the model properties in PFC are size-dependent. Also, the classic constitutive laws applied in continuum mechanics cannot be used in PFC and specific contact laws have to be applied. These contact laws are characterized by so-called micro-mechanical parameters, which have to be defined in such a way that they represent the observed macroscopic behavior.

In this preliminary study, PFC^{2D} is applied to model the first crack formation and pull-apart basin evolution in releasing sidesteps where dextral faults step to the right. The rocks mass in PFC^{2D} is represented by circular rigid particles which are bonded together (Figure 3.1). The particles are allowed to have very small overlaps at particle-particle contacts and particle-wall contacts. Walls are regarded as rigid boundaries. The boundary conditions such as constant velocity or stress can be given through the walls. The particles move and interact with each other via the force displacement law. The velocity and position of each particle are updated

by the law of motion. The force-displacement law is applied to each contact [*Itasca*, 2004]. In this work, the linear contact model is used. It is defined by normal stiffness (K_n) and shear stiffness (k_s), and provides an elastic relationship between the contact forces and relative displacements of particles.

$$F^n = K_n U^n \tag{3.1}$$

$$\Delta F^s = -k_s \Delta U^s \tag{3.2}$$

Where K_n and k_s are the normal and shear stiffness at the contact, respectively. For a ball-ball contact or a ball-wall contact, U^n is the overlap in the normal direction. F^n denotes the normal contact force, ΔF^s and ΔU^s represent the shear contact force increment and shear contact displacement increment, respectively.

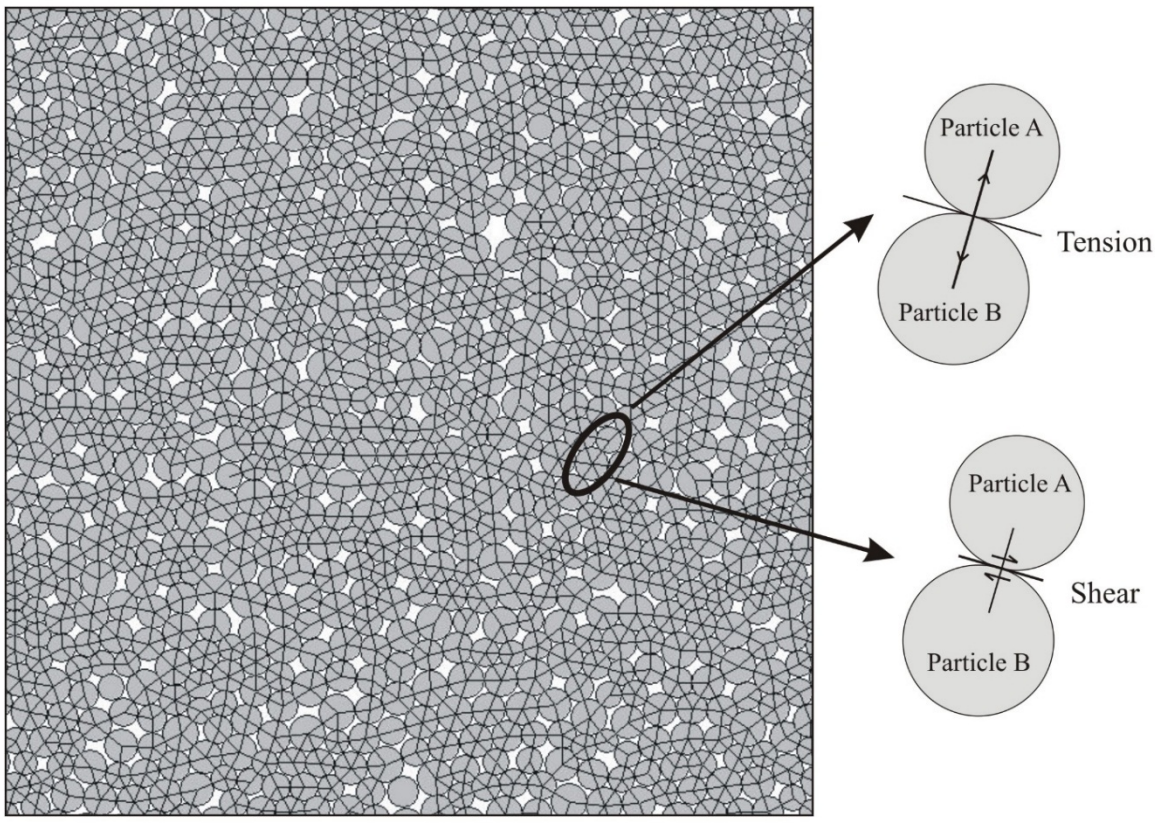

Figure 3.1 PFC^{2D} model illustrating balls and contacts. Details show contacts under tension (above) and shear (below).

Bonds can only exist between particle and particle, while bonds cannot exist between particles

and walls [*Itasca*, 2004]. In this work, the contact-bond model is defined by the parameters of normal contact bond strength (n-bond), shear contact bond strength (s-bond) as well as particle friction coefficient (μ). The contact-bond glue acts only at the contact point, and can only transmit a force [*Itasca*, 2004]. If the tensile normal force of a contact equals or exceeds the normal tensile strength, the bond breaks and both the tensile normal and shear forces are set to zero. If the shear force equals or exceeds the shear strength, and it exceeds the friction limit as well, the bond breaks and the shear force is restricted to a value governed by friction and normal force (Figure 3.2).

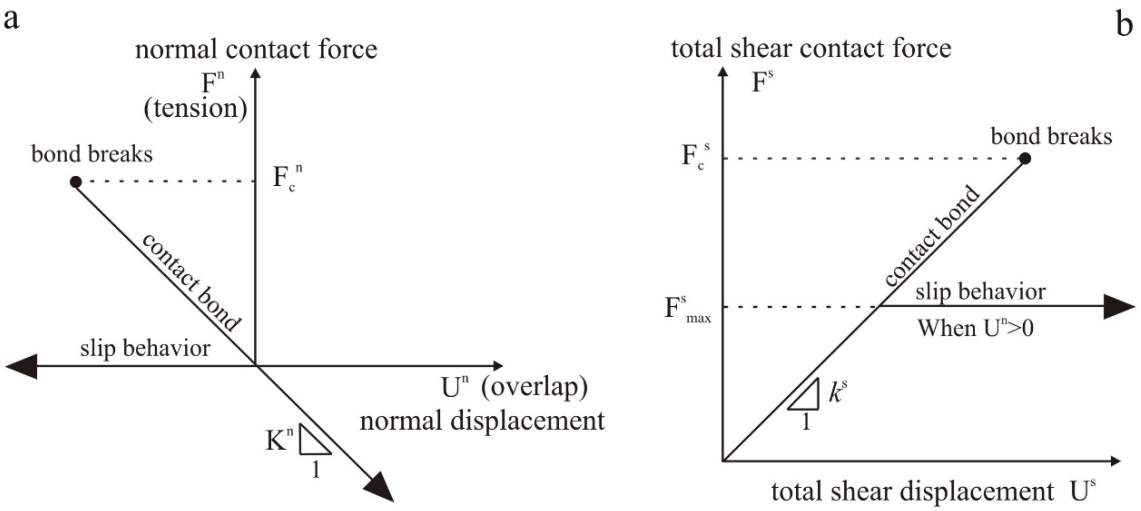

Figure 3.2 Constitutive behavior of contact-bond model: (a) normal component, (b) shear component. F_c^n and F_c^s are normal and shear contact bond strength, respectively (according to *Itasca*, 2004).

3.3 Scale-independency

As is well known, length and width of pull-apart basins in nature can be quite different and they are several orders of magnitudes bigger than physical models. For instance, the size of pull-apart basins in nature can be up to 1100 km long and 100 km wide such as the Cayman trough pull-apart basin of the Caribbean [*Mann*, 2007]. To be able to draw general conclusions and to use physical models for numerical model validation, scale-independence of the numerical simulation approach should be proven. Within this chapter scale-independency is investigated, considering model and particle size as well as scaled contact properties and applied boundary conditions.

3.3.1 General model set-up

To demonstrate scale-independency, a model with the fault overlap and underlap of zero is chosen (Figure 3.3). Five models of different scale i.e., a micro-scale, a big micro-scale, a meso-scale, a small macro-scale and a macro-scale model are set up (Table 3.1). The strike-slip faults are pre-defined. Take the micro-scale model as an example: length and width of the micro-scale model are both 3.60 m, and fault separation is 0.40 m. Model dimensions including fault separation and particle diameters were chosen in such a way that boundaries do not influence model results and pull-apart basin evolvement takes place in a natural way. Every scale model has the same particle number (189,192) and porosity (0.12). But the model size (model length and width) increases proportionally from 3.6 m (micro-scale), 36 m (big micro-scale), 360 m (meso-scale), 3 600 m (small macro-scale) to 36 000 m (macro-scale). Correspondingly, the fault separation increases from 0.4 m, 4 m, 40 m, 400 m, to 4 000 m. The particle radii also increase (Table 3.1). Model geometries are given in Table 3.1.

Table 3.1 Geometric parameters of the five scaled PFC^{2D} models.

Scale	Length* Width /m	Separation /m	Ball Radii /m	Ball number	Velocity /m·s^{-1}
Micro-scale	3.6*3.6	0.4	0.00348-0.00522	189,192	5.4
Big Micro-scale	36*36	4	0.0348-0.0522	189,192	1.8
Meso-scale	360*360	40	0.348-0.522	189,192	0.6
Small Macro-scale	3600*3600	400	3.48-5.22	189,192	0.2
Macro-scale	36000*36000	4	34.8-52.2	189,192	0.067

After the generation of the numerical model, boundary conditions are applied by walls. As an example, the meso-scale model is shown in Figure 3.3. The strike-slip movement of master faults (fault A and fault B in Figure 3.3) is modeled by moving the walls toward each other at a specified velocity. Constant normal (horizontal) velocity from right side is applied to the model through the blue walls (Walls 1, 5, and 8). Meanwhile, constant normal (horizontal) velocity from left side is applied to the other walls (Walls 3, 6, and 7). To keep the results of the different scaled models comparable, velocities of the walls in each model are scaled

according to model size (Table3.1).

For each scaled model, the macro-mechanical parameters like Young's modulus (E) and tensile strength (σ_t) are kept constant. Young's modulus of 5 MPa and tensile strength of 1 MPa are chosen for the modeling and will be discussed in detail in chapter 3.3. The corresponding micro-mechanical parameters like normal stiffness (k_n) and bond normal strength (n-bond) are deduced according to scaling relations (Table 3.2).

Table 3.2 Geometries and model parameters of the five scaled models.

	Micro-scale	Big Micro-scale	Meso-scale	Small Macro-scale	Macro-scale
Length * Width	3.6*3.6 m	36*36 m	360*360 m	3.6*3.6 km	36*36 km
Fault separation d (m)	0.4	4	40	400	400
Model length/width ratio	1	1	1	1	1
Ball size ratio d_{max}/d_{min}	1.5	1.5	1.5	1.5	1.5
Frictional coefficient μ	1.73	1.73	1.73	1.73	1.73
Young's modulus E (MPa)	5	5	5	5	5
Normal stiffness k_n (N/m)	1e7	1e7	1e7	1e7	1e7
Shear stiffness k_s (N/m)	1e7	1e7	1e7	1e7	1e7
Tensile strength σ_t (MPa)	1	1	1	1	1
Normal contact bond strength n-bond (N)	8e3	8e4	8e5	8e6	8e7
Shear contact bond strength s-bond (N)	8e3	8e4	8e5	8e6	8e7

3.3.2 Basin formation

To make crack formation and propagation visible, particles along predefined lines are marked with different colors (Figure 3.4). Figure 3.5, which is the enlarged view of the black frame in Figure 3.4a, shows the development of the first cracks and the formation of the pull-apart basin in the five different scaled models. In each of them the first cracks occur at the tips of the master faults (Fault A, Fault B). These first cracks are known as Riedel shear fractures (Riedel-shears). After more dextral strike-slip displacements, the cracks propagate and

become longer. A short rhomboidal depression is bounded by master faults and the Riedel-shears. As shown in Figure 3.5, the angel between master fault and the first cracks in each of the scaled model is almost the same. The first cracks produced by the dextral strike-slipping movement occur at the same position in the five scaled models. The crack patterns and pull-apart basin geometries generated by the different scaled models are also nearly the same.

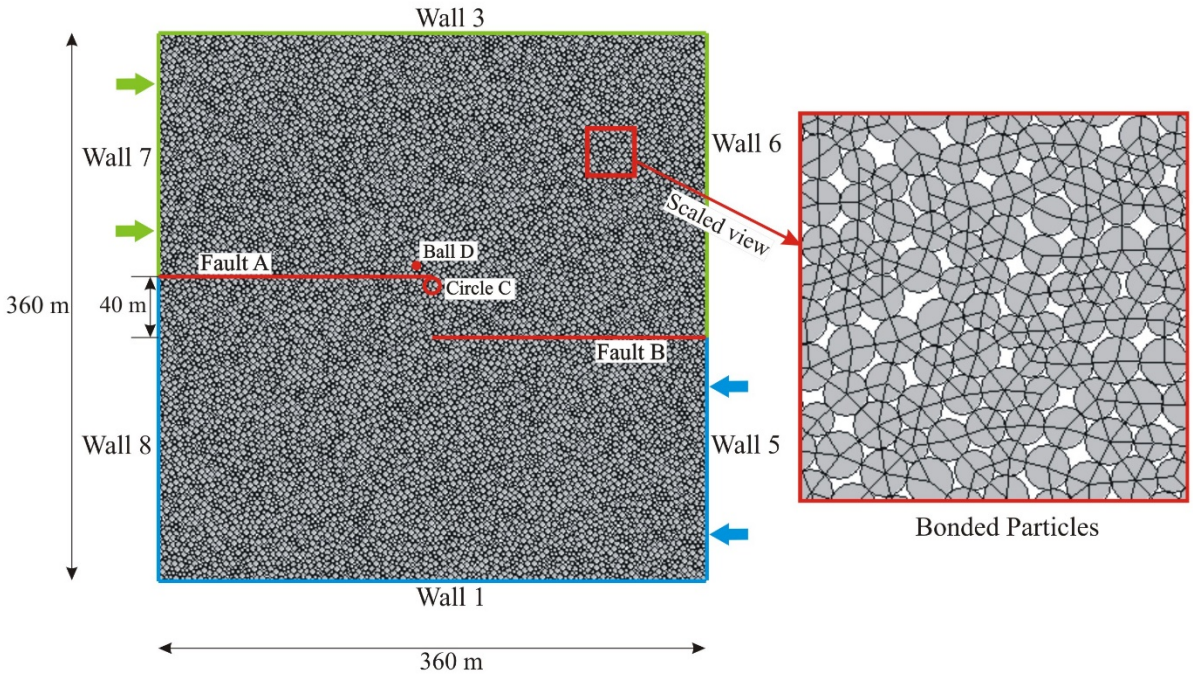

Figure 3.3 PFC^{2D} meso-scale model: fault underlap and overlap are both zero, fault A and B are predefined, circle C is the measurement circle, horizontal displacement of ball D (Ux) is measured.

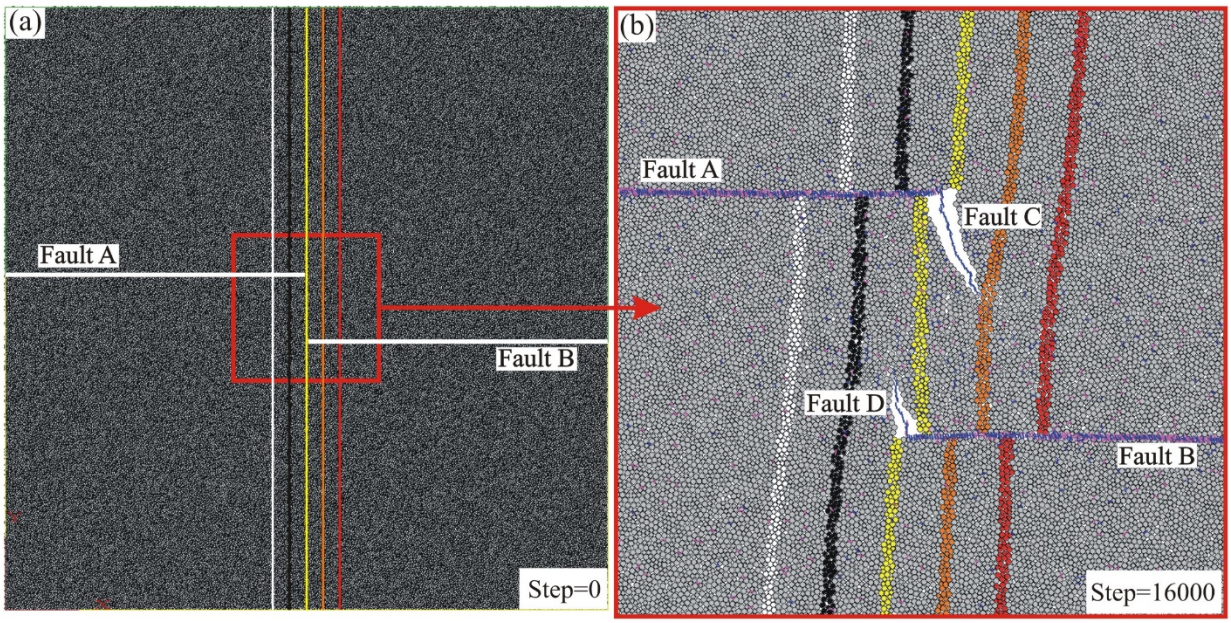

Figure 3.4 Meso-scale model: (a) Plan view of the model at the beginning of the simulation (step=0), (b) Enlarged view of the red frame at later stage of simulation (step=16000).

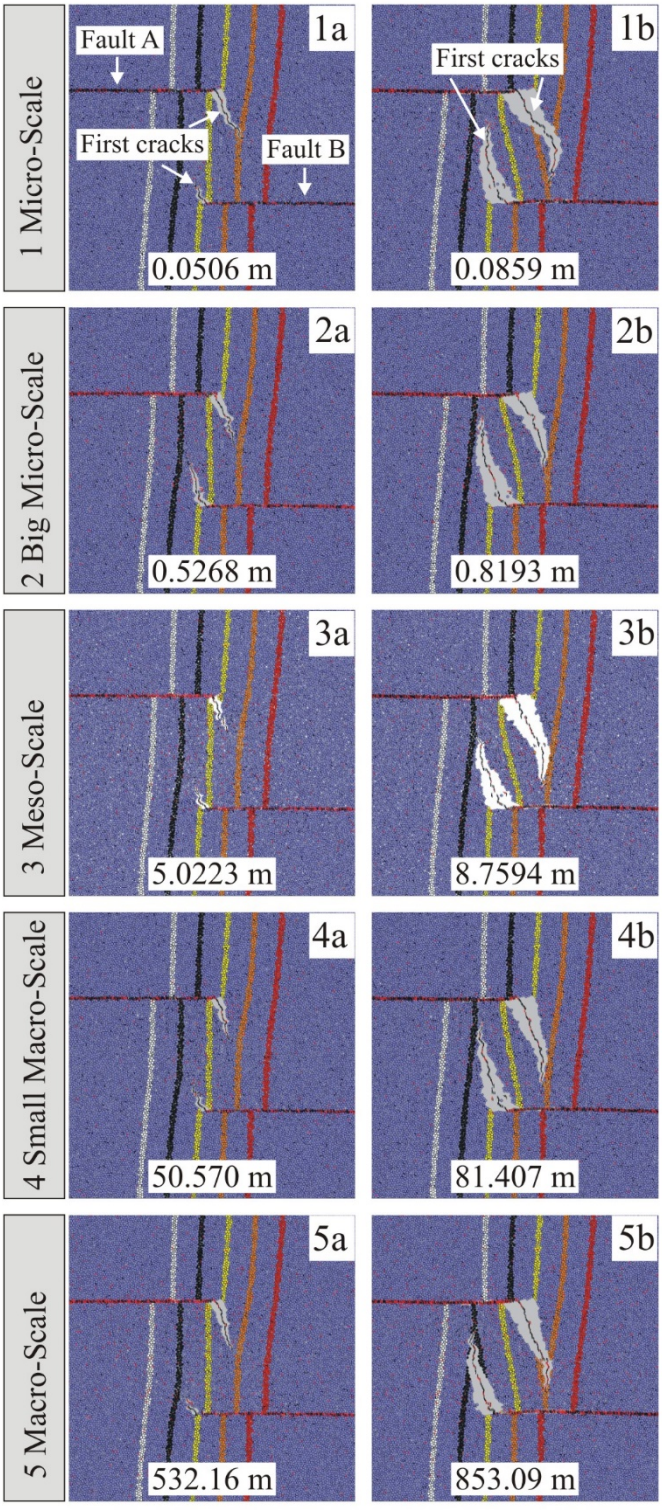

Figure 3.5 Evolution of pull-apart basins at different scales. Early stage (a) and advanced stage (b) with corresponding displacements Ux.

3.3.3 Stress-deformation behavior

During the modeling, the average values of horizontal normal stress (σ_{11}), vertical normal stress (σ_{22}) and shear stress (σ_{12}) in measurement Circle C located at the point where crack propagation starts are monitored (Figure 3.6). The average major principal stress (σ_1) is calculated according to Eq. 3.3.

$$\sigma_1 = \frac{\sigma_{11} + \sigma_{22}}{2} + \frac{1}{2}\sqrt{(\sigma_{11} - \sigma_{22}) + 4\sigma_{12}^2} \tag{3.3}$$

Relative extension (ε_x^*) is defined by Eq. 3.4.

$$\varepsilon_x^* = \frac{U_x}{d} \tag{3.4}$$

U_x is the horizontal displacement of Ball D (ball located at the point near fault tip) and d refers to the amount of fault separation (Figure 3.6). Relative extension (ε_x^*) is defined by horizontal opening divided by fault separation. $\varepsilon_x^*{}_{max}$ donates the relative extension (ε_x*) when the peak stress is reached.

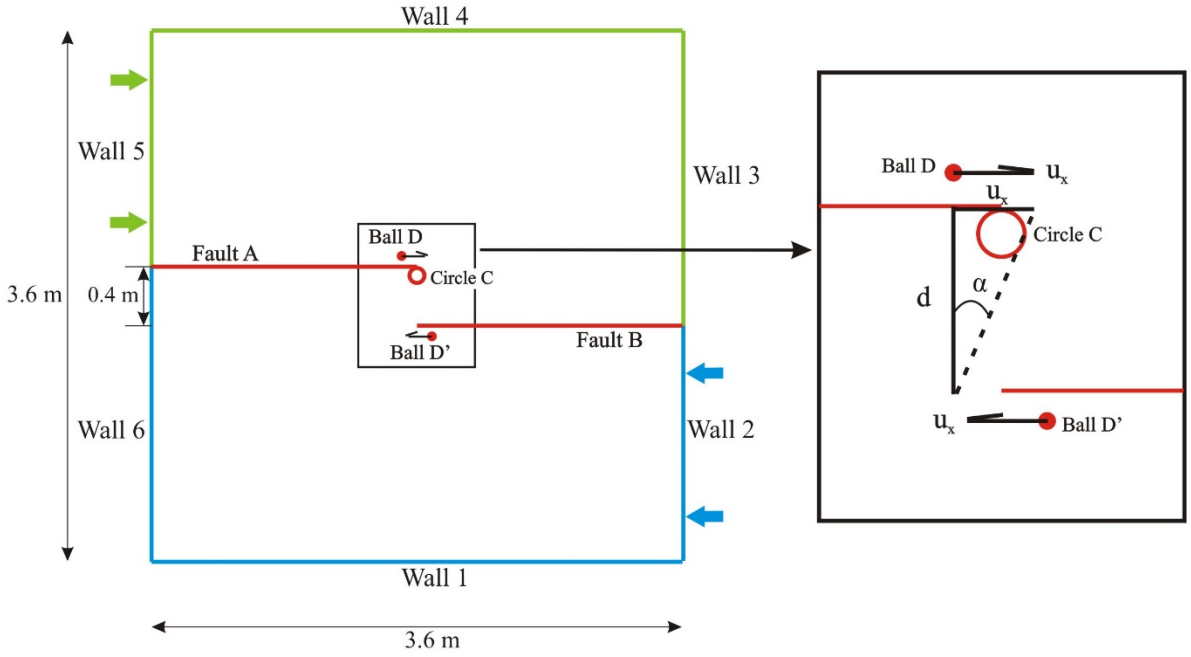

Figure 3.6 PFC^{2D} model indicating the positons of Ball D and Circle C. U_x is the horizontal displacement of ball D and d refers to the amount of fault separation.

Horizontal normal stress - relative extension curve (σ_{11}-ε_x* curve)

Figure 3.7 shows relationship between horizontal normal stress (σ_{11}) and relative extension (ε_x^*) for the micro-scale model. At the initial modeling stage (section OM), the value of σ_{11} is negative, which represents compression in Circle C during this stage. When ε_x^* becomes 0.04 (point M), the value of horizontal normal stress (σ_{11}) is zero. When ε_x^* is larger than 0.04, σ_{11} becomes positive, and the horizontal normal stress σ_{11} at Circle C changes from compression to tension. At the first tension stage (section MP), the value of σ_{11} increases with the relative extension ε_x^*. When ε_x^* has reached 0.0804, the peak stress σ_{11} is 0.26 MPa (Point P), and the first cracks at Circle C begin to appear. During the fracture evolution stage (section PN), σ_{11} suddenly drops down to zero. After point N, σ_{11} at measurement Circle C becomes very small ($\sigma_{11} \approx 0$).

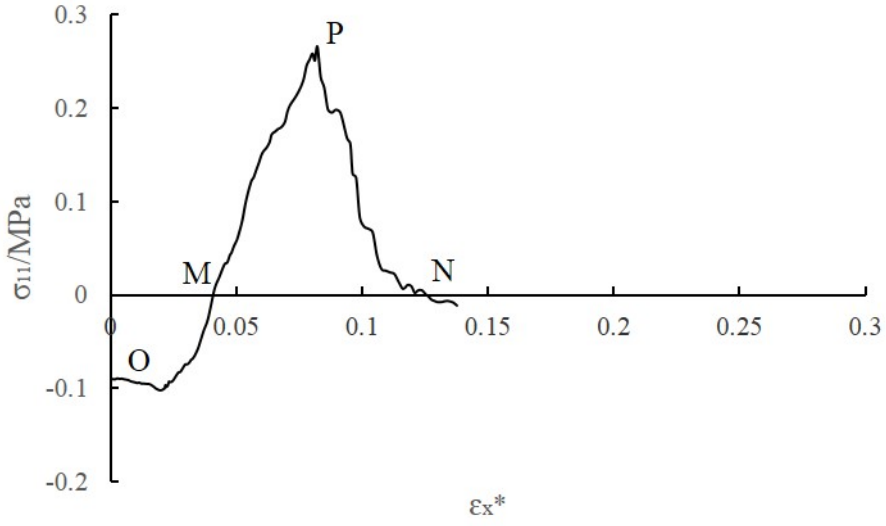

Figure 3.7 Horizontal normal stress (σ_{11}) versus relative extension (ε_x^*) for the micro-scale model ($\sigma_{11} > 0$: tension; $\sigma_{11} < 0$: compression).

The curves of horizontal normal stress (σ_{11}) and relative extension (ε_x*) measured for each scaled model are illustrated in Figure 3.8. All the five scaled models show nearly the same behavior in respect to the σ_{11}- ε_x*curve. In addition, at point P when peak stress is reached, the ε_x* value of each scaled model is very similar. This reveals that when the value of ε_x*is about 0.075 in each scaled model cracks begin to occur. Moreover, after the first cracks appear, σ_{11} decreases significantly and becomes zero in all the five scale models.

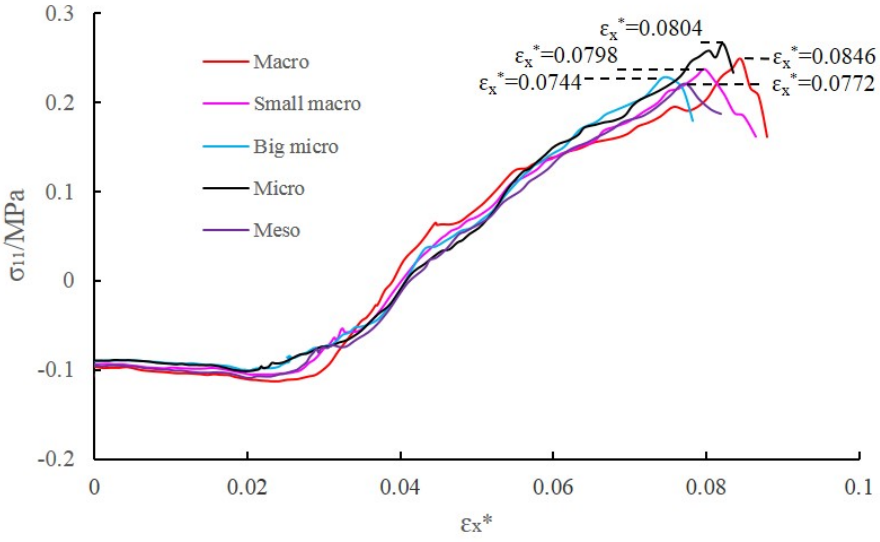

Figure 3.8 Horizontal normal stress versus relative extension for the five scaled models ($\sigma_{11} > 0$: tension; $\sigma_{11} < 0$: compression).

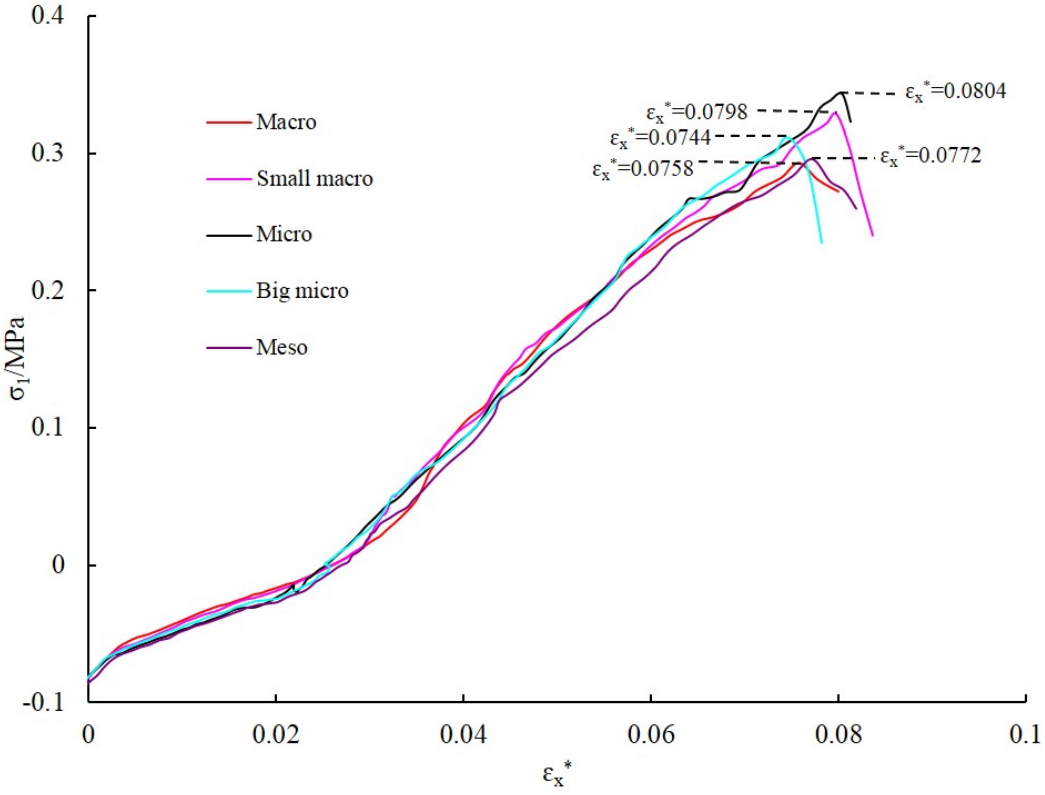

Figure 3.9 Major principal stress versus relative extension for the five scaled models ($\sigma_1 > 0$: tension; $\sigma_1 < 0$: compression).

Major principal stress-relative extension curve (σ_1-ε_x^*curve)

Major principal stress (σ_1) and relative extension (ε_x^*) measured for each model are illustrated in Figure 3.9. As shown in Figure 3.9, each scaled model produces nearly the same σ_1-ε_x^* curve, although the model areas are different up to eight orders of magnitude. Figure 3.9 also indicates that when ε_x^* reaches a value of about 0.075 ($\varepsilon_{x\,max}^* \approx 0.075$), peak stress is reached and fracture propagation starts.

Comparison of σ_1-ε_x* curves in different measure circles

Stresses are based on continuum mechanical concepts. In contrast, DEM based particle modeling is based on contact forces, and therefore, stresses have to be deduced by integration of forces over a certain volume. To get meaningful stress values, the average stress state within a circle (2D) can be measured by a stress homogenization method [*Potyondy and Cundall*, 2004]. As shown in Figure 3.10, four circles with different radius are chosen to measure the major principal stress (σ_1) whereas the same ball (ball D) is chosen to measure relative extension (ε_x^*). Circle 1 is identical with circle C in Figure 3.6. Circles 2, 3 and 4 are chosen randomly. Moreover, Circle 3 has the same radii as circle 1, while Circle 2 and Circle 4 have radius twice as big as Circle 1.

Let us take micro-scale, meso-scale and macro-scale models as examples. Figure 3.11 shows the curves of major principal stress (σ_1) and relative extension (ε_x^*) for each scaled model in different circles. The three different scaled models show nearly the same behavior in respect to σ_1 versus ε_x^* in each circle. It can be concluded that the σ_1-ε_x^*curves of the different scaled models show great similarities, no matter where the stress is measured.

This chapter investigated the effect of model scale and particle size on the simulation results. Even though the five scaled models have different dimension and particle sizes, the behavior is almost the same or in other words scale-independent. Therefore, further modeling to simulate the formation and development of large-scale pull-apart basins in nature can be restricted to micro-scale models.

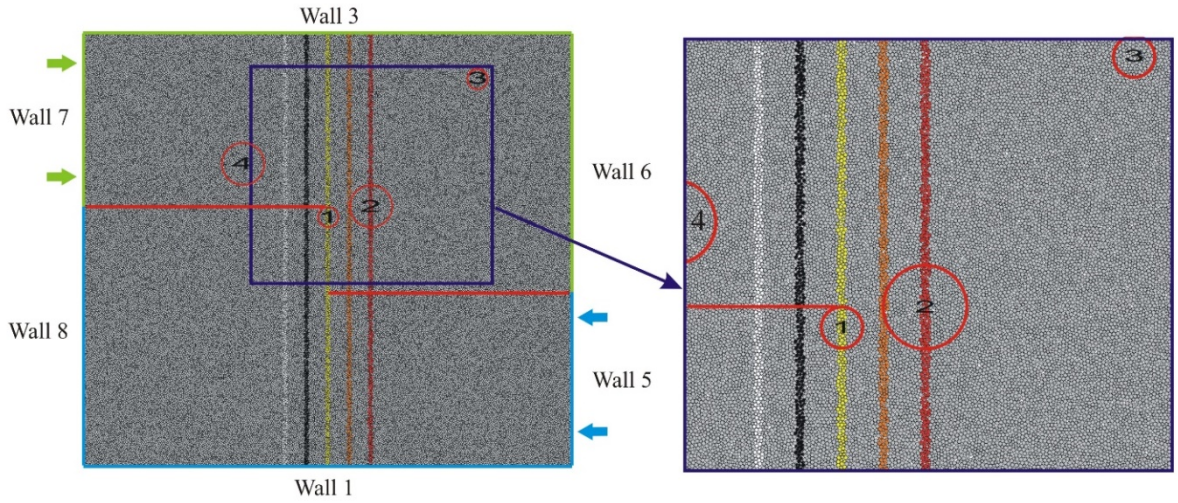

Figure 3.10 The positions of measured circles 1, 2, 3 and 4 in each scaled model. Circle 1 is the same with Circle C in Figure 3.6.

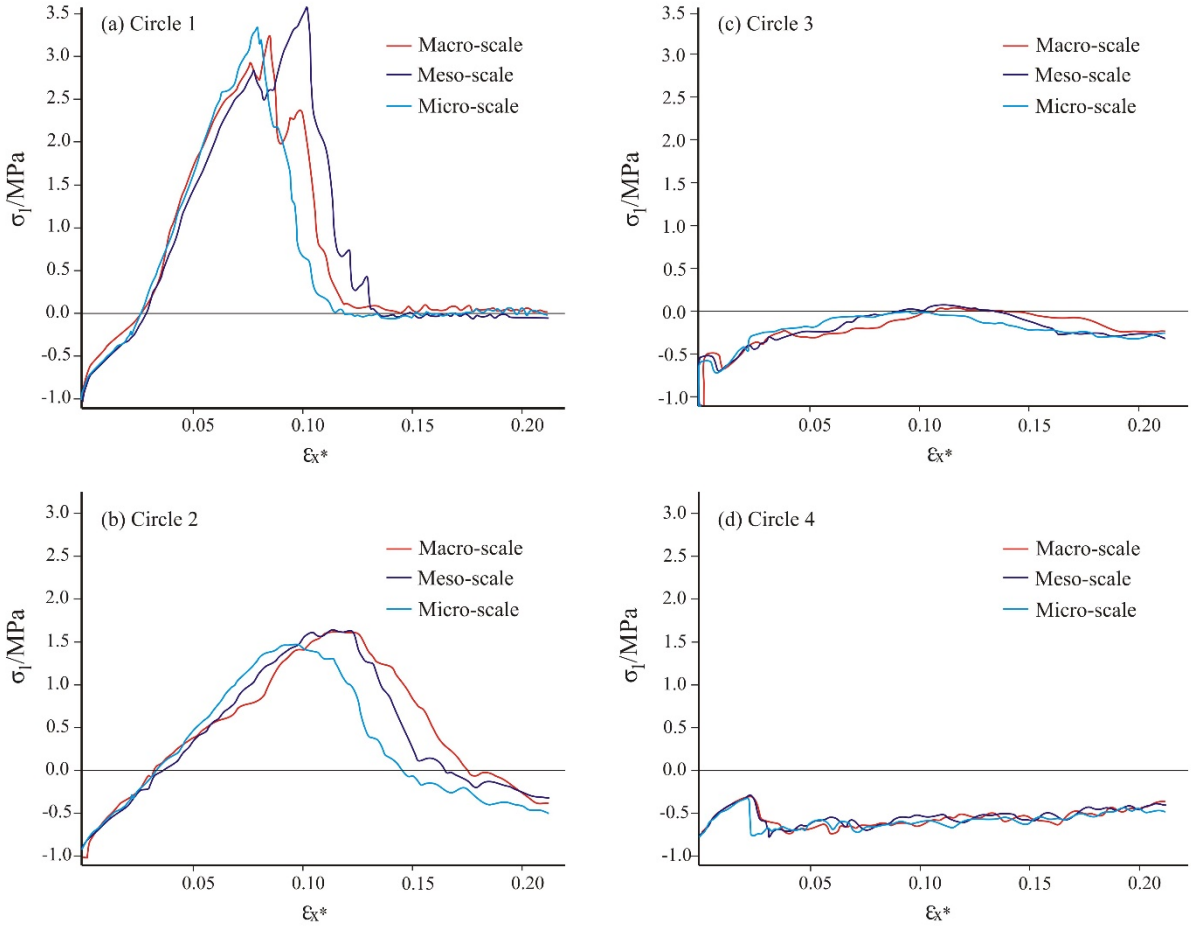

Figure 3.11 Comparison of σ_1 - ε_x^* curves for three scaled models (micro-scale, meso-scale, macro-scale) for different circles (Circles 1, 2, 3, and 4; $\sigma_1 > 0$: tension, $\sigma_1 < 0$: compression).

3.4 Parameter study

Based on the scale-independency within this chapter, we consider only a micro-scale model according to Table 3.2 with 90° non-overlapping releasing sidestep. Microscopic contact parameters in our models are chosen in such a way that they match general mechanical parameters of rock masses. Eq. 3.5 and Eq. 3.6 are used to estimate the micro-parameters like particle stiffness and bond strength [*Itasca*, 2004].

$$E = k_n / (2t) \tag{3.5}$$

$$\sigma_t = S_n / (2Rt) \tag{3.6}$$

E is the Young's modulus of the rock mass and k_n is the particle normal stiffness. S_n is the normal strength of the contact bond (n-bond), R is the particle radius and σ_t is the tensile strength of the rock mass. A unit thickness of t=1 is used in all models. Eq. 3.5 shows that Young's modulus is direct proportional to particle stiffness and has no relationship with particle radius. Eq. 3.6 indicates that tensile strength is direct proportional to bond normal strength and inverse proportional to the particle radius.

3.4.1 Effect of Young's modulus on fault pattern and basin geometry

Figure 3.12 shows the fault geometries of 18 models with different values of Young's modulus (E) and different ratios of normal to shear stiffness (k_n/k_s). Figure 3.12a presents models with Young's modulus of 5, 10, 25, 50, 250, and 500 MPa. According to Eq. 3.5, the corresponding values of normal stiffness (k_n) are 1e7, 2e7, 5e7, 1e8, 5e8, and 1e9 N/m, respectively. The other parameters of these models are the same including the tensile strength of 1 MPa. When Young's modulus is 5 MPa, the first cracks occur at the tips of the master faults and a short rhomboid pull-apart basin occurs. Cracks formation and pull-apart basin geometries match well with the sandbox modeling results [*Dooley and McClay*, 1997]. The acute angle between master faults and the first cracks is about 70°. When the Young's modulus is 25 MPa, crack pattern and basin geometry are nearly the same, but the acute angle decreases to about 50°. When the Young's modulus is larger than 25 MPa, crack patterns are quite different and pull-apart basins cannot form. Therefore, for further modeling either 5 or 25 MPa were chosen for the Young's modulus (see also chapter 3.4.3 for further explanation).

Six different normal and shear stiffness ratios, i.e., k_n/k_s = 0.1, 0.5, 1, 2, 5 and 10 are considered (Figure 3.12b, Figure 3.12c). The results in Figure 3b indicate that the ratio of normal to shear stiffness has no significant effect on the model results when the normal stiffness is fixed at 1e7 N/m, which corresponds to a Young's modulus of 5 MPa. The calculation cases shown in Figure 3.12c are similar to those shown in Figure 3.12a. In other words, it is the normal stiffness rather than the ratio of normal to shear stiffness that plays the dominant role in crack evolution and basin formation. This makes sense if we take into account that the pull-apart basin formation is dominated by tensile fracturing.

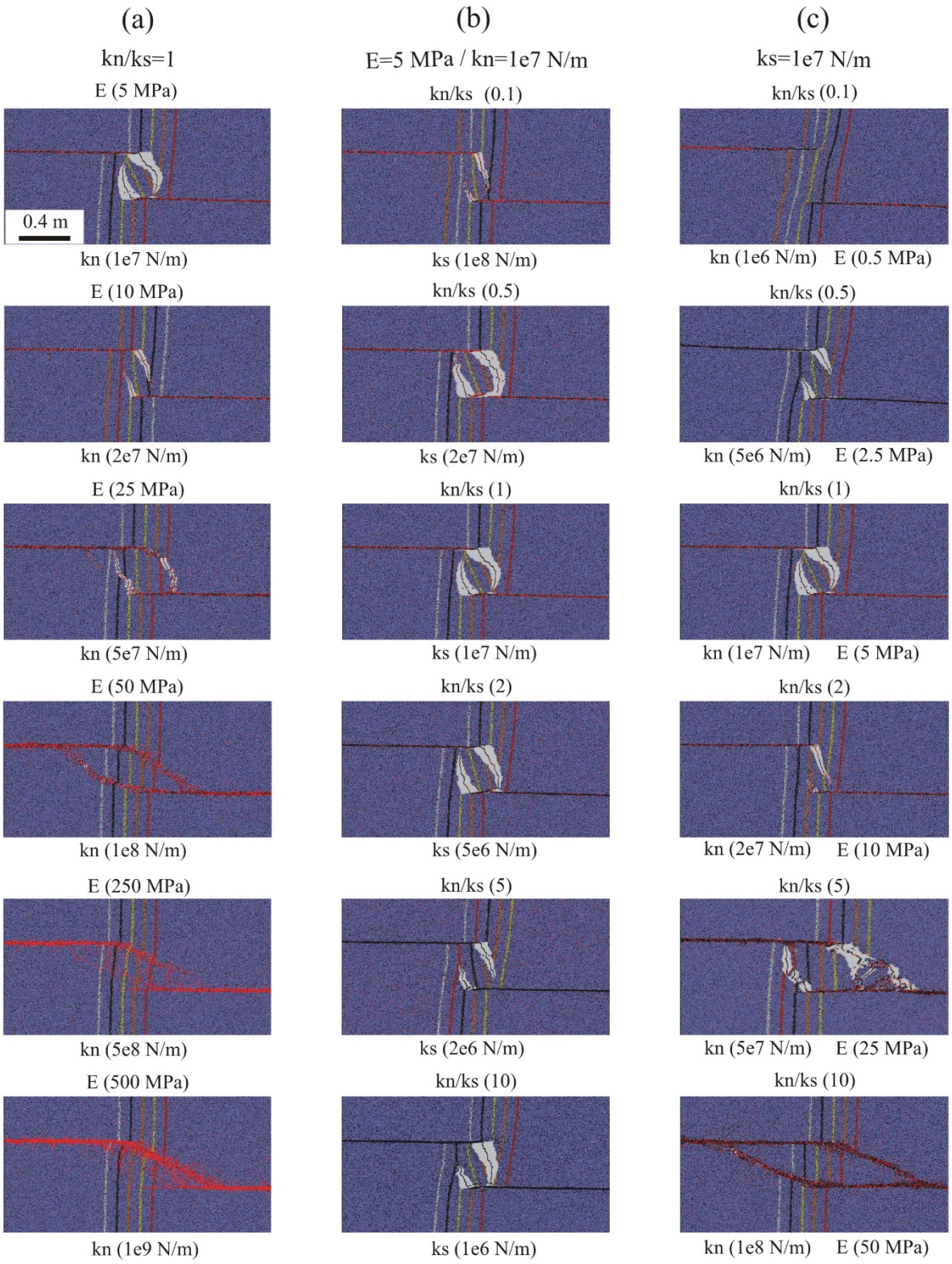

Figure 3.12 Fault geometries of models with different values of Young's modulus (E) and different ratios of normal to shear stiffness (k_n/k_s).

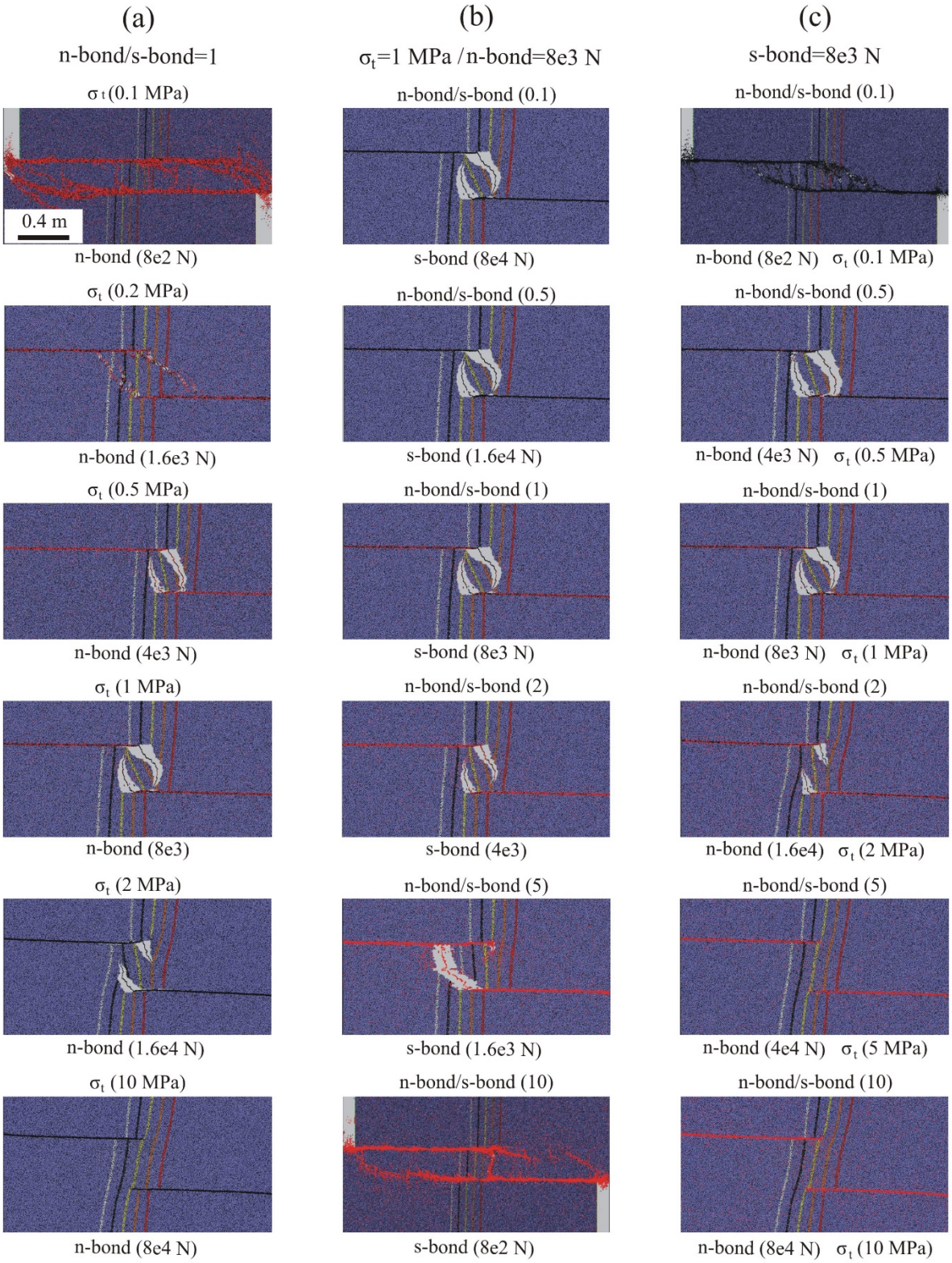

Figure 3.13 Fault geometries of models with different values of tensile strength (σ_t) and different ratios of normal to shear contact bond strength (n-bond/s-bond).

3.4.2 Effect of tensile strength on fault pattern and basin geometry

Figure 3.13 shows the fault geometries of the 18 models with varying tensile strength (σ_t) and different ratios of normal to shear contact bond strength (n_b/s_b). Figure 3.13a shows the crack generation and basin geometries for tensile strength of 0.1, 0.2, 0.5, 1, 2 and 10 MPa. Based on Eq. 3.6, the corresponding normal contact bond strength (n-bond) are 8e2, 1.6e3, 4e3, 8e3, 1.6e4, and 8e4 N, respectively. Young's modulus is 5 MPa and other parameter are unchanged. When the tensile strength is about 0.5 to 2 MPa, a short rhomboid pull-apart basin occurs with development of first cracks. The acute angle between master faults and the first cracks is about 70°. When the tensile strength is only 0.2 MPa, crack pattern and basin geometry are nearly the same, but the acute angle decreases to about 50° (Figure 3.13a). When the tensile strength is large, e.g. 10 MPa, which is even larger than the Young's modulus, cracks cannot form.

Six different ratios of normal to shear contact bond strength of 0.1, 0.5, 1, 2, 5, and 10, are also tested. Figure 3.13b shows six cases with the same normal contact bond strength but different shear contact bond strength. Figure 3.13c presents six models with the same shear contact bond strength but different normal contact bond strength. The results indicate that ratios of normal to shear contact bond strength equal or smaller than 1 show a behavior similar to those observed during sandbox tests [Dooley and McClay, 1997].

3.4.3 Explanation of low Young's modulus

Young's modulus of 5 and 25 MPa, respectively, are used for the simulations. Interestingly, significant higher or lower values for the Young's modulus cannot reproduce correct pattern for the pull-apart basin formation (see also chapter 3). The following arguments give an explanation for this phenomenon. Young's modulus, or more generally speaking the deformation modulus, of rocks tested in the laboratory on small samples is typically in the order of 1 to 50 GPa. The value is somewhat lower (may be up to one order of magnitude) if we consider rock masses at large scale including different kinds of discontinuities. On the other hand, geologic processes considered within this thesis are time-dependent and the rheological (viscous) behavior of the rock mass should be taken into account. According to

previous geologic studies [*Kaufmann and Amelung*, 2000; *Vergnolle et al*., 2003; *Hilley et al*., 2005; *Rousset et al*., 2012] and rheological rock mechanical lab tests [*Itô*, 1979; *Rosenberg*, 2001; *Bürgmann and Dresen*, 2008], the viscosity η of the crust is in the order of about 10^{19} to 10^{21} Pa·s. The simplest expression to describe viscous stress-strain behavior is given by Eq. 3.7. If we rearrange Eq. 3.7 and replace differential quotient (dt) by differences (Δt), Eq. 3.8 can be obtained.

$$\sigma = \eta \frac{d\varepsilon}{dt} \tag{3.7}$$

$$\Delta t = \eta \frac{\Delta\varepsilon}{\sigma} \tag{3.8}$$

Based on stress and deformation at the point when peak stress is reached, which corresponds to the onset of the pull-apart basin formation, we can estimate the duration until pull-apart basin formation starts (Eq. 3.8). Our models give a consistent value for Δε/σ of about 2.3×10^{-7} Pa^{-1} (Table 3.3). If we multiply this value with a realistic viscosity η of the crust (10^{19} to 10^{21} Pa·s), the corresponding time to form first cracks is in the order of 10^4 to 10^6 years (Eq. 3.8), which is in close agreement with geologic considerations [*Deng et al*., 1989; *IG and SBNHAP*, 1990]. Consequently, the low value for the chosen Young's modulus can be justified by the viscous nature of the geologic process.

Table 3.3 Values of Δε/σ for the five scaled models

	Micro-scale	Big Micro-scale	Meso-scale	Small Macro-scale	Macro-scale
Δε	0.0804	0.0924	0.1017	0.0798	0.0846
σ /(Pa)	343040	338580	372290	328914	325989
Δε/σ /Pa^{-1}	2.34×10^{-7}	2.73×10^{-7}	2.73×10^{-7}	2.43×10^{-7}	2.60×10^{-7}

Table 3.4 Micro-parameters for subsequent documented models

Normal stiffness k_n (N/m)	Shear stiffness k_s (N/m)	Normal contact bond strength n-bond (N)	Shear contact bond strength s-bond (N)
5e7	5e7	8e3	8e3

3.5 Conclusions

Firstly, this chapter investigated the effect of model scale and particle size on the simulation results, including the generation of the first cracks, the formation and development of pull-apart basins and the stress-deformation curves for each of the scaled models. Even though the five scaled models have different dimensions and particle sizes, the behavior is almost the same or in other words the applied procedure is scale-independent. Therefore, further modeling is restricted to the micro-scale models to investigate the evolution of large-scale pull-apart basins in nature.

Later on, a parameter study has been conducted. The parameter study revealed that a ratio of Young's modulus to tensile strength of about 5 leads to crack formation and pull-apart basin geometries which match well the sandbox tests [*Dooley and McClay*, 1997] with an acute angle of about 70°. When the ratio between Young's modulus and tensile strength is about 25, the acute angle decreases to about 50° whereby fracture pattern and basin geometry still match the sandbox tests. However, models with Young's modulus of 25 MPa and tensile strength of 1 MPa produce better basin evolution processes.

Therefore, Young's modulus of 25 MPa and tensile strength of 1 MPa were considered in subsequent documented models. The corresponding normal stiffness (k_n) and shear stiffness (k_s) are 5e7 N/m, and the corresponding normal contact bond strength (n-bond) and shear contact bond strength (s-bond) are 8e3 N (Table 3.4).

4 Numerical simulation of pull-apart basin development

4.1 Introduction

Nature is complex. Pull-apart basins in nature can form in different tectonic settings. To reproduce the evolution of natural basins, the micro-scale PFC models are used in this chapter to investigate crack formation and propagation, basin development of pull-apart basins formed in releasing sidesteps with pure strike-slip, transtensional, and transpressional master fault systems, respectively. In each system, three typical models including 30° underlapping, 90° non-overlapping, and 150° overlapping releasing sidestep are chosen. This chapter also compares the crack propagation and basin geometries for each system. Finally, the formation and development of pull-apart basins which form in releasing sidestep with three or more parallel fault strands are studied.

Moreover, a parameter study in terms of different particle radii as well as various mechanical parameters has been conducted to test robustness and stability of the numerical simulations. 30° underlapping releasing sidestep models with pure strike-slip have been selected for the robustness analyses.

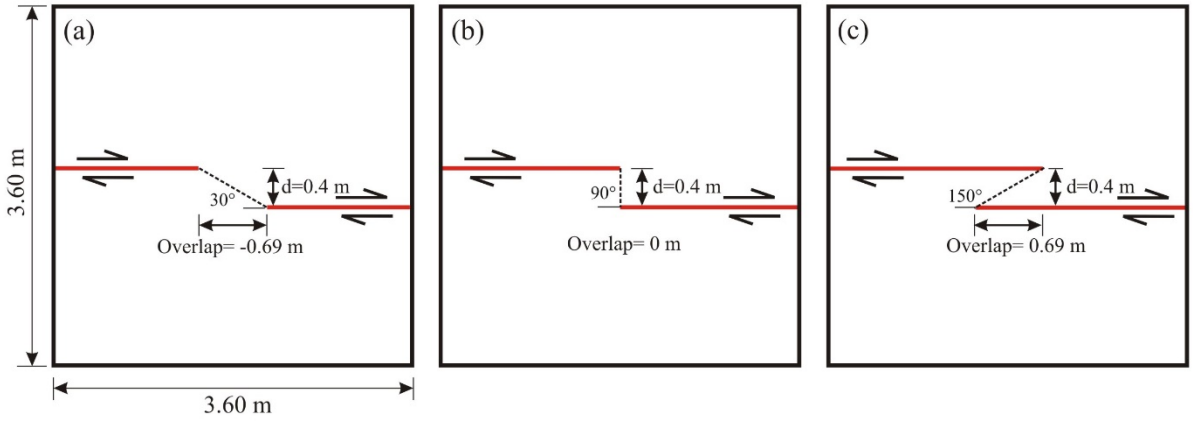

Figure 4.1 Models with different overlaps between master faults for pure strike-slip: (a) 30° underlapping releasing sidestep, (b) 90° non-overlapping releasing sidestep, (c) 150° overlapping releasing sidestep.

4.2 Pure strike-slip

4.2.1 Model set-up

Two-dimensional micro-scale models with length and width of both 3.6 m are chosen to model the evolution of pull-apart basins with pure strike-slip. Three representative models [*Dooley and McClay*, 1997], i.e., 30° underlapping releasing sidestep, 90° non-overlapping releasing sidestep and 150° overlapping releasing sidestep are selected (Figure 4.1). The overlap of the two master faults are -0.69 m, 0 m and 0.69 m, respectively. Fault separation is fixed at 0.40 m to allow direct comparison of simulation results between these three cases.

4.2.2 Pull-apart basin development

30° underlapping releasing sidestep model

Figure 4.2 shows the contact force distribution and crack evolution which is observed in the 30° underlapping releasing sidestep model. Three characteristic stages of crack development are detected, i.e. before peak stress, at peak stress, and after peak stress (always measured in circle C, Figure 3.6). Before the peak stress is reached, tensile contact forces reach maximum at the tips of the master faults. Later on, crack propagation starts and maximum tensile forces concentrate near the new crack tips.

Figure 4.3 presents the development in a sequence for the 30° underlapping model, including contact force distribution (1a-1e), crack propagation (2a-2e), particle distribution (3a-3e) and crack interpretation (4a-4e). During the initial evolution stage (0-0.0126 m strike-slip displacement), the peak stress is not yet reached, and tensile contact forces reach maximum at the tips of the master faults. When the peak stress is reached (underlapping-30°, Figure 4.8), first cracks begin to occur at the tips of the master faults. The first cracks in this study are the so-called right-lateral Riedel-shear fractures which occur at the very beginning of the evolution (4a, Figure 4.3). Later on, the Riedel-shears propagate (Stage a, Figure 4.3). At around 0.0666 m of strike-slip displacement, the Riedel-shears link with the tips of the master faults, forming a spindle-shaped area of subsidence (Stage b, Figure 4.3). At about 0.1899 m of right-lateral strike-slip offset, basin sidewalls form, bounding a lazy-Z-shaped pull-apart basin (Stage c, Figure 4.3). The master faults are linked by the cross-basin faults (red lines in

4c, Figure4.3). The term “lazy-Z-shaped” is used for basins between right-lateral faults and the term “lazy-S-shaped” is used for basins between left-lateral faults.

From the modeling point of view, as displacement increases, particles in the model are carried outward, the area bounded by the Riedel-shears becomes empty, and the crack propagation in this area cannot be duplicated in a complete manner. However, the basin sidewalls and the depression area geometries are still meaningful. Therefore, with further strike-slip offset (0.1899-0.3999 m), basin sidewalls move outward and the basin lengthen, forming a rhomboidal pull-apart basin (Stage d, Figure 4.3). With continued right-lateral strike-slip displacement, rhomboidal pull-apart basin lengthens to a stretched rhomboidal basin (Stage e, Figure 4.3). With further offset, the stretched rhomboidal basin may lengthen indefinitely, forming an extreme pull-apart basin with a ratio between basin length and width of more than 10. This extreme example exists in nature such as the Cayman trough pull-apart basin of the Caribbean which is 1100 km long and 100 km wide [*Mann*, 2007].

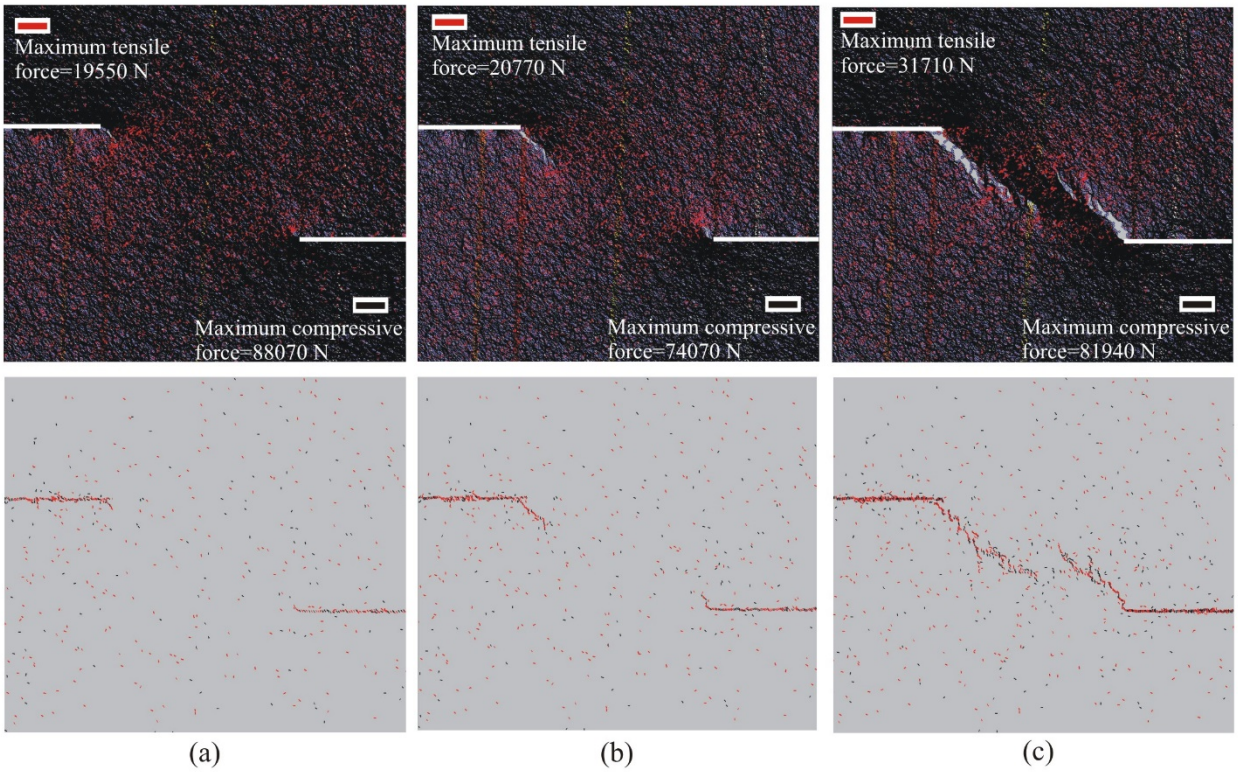

Figure 4.2 Contact force evolution and crack development of 30° underlapping releasing sidestep model for pure strike-slip: (a) before peak stress, (b) at peak stress, (c) after peak stress.

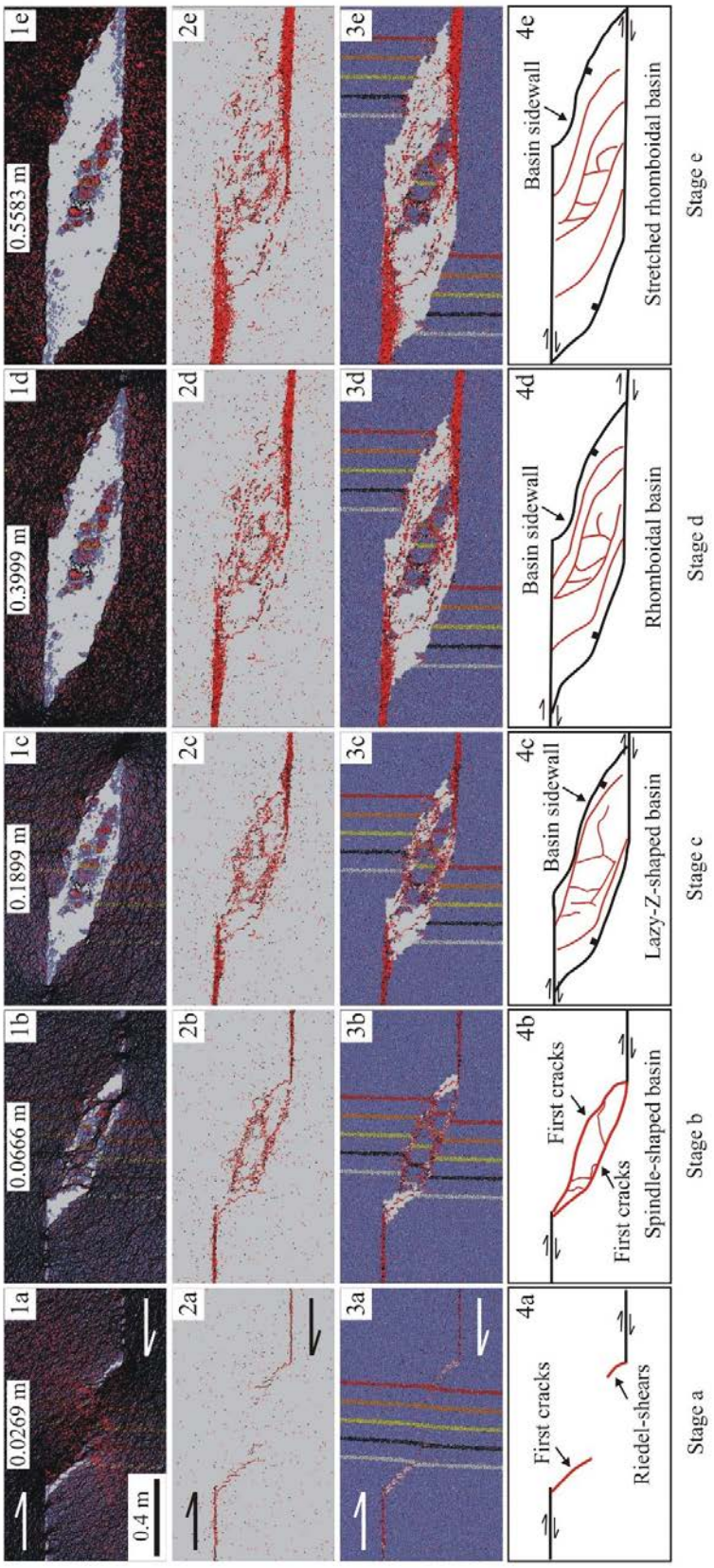

Figure 4.3 Evolution of 30° underlapping releasing sidestep model for pure strike-slip. 1a-1e: contact force distribution; 2a-2e: crack propagation; 3a-3e: particle distribution with crack propagation; 4a-4e: crack interpretation and basin geometry evolution. The evolution stages of a-e correspond to different displacements of ball D (Ux).

90° non-overlapping releasing sidestep model

Contact force distribution and crack propagation of the 90° non-overlapping releasing sidestep model are presented in Figure 4.4. Before peak stress is reached (0 - 0.0153 m strike-slip displacement), the tensile contact forces reach maximum at the tips of the two master faults. Then, cracks propagate and maximum tensile forces concentrate near the new crack tips.

Figure 4.5 shows the development of pull-apart basin for the 90° non-overlapping releasing sidestep model. When the peak stress is reached (non-overlapping-90°, Figure 4.8), first cracks (Riedel-shears) develop. Later on, with increased strike-slip offset, the Riedel-shears propagate. The Riedel-shears not only form at the tips of the master faults, but also intersect with the master faults (Stage a, Figure 4.5). At about 0.0681 m of strike-slip displacement, the Riedel-shears link with the master faults, forming a rhomboidal area of depression (Stage b, Figure 4.5). With further strike-slip offset, basin sidewalls move outward and the rhomboidal pull-apart basin lengthens (Stage c-Stage e, Figure 4.5).

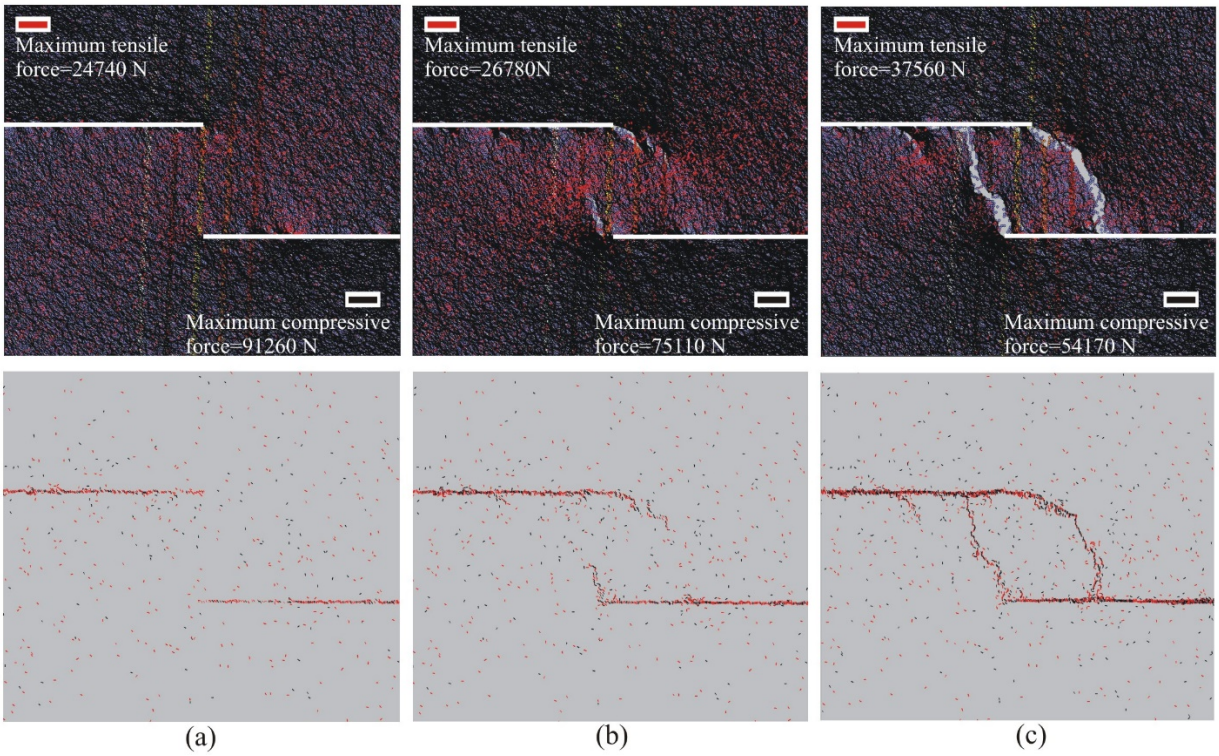

Figure 4.4 Contact force evolution and crack development of 90° non-overlapping releasing sidestep model for pure strike-slip: (a) before peak stress, (b) at peak stress, (c) after peak stress.

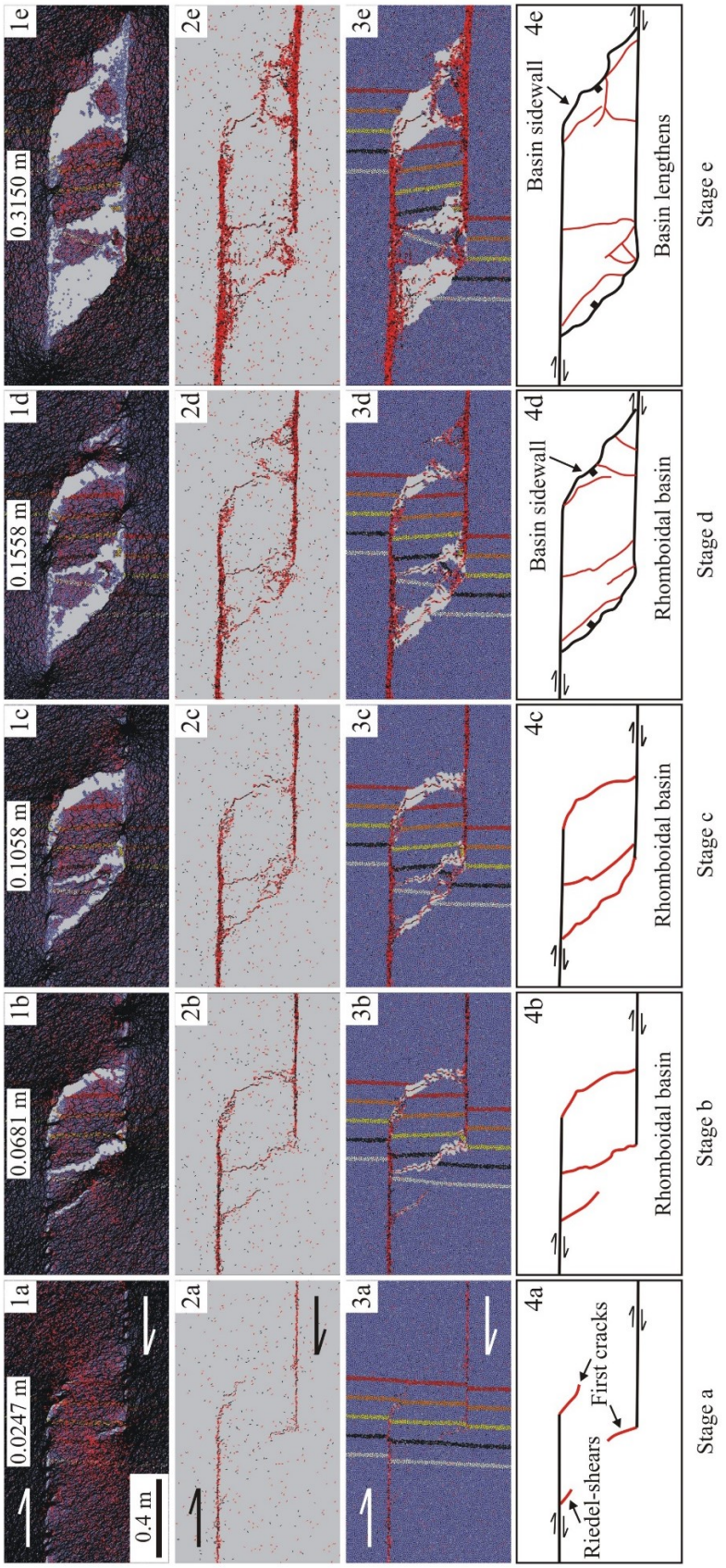

Figure 4.5 Evolution of 90° non-overlapping releasing sidestep model for pure strike-slip. 1a-1e: contact force distribution; 2a-2e: crack propagation; 3a-3e: particle distribution with crack propagation; 4a-4e: crack interpretation and basin geometry evolution.

150° overlapping releasing sidestep model

Contact force distribution and crack evolution of the 150° overlapping model at different representative stages are shown in Figure 4.6. Before peak stress is reached, concentration of tensile contact forces at the tips of the master faults is observed. As shown in Figure 4.6b, when peak stress is reached, cracks initiate at the tips of the two master faults, and maximum tensile force concentrates near the new crack tips.

Figure 4.7 illustrates the evolution of 150° overlapping releasing sidestep model in a plane view. With increased strike-slip offset, the Riedel-shears propagate continuously (Stage a-Stage c, Figure 4.7). At about 0.0623 m of strike-slip offset, the Riedel-shears link with the master faults, forming a rhomboidal area of subsidence (Stage c, Figure 4.7). With further strike-slip offset, basin sidewalls move outward and the rhomboidal pull-apart basin lengthens (Stage d-Stage e, Figure 4.7).

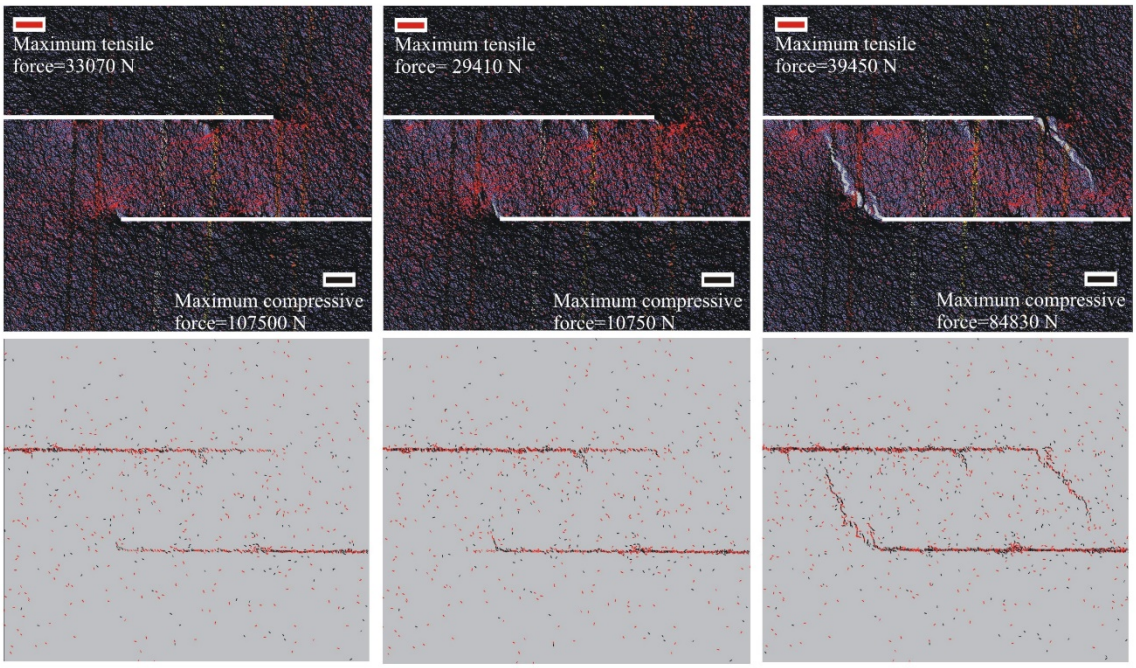

Figure 4.6 Contact force evolution and crack development of 150° overlapping releasing sidestep model for pure strike-slip: (a) before peak stress, (b) at peak stress, (c) after peak stress.

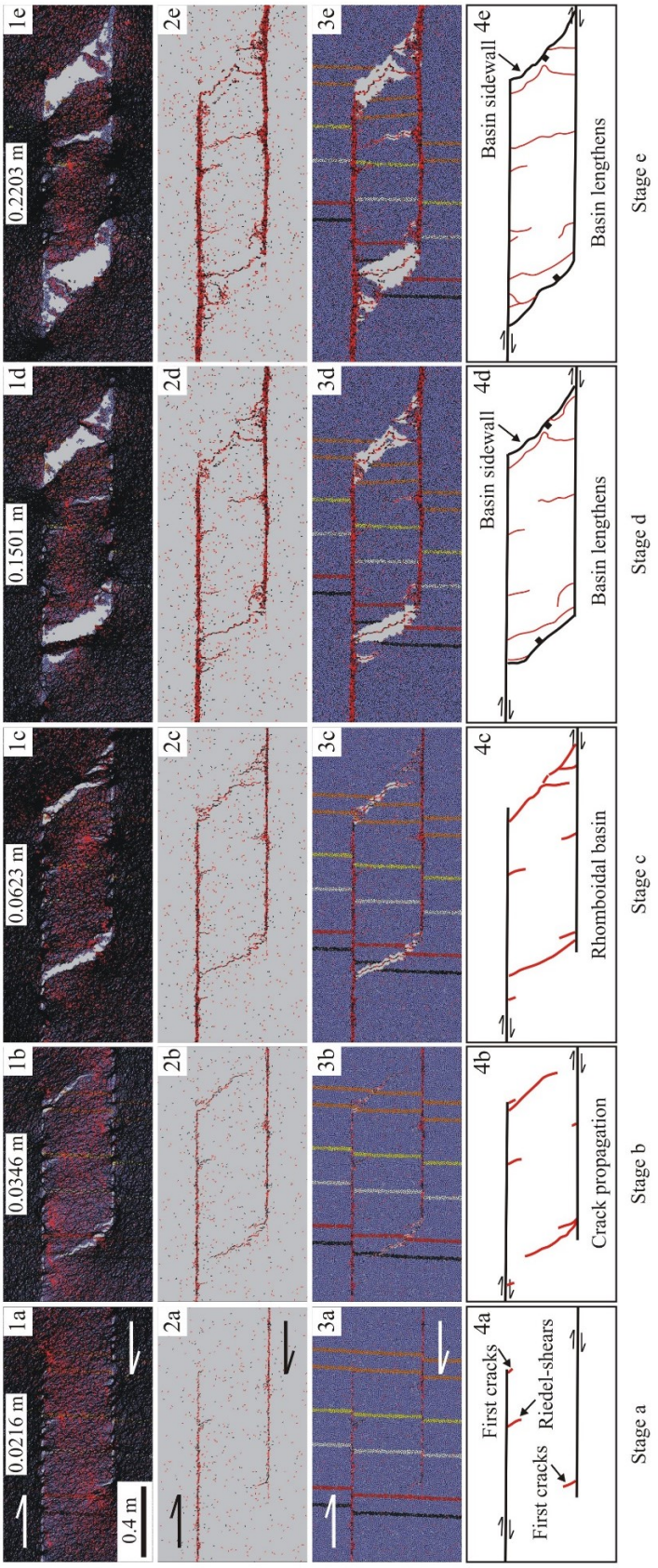

Figure 4.7 Evolution of 150° overlapping releasing sidestep model for pure strike-slip. 1a-1e: contact force distribution; 2a-2e: crack propagation; 3a-3e: particle distribution with crack propagation; 4a-4e: crack interpretation and basin geometry evolution.

4.2.3 Stress-deformation behavior

Figure 4.8 shows the relationship between major principal stress (σ_1) and relative extension (ε_x^*) for 30° underlapping, 90° non-overlapping, and 150° overlapping releasing sidestep models. The three models show very similar behavior with nearly identical relative extension at peak stress. For each model, when the value of ε_x^* reaches about 0.035, peak stress is reached and first cracks (Riedel-shears) begin to occur. Using the micro-model, Table 4.1 documents that even for quite different fault separations and different overlapping constellations, the relative extensions at peak stress are nearly the same.

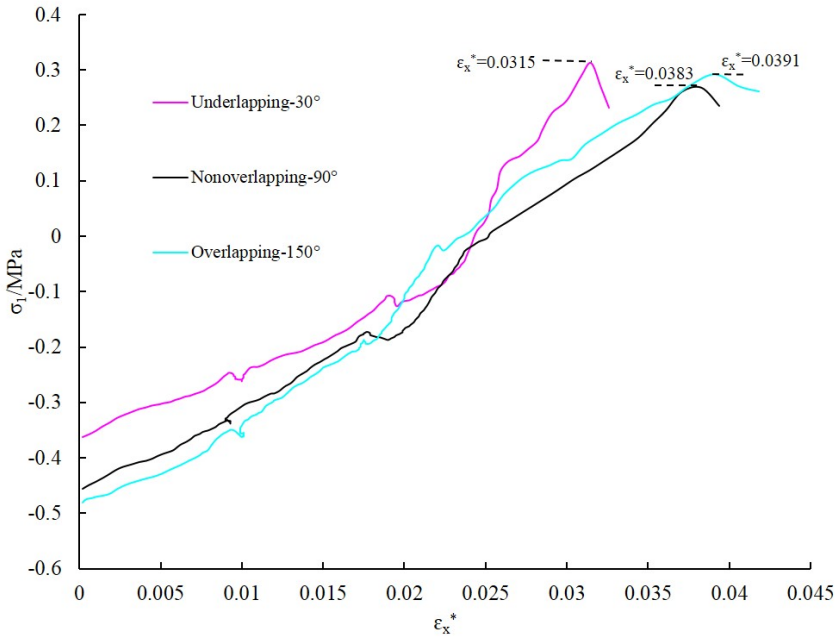

Figure 4.8 Major principal stress versus relative extension for the three representative models (30°, 90° and 150° releasing sidesteps) for pure strike-slip.

Table 4.1 Relative extension when the peak stress is reached ($\varepsilon_x^*{}_{max}$) for models with different fault separations (d).

Fault pattern	Length* Width (m)	$\varepsilon_x^*{}_{max}$		
		d = 0.2 m	d = 0.4 m	d = 0.6 m
Underlapping-30°	3.6*3.6	0.0352	0.0315	0.0362
Nonoverlapping-90°	3.6*3.6	0.0390	0.0383	0.0350
Overlapping-150°	3.6*3.6	0.0409	0.0391	0.0335

4.2.4 Robustness analyses

In order to generate confidence in numerical simulation results, robustness and stability have to be proven. To avoid numerical instabilities during the modeling, equilibrium conditions have been controlled during the simulations and time-steps were adjusted accordingly in a permanent manner. Robustness is documented by a parameter study in terms of different particle radii as well as various mechanical parameters. 30° underlapping releasing sidestep model with pure strike-slip is chosen for the robustness analysis. This model is called "basic model", with particle radius range of 0.00348 to 0.00522 m. Based on calibration procedure given above, normal stiffness (k_n) and shear stiffness (k_s) of the basic model are 5e7 N/m, and the corresponding normal contact bond strength (n-bond) and shear contact bond strength (s-bond) are 8e3 N.

Particle radii

In order to test the robustness of the simulations, several models with varying particle radius ranges have been built (Table 4.2). For the basic model, balls are generated randomly with ball radii range of 0.00348 to 0.00522 m. The basic model porosity is about 0.12. To keep the models comparable, the same porosity was used in all models, which leads to a change in ball number for each case. The average ball radius varies with the different ball radii ranges. According to Eq. 3.5, Young's modulus has no relationship with particle radius. Eq. 3.6 indicates that tensile strength is direct proportional to bond normal strength (n-bond) and inverse proportional to the particle radius. Therefore, to keep the tensile strengths constant in all models, bond normal strength (n-bond) has been adjusted (Table 4.2).

Table 4.2 Basic model and modified models with different particle radii ranges

Cases		Ball Radii R (m)	Average radius (m)	Ball number	n-bond (N)
Basic model		0.00348-0.00522	0.00435	189192	8e3
Modified models	Case1	0.003-0.00522	0.00411	209552	7.56e3
	Case2	0.00348-0.006	0.00474	157790	8.72e3
	Case3	0.003-0.006	0.00450	172694	8.28e3
	Case4	0.003-0.0045	0.00375	254587	6.89e3

Figure 4.9 shows the development sequence which was observed in the basic model and the modified models, including basin geometries and crack propagation. The initial evolution stage which contains first crack (Riedel-shears) formation is visible. The later development

stages which show the basin geometry features are also given. For the basic model, Riedel-shears occur at the tips of the master faults. Later on, the Riedel-shears propagate and link with the tips of the master faults, forming a spindle-shaped area of subsidence. With more strike-slip offset, the subsidence lengthens. In each modified model, Riedel-shears also occur at the tips of the master faults. However, the propagation and coalescence of the Riedel-shears are subtly different. For Case 1, the Riedel-shears propagate and then link with the tips of the master faults. For Case 2, 3, and 4, the Riedel-shears propagate and coalesce with each other. The geometries of the first depressions in the modified models are similar and the final basin shapes are nearly the same (Figure 4.9).

Riedel-shears occur at the tips of the master faults for both the basic model and the modified models as shown in Table 4.2. Although the propagation and coalescence of the Riedel-shears are subtly different for models with various particle radius ranges, the first depression geometries of these models are similar and the final basin shapes are nearly identical. Each model produces pull-apart basins that evolve through a sequence of closely related states, from spindle-shaped through lazy-Z-shaped to the rhomboidal and stretched rhomboidal basin.

Figure 4.10 and Figure 4.11 show the relationships between major principal stress (σ_1) and relative extension (ε_x^*) for the basic model and the modified models. These models show very similar behavior with nearly identical relative extension at peak stress. For each model, when the value of ε_x^* reaches about 0.035, the maximum of σ_1 is obtained and first cracks (Riedel-shears) begin to occur. For Case 1 and Case 4 which have smaller average particle radii, the peak stresses are slightly smaller than that of the basic model. For Case 2 and Case 3 with larger average particle radii, the peak stresses are slightly bigger than that of the basic model.

Comparison of the basic model with the modified models which have different particle radii ranges, stability and robustness of the basic model has been proved in terms of crack formation, basin geometries and development as well as σ_1-ε_x^*curves. It should be noticed that the change in particle radii is connected with change of particle packing and force-chain development. Therefore, this type of robustness test considers also smaller changes in structure (local inhomogeneity).

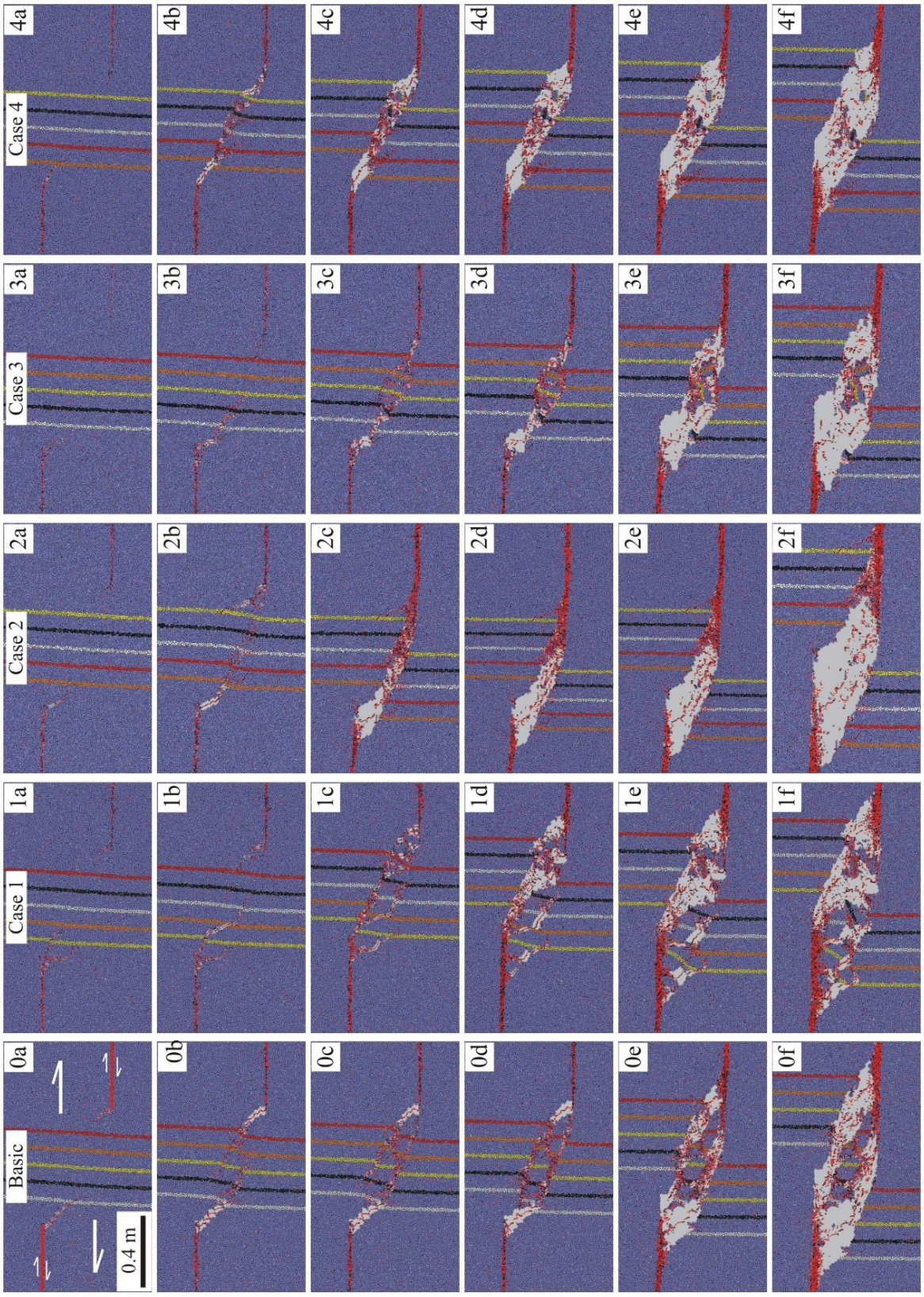

Figure 4.9 Development of pull-apart basins for basic model and modified models with varying particle radius ranges listed in Table 4.2.

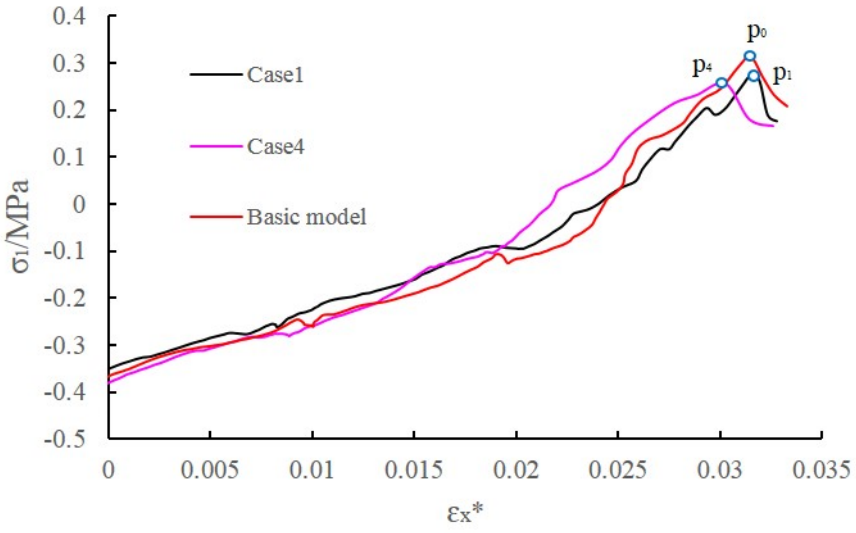

Figure 4.10 Major principal stress versus relative extension for the basic model and the modified models (Case 1 and Case 4).

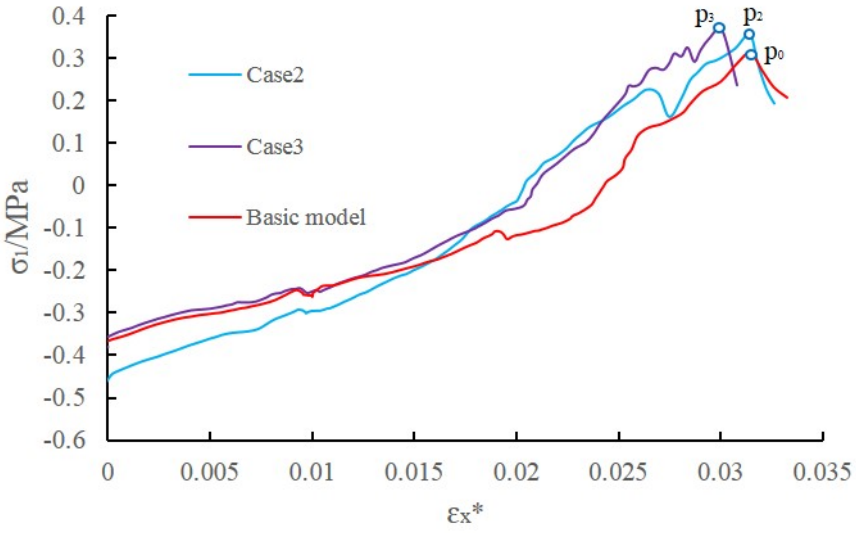

Figure 4.11 Major principal stress versus relative extension for the basic model and the modified models (Case 2 and Case 3).

Material parameters

Robustness of the simulations is also tested against small variations in mechanical parameters using the basic model (Table 4.3). Taking Case 1 as an example: the mechanical parameters such as kn, n-bond strength, s-bond strength and μ are the same as those in the basic model, however, the values of shear stiffness between particles (ks) are set randomly (0.8 - 1.2 times those of the basic model).

Figure 4.12 shows the evolution of the basic model and the five modified models with

various parameters. For the models with different mechanical parameters, the Riedel-shears all occur at the tips of the master faults. For all cases, although the propagation of the Riedel-shears could be subtly different from the basic model, the depression geometries are similar and the final basin shapes are the same (Figure 4.12).

Figures 4.13, 4.14 and 4.15 present the relationships between major principal stress (σ_1) and relative extension (ε_x^*) for the basic model and the five modified models as listed in Table 4.3. All models show nearly the same behavior for σ_1 versus ε_x^*. In addition, when peak stress is reached and crack propagation starts, the ε_x* values for all models are similar.

Table 4.3 Basic model and calibration models with different mechanical parameters

Cases	k_n (N/m)	k_s (N/m)	n-bond (N)	s-bond (N)	Frictional coefficient (μ)
Basic model	5e7	5e7	8e3	8e3	1.73
Case1	5e7	(0.8-1.2)* 5e7	8e3	8e3	1.73
Case2	(0.8-1.2)* 5e7	5e7	8e3	8e3	1.73
Case3	5e7	5e7	8e3	(0.8-1.2)* 8e3	1.73
Case4	5e7	5e7	(0.8-1.2)* 8e3	8e3	1.73
Case5	5e7	5e7	8e3	8e3	(0.8-1.2)*1.73

Crack formation, basin geometries, and σ_1-ε_x^* curves of the modified models with various parameters are nearly the same compared with the basic model. Robustness and stability of the basic model in terms of parameters have been proven.

The sensitivity of the simulation results in respect to particle radius ranges and material parameter values is tested in this study. The Riedel-shears coalescence is slightly dependent on the radii and parameters, but not the pull-apart basin geometries and σ_1-ε_x^* curves. Thus they do not influence the conclusions drawn within this thesis.

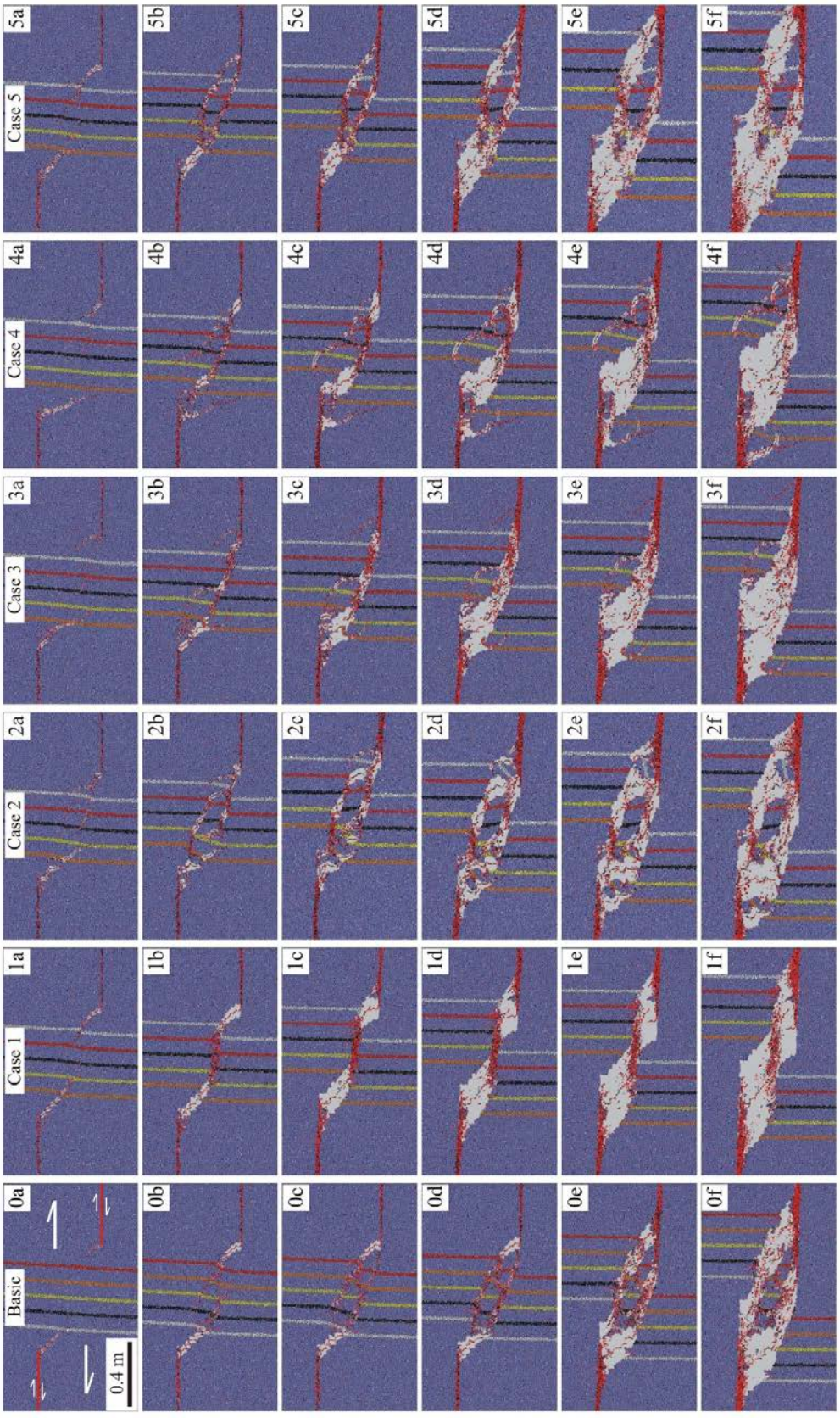

Figure 4.12 Development of pull-apart basins for basic model and modified models with varying mechanical parameters listed in Table 4.3.

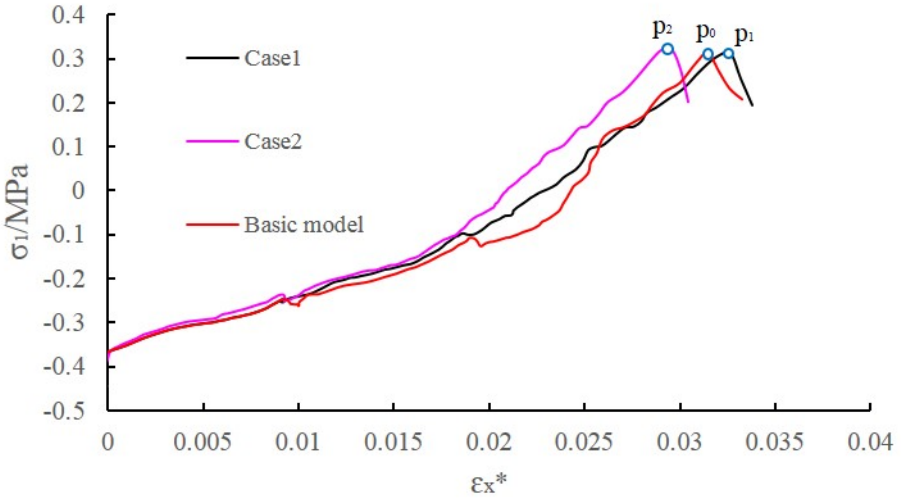

Figure 4.13 Major principal stress versus relative extension for the basic model and the modified models (Case 1 and Case 2).

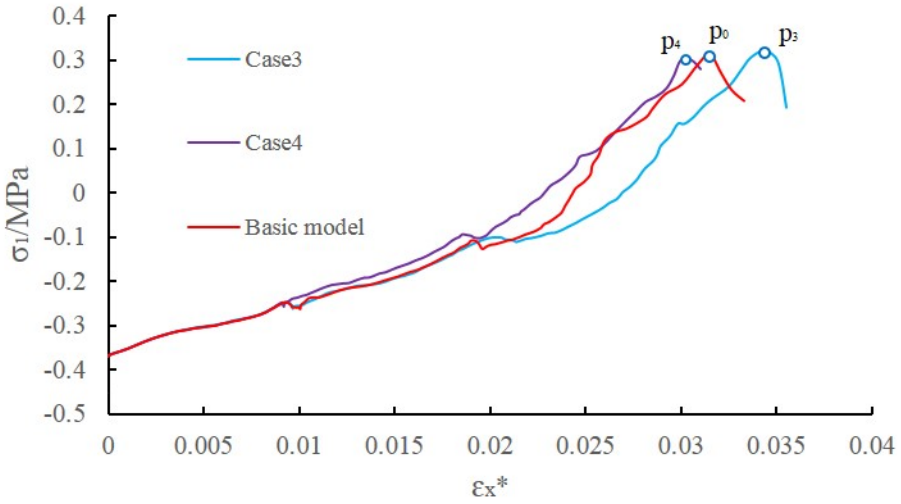

Figure 4.14 Major principal stress versus relative extension for the basic model and the modified models (Case 3 and Case 4).

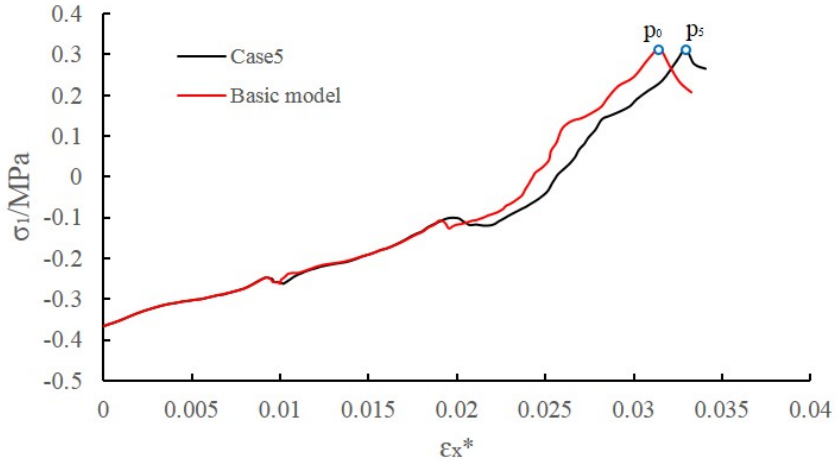

Figure 4.15 Major principal stress versus relative extension for the basic model and the modified model (Case 5).

4.3 Transtensional strike-slip

4.3.1 Model set-up

Two-dimensional micro-scaled models with length and width of 3.6 m are built to simulate pull-apart basin development with 5° inclined transtensional displacement across the master faults. The master faults are predefined at an angle of 5° oblique and divergent to the applied wall velocities. Three representative models, i.e., 30° underlapping transtensional, 90° non-overlapping transtensional and 150° overlapping transtensional models are investigated (Figure 4.16). The horizontal overlap of the master faults' tips are -0.69 m, 0 m and 0.69 m, respectively. The vertical separation of the master faults' tips is fixed at 0.40 m to allow direct comparison of modeling results between the three situations.

Young's modulus of 25 MPa and tensile strength of 1 MPa are selected for the modeling. The corresponding normal stiffness (k_n) and shear stiffness (k_s) are 5e7 N/m, and the corresponding normal contact bond strength (n-bond) and shear contact bond strength (s-bond) are 8e3 N.

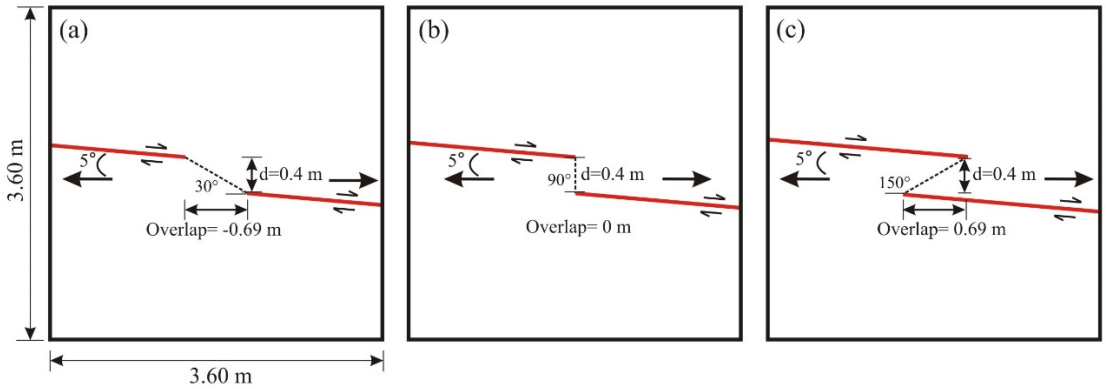

Figure 4.16 Models with different overlaps between master faults for transtension: (a) 30° underlapping releasing sidestep, (b) 90° non-overlapping releasing sidestep, (c) 150° overlapping releasing sidestep.

4.3.2 Pull-apart basin development

30° underlapping transtensional model

Figure 4.17 shows the development of a pull-apart basin observed in the 30° underlapping releasing sidestep model, with 5° of inclined transtensional displacement across the master faults. Contact force distribution (1a - 1e), crack propagation (2a - 2e), particle distribution (3a - 3e), and crack interpretation (4a - 4e) are presented, respectively. During the initial evolution stage (0 - 0.0144 m transtensional displacement), maximum tensile contact forces concentrate at the tips of the master faults, and peak stress is not reached. Peak stress is observed for ε_x^* of 0.0361. At 0.0144 m of transtensional offset, peak stress is obtained and crack propagation starts.

With further transtensional offset, right-lateral Riedel-shears occur and maximum tensile forces concentrate near the Riedel-shears' tips (Stage a, Figure 4.17). Later on, new Riedel-shears begin to occur. Oblique-extensional cracks connecting with the Riedel-shears also form (Stage b, Figure 4.17). At about 0.0630 m of displacement, the Riedel-shears propagate continuously and coalesce with the master faults, creating an oblique, lazy-Z-shaped depression. Meanwhile, the oblique-extensional cracks inside of the depression propagate and coalesce with the master faults and Riedel-shears, forming a cross-basin fault (Stage c, Figure 4.17).

With further offset, extensional basin sidewalls form, bounding an oblique, rhomboidal-shaped pull-apart basin (Stage d, Figure 4.17). As the transtensional offset increases, the basin sidewalls move outward. The basin lengthens, producing an oblique, elongated, rhomboidal-shaped basin. Different from the pure strike-slip case, the pull-apart basin of the transtensional case not only lengthens, but also widens (4d and 4e, Figure 4.17).

Therefore, with the same offset, the basin forming in transtensional case is wider than the basin in pure strike-slip system.

90° non-overlapping releasing sidestep model

Figure 4.18 illustrates the evolution sequence of transtensional movement in 90° non-overlapping releasing sidestep model. Peak stress and onset of crack propagation are observed for ε_x^* of 0.0328 (non-overlapping-90°, Figure 4.20). When the peak stress is reached, Riedel-shears begin to occur. Later on, the Riedel-shears propagate (Stage a, Figure 4.18). At about 0.0653 m of transtensional displacement, the Riedel-shears coalesce with the master faults, bounding a short, rhomboidal subsidence (Stage b, Figure 4.18). With increasing transtensional offset, new Riedel-shears which intersect with the master faults occur (Stage c, Figure 4.18). The new Riedel-shears propagate and connect with the closest Riedel-shears, bounding a rhomboidal-shaped basin (Stage d, Figure 4.18). With more transtensional displacement, basin sidewalls form and then move outward. The rhomboidal pull-apart basin lengthens (Stage e, Figure 4.18).

150° overlapping releasing sidestep model

Figure 4.19 presents the evolution of transtensional motion for 150° overlapping releasing sidestep model. Riedel-shears initiate at the tips of the two master faults when peak stress is reached (at 0.0150 m of transtensional offset). With increased strike-slip offset, the Riedel-shears propagate (Stage a). Later on, new Riedel-shears which intersect with the master faults occur as well (Stage b). At about 0.0673 m of transtensional displacement, the Riedel-shears coalesce with the master faults, bounding a rhomboidal depression (Stage c). With further offset, new Riedel-shears outside of the depression form and propagate (Stage d). With more transtensional offset, basin sidewalls occur and move outward, producing an elongated rhomboidal (Stage e).

The crack propagation and basin evolution in the transtensional 150° overlapping case are similar to the transtensional 90° non-overlapping model described above. Moreover, both, the transtenional 150° overlapping and 90° non-overlapping systems show great similarities to the pure strike-slip 150° overlapping and 90° non-overlapping cases, respectively. In conclusion, for both pure strike-slip and transtension in 90° non-overlapping and 150° overlapping cases, Riedel-shears occur at the tips of the predefined master faults when peak stress is reached. With further strike-slip displacement, the Riedel-shears propagate and coalesce with the master faults, bounding a rhomboidal subsidence. Later on, as the displacement increases, the basin sidewall move outward, the basin length becomes larger, forming an elongated rhomboidal-shaped pull-apart basin. At the beginning evolution stage, the basin length is direct proportional to the fault overlap. With more and more displacement,

the basin length is direct proportional to the displacement. The basin width which is decided by the separation of the predefined master faults varies very little with increasing displacement.

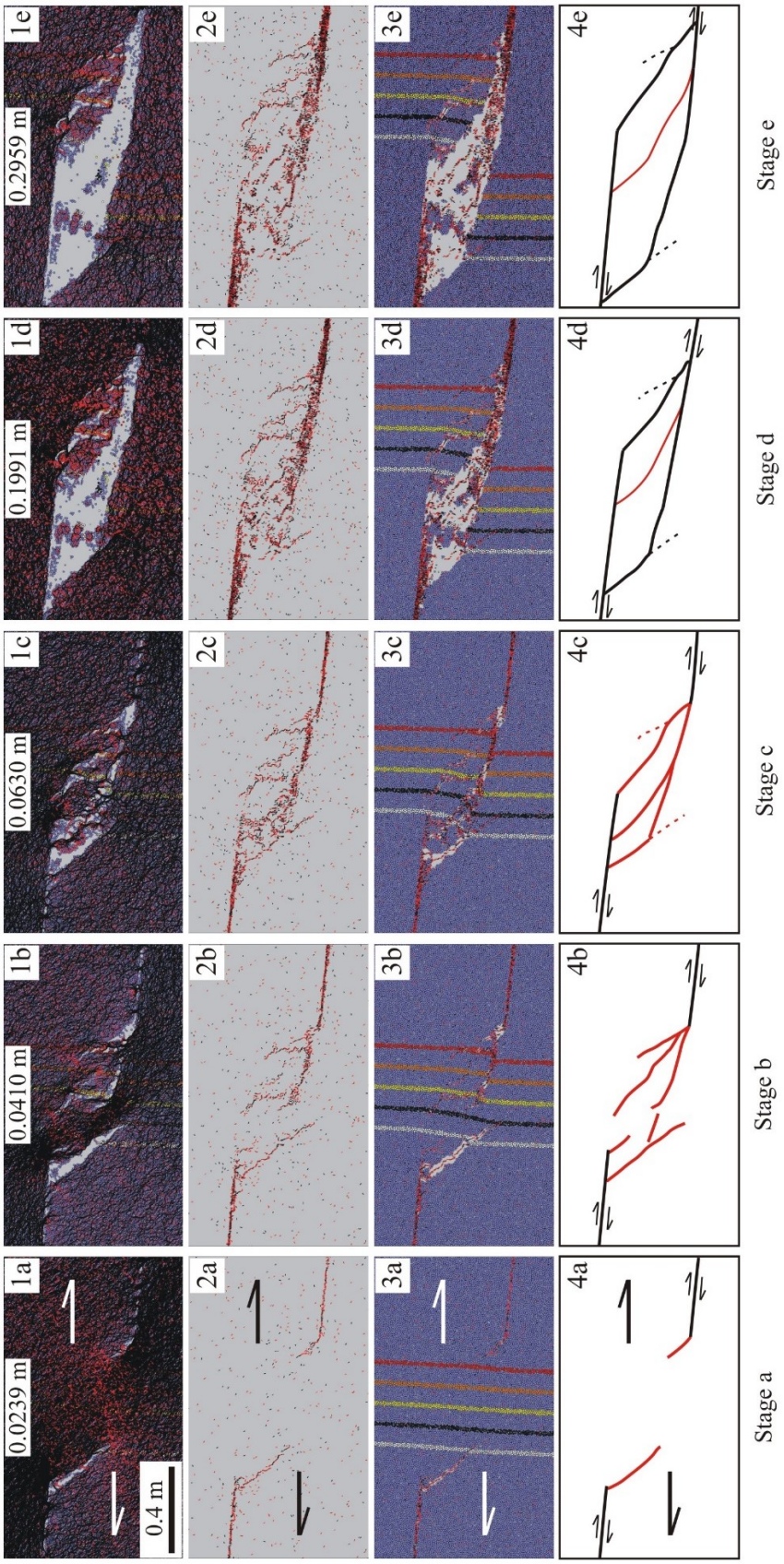

Figure 4.17 Evolution of 30° underlapping releasing sidestep model for transtension. 1a-1e: contact force distribution; 2a-2e: crack propagation; 3a-3e: particle distribution with crack propagation; 4a-4e: crack interpretation and basin geometry evolution.

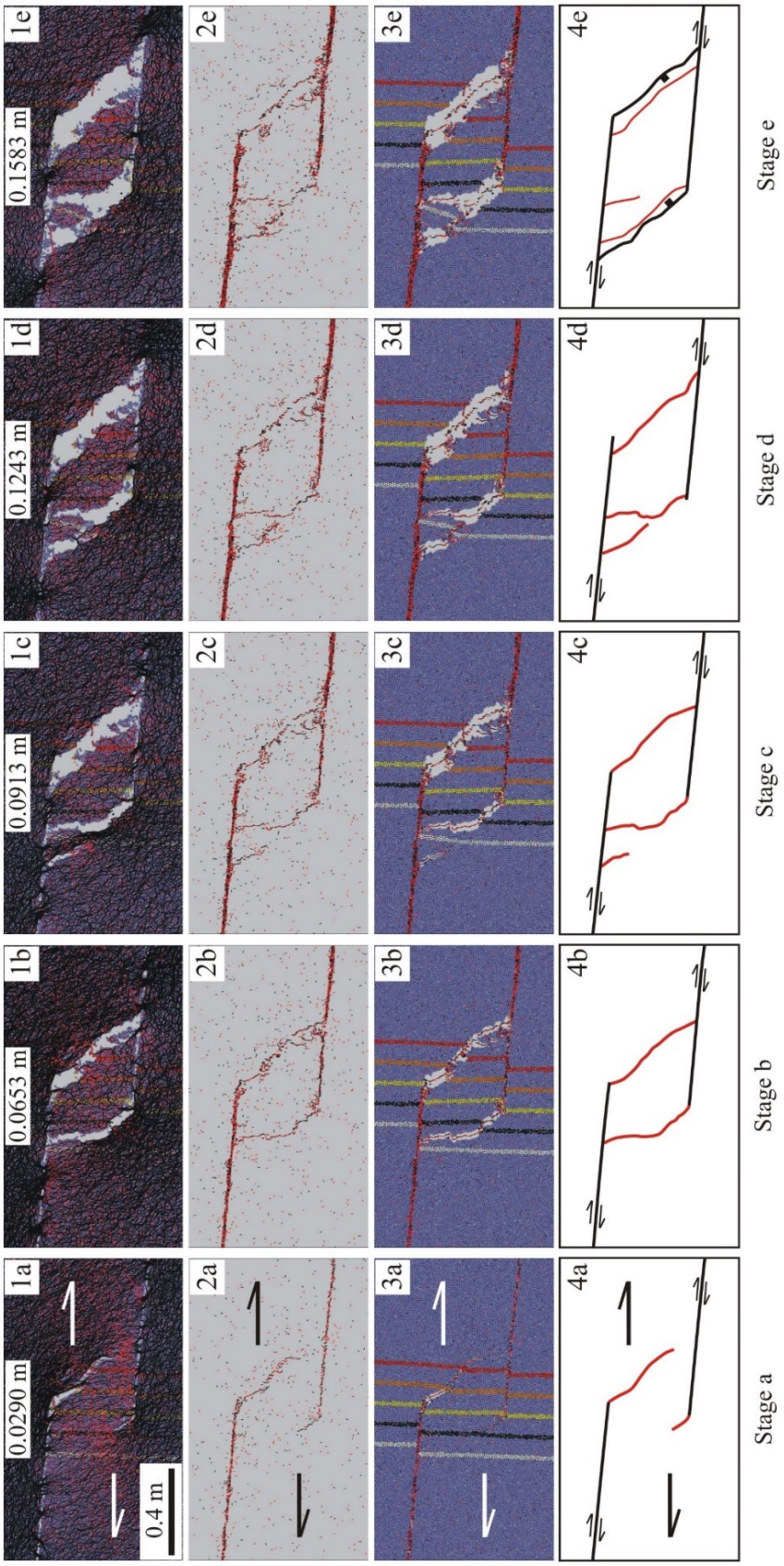

Figure 4.18 Evolution of 90° non-overlapping releasing sidestep model for transtension. 1a-1e: contact force distribution; 2a-2e: crack propagation; 3a-3e: particle distribution with crack propagation; 4a-4e: crack interpretation and basin geometry evolution.

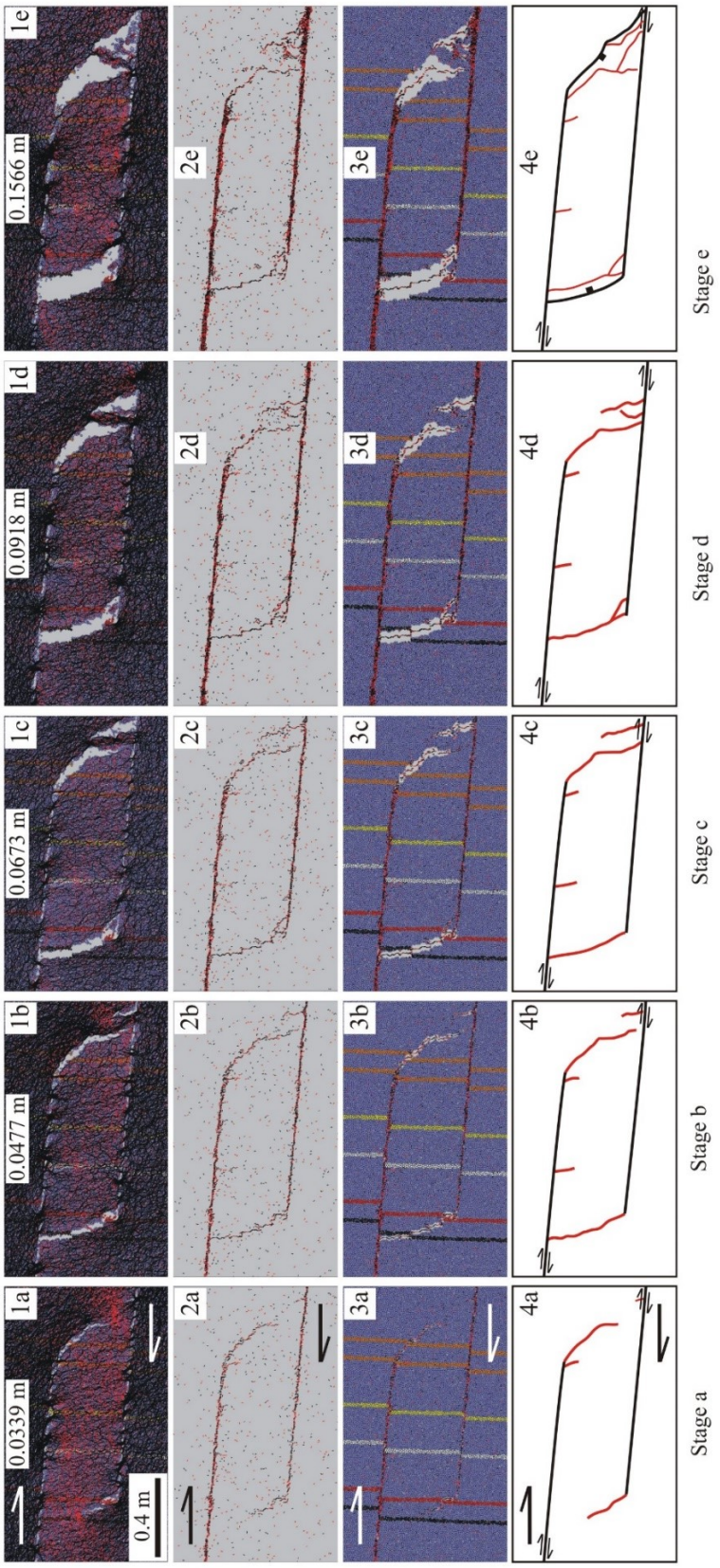

Figure 4.19 Evolution of 150° overlapping releasing sidestep model for transtension. 1a-1e: contact force distribution; 2a-2e: crack propagation; 3a-3e: particle distribution with crack propagation; 4a-4e: crack interpretation and basin geometry evolution.

4.3.3 Stress-deformation behavior

Figure 4.20 shows the relationship between major principal stress (σ_1) and relative extension (ε_x^*) of the transtensional movement for 30° underlapping, 90° non-overlapping, and 150° overlapping releasing sidestep models. The three models show similar σ_1-ε_x^* curves. For each model, when the value of ε_x^* reaches 0.0361, 0.0328, 0.0375, respectively, first cracks (Riedel-shears) begin to occur. In conclusion, the three transtension models show very similar behavior with nearly identical relative extension at peak stress. Peak stress and onset of crack propagation are observed for ε_x^* of around 0.035.

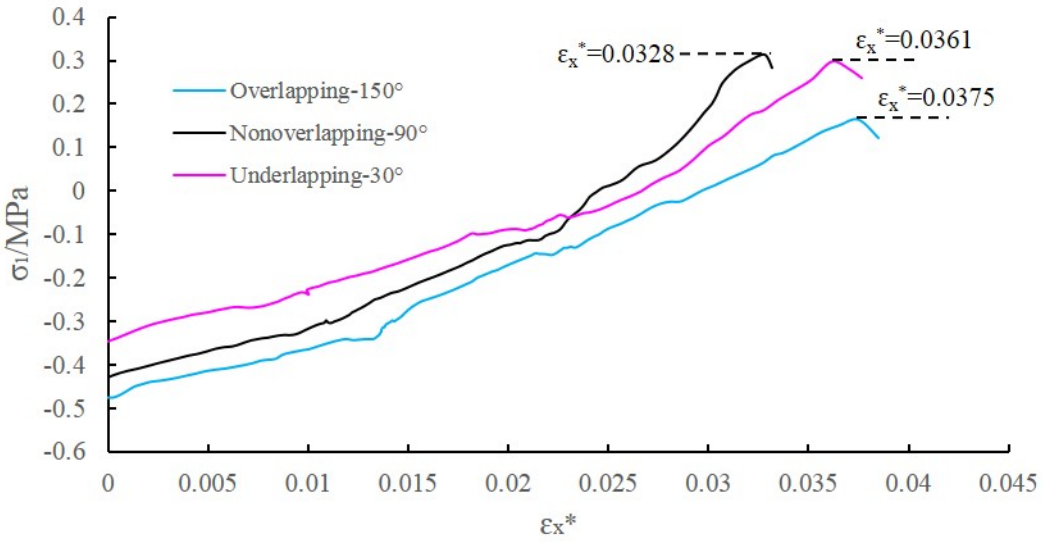

Figure 4.20 Major principal stress versus relative extension of the three representative transtensional models (30°, 90° and 150° releasing sidestep).

4.4 Transpressional strike-slip

4.4.1 Model set-up

Micro-scale models with edge length of 3.6 m are set up to simulate pull-apart basin development with 5° inclined transpressional offset across the master faults. The master faults are predefined at an angle of 5° oblique and convergent to the wall velocities. Three representative models, i.e., 30° underlapping transpressional, 90° non-overlapping transpressional, and 150° overlapping transpressional models are chosen. The overlap and separation of master faults for each model are shown in Figure 4.21. Young's modulus of 25 MPa and tensile strength of 1 MPa are selected for the modeling.

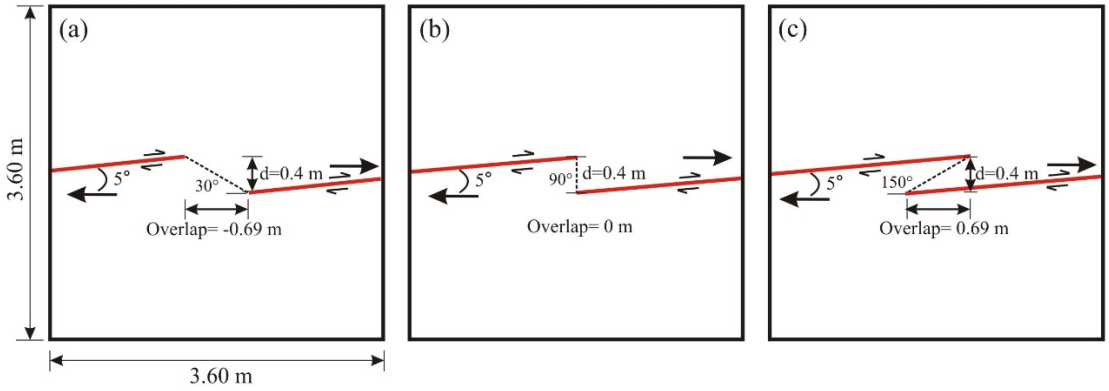

Figure 4.21 Models with different overlaps between master faults for transpression: (a) 30° underlapping releasing sidestep, (b) 90° non-overlapping releasing sidestep, (c) 150° overlapping releasing sidestep.

4.4.2 Pull-apart basin development

30° underlapping transpressional model

Figure 4.22 shows the pull-apart basin evolution observed in 30° underlapping model, with 5° inclined transpressional displacement across the master faults, including contact force distribution, crack propagation, particle distribution, and crack interpretation. During the initial evolution stage (0-0.0146 m transpressional offset), maximum tensile contact forces concentrate at the tips of the master faults, and peak stress is not reached. Peak stress is observed for ε_x^* of 0.0364. At 0.0146 m of transpressional offset, peak stress is reached and Riedel-shears occur at the tips of the master faults.

With further transpressional displacement, crack propagation starts and maximum tensile forces concentrate near the tips of the Riedel-shears (Stage a, Figure 4.22). Later on, oblique-extensional cracks form between the Riedel-shears (Stage b, Figure 4.22). The oblique cracks and Riedel-shears propagate. At about 0.0636 m offset, the Riedel-shears coalesce with the oblique cracks, leading to the formation of a diagonal fault which connects the two master faults (Stage c, Figure 4.22). As offset increases, the first subsidence area forms along the cross-basin fault. Basin sidewalls also develop, bounding an oblique, asymmetric pull-apart basin (Stage d, Figure 4.22).

With more transpressional offset, the cross-basin fault propagation seems to be stopped. However, basin sidewalls move outward and the basin lengthens, producing an oblique, elongated, asymmetric basin (Stage e, Figure 4.22). The basin lengths along the two master faults are not the same. This leads to the asymmetry of the basin shape. The crack propagation and basin geometry in the transpressional system are both different from those in pure strike-slip and transtensional systems.

90° non-overlapping transpressional model

Figure 4.23 illustrates the development sequence of transpressional motion in 90° non-overlapping model. When the peak stress is reached (at 0.0216 m of transpressional offset), Riedel-shears begin to occur at the tips of the master faults. Then, the Riedel-shears propagate (Stage a, Stage b). At 0.0607 m of transpressional offset, the Riedel-shears connect with the master faults, forming a short, rhomboidal depression (Stage c, Figure 4.23). With ongoing transpressional offset, new Riedel-shears propagate and connect with the master fault, lengthening the basin (Stage d, Figure 4.23). With further displacement, basin sidewalls form and then move outward. The rhomboidal pull-apart basin lengthens (Stage e, Figure 4.23).

150° overlapping transpressional model

Figure 4.24 shows the transpressional movement for 150° overlapping releasing sidestep model. When peak stress is reached (at 0.0160 m of transpressional offset), Riedel-shears initiate, but not all initiate at the tips of the master faults. With increased strike-slip offset, the Riedel-shears propagate (Stage a, Figure 4.24). Then, more Riedel-shears which intersect with the master faults form (Stage b, Figure 4.24). At about 0.0604m of transtensional offset, the Riedel-shears coalesce with the master faults, producing a rhomboidal depression (Stage c, Figure 4.24). With increasing offset, more Riedel-shears inside of the depression form and propagate (Stage d, Figure 4.24). As displacement increases, basin sidewalls occur and move outward, and an elongated rhomboidal-shaped pull-apart basin forms (Stage e, Figure 4.24).

The crack propagation and basin evolution developed in the transpressional 150° overlapping and 90° non-overlapping models show great similarities to the pure strike-slip 150° overlapping and 90° non-overlapping models, respectively. But the crack propagation and basin geometries of transpressional 30° underlapping model are quite different from those of pure strike-slip and transtension. A diagonal fault which coalesces the tips of the two master faults occurs before the basin formation. The first depression area forms along the diagonal fault. With further transpressional offset, the basin lengthens, but the fault inside the basin seems to stop propagation. So the depocenter of the basin may not migrate.

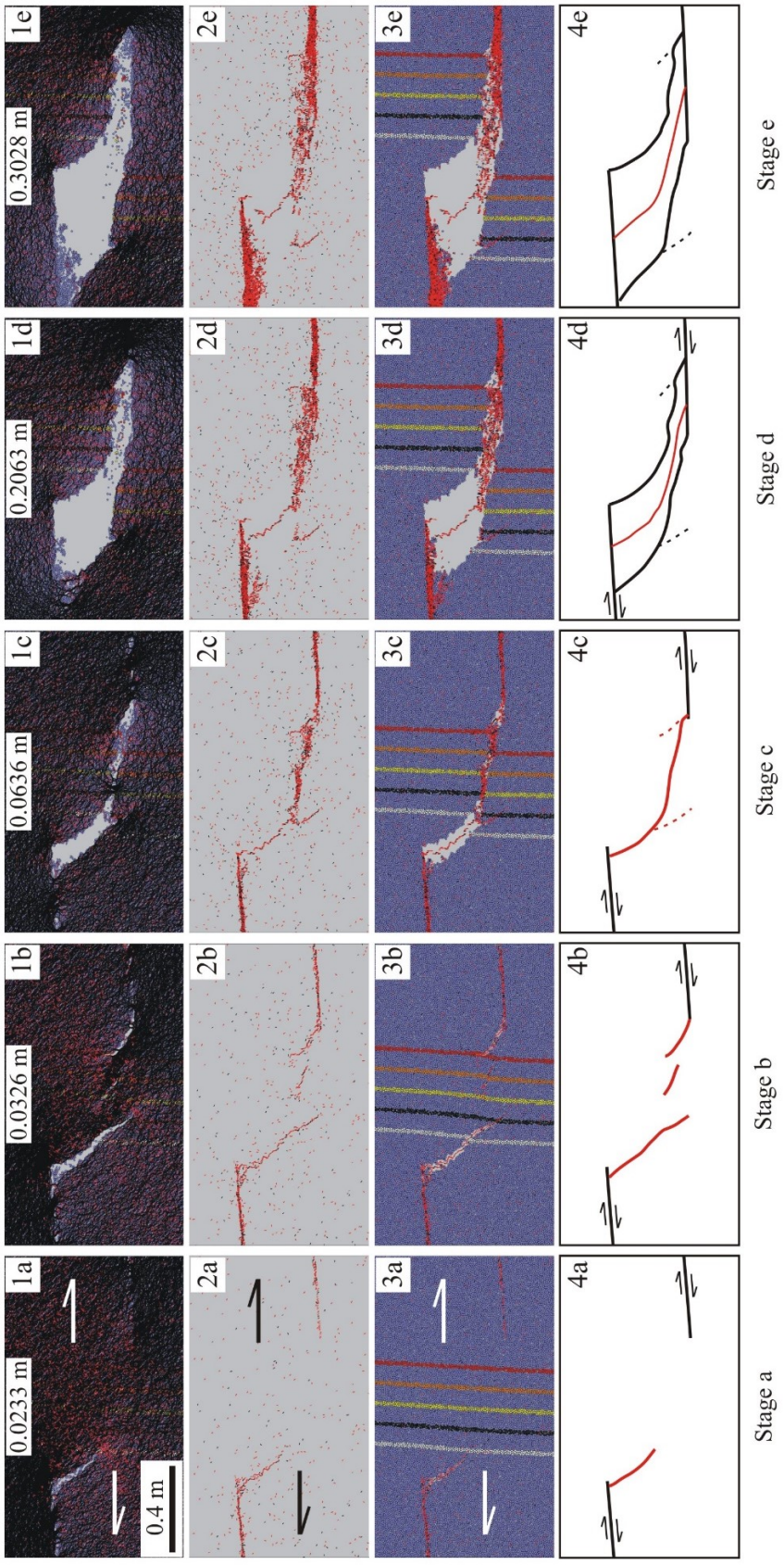

Figure 4.22 Evolution of 30° underlapping releasing sidestep model for transpression. 1a-1e: contact force distribution; 2a-2e: crack propagation; 3a-3e: particle distribution with crack propagation; 4a-4e: crack interpretation and basin geometry evolution.

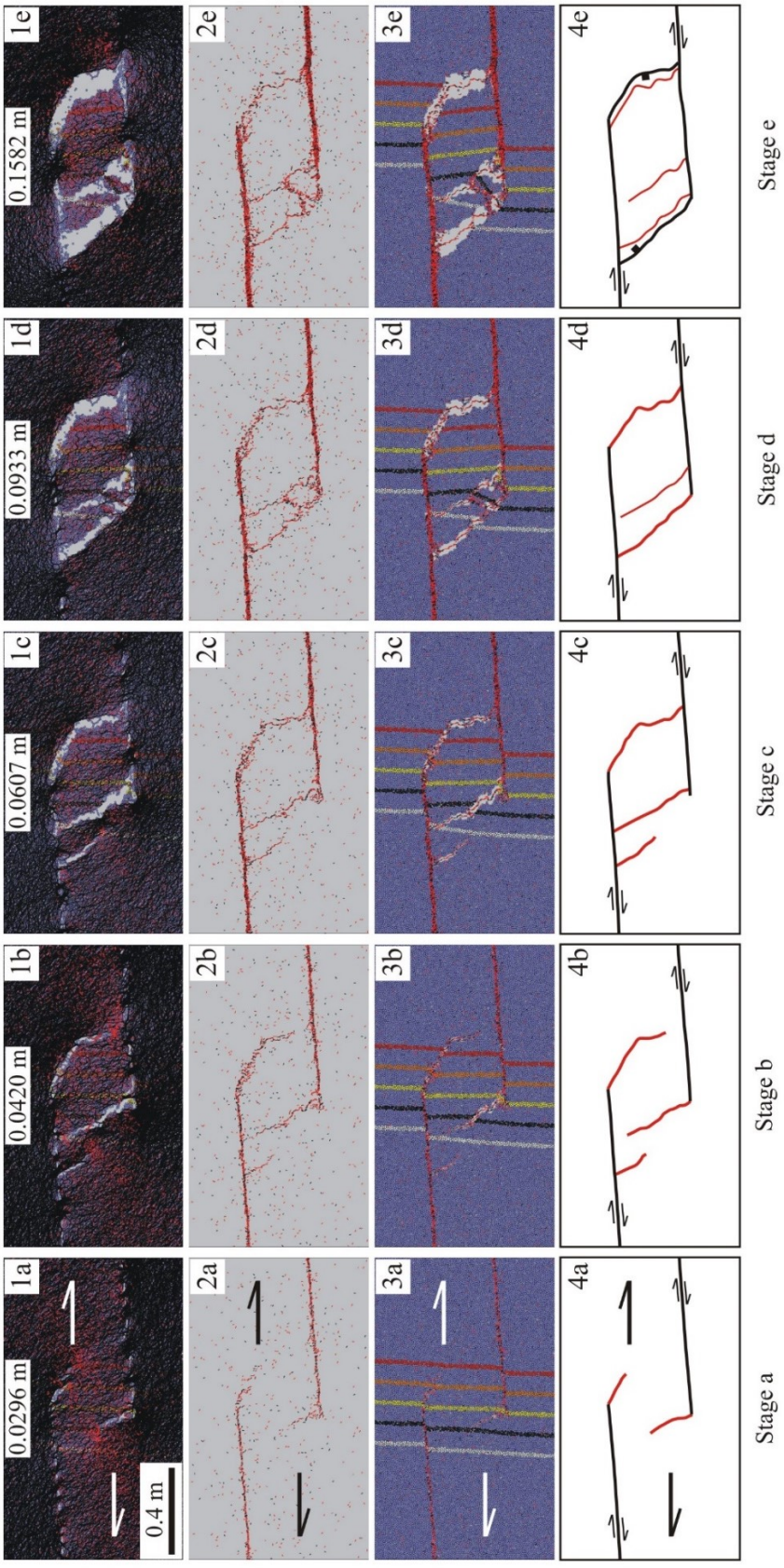

Figure 4.23 Evolution of 90° non-overlapping releasing sidestep model for transpression. 1a-1e: contact force distribution; 2a-2e: crack propagation; 3a-3e: particle distribution with crack propagation; 4a-4e: crack interpretation and basin geometry evolution.

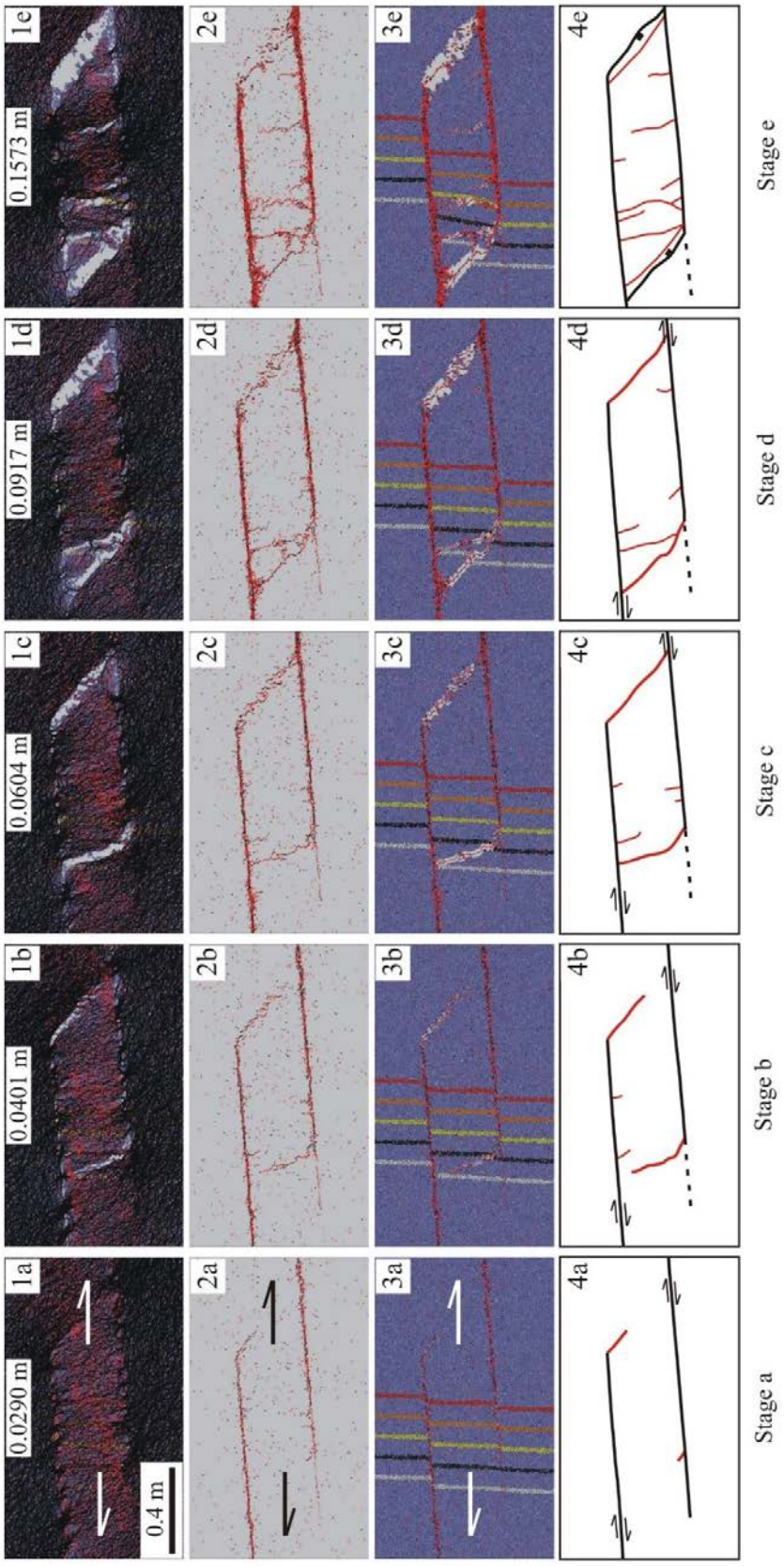

Figure 4.24 Evolution of 150° overlapping releasing sidestep model for transpression. 1a-1e: contact force distribution; 2a-2e: crack propagation; 3a-3e: particle distribution with crack propagation; 4a-4e: crack interpretation and basin geometry evolution.

4.4.3 Stress-deformation behavior

Figure 4.25 displays the relationship between major principal stress (σ_1) and relative extension (ε_x^*) of the transpressional motion for 30° underlapping, 90° non-overlapping, and 150° overlapping models. The σ_1-ε_x^* curves of the three typical transpressional models show similarity. For each model, when the value of ε_x^* reaches 0.0364, 0.0539, 0.0399, respectively, peak stress is reached and Riedel-shears begin to occur. Although the relative extension (ε_x^*) of the 90° non-overlapping model at peak stress is larger than that of the 30° underlapping and 150° overlapping models, the offsets needed to form the first depression for the three models are nearly the same (0.0636, 0.0607, 0.0604, respectively).

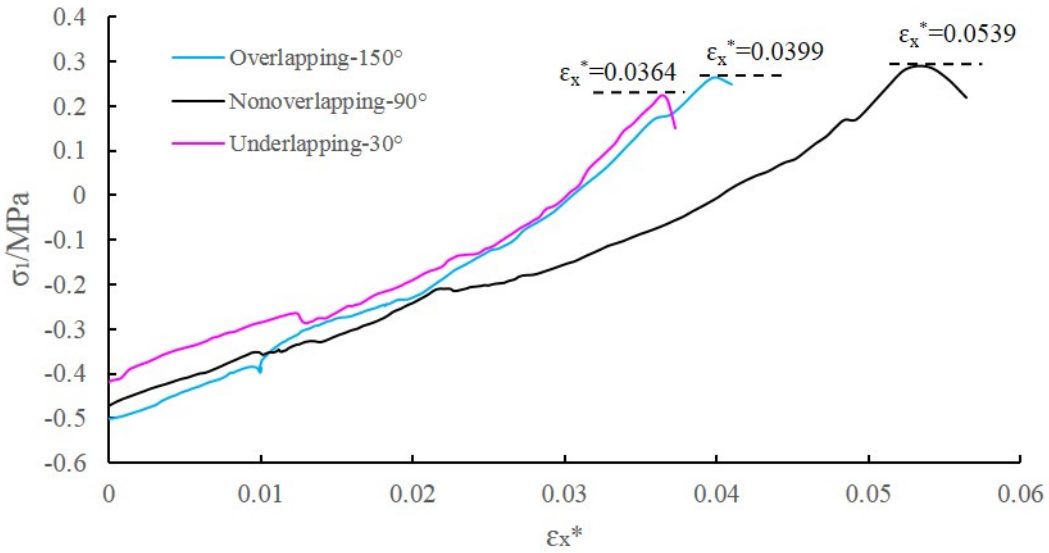

Figure 4.25 Major principal stress versus relative extension of the three representative transpressional models (30°, 90° and 150° releasing sidestep).

4.5 Comparison with pure strike-slip model

This part compares the modeling results of crack propagation and pull-apart basin evolution in pure strike-slip, transtensional, and transpressional systems. Model length and width are both 3.6 m. 30° underlapping models with fault separation of 0.4 m are chosen (Figure 4.26). Young's modulus of 25 MPa and tensile strength of 1 MPa are selected for the models.

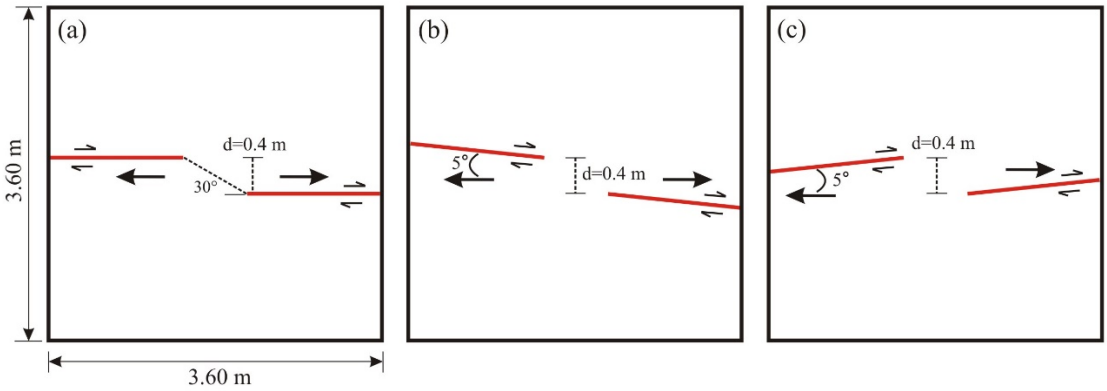

Figure 4.26 Pure strike-slip, transtensional, and transpressional models of 30° underlapping releasing sidesteps.

4.5.1 Evolution of pull-apart basins in plan view

Strike-slip

Figure 4.27 illustrates the detailed sequence of crack propagation and pull-apart basin development observed in the pure strike-slip modeling, including particle distribution (1a - 1h, Figure 4.27), crack propagation and basin development (2a - 2h, Figure 4.27), and crack and basin interpretation (3a - 3h, Figure 4.27). The particles marked with different colors in vertical directions can help to identify the major cracks by tracing the movement and offset of the marked particles.

At the initial stage, Riedel-shears occur at the tips of the master faults (a, Figure 4.27). Later on, the Riedel-shears propagate and link with each other (b-e, Figure 4.27). With increased strike-slip displacement, the major cracks coalesce with the master faults, forming a spindle-shaped area which contains the colored marked particles (f, Figure 4.27). Because of the limitation of the two-dimensional modeling (PFC^{2D}), the particles in this spindle-shaped area stop moving, and we cannot directly see the subsidence in the out-of-plane direction. In nature, this spindle-shaped area is the first subsidence area. With more strike-slip offset, basin sidewalls form and the basin lengthens. The first subsidence area become deeper. This area is the depocenter (3f, Figure 4.27). At the same time, empty areas in the modeling form between the basin sidewalls and the first spindle-shaped depression. The subsidence of these empty areas is smaller than the first depression area. Therefore, a single, central depocenter is formed under pure strike-slip. With further offset, the basin lengthens and subsidence areas increase, forming a flat-bottomed, deep, lazy-Z-shaped to rhomboidal-shaped pull-apart basin (h, Figure 4.27).

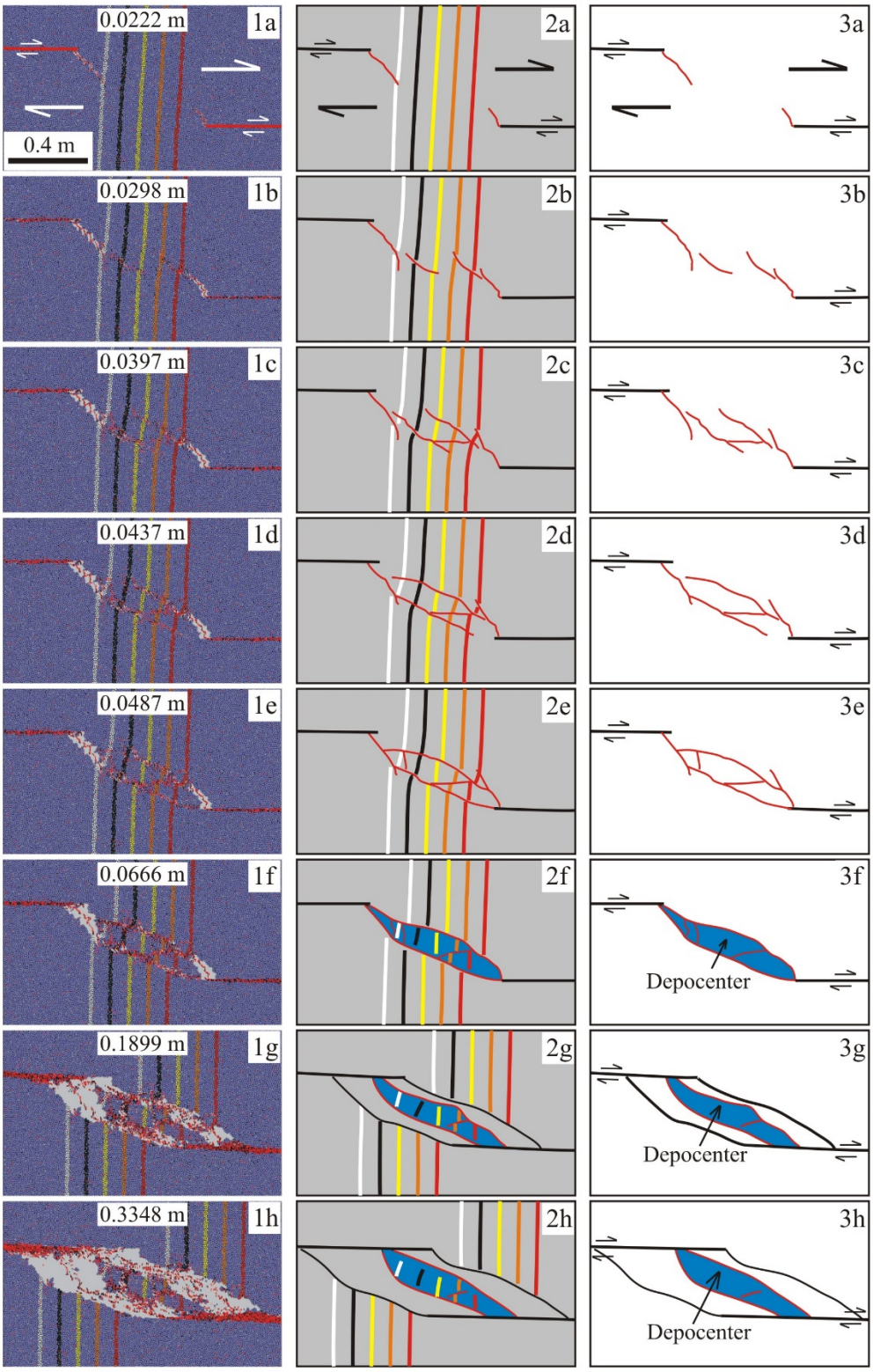

Figure 4.27 Detailed evolutional sequence of 30° underlapping releasing sidestep for pure strike-slip.

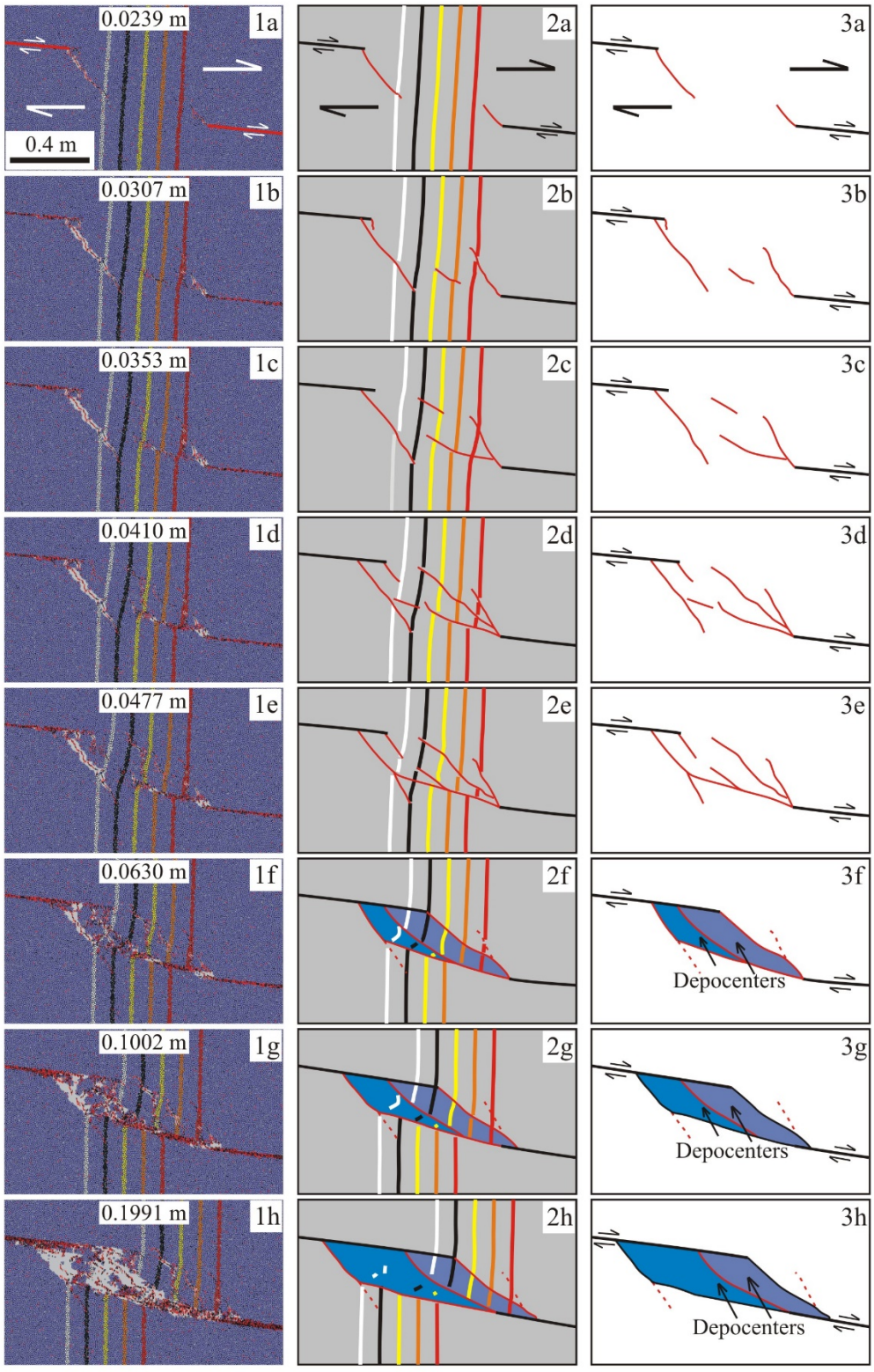

Figure 4.28 Detailed evolutional sequence of 30° underlapping releasing sidestep for transtension.

Transtension

Figure 4.28 shows the detailed evolution process of a pull-apart basin with 5° of transtensional displacement across the predefined master faults. Right-lateral Riedel-shears occur at the tips of the master faults at the initial evolution phase (a, Figure 4.28). Then, the Riedel-shears propagate and lengthen. With more transtensional offset, oblique-extensional cracks form between the Riedel-shears (b-c, Figure 4.28). Later on, the oblique-extensional cracks propagate and coalesce with the closest Riedel-shears and master faults, creating a longitudinal depression area (d-e, Figure 4.28). As shown in Figure 4.28d and Figure 4.28e, the right-lateral offsets of the marked particles (2d-2e, Figure 4.28) help us to detect the major cracks among many micro-cracks. With further displacement (f, Figure 4.25), the Riedel-shears which form at the tips of the master faults at the initial stage become the basin sidewall faults. The subsidence areas are bounded by basin sidewall faults. The oblique-extensional crack segments at the subsidence center propagate and link, forming a cross-basin strike-slip fault zone. Therefore, two depocenters separated by the dip-slip cross-basin fault form. Subsequently, the basin lengthens and an elongated rhomboidal subsidence area with two depocenters forms (g-h, Figure 4.28). Based on the marked particles in Figure 4.28g and 4.28h, the Riedel-shears which form at the tips of the master faults stop propagating longitudinally. The results in terms of crack propagation and depocenter distribution for pure strike-slip and transtensional systems in underlapping releasing sidesteps show a behavior similar to those observed in scaled sandbox tests [*Wu et al*., 2009], which verifies our results.

Transpression

As shown in Figure 4.22, crack propagation in transpressional system is relatively easier. With transpressional displacement, Riedel-shears occur at the tips of the master faults (stage a, Figure 4.22). Then, oblique-extensional cracks form between the Riedel-shears (Stage b, Figure 4.22). With more offset, the Riedel-shears coalesce with the oblique cracks, resulting in the formation of a diagonal fault. This diagonal or basin-cross fault connects the tips of the two master faults (Stage c, Figure 4.22). As offset increases, the first depression area along the diagonal fault forms. With further offset, basin sidewalls develop, producing an oblique, asymmetric pull-apart basin (Stage d, Figure 4.22). The depocenter of the basin is along the diagonal fault. The crack propagation and basin geometry in the transpressional system are different from those in pure strike-slip and transtensional systems.

4.5.2 Evolution interpretation based on vertical sections

Compared with continuum methods, the advantage of the documented DEM modeling is that we can intuitively see the physical based crack propagation and coalescence during the

pull-apart basin development. The disadvantage is lack of information about subsidence and uplift in vertical direction because of the limitations of two-dimensional models in general. However, the cracks and empty areas in our 2D models can be interpreted as opening of the basins. Combining the DEM modeling results with sandbox tests by *Wu et al*. [2009], one can reconstruct the evolution in vertical sections for both pure strike-slip and transtensional models.

Pure strike-slip

Three profiles along lines AA', BB', and CC' in Figure 4.29 are chosen to study the features of each evolutional stage along vertical section. Figure 4.29 is a schematic diagram which shows the general dip direction of the oblique-extension faults whereas the dip angle of the oblique-extension faults is not accurate. Vertical sections near the master fault tips (section AA' and section CC') and at the center of the basin (section BB') with increasing offset show the crack propagation and graben formation and evolution in different areas within the master strike-slip faults. At the center of the model, a deep and narrow depression bounded by several upward-divergent, symmetric, steeply dipping faults forms.

Transtension

Figure 4.30 presents the schematic diagram of vertical sections (AA', BB', and CC') longitudinally across the transtensional model. Vertical sections near the master fault tips (section AA' and section CC') and at the center of the basin (section BB') with increasing offset show the crack evolution and basin development which have been described in chapter 4.3.2. At the center of the model, two symmetric depressions bounded by several upward-divergent concave-up dipping fault segments form [*Wu et al*., 2009]. These fault segments become the cross-basin fault of the strike-slip fault system.

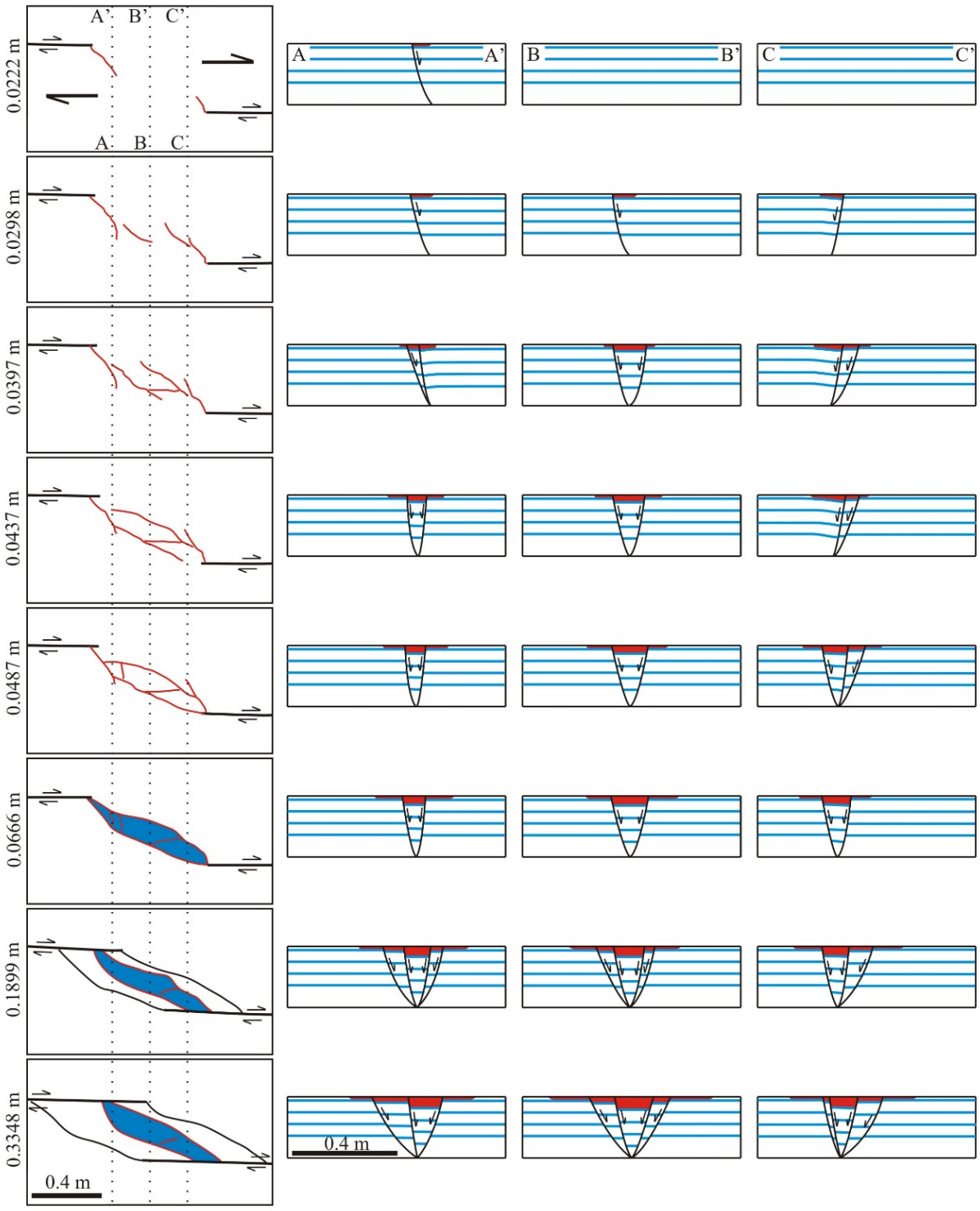

Figure 4.29 Vertical sections with fault interpretation (right) for three locations (AA', BB', and CC') in pure strike-slip underlapping model with increasing strike-slip displacement, and corresponding plan view evolution (left).

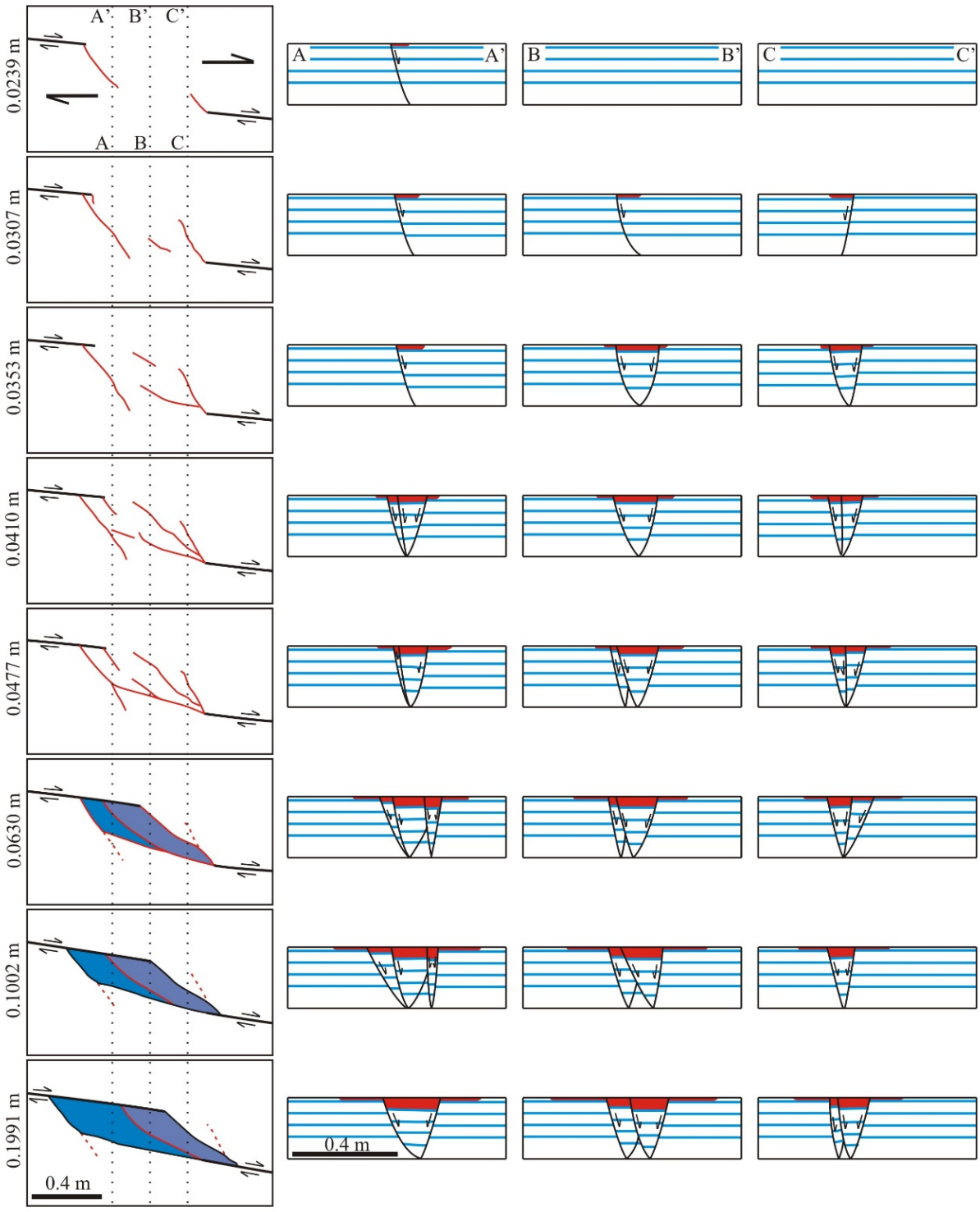

Figure 4.30 Vertical sections with fault interpretation (right) for three locations (AA', BB', and CC') in transtensional underlapping model with increasing strike-slip displacement, and corresponding plan view evolution (left).

4.6 Pure strike-slip of several fault strands

4.6.1 Model set-up

Micro-scale models with length and width of both 3.6 m are chosen to model pull-apart basin evolution with four pre-defined strike-slip faults (master faults). Three typical models, i.e., 30° underlapping, 90° non-overlapping, and 150° overlapping releasing sidestep models are selected (Figure 4.31). The overlaps of the master faults are -0.3464 m, 0 m and 0.3464 m, respectively. Fault separation between each parallel fault strand is fixed at 0.20 m to allow direct comparison of simulation results between the three cases. Young's modulus of 25 MPa and tensile strength of 1 MPa are given for the modeling. The corresponding normal stiffness (k_n) and shear stiffness (k_s) are 5e7 N/m, and the corresponding normal contact bond strength (n-bond) and shear contact bond strength (s-bond) are 8e3 N.

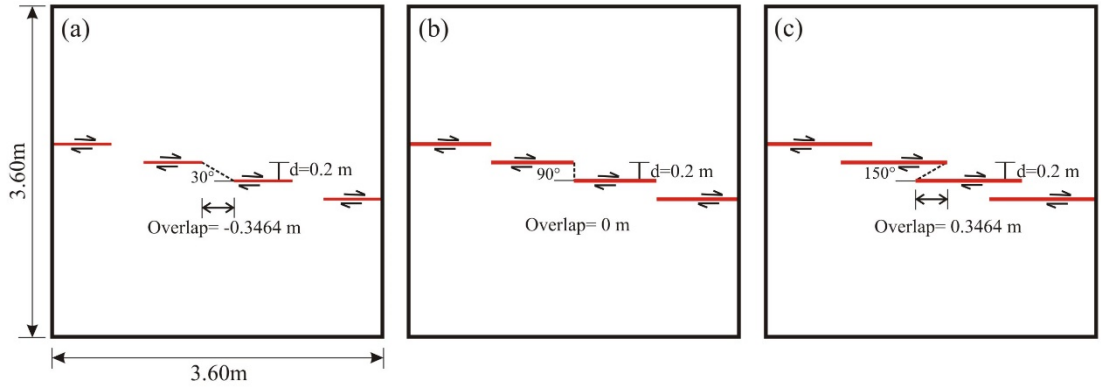

Figure 4.31 Models with four pre-defined strike-slip faults (master faults) for pure strike-slip: (a) 30° underlapping releasing sidestep, (b) 90° non-overlapping releasing sidestep, (c) 150° overlapping releasing sidestep.

4.6.2 Basin development

30° underlapping releasing sidestep model

Figure 4.32 presents the development sequence which was observed in the 30° underlapping releasing sidestep model with four predefined strike-slip faults, including contact force distribution (1a-1f, Figure 4.32), and crack propagation (2a-2f, Figure 4.32). Figure 4.33 shows the corresponding particle distribution (1a-1f, Figure 4.33) and crack interpretation (1a-1f, Figure 4.33). With right-lateral strike-slip offset, extensional areas form at the linkages of the master faults. As slip increases, right-lateral Riedel-shears propagate at a small angle (acute angle) clockwise to the trace of the master faults (Figure 4.32a and 4.33a). Later on, the Riedel-shears propagate. In the first (left) releasing sidestep, the Riedel-shears

link with each other. In the second (middle) releasing sidestep, the Riedel-shears link with the master faults (Figures 4.32b, 4.33b, 4.32c and 4.33c). With further strike-slip offsets, basin sidewalls form, the first releasing sidestep produces a spindle-shaped depression and the other two sidesteps form rhomboidal basins (Figure 4.32d and 4.33d). With continued displacements, basin sidewalls move outward and the basin lengthen, forming a lazy-Z-shaped, rhomboidal basin, from left to right, respectively (Figure 4.32e and 4.33e). As slip increases, the basins lengthen, and three rhomboidal basins form (Figure 4.32f and 4.33f).

90° non-overlapping releasing sidestep model

Figure 4.34 and Figure 4.35 show the development of pull-apart basin in 90° non-overlapping releasing sidestep model with four predefined strike-slip faults. At the initial stage, three extensional areas form at the linkage of each master faults. As slip increases, right-lateral Riedel-shears begin to occur (Figures 4.34a and 4.35a). Later on, the Riedel-shears propagate and link with the master faults (Figures 4.34b and 4.35b). With further strike-slip displacements, basin sidewalls form, bounding short squat depressions (Figures 4.34c and 4.35c). As slip increases, the basin sidewalls move outward, and the depressions lengthen (Figure 4.34 d-e, 4.35d-e). With continued strike-slip offsets, the depressions become longer, forming three elongated rhomboidal basins (Figures 4.34f and 4.35f).

150° overlapping releasing sidestep model

Figure 4.36 and Figure 4.37 illustrate the evolution of 150° overlapping releasing sidestep with four predefined strike-slip faults. At the very beginning, maximum contact forces concentrate at the linkage of the master faults. With right-lateral strike-slip displacements, right-lateral Riedel-shears begin to occur at a low angle measured clockwise to the trace of the master faults (Figure 4.36a and 4.37a). As slip increases, the Riedel-shears propagate and some of them link with the master faults (Figure 4.36b and 4.37b). Later on, several basin sidewalls form (Figure 4.36c and 4.37c). With more offsets, new Riedel-shears continue to form, and almost all Riedel-shears link with the master faults (Figure 4.36d and 4.37d). It is worth mentioning that, in this stage, cracks in another direction called P-shears begin to occur. P-shears usually develop after the establishment of Riedel-shears (2d, Figure 4.37). Based on *Fossen* [2016], the development of P-shears is probably related to temporal variations in the local stress field along the shear zone as offset accumulates. With further strike-slip displacement, more Riedel-shears and P-shears occur, and three extensional rhomboidal pull-apart basins form (Figure 4.36e and 4.37e). As slip continues, the basins lengthen, and more P-shears develop (Figure 4.36f and 4.37f).

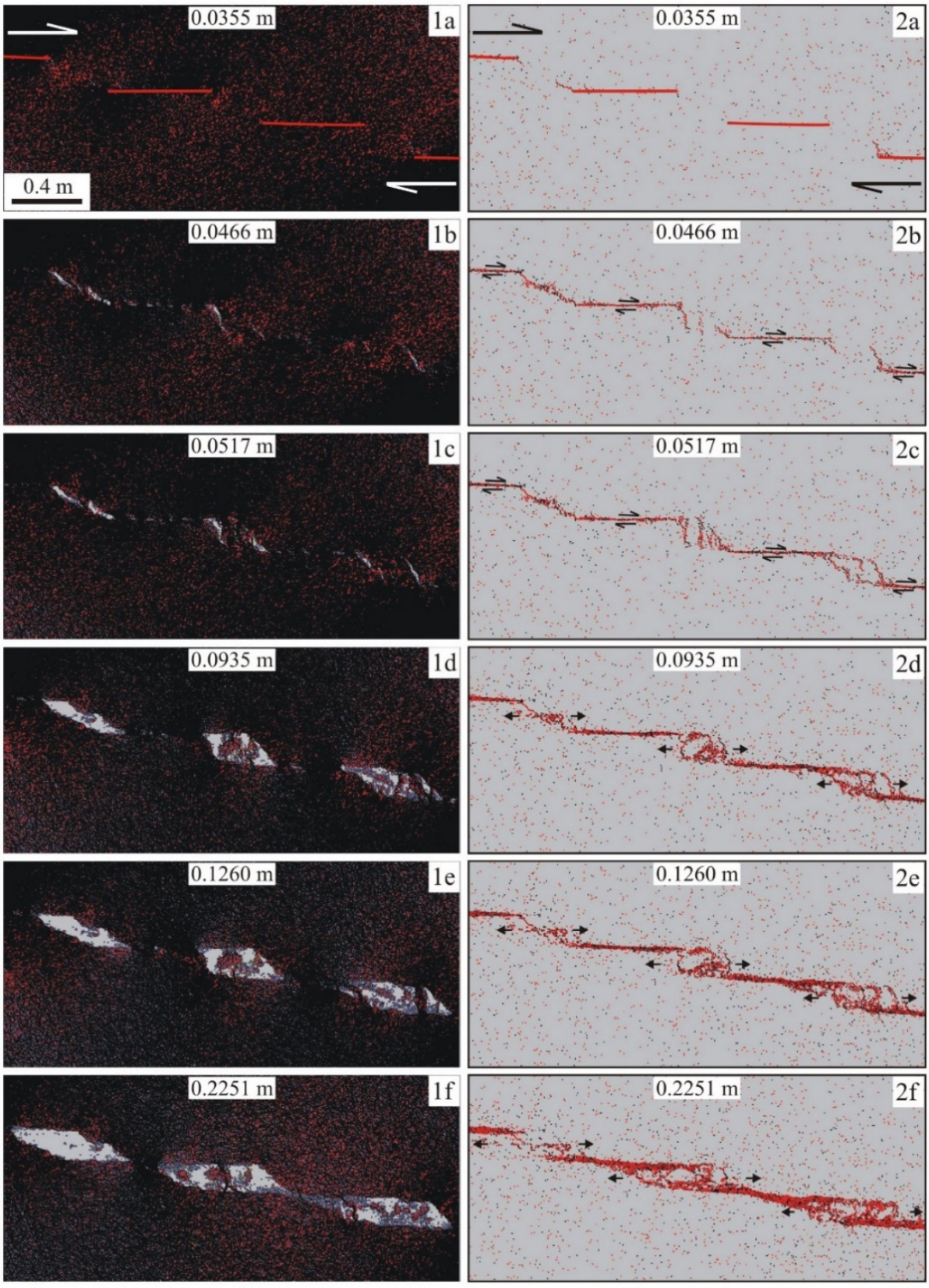

Figure 4.32 Evolution of 30° underlapping releasing sidestep model with four pure strike-slip faults. 1a-1f: contact force distribution; 2a-2f: crack propagation.

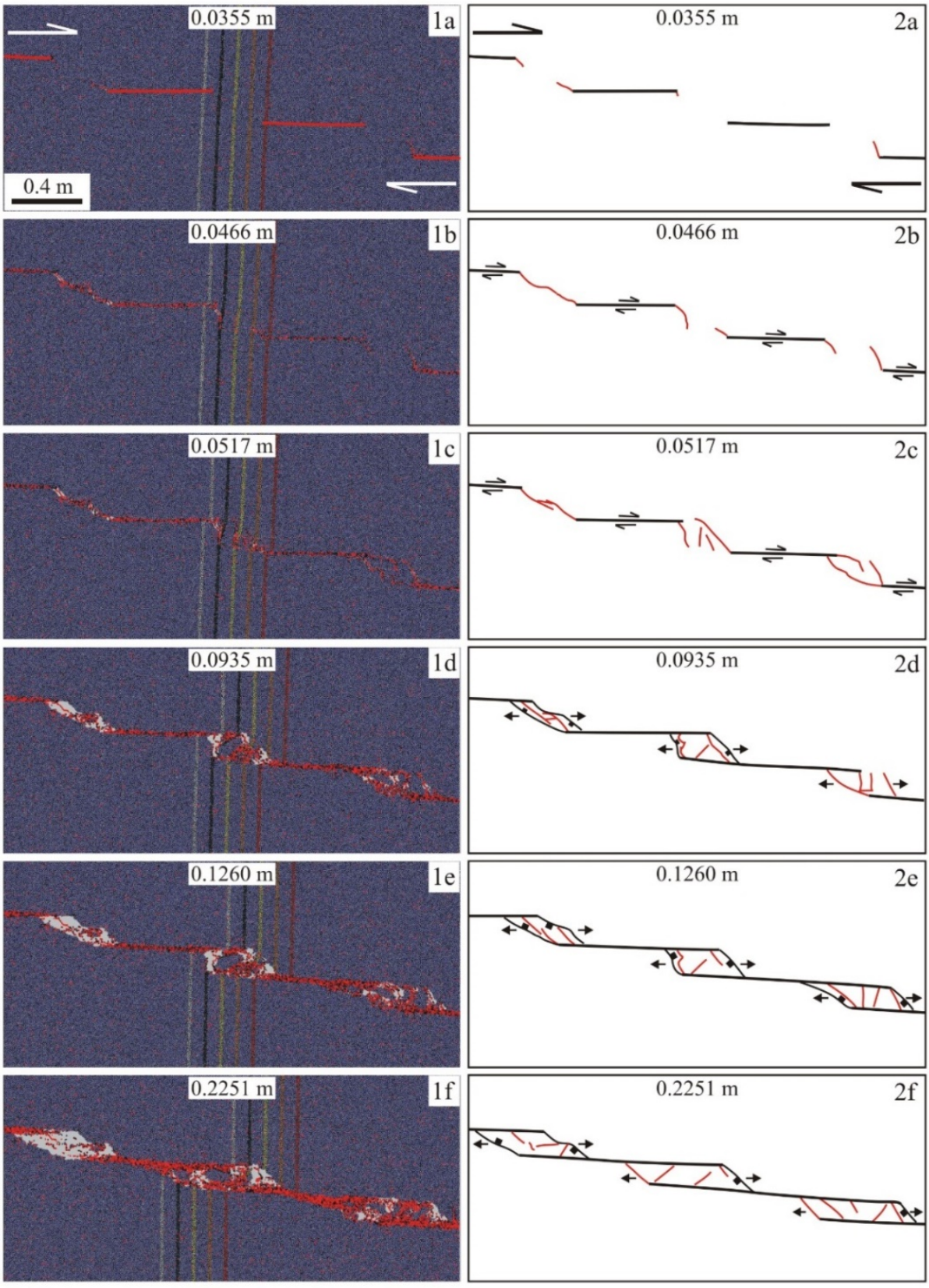

Figure 4.33 Evolution of 30° underlapping releasing sidestep model with four pure strike-slip faults. 1a-1f: particle distribution with crack propagation; 2a-2f: crack interpretation and basin geometry evolution.

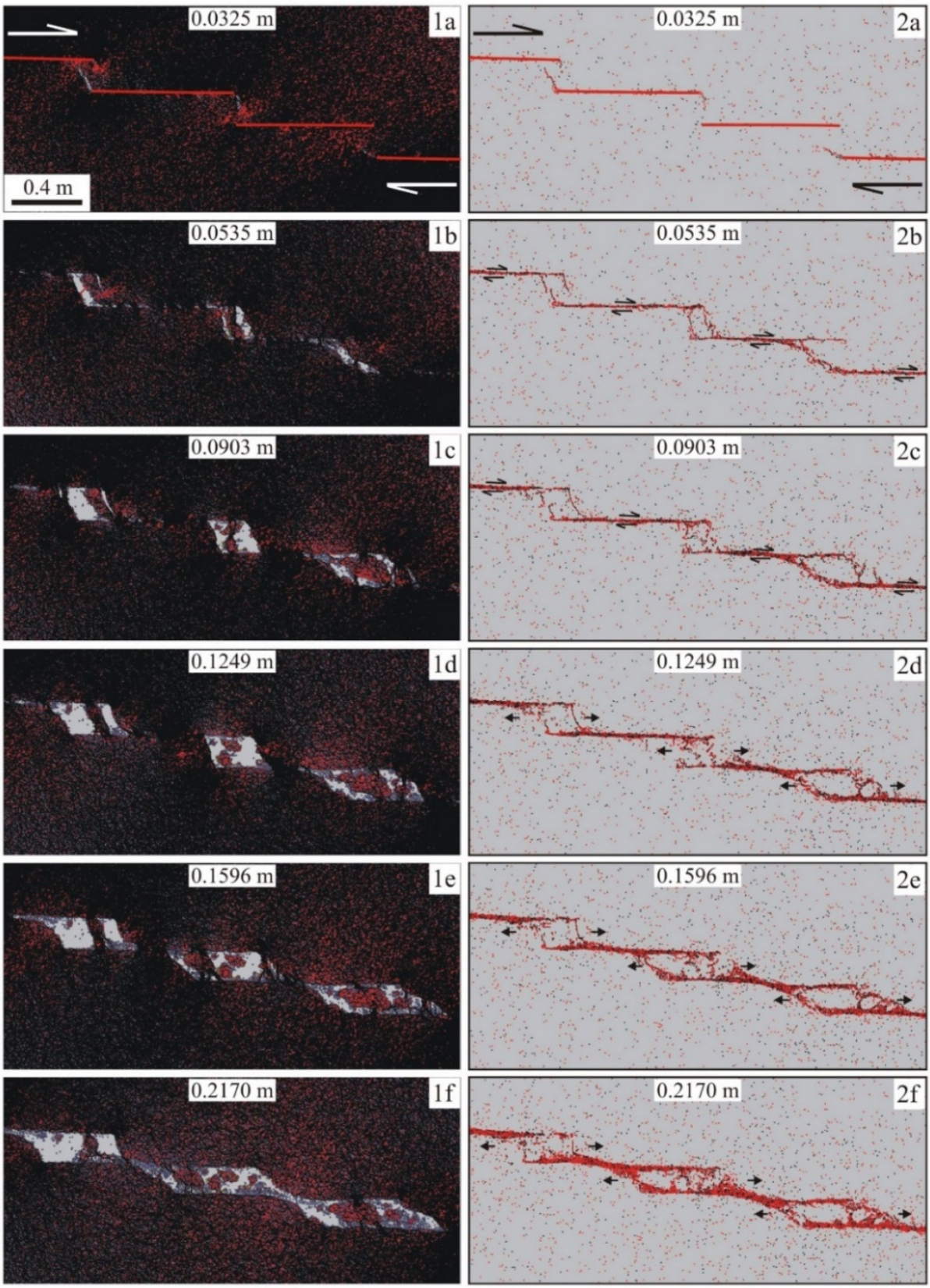

Figure 4.34 Evolution of 90° non-overlapping releasing sidestep model with four pure strike-slip faults. 1a-1f: contact force distribution; 2a-2f: crack propagation.

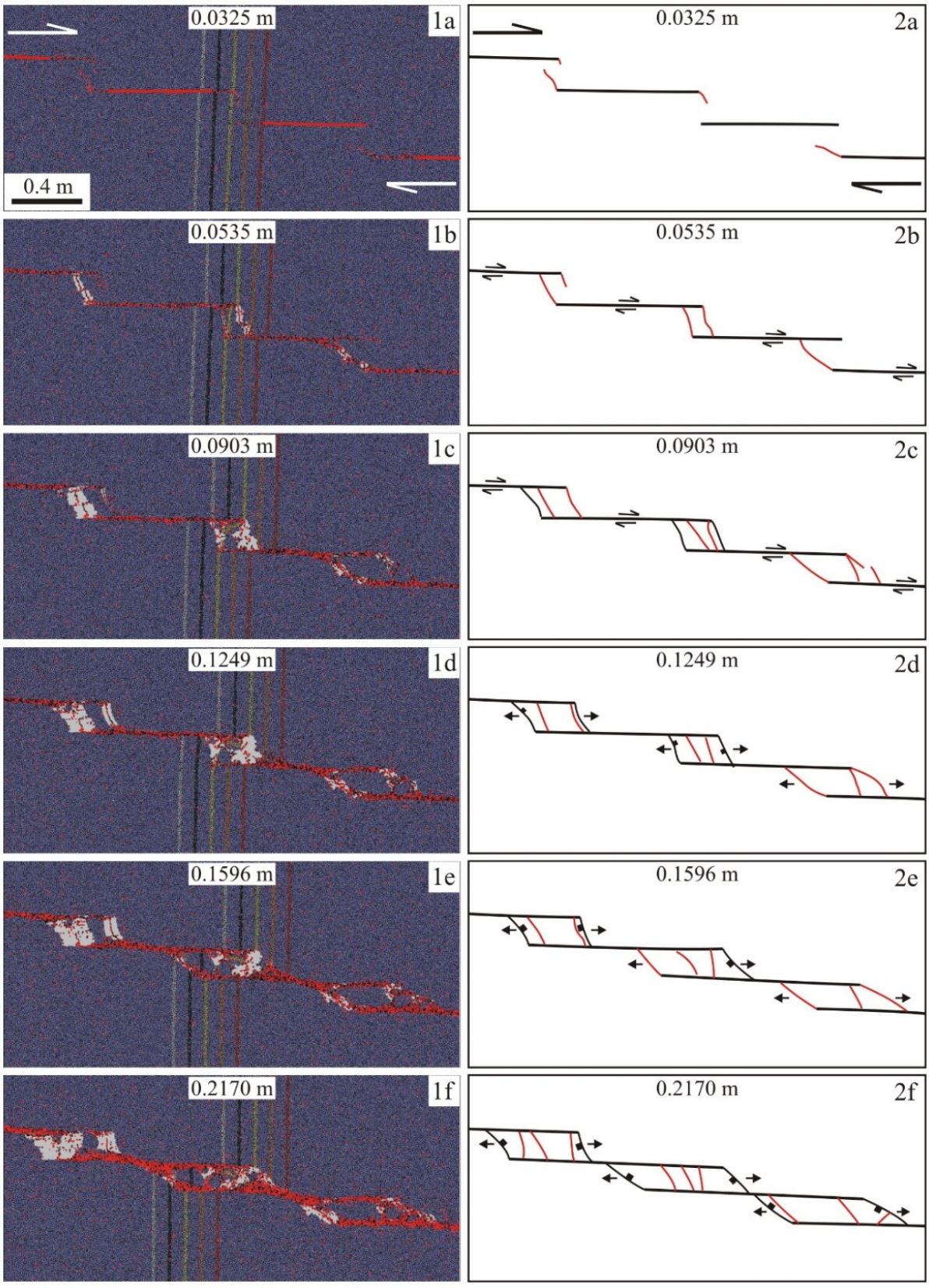

Figure 4.35 Evolution of 90° non-overlapping releasing sidestep model with four pure strike-slip faults. 1a-1f: particle distribution with crack propagation; 2a-2f: crack interpretation and basin geometry evolution.

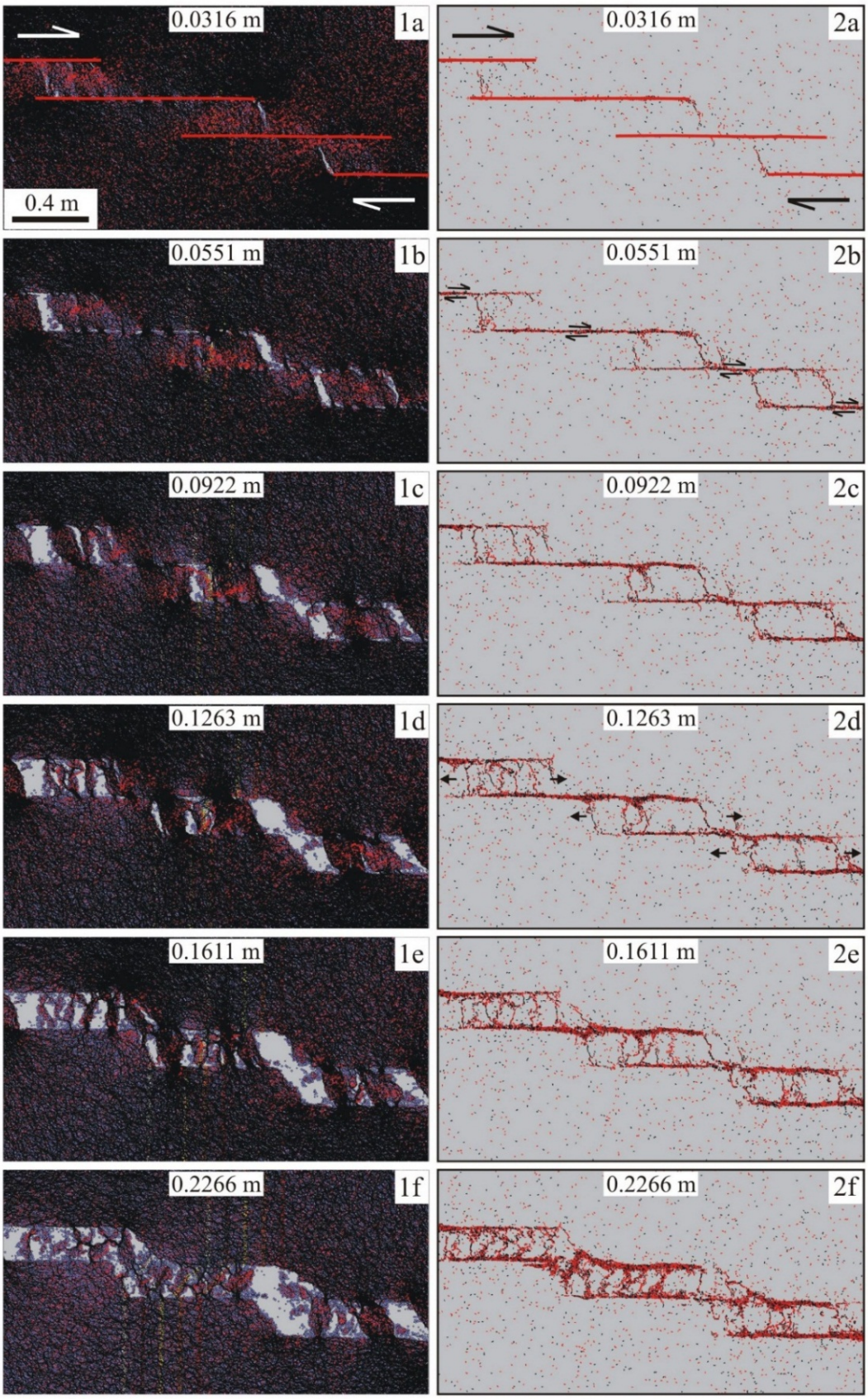

Figure 4.36 Evolution of 150° overlapping releasing sidestep model with four pure strike-slip faults. 1a-1f: contact force distribution; 2a-2f: crack propagation.

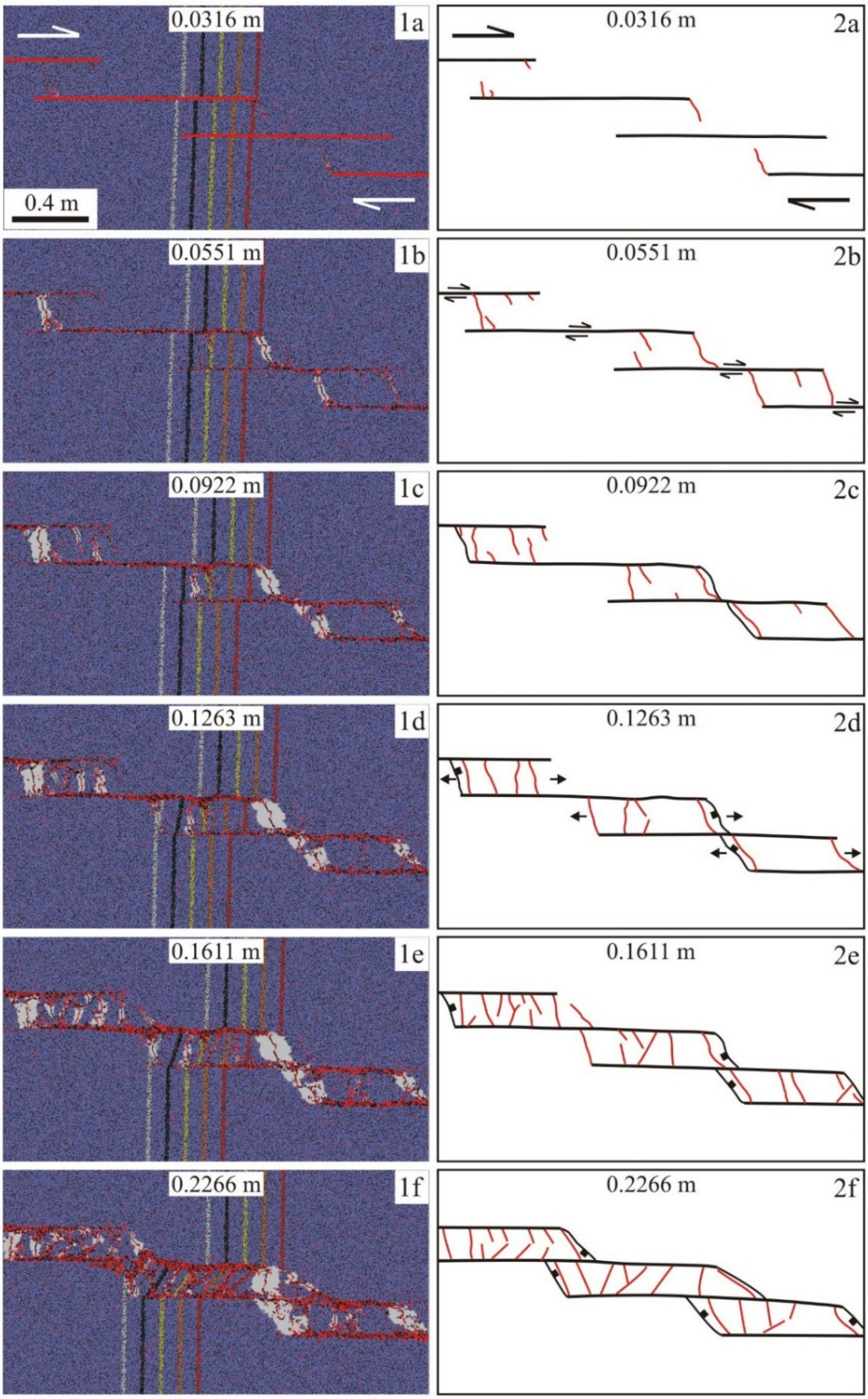

Figure 4.37 Evolution of 150° overlapping releasing sidestep model with four pure strike-slip faults. 1a-1f: particle distribution with crack propagation; 2a-2f: crack interpretation and basin geometry evolution.

4.7 Conclusions

4.7.1 Crack propagation and basin development of two master faults

The particle-based models presented in this study have firstly simulated the crack propagation and coalescence on a sound physical basis during pull-apart basin development. Geometric differences of pull-apart basins result from both the initial strike-slip fault geometries and its various evolution stages. Thus, crack propagation and basin evolution in 30° underlapping releasing sidestep model are different from 90° non-overlapping and 150° overlapping models.

30° underlapping model

In 30° underlapping releasing sidestep model with pure strike-slip, first cracks (Riedel-shears) begin to occur at the tips of master faults when peak stress is reached. Then, the Riedel-shears propagate and coalesce with the master faults, bounding a spindle-shaped depression. As seen in Figure 4.38, pull-apart basins do not suddenly come into existence. They evolve through a sequence of closely related states. 30° underlapping releasing sidestep model produces pull-apart basins that evolve from spindle-shaped through lazy-Z-shaped to the rhomboidal and stretched rhomboidal basin.

For 30° underlapping transtensional model, the Riedel-shears also form at the tips of the master faults at the initial stage. Then subsidence area bounded by Riedel-shears occurs. Meanwhile, oblique-extensional crack segments at the subsidence center propagate and link, forming a cross-basin strike-slip fault zone. Therefore, two depocenters separated by the dip-slip cross-basin fault form. With increasing transtensional offset, the basin lengthens, producing an oblique, elongated, rhomboidal-shaped basin. Different from the pure strike-slip system, the basin not only lengthens, but also widens because of the increase of fault separation away from the tips of the master faults. Therefore, with the same offset, the basin forming in transtensional system is wider than the basin in pure strike-slip system.

In 30° underlapping transpressional system, Riedel-shears propagate at the tips of the master faults. Then, oblique-extensional cracks form between the Riedel-shears. With further transpressional offset, the Riedel-shears coalesce with the oblique cracks, forming a diagonal fault which coalesces the tips of the two master faults. As offset increases, the first subsidence area forms along the diagonal fault. Basin sidewalls also develop, bounding an oblique, asymmetric pull-apart basin. With more transpressional offset, the basin lengthens. The depocenter of the basin is along the diagonal fault and may not migrate.

90° non-overlapping and 150° overlapping models

In 90° non-overlapping and 150° overlapping systems with pure strike-slip, transtensional, and transpressional master faults, Riedel-shears always form at the tips of master faults when peak stress is reached. Then, the Riedel-shears propagate and link with the master faults, forming a rhomb-shaped depression. The non-overlapping and overlapping systems directly generate rhomboidal pull-apart basins, without evolving through spindle and lazy-Z-shaped stages. Basin width does not change significantly and is governed by the separation of the master strike-slip faults. Basin length increases with increasing strike-slip displacements. The shape of a pull-apart basin in 90° non-overlapping and 150° overlapping systems is the consequence of the initial overlap of master faults and its various evolution stages.

4.7.2 Stress-deformation curves

All three typical models (30°, 90°, 150° releasing sidestep) with pure strike-slip, transtensional, and transpressional master faults show nearly the same behavior in respect to the σ_1-ε_x^*curve. Peak stress and onset of crack propagation are observed for relative extension ε_x^* of approximately 0.035. The relative extension ε_x^* to form the first depression area is about 0.155.

4.7.3 Pure strike-slip of several fault strands

The models with four predefined strike-slip faults in 30°, 90°, 150° releasing sidestep systems show the same trends of crack propagation and pull-apart basin evolution. At the initial stage, Riedel-shears begin to occur at a low angle clockwise to the trace of the master faults. As slip increases, the Riedel-shears propagate. Later on, basin sidewalls form, and three extensional depressions appear. With more offsets, the depressions coalesce into composite basins, forming a large basin. The basin length is comparable to the strike-slip displacement which corresponds to the evolution stage. The basin width is the sum of the separation between the master strike-slip faults. Moreover, the 30° underlapping releasing sidestep with several pure strike-slip fault strands show the tendency of the en-echelon strike-slip faults to straighten themselves because of the formation of the diagonal faults in each small pull-apart.

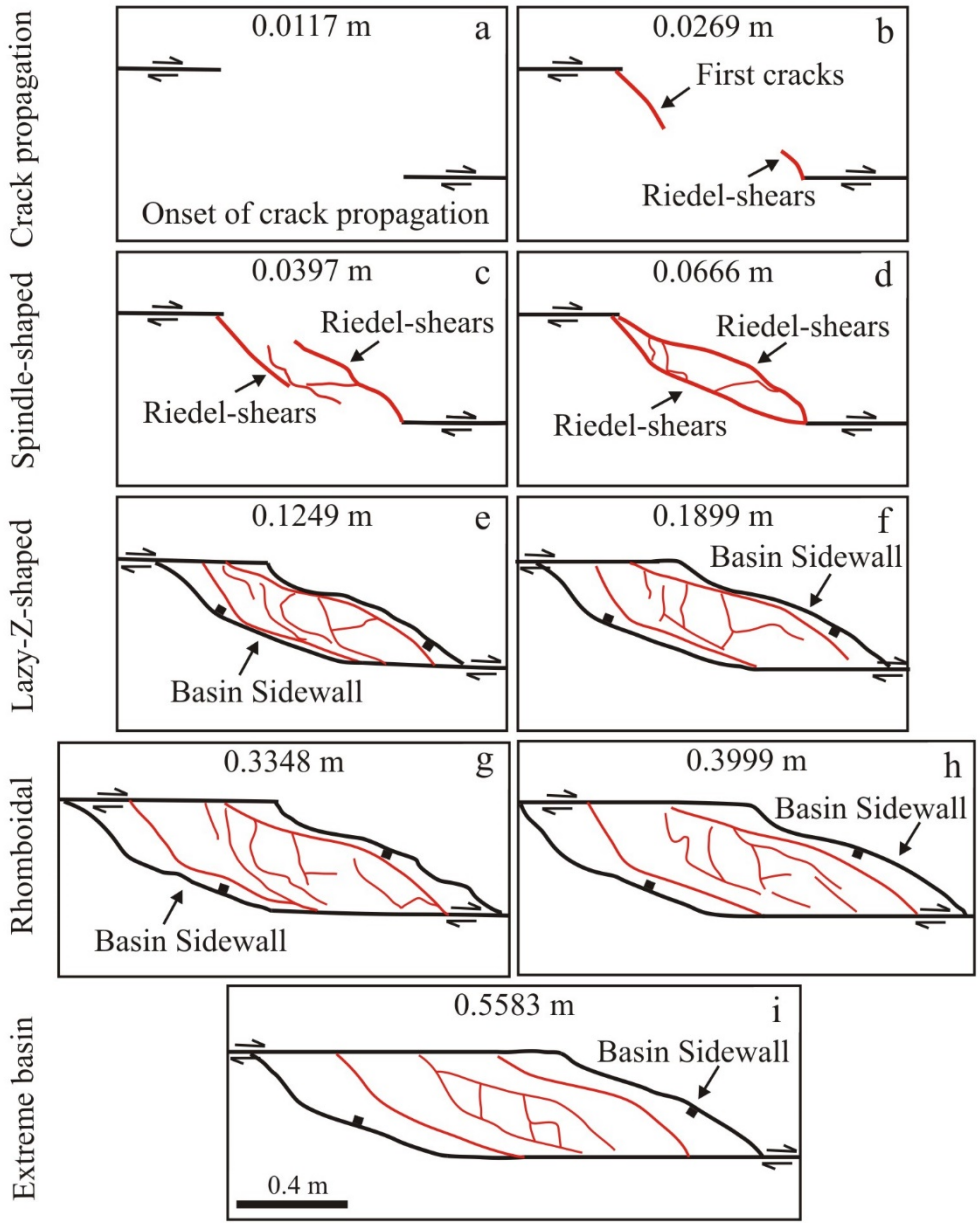

Figure 4.38 Detailed evolutionary process of pull-apart basins in underlapping system based on modeling results.

5 Applications of modeling results

5.1 Introduction

In this chapter, modeling results are compared with natural examples. Pull-apart basins in Colombia, China, and Turkey show strong similarities to the basin geometries produced by the numerical modeling with different initial fault geometries. Dead Sea basin is selected as an example to discuss the origin of rhomboidal pull-apart basins. Then, depocenters of pull-apart basins, cross-basin faults and their significances, and models for pull-apart basin development are discussed. Finally, minimum displacements to form pull-apart basins and minimum ages of initiation of pull-apart basins are estimated.

5.2 Comparison of numerical models with natural examples

5.2.1 Single basin

Algeciras Fault System, SW Colombia

El Paraiso basin, Algeciras basin, Pitalito basin and Sibundoy basin are active pull-apart basins located at the right-lateral Algeciras fault system (AFS), central part of the Eastern Cordillera in SW Colombia (Figure 5.1a-5.1c) [*Chorowicz et al*., 1996; *Velandia et al*., 2005]. The age of activity is late Quaternary. The exact age of these basin is not so clear because of the chronological limitation on quaternary sediments.

El Paraiso basin (Figure 5.1a) displays close geometric similarities to spindle-shaped basin presented in the 30° underlapping model (stage b, Figure 4.3). The master fault separation is 1.5 km. The basin occupies a right step between the secondary faults of the Algeciras fault. Algeciras basin (Figure 5.1a) is a pull-apart basin located at the southwest side of the El Paraiso basin. The master fault separation is 3 km. Algeciras basin is a lazy-Z-shaped depression and the master faults are linked by the cross-basin faults. It shows strong structural similarities to the lazy-Z-shaped basin in the 30° underlapping model (stage c, Figure 4.3).

Pitalito basin (Figure 5.1b) occupies a right step between the El Cedro fault (CF) and Pitalito fault (PF) in SW Colombia [*Chorowicz. et al*., 1996; *Velandia et al*., 2005]. This basin is a rhomboidal pull-apart basin with a width of approximately 10 km. Neotectonic studies on Quaternary deposits suggested right-lateral displacement along the faults [*Velandia et al*., 2005]. The rhomboidal pull-apart basin is similar to the rhomboidal model in 30° underlapping model (stage d, Figure4.3) and 90° non-overlapping model (stage b and stage c,

Figure 4.5).

Sibundoy basin (Figure 5.1c) is a rhomboidal pull-apart basin developed at the releasing sidestep of the right-lateral San Francisco fault (SFF). The master fault separation is about 9 km, and the fault overlap is larger than the Pitalito basin. Sibundoy basin shows an elongated rhomboidal shape which is similar to the rhomboidal basin in the 30° underlapping model (between stage d and stage e, Figure 4.3), 90° non-overlapping model (stage d, Figure 4.5) and 150° overlapping model (stage c, Figure 4.7).

North Anatolian Fault Zone, Turkey

Tasova-Erbaa basin (Figure 5.1d) and Niksar basin (Figure 5.1e) are two adjacent pull-apart basins along the North Anatolian fault zone (NAFZ), Turkey. Tasova-Erbaa basin is an ancient pull-apart basin and a present-day morphological depression, bounded by historically active faults [*Barka et al*., 2000]. The elongated rhomboidal shape of the Tasova-Erbaa basin displays close similarities to the elongated rhomboidal basin in the numerical models. In contrast, Niksar basin (Figure 5.1e) is an active pull-apart basin bounded by offset fault segments of the NAFZ [*Barka et al*., 2000]. The active Niksar basin has master fault separation of about 12 km, and exhibits lazy-Z shape of a classic pull-apart basin [*Mann et al*., 1983; *Barka et al*., 2000], which is similar to the 30° underlapping model (stage c, Figure4.3). The starting age of Niksar basin is early Pleistocene.

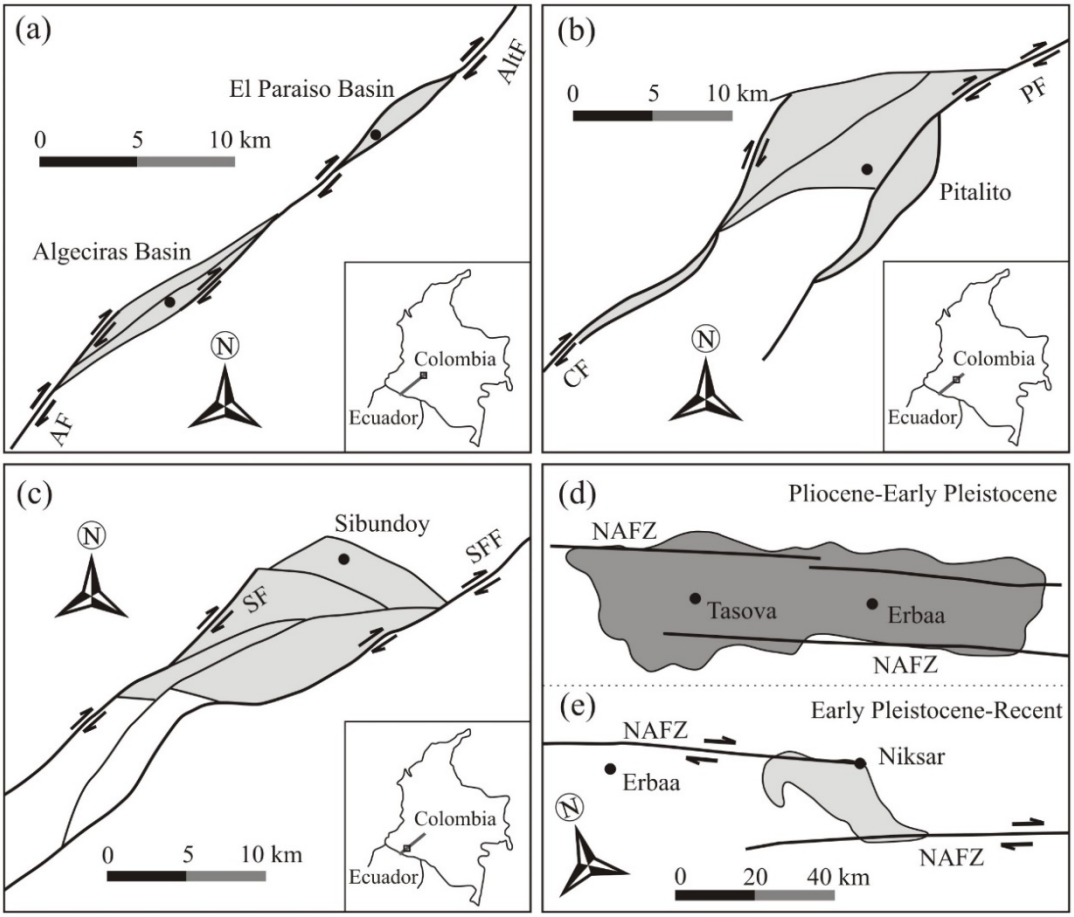

Figure 5.1 Examples of pull-apart basins in nature.
(a) Map of active spindle-shaped pull-apart basin (El Paraiso basin) and lazy-Z-shaped pull-apart basin (Algeciras basin) along Algeciras fault system (AFS), central part of the Eastern Cordillera in SW Colombia, modified from *Velandia et al*. [2005]. AltF: Altamira fault, HF: El Hobo fault, AF: Algeciras fault. (b) Map of active rhomboidal pull-apart basin (Pitalito basin) along the AFS, modified from *Velandia et al*. [2005]. PF: Pitalito fault, GF: Granadillo fault, CF: El Cedro fault. (c) Map of active rhomboidal pull-apart basin (Sibundoy basin) along the AFS, modified from *Velandia et al*. [2005]. SF: Sibundoy fault, SFF: San Francisco fault. (d) Map of ancient rhomboidal pull-apart basin (Tasova-Erbaa basin) along the North Anatolian fault zone (NAFZ) in Turkey [*Barka et al*., 2000]. (e) Map of active lazy-Z-shaped pull-apart basin (Niksar basin) along the NAFZ [*Barka et al*., 2000].

Haiyuan fault, China

Haiyuan fault is a strike-slip fault which is located at the northeastern margin of the Tibetan Plateau in Western China (Figure 5.2). It consists of several secondary faults which have different strikes changing from N30 - 45W to N75 - 90W, from southeast to northwest segment. It appears as a convex-to-the-northeast oroclinal structure. Several pull-apart basins (XNCB, LHYXB, GYCB, SJCB, DYSB, SSB, HLTB and SJZB) (Figure 5.2) developed at the releasing sidestep of the secondary faults where sinistral strike-slip faults step to the left since the Middle or Late Pleistocene [*Deng et al*., 1989; *IG and SBNHAP*, 1990; *Shi et al*.,

2015]. Although the numerical models are right-lateral, fault pattern and basin geometries are still valid because they can be simply mirror-inverted.

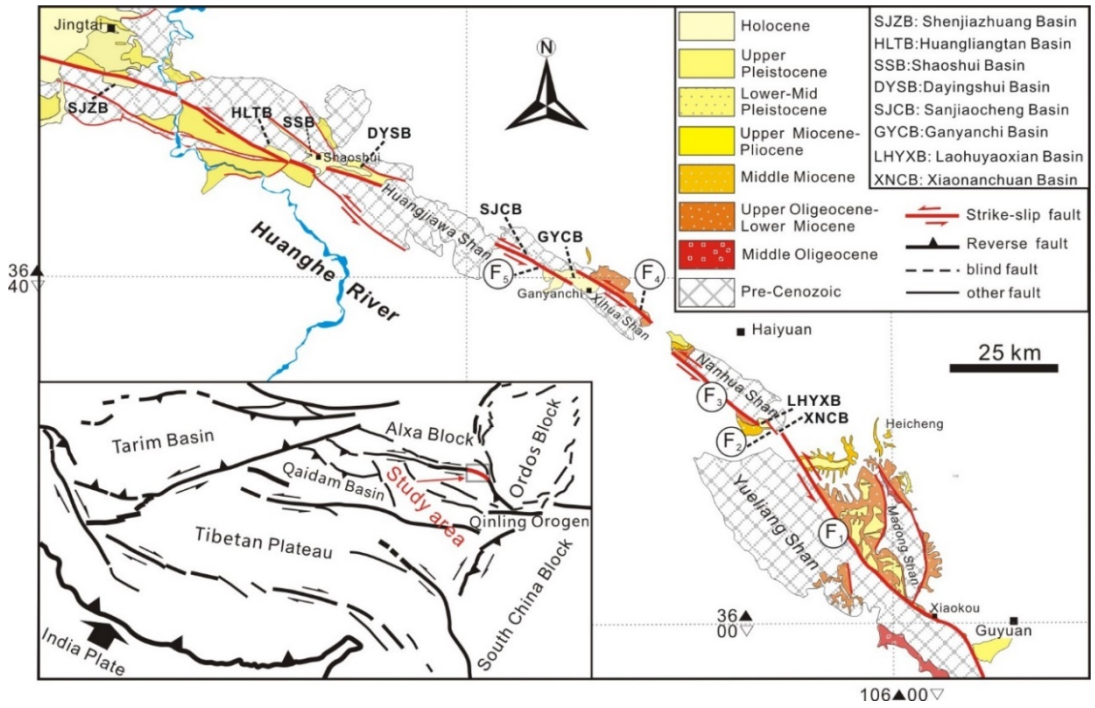

Figure 5.2 Geologic map of the South Ningxia region in the northeastern Tibetan Plateau (according to the regional geologic maps (1:200000) of the Ningxia Hui Autonomous Region and Gansu Province; *IG and SBNHAP*, 1990; *Shi et al*., 2015).

Ganyanchi basin (GYCB) is a pull-apart basin situated at the releasing sidestep of sinistral strike-slip faults (Figures 5.2 and 5.3, F4 and F5). The epicenter of the 1920 Haiyuan earthquake (M=8.7) was in this basin. The basin length and width are about 8 and 3 km, respectively. It is a typical rhomboidal depression (Figure 5.3). Basin structure and fault pattern show great similarities to the numerical model obtained from the 30° underlapping releasing sidestep model. Haiyuan fault is still an active fault and Ganyanchi basin is still receiving sedimentation. Previous drilling data reveal that the depth of the Quaternary sediments of this basin are at least 176 m [*IG and SBNHAP*, 1990]. Limited by geologic chronology on quaternary sediments, the exact age of the deposits in Ganyanchi basin is not clear. The basin formation started probably at middle Pleistocene to Holocene [*IG and SBNHAP*, 1990].

Luhuyaoxian basin (LHYXB) developed at the fault linkage of the secondary strike-slip faults (Figures 5.2 and 5.4, F2 and F3) with strike of 330°. This basin is smaller than the Ganyanchi basin and is a typical rhomboidal graben, with the same basin length and width of about 2 km. This extensional graben formed where left-lateral strike-slip faults step to the left.

Fault architecture and basin geometry are similar to the numerical 90° underlapping releasing sidestep model. Inferring from the fault cutting patterns and the sediments in the basin, the approximate starting age of the Luhuyaoxian basin formation is late Pleistocene to Holocene [*IG and SBNHAP*, 1990].

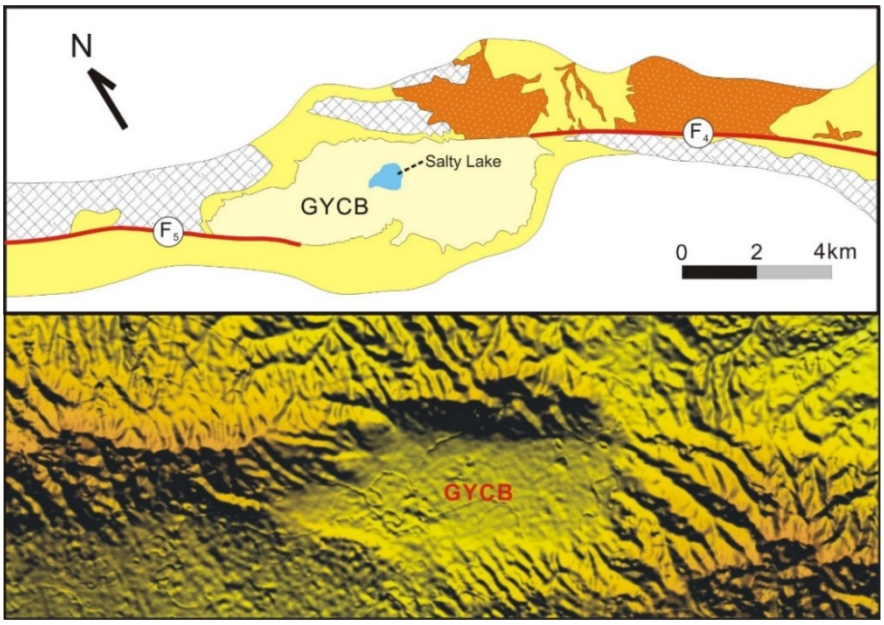

Figure 5.3 Geologic map of Ganyanchi Basin (GYCB) [*IG and SBNHAP*, 1990] above and corresponding Digital Elevation Model below.

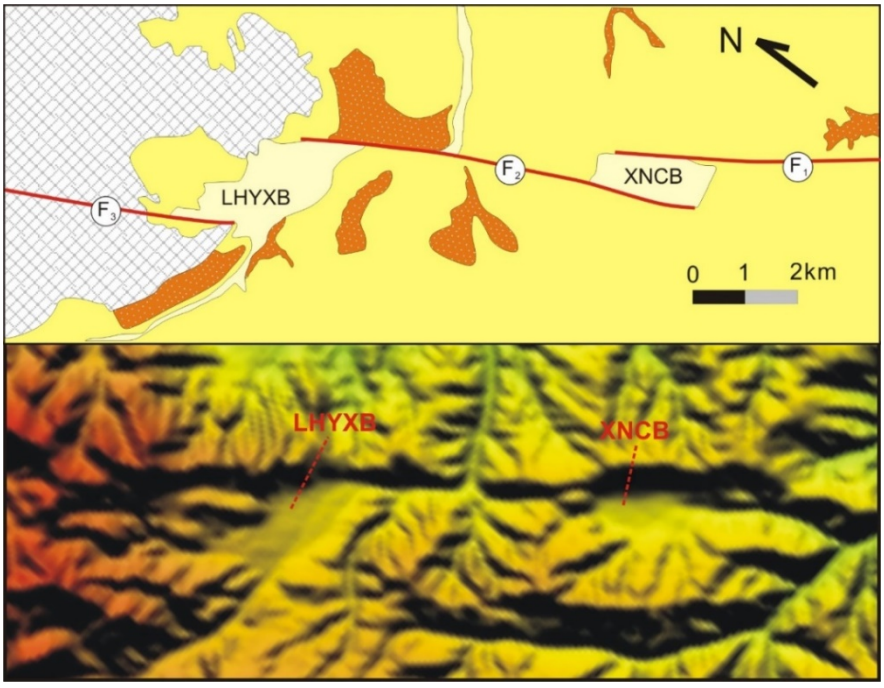

Figure 5.4 Geologic map of Laohuyaoxian basin (LHYXB) and Xiaonanchuan basin (XNCB) [*IG and SBNHAP*, 1990] above and corresponding Digital Elevation Model.

Xiaonanchuan basin (XNCB) is located at the releasing sidestep of the sinistral strike-slip faults, west of the Laohuyaoxian basin (Figure 5.2 and 5.4, F1, F2). Moreover, the Xiaonanchuan basin shares the same master fault with the Laohuyaoxian basin (Figure 5.4, F2). The orientation of Haiyuan fault in this segment is also 330°. The basin appears as a box-shaped graben with basin length and width of 2-3 km and 1 km, respectively. The basin geometry shows close similarities to the structure of the 150° underlapping releasing sidestep model. According to *IG and SBNHAP* [1990], the approximate onset of the Luhuyaoxian basin formation is late Pleistocene to Holocene.

Comparison of numerical prediction with natural examples

Our models show that 30° underlapping model produces pull-apart basins that evolve through a sequence of closely related states, from spindle-shaped through lazy-Z-shaped to the rhomboidal basin. 90° non-overlapping and 150° overlapping releasing sidesteps directly generate rhomboidal shaped pull-apart basins, without evolving through spindle and lazy-Z-shaped states. All the three typical cases (30°, 90°, 150° releasing sidestep) could generate rhomboidal pull-apart basins, with different strike-slip offsets. Therefore, the shape of a pull-apart basin in nature is the consequence of both the initial strike-slip geometry and its various evolution stages.

A spindle-shaped depression forms from an underlapping releasing sidestep. As an example, the El Paraiso basin, located at the right-lateral Algeciras fault system (AFS), SW Colombia, displays close geometric similarity to a spindle-shaped basin [*Velandia et al., 2005*]. Our models show that a lazy-Z-shaped basin evolves from an underlapping system. For instance, the Algeciras basin, which is located at the southwest side of the El Paraiso basin, is a lazy-Z-shaped depression and the master faults are linked by the cross-basin faults (Figure 5.1a). This basin structure shows strong structural similarity to the lazy-Z-shaped basin in the 30° underlapping model.

For a rhomboidal pull-apart basin, the initial strike-slip fault geometry could be quite different. Based on our numerical studies, a rhomboidal basin might be originated from the three representative initial fault systems, with different offsets. Pitalito basin in SW Colombia, is a rhomboidal pull-apart basin with length and width of about 10 km (Figure 5.1b). This rhomboidal pull-apart basin might evolve from an overlapping, non-overlapping, or underlapping system with larger displacement. The Dead Sea basin with length of ~132 km and width of 7-10 km [*ten Brink et al*., 1993] is one of the best known pull-apart basins in the world. It shows strong structure similarities to the rhomboidal basin which might originate from an underlapping, non-overlapping or overlapping releasing sidestep. These results are in agreement with the findings of *Katzmann et al*. [1995] and *van Wijk et al*. [2017].

5.2.2 Coalescence of adjacent basins

Alpine Fault is a continental right-lateral strike-slip fault in South Island, New Zealand, with the total length of about 850 km. It accommodates the major convergent motion between the Pacific and Australian Plates [*Barnes et al*., 2005]. Secretary-Nancy section is located at the southern segments of the Alpine Fault. It is a 35 km long area of fault overlap, and has a strike of about 040°. The slip rate on the Alpine Fault cannot be accurately constrained because of different estimating methods. The range of the slip rate is 4-35 $mm \cdot a^{-1}$ [*Sutherland and Norris*, 1995; *Norris and Cooper*, 2001]. Secretary and Nancy basin are two pull-apart basins which developed at the releasing sidestep along the right-lateral right-stepping segments of Alpine Fault. The composite Secretary-Nancy basin shown in Figure 5.5 can be considered as a composite of at least two major strands. In addition, Koehn Lake basin on Garlock Fault in southern California is considered as a composite pull-apart basin formed by coalescence of four en-echelon faults [*Aydin and Nur*, 1982].

Secretary-Nancy basin and Koehn Lake basin show the formation of a wide composite basin with increasing strike-slip offset which is similar to the predictions by the numerical models with several pure strike-slip fault strands. For releasing sidesteps with two master faults, basin width does not change significantly and remain fixed by the separation of the master strike-slip faults. However, basin width could become larger when there are more than two strands of master faults. The natural examples of Secretary-Nancy basin and Koehn Lake basin show how this takes place. Our numerical modeling reproduced the processes.

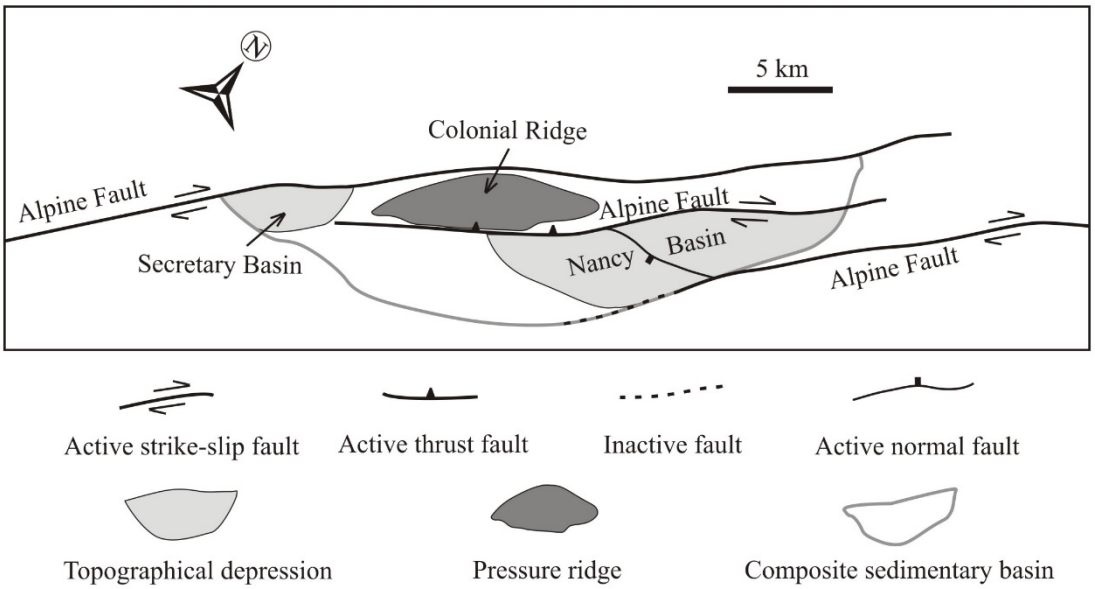

Figure 5.5 Simplified structural map of composite Secretary-Nancy basin, southern segment of Alpine Fault, New Zealand.

5.3 Origin of rhomboidal basins

How to identify the initial strike-slip fault geometry of a rhomboidal or stretched rhomboidal pull-aparts in nature? This means how to decide that this basin is a basin evolving from spindle-shaped through lazy-Z-shaped (right-lateral) to the rhomboidal basin, or a basin evolving to the rhomboidal shape without the spindle and lazy-Z-shaped states.

The Dead Sea basin is a well-studied example of stretched rhomboidal pull-apart basins, with a length of about 132 km and width of 7 - 10 km (Figure 5.6). The left-lateral offset of around 105 km was obtained from matching the pre-Cenozoic sedimentary rocks and some of the old basement complex on opposite sides of the transform rift [*Freund et al*., 1970; *Bandel and Khouri*, 1981] and comparing the lineaments of the central Negev-Sinai shear belt [*Quennell*, 1959]. The direction and amount of slip inferred from local geology is in agreement with the data got from regional plate kinematics [*Garfunkel*, 1981]. 60-70 km left-lateral slip of the Dead Sea fault systems took place in the Early to Late Miocene. 40-45 km left-lateral slip occurred probably from early Pliocene to present day (from about 7-12 Ma to present day). Therefore, the average slip rate is approximately 3.5 to 6 $mm \cdot a^{-1}$ [*Freund et al*., 1970]. With ongoing left-lateral displacement, the subsidence area of the basin shifts northward.

It is worth noting that the length of the Dead Sea basin is larger than the total amount of left-lateral slip along the Dead Sea rifts. If the initial faults have no overlap, which means that this basin evolves from an underlapping releasing sidestep, the basin length cannot be larger than the slip offset. Only when the Dead Sea rifts have overlap at the beginning, the basin length (132 km) can be larger than the total amount of left-lateral slip (105 km). Therefore, it can be concluded that the elongated rhomboidal Dead Sea pull-apart basin evolved directly from overlapping releasing sidestep. In other words, the basin did not evolve through spindle-shaped and lazy-Z-shaped stages. This conclusion is in agreement with earlier numerical studies based on continuum methods [e.g., *Katzmann et al., 1995; van Wijk et al., 2017*].

20°N pull-apart basin located along the India-Arabia transform boundary (Owen Fracture Zone) is a young pull-apart basin initiated about 3 Ma ago. The basin is 90 km long and 35 km wide, while the right-lateral offset of the Owen Ridge along the Owen Fracture Zone observed on the seafloor is 10-12 km. Estimated from geodetic [*Reilinger et al*., 2006] and geologic data [*DeMets et al*., 2010], the Arabian plate moves northward faster than the Indian plate with a relative slip rate of 3 ± 1 $mm \cdot yr^{-1}$. This indicates that the initiation of the 20°N pull-apart basin began some 3 Ma ago. *Rodriguez et al*. [2013] thought that the 20°N basin might stand for a good analog of the initial evolution stage of the Dead Sea basin. The length of the 20°N basin (90 km) is quite larger than the total slip amount (10-12 km) along the

Owen Fracture Zone. So the stretched rhomboidal 20°N basin did not go through the spindle-shaped and lazy-Z-shaped states, but evolved directly from a releasing sidestep with certain overlapping between the master faults.

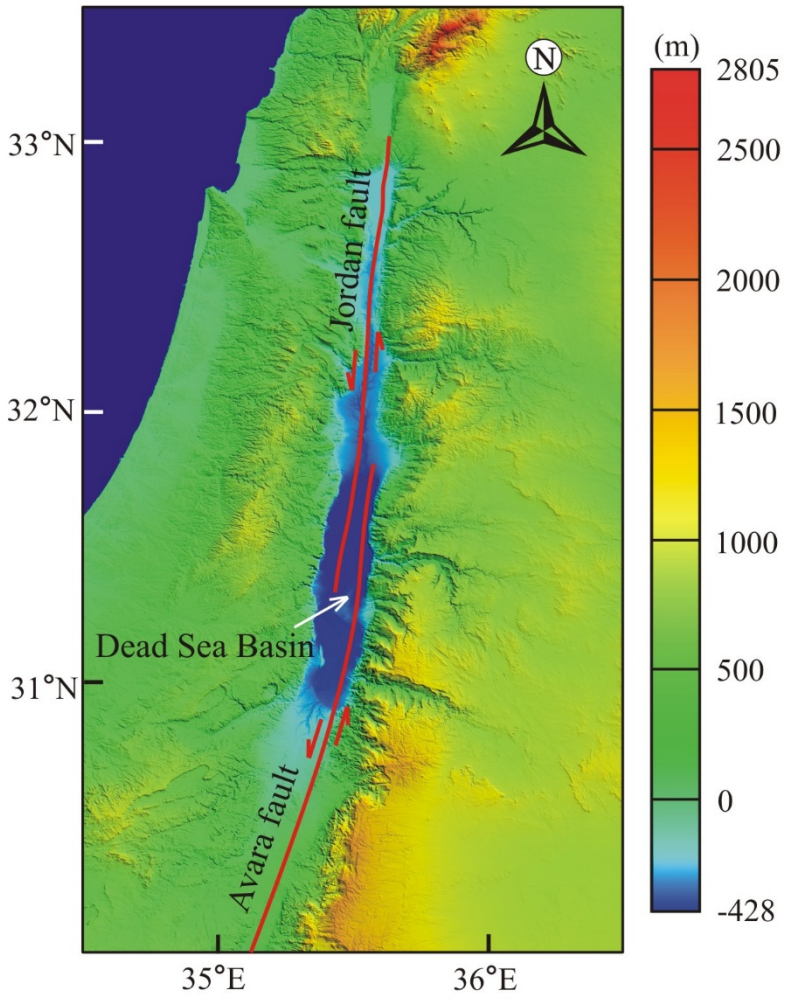

Figure 5.6 Simplified structural map of the Dead Sea basin based on SRTM digital elevation model topography (from https://www2.jpl.nasa.gov/srtm/; http://srtm.csi.cgiar.org/index.asp).

A spindle-shaped or a lazy-Z-shaped pull-apart basin forms definitely in an underlapping releasing sidestep. For a rhomboidal or a stretched rhomboidal pull-apart basin, the initial strike-slip fault geometry could be quite different. A rhomboidal basin could evolve through spindle-shaped and lazy-Z-shaped depression, with initial fault geometry of underlapping. There are also rhomboidal basins that don't go through the spindle and lazy-Z-shaped states, but instead form from an initial non-overlapping or overlapping system (Figure 5.7). To identify whether a rhomboidal basin has gone through the spindle-shaped and lazy-Z-shaped stages or not, the basin length and the total strike-slip displacement obtained from matching the strata or basement rocks across the pull-apart are compared. If the basin length is larger

than the total slip amount, the basin forms in an overlapping system without going through spindle-shaped and lazy-Z-shaped stages. If the basin length is smaller than the total slip offset, the rhomboidal basin generates in an underlapping releasing sidestep, evolving from spindle-shaped through lazy-Z-shaped state.

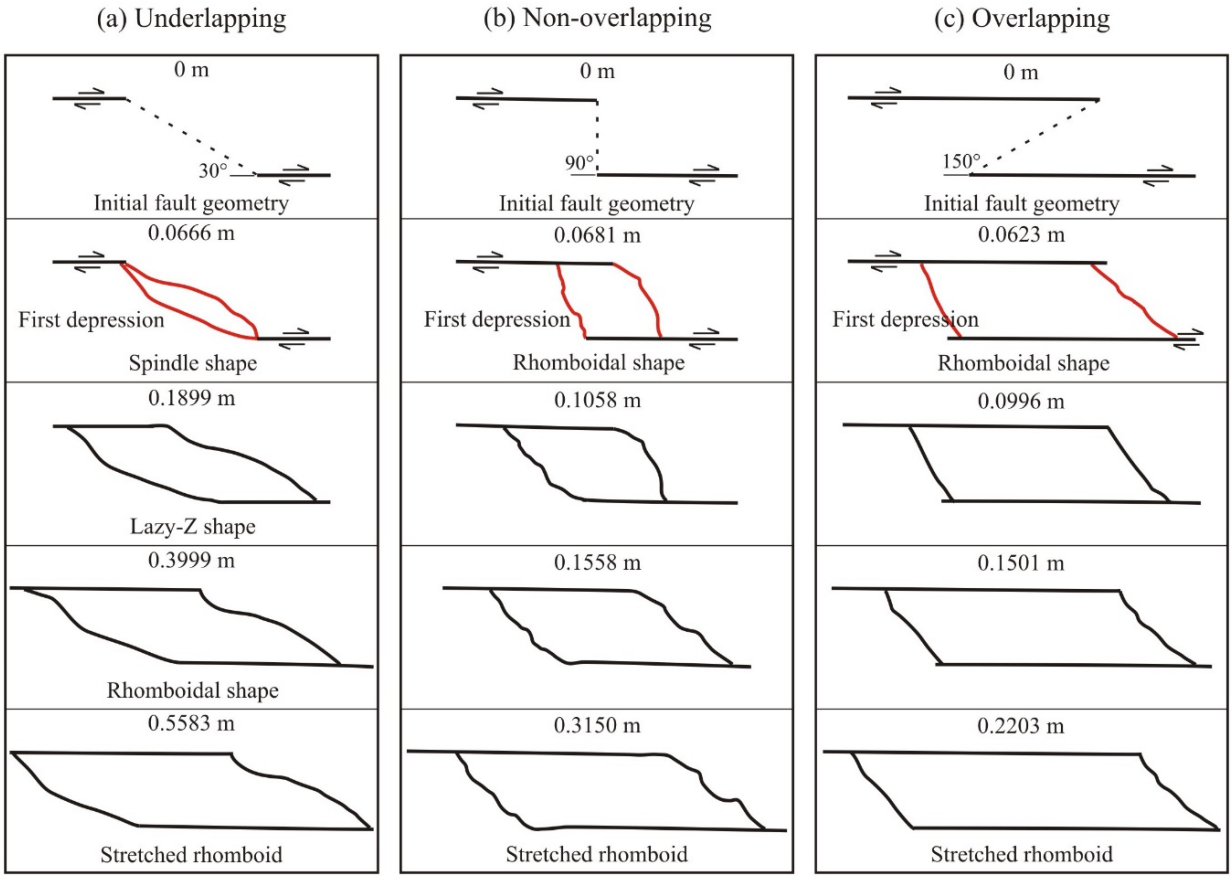

Figure 5.7 Summary of pull-apart basin development for three different initial strike-slip fault geometries based on the modeling results.

However, for some strike-slip systems, it is not so easy to obtain the amount of motion along the strike-slip system because of lacking offset of the older strata or basements across the basin. So comparison of slip offset with the basin length is difficult. Based on the modeling results, the rhomboidal basins which have cross-basin faults generally form in underlapping system, for instance Dayingshui basin in China [*Zhang et al*., 1989] and Nancy basin in New Zealand [*Barnes et al*., 2005]. These small scale rhomboidal basins with cross-basin faults have gone through the spindle and lazy-Z-shaped stages. The large scale rhomboidal or stretched rhomboidal basins without cross-basin faults such as the Dead Sea basin and 20°N basin tend to form in an overlapping system which don't go through the spindle-shaped and lazy-Z-shaped stages.

5.4 Depocenters of pull-apart basins

During pull-apart basin development, the existence of deeps or depocenters, the number of depocenters, and whether the depocenters have migrated or not remain controversial even with so many studies based on natural pull-apart examples, physical modeling, and continuum numerical simulations.

Rodgers [1980] proposed a theoretical model that the depocenters exist within the distal ends of rhomboidal pull-apart basins. Rodgers' model predicts well the distribution of depocenters in the Cariaco basin [*Mann et al*., 1983]. *Aydin and Nur* [1982] suggested an alternative model to illustrate the existence of the depocenters. This model includes two or more small pull-aparts in a large pull-apart depression. With increased offset along the master faults, the small basins coalesce and become a larger and wider composite basin.

Detailed outcrop mapping and subsurface mapping based on geophysical methods indicate that depocenters of pull-apart basins do not remain stationary with time, but instead migrate with increasing strike-slip along the master faults [*Zak and Freund*, 1981; *Wakabayashi et al.,* 2004; *ten Brink et al*., 1999; *Lazar et al*., 2006]. Among them, a well-known example is the Dead Sea pull-apart basin. *Zak and Freund* [1981] first noticed that the Dead Sea depression is occupied by three distinct Miocene to recent sedimentary basins, and the depocenters migrated northward along the strike-slip fault with ongoing left-lateral offset over time.

Some detailed stratigraphic studies on strike-slip basins suggest that the basins seem to migrate with respect to the sediment source region with continuing strike-slip offset over time [*Crowell*, 1982; *Noda and Toshimitsu*, 2009]. Based on their continuum simulation results with elastic models, *van Wijk et al*. [2017] recently proposed that the depocenters remain stationary while the tips of master faults as well as the sediment source region propagate. Their models show no migration of the depocenters with respect to the basement.

The numerical models in this study predict the existence of depocenters in 30° underlapping releasing sidestep with two master faults. In pure strike-slip system, one depocenter at the center of the basin forms and remains stationary with increasing strike-slip offset. In transtensional system, two depocenters exist and show no migration. In transpressional system, a depocenter along the diagonal fault forms and does not migrate. Elastic models set up by *van Wijk et al*. [2017] showed that the depocenters of nonverlapping and overlapping systems also remain stationary with respect to the basement.

The models with several pure strike-slip fault strands in this study indicate that there are several deeps (depocenters). Each releasing sidestep develops a depocenter. With further

strike-slip offset, the small basins coalesce and become a larger and wider composite basin.

Compared with the continuum methods [e.g., *Katzmann*, 1995; van *Wijk et al*., 2017], the advantage of the proposed DEM modeling is that we can intuitively see the crack propagation and coalescence during the pull-apart basin development. The disadvantage is lack of subsidence and uplift in vertical direction because of the limitations of two-dimensional models. Therefore, three-dimensional DEM models should be built in future to see the subsidence and uplift in vertical direction intuitively which reflect the distribution and migration of the basin depocenter and rift flank uplift.

5.5 Cross-basin faults and their significances

Based on detailed outcrop-based mapping of the several small-scale pull-apart basins within Haiyuan fault, China, *Zhang et al*. [1989] proposed that the development of basin-cross faults or diagonal faults across pull-apart basins leads to the extinction of pull-apart basins. Dayingshui basin located at the western segment of Haiyuan fault developed a cross-basin diagonal fault which took over most of the displacement from the sidewall faults [*Zhang et al*., 1989]. *Schattner and Weinberger* [2008] stated that the Hula basin along the Dead Sea fault system also developed diagonal faults, connecting the two en-echelon faults. *Van Wijk et al.* [2017] discussed the extinction of pull-apart basins based on their elastic models. Their models showed that a zone of compressional stress concentration forms that connect the tips of the master faults in underlapping systems, and they predicted that these might connect the master faults, resulting in the extinction of pull-apart basins. However, their continuum models do not allow new cracks to form, so cross-basin faults cannot be observed in their model.

The DEM models presented in this study can intuitively represent crack formation and propagation. In underlapping models, Riedel-shears form at the distal ends of the master faults and propagate at an average strike of ~30° clockwise to the trace of the master faults. Therefore, cross-basin faults which connect the two tips of the master faults could form because of the underlap of the master faults. Take the model called case 4 in Table 4.3 (see robustness analyses in chapter 4.2.4) as an example. Riedel-shears form at the distal ends of the master faults. The Riedel-shears propagate at a strike of about 65°clockwise to the trace of the master faults. Later on, new Riedel-shears form at the master faults' tips at a smaller strike of about ~30° clockwise to the trace of the master faults. With more offset, the new Riedel-shears propagate and connect together, forming a cross-basin fault which coalesce the two tips of the master faults. At the same time, the propagation of the old Riedel-shears with strikes of about 65° ceases (Figure 4.12).

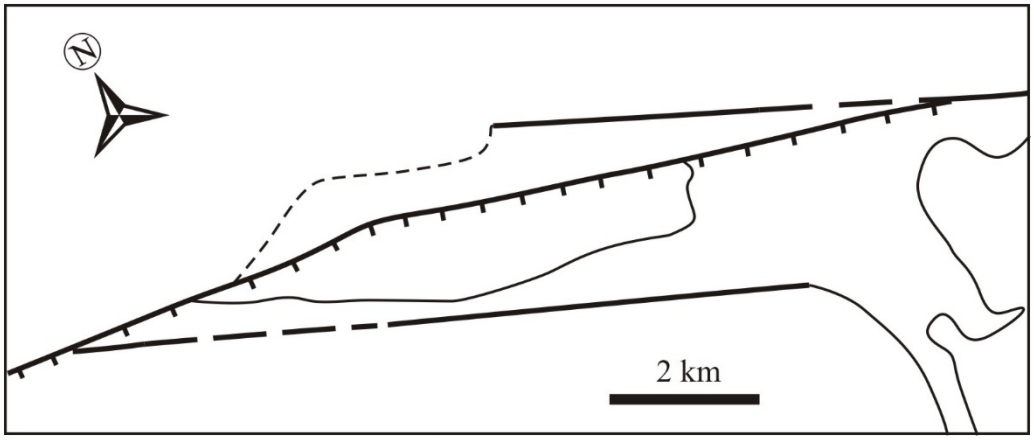

Figure 5.8 Simplified structural map of Dayinshui basin (DYSB) on Haiyuan fault, China, based on *Zhang et al*. [1989]. The location of DYSB is shown in Figure 5.2.

The diagonal fault in Dayinshui basin on Haiyuan fault controls the subsidence of the basin and the master faults are inactive (Figure 5.8). *Zhang et al*. [1989] thought that development of the diagonal strike-slip fault has resulted in the near extinction of the Dayinshui basin. The crack development in the above mentioned numerical model shows great similarity to the Dayinshui basin on Haiyuan fault. The modeling results also show that the new cross-basin fault takes over the offset from the old Riedel-shears. Displacement concentrates on the cross-basin fault and a subsidence area along this fault forms. Then, new basin sidewall faults which bound a depression occur. With more offset, the depression lengthens. The numerical modeling indicates that the formation of the cross-basin fault doesn't lead to the extinction of the basin. Instead, the first depression form along the cross-basin fault and the depocenter is later orientated along the cross-basin fault. Based on the modeling, Dayinshui basin was inherited from a system with initial fault geometry of underlapping. The overlap of the master faults we see today (Figure 5.8) is the consequence of the propagation of the underlapping master faults during strike-slip motion.

In non-overlapping and overlapping models, Riedel-shears not only form at the tips of the master faults, but also intersect with the master faults. The Riedel-shears propagate at an average strike of ~35° clockwise to the trend of the master faults. With more strike-slip offset, the Riedel-shears at the distal end of each master fault propagate along the strike of the Riedel-shears (~35°) and then connect with another master fault, bounding a rhomboidal depression. Cross-basin faults which connect two tips of the master faults cannot form in the models with initial fault geometries of non-overlapping and overlapping.

In conclusion, the numerical modeling indicates that cross-basin faults which connect two tips of the master faults cannot form in non-overlapping and overlapping systems, but cross-basin faults could form in underlapping systems because of the underlap of the master

faults. The formation of the cross-basin fault may not lead to the extinction of the basin as proposed by *Zhang et al*. [1989]. Instead, the first depression form along the cross-basin fault and the depocenter is later orientated along the cross-basin fault.

5.6 Models for pull-apart basin development

Comparison of models for the development of Dead Sea basin and the Gulf of Aqaba (Elat)

The Dead Sea transform with length of about 1000 km forms the boundary between Arabian plate and African plate. It connects the divergent plate boundary along the Red Sea with convergent orogenic belt-the Alpine orogenic belt in Turkey. Because of the considerable structural and physiographical differences along this long transform, some areas along the transform converge while others diverge. Left-stepping en-echelon strike-slip faults developed inside of the transform valley, which produced several deep pull-apart basins. Among them, the largest and deepest are the Dead Sea basin and the Gulf of Aqaba (Elat) at the southern end of the transform [*Quennell*, 1959; *Garfunkel*, 1981; *Garfunkel and Ben-Avraham*, 1996]. The Dead Sea basin is a deep depression located between the en-echelon Jordan and Arava left-stepping faults called Dead Sea Fault System (DSFS). The Gulf of Aqaba located along the Gulf of Aqaba Fault System (GAFS) is deeper and wider than the Dead Sea basin. Due to the en-echelon configuration of the strike-slip faults, the trend of the strike-slip faults deviate from the overall strike of the transform [*Garfunkel and Ben-Avraham*, 1996]. During the latest strike-slip stage, 2°-5° transtensional motion along the en-echelon GAFS began to take place. At the same time, the DSFS went through pure strike-slip movement [*Garfunkel*, 1981].

Dead Sea basin

Dead Sea basin is a well-studied example of stretched rhomboidal pull-apart basins. Based on sedimentary studies, the basin fill history consists of three stages with three distinct sedimentary regimes [*Zak and Freund*, 1981]. The first stage was Miocene when the Hazeva Formation (continental red beds) was deposited. The next phase was from Pliocene to Early Pleistocene when the Sedom Formation with thick rocksalt formed. The third stage was from Early Pleistocene to present age. During this stage, thick clastics including fluviatile and lacustrine sediments were deposited. The Hazeva Formation, Sedom Formation, and thick clastic sediments display along the master strike-slip fault from south to north. With ongoing left-lateral displacement, the depocenter of the pull-apart basin migrates northward along the strike-slip fault with time. Old basins cease to be active.

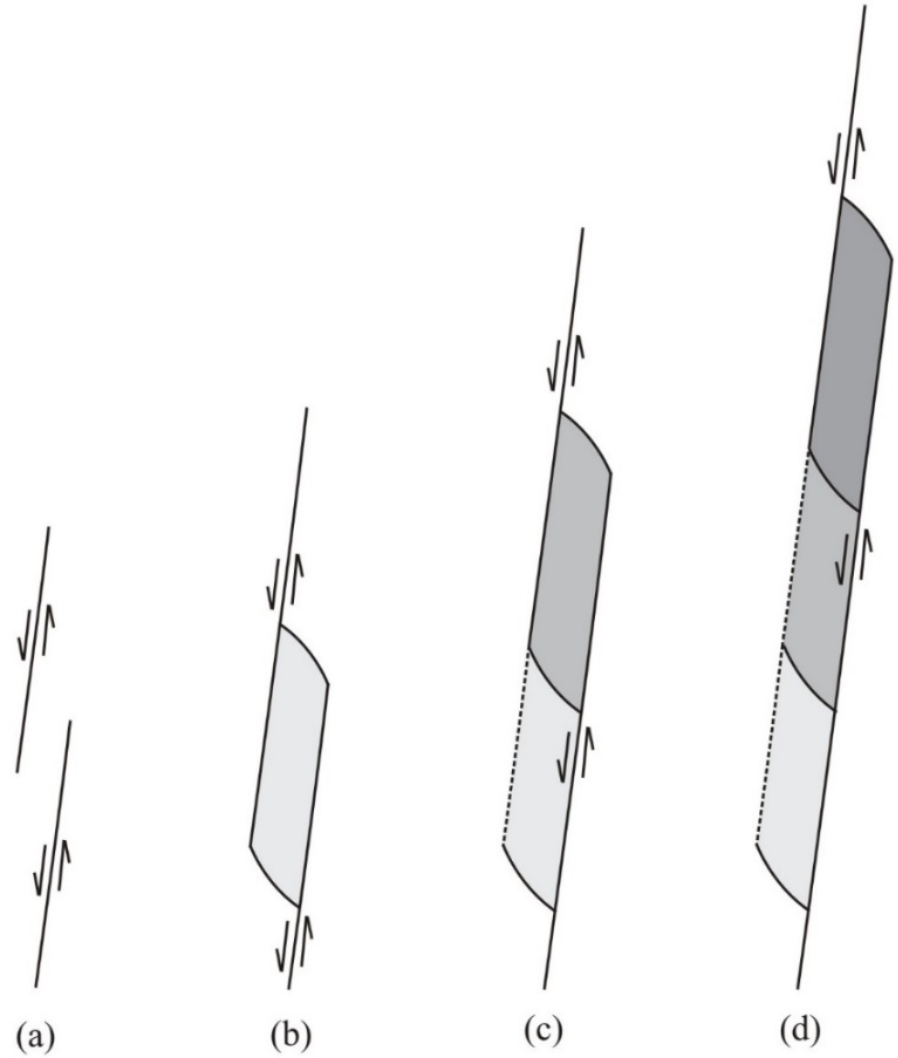

Figure 5.9 Model for the development of the Dead Sea basin proposed by this study.

Lazar et al. [2006] summarized the previous models of the Dead Sea basin development [*Aydin and Nur*, 1982; *ten Brink and Ben-Avraham*, 1989; *Garfunkel and Ben-Avraham*, 1996] and proposed their new model. Based on the analyses of Dead Sea basin provided in chapter 5.2, the length of the Dead Sea basin is larger than the amount of left-lateral slip. Therefore, the elongated rhomboidal Dead Sea pull-apart basin evolved directly from overlapping releasing sidestep and didn't evolve through spindle-shaped and lazy-Z-shaped stages. This study proposed the new model of Dead Sea basin development according to the previous models and the numerical modeling results (Figure 5.9).

Gulf of Aqaba (Elat)

The Gulf of Aqaba located at the southern segment of the Dead Sea transform, also forms the northern extension of the Red Sea [*Ben-Avraham et al*., 1979]. It is about 180 km long and, 23-25 km wide in its southern part and 16-17 km wide in its northern part (Figure 5.10a). The

Gulf of Aqaba narrows and shallows northward. The water depth in the Gulf of Aqaba is up to 1850 m. Bathymetric data suggest that the classical models for the pull-apart basin development are incompatible with the Gulf of Aqaba. Only one longitudinal fault of each depression is a strike-slip fault, while the other is a normal fault [*Ben-Avraham*, 1985]. The depression is asymmetric, bounded by linear strike-slip faults on eastern side and subparallel normal faults on western side, indicating strike-slip motion and transform-normal extension at the same time [*Ben-Avraham and Zoback*, 1992]. Figure 5.10b shows the model for the development of the Gulf of Aqaba. It is a composite basin which formed by coalescence of four en-echelon faults. There are three deeps in the composite basin.

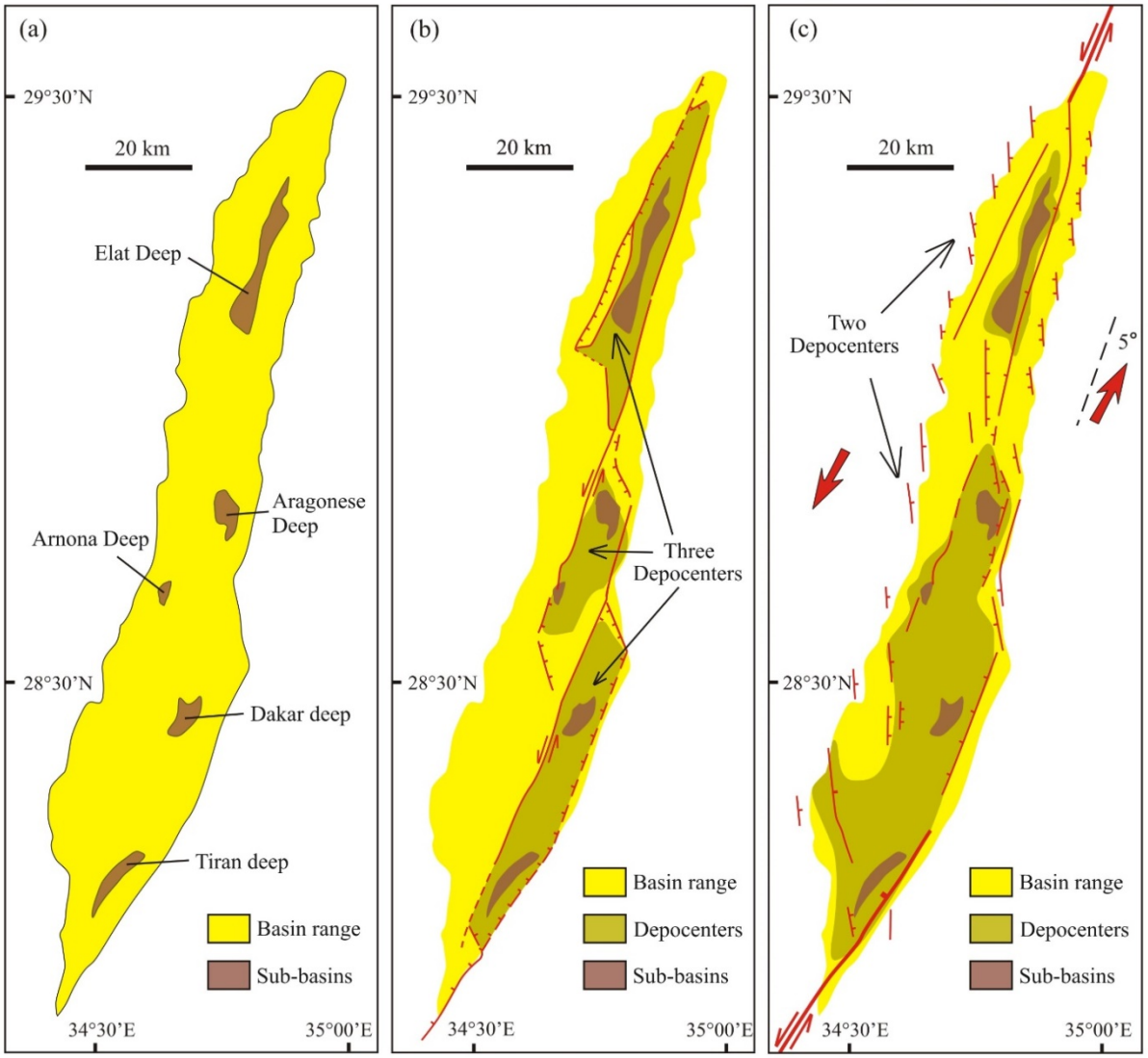

Figure 5.10 Simplified map of the Gulf of Aqaba. (a) Geometry of the Gulf of Aqaba based on bathymetric data simplified after *Ben-Avraham* (1985, Figure 1 therein). (b) Structural map of the Gulf of Aqaba (after *Ben-Avraham and Zoback*, 1992). (c) Structural map of the Gulf of Aqaba (after *Wu et al*., 2009).

Wu et al. [2009] proposed that the Gulf of Aqaba is the consequence of transtensional motion of the Gulf of Aqaba Fault System (GAFS) (Figure 5.10c). They conducted sandbox modeling to simulate the pull-apart basin evolution for both pure strike-slip and transtensional systems. Results showed that the basins forming in transtensional system are wider and there are two depocenters. They thought that's why the Gulf of Aqaba is slightly wider and longer than the Dead Sea basin formed in pure strike-slip.

The modeling results of underlapping transtensional system in this study show results similar to those given by *Wu et al.* [2009], but the fault configuration and depocenters distribution of the Gulf of Aqaba are difficult to determine. Therefore, this study does not predict the type of the basin and the development of the Gulf of Aqaba.

Central basin, Sea of Marmara

Sea of Marmara is a large pull-apart between the right-lateral segments of North Anatolian Fault System (NAFS), Turkey. Within the Sea of Marmara, a smaller pull-apart which is called the North Marmara Fault System (NMFS) formed between the oblique submarine faults. Three deep basins, from east to west, Cinarcik, Central, and Tekirdag basins, develop within the NMFS (Figure 5.11). Bathymetric data indicate that right-stepping fault segments developed in the middle of the Central basin, enclosing a rhomboidal pull-apart basin [*Armijo et al*., 2002]. Both, the inner and outer faults bounding the central basin have normal slip components (Figure 5.12).

The master fault east of the Central basin (Fault A in Figure 5.11) is a strike-slip fault with strike of N80°E that separates the Central and Cinarcik basins. A ridge intersecting Fault A is offset 3.5 km right-laterally. The master strike-slip fault west of the Central basin (Fault B in Figure 5.11) has the strike of N86°E that connects the Central and Tekirdag basins. The two master strike-slip faults of the Central basin are not parallel. The strike of the Fault A (N80°E) is parallel to the direction of motion of Anatolia relative to Eurasia [*Armijo et al*., 2002; *Flerit et al*., 2003]. Fault B strikes at an angle of 6° oblique and divergent to the direction of Anatolia/Eurasia motion.

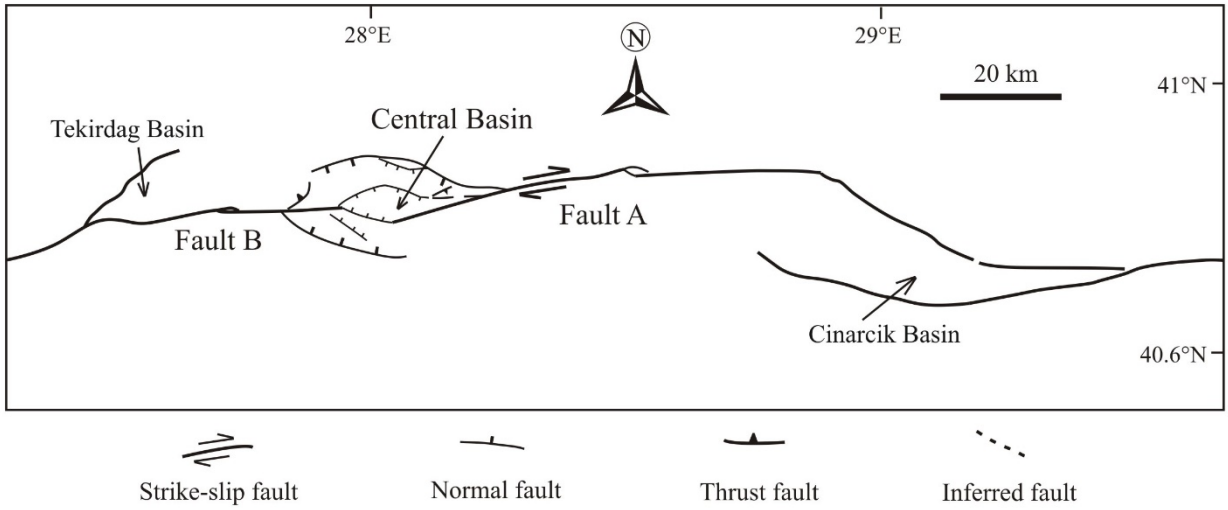

Figure 5.11 Simplified structural map of the Sea of Marmara pull-apart basins on the North Marmara Fault System (NMFS), Turkey (after *Armijo et al*., 2002).

A simplified numerical model based on the Central basin is built to simulate crack propagation and basin development. The strike of Fault A is parallel to the direction of motion while Fault B strikes at an angle oblique and divergent to the direction of movement (Figure 5.13a). Figure 5.14 presents the development sequence for the transtensional model based on the Central basin, including contact force distribution (1a-1e), crack propagation (2a-2e), particle distribution (3a-3e) and crack interpretation (4a-4e). During the initial evolution stage, the first cracks (Riedel-shears) occur at the tips of the master faults. Later on, new Riedel-shears begin to occur. The Riedel-shears propagate continuously and coalesce with each other, bounding an oblique, inner depression (Stage d, Figure 5.16). The Riedel-shears which form at the beginning develop as the boundary faults of the outer depression (Stage e, Figure 5.16). Fault geometry and basin shape of the model display close similarities to the rhombic-shaped Central basin in the Sea of Marmara.

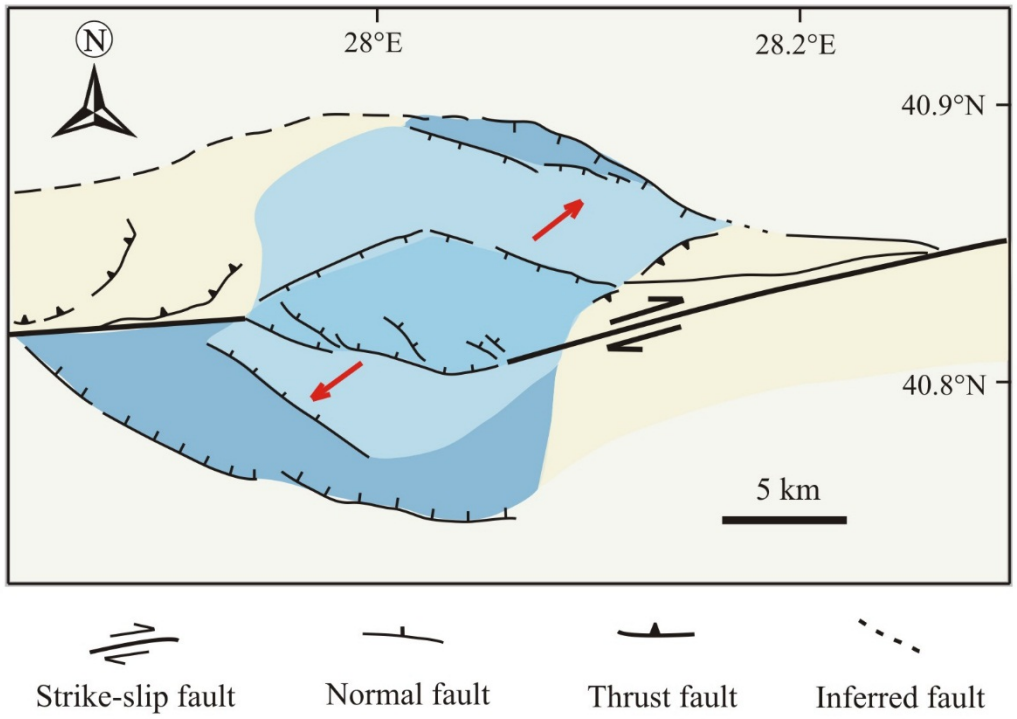

Figure 5.12 Structural map of Central basin in the Sea of Marmara (after *Armijo et al*., 2002).

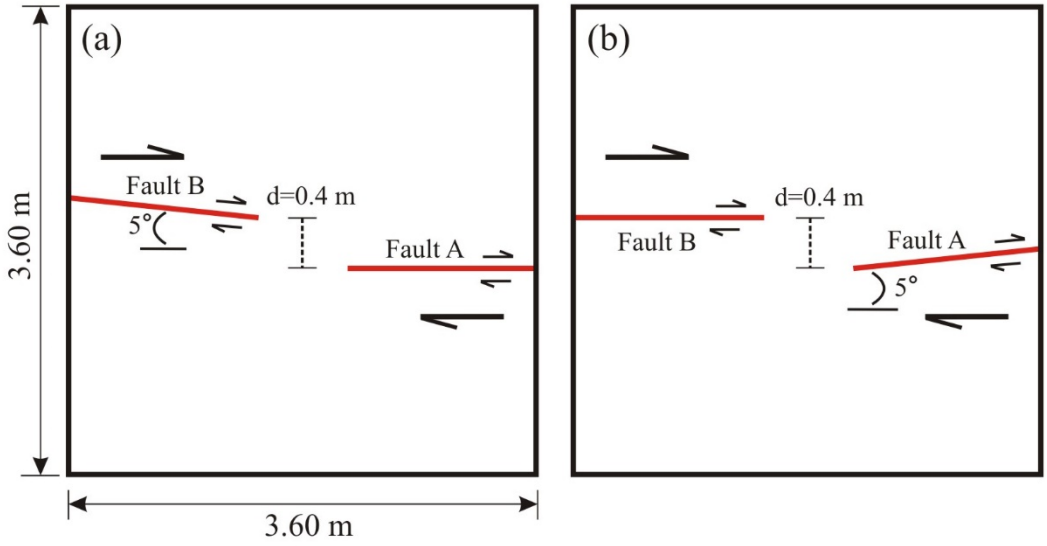

Figure 5.13 Simplified numerical models based on Central basin (a) and Hanmer basin (b) .

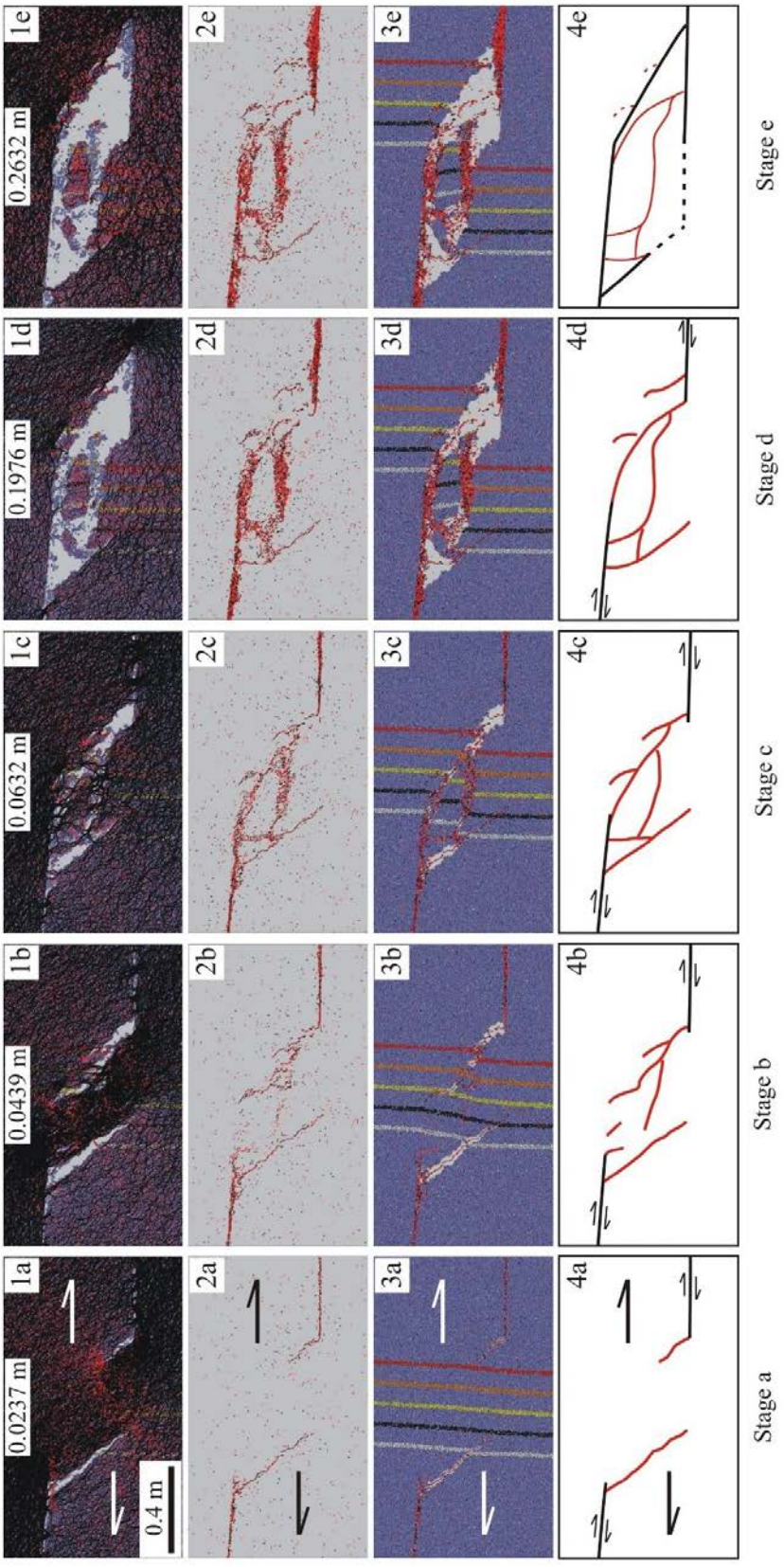

Figure 5.14 Evolution of the transtensional model based on Central basin in the Sea of Marmara. 1a-1e: contact force distribution; 2a-2e: crack propagation; 3a-3e: particle distribution with crack propagation; 4a-4e: crack interpretation and basin geometry evolution.

Hanmer basin

Hanmer basin in northern South Island, New Zealand, is a well-studied pull-apart basin developed at a ~7 km-wide releasing sidestep between the en-echelon segments of the right-lateral strike-slip Hope Fault. The basin is some 15 km long and 7 km wide. The basin occupies a right step between Hope River segment and Conway segment of the Hope Fault. The two master fault segments have no overlap and are connected with each other by an oblique-slip fault at the southwestern margin of the subsidence (Figure 5.15). The end of Hope River segment at the northeast margin splay and branch outward. Inferred from the slip rate of the master faults, the climate factor, and sediment fill inside the basin, the onset of basin formation might be in the middle Pleistocene [*Wood et al*., 1994]. The depocenter is located at the south margin of the basin, with sediment fill thickness of > 1000 m. The basin fill in the western end of the basin is thinner (< 500 m).

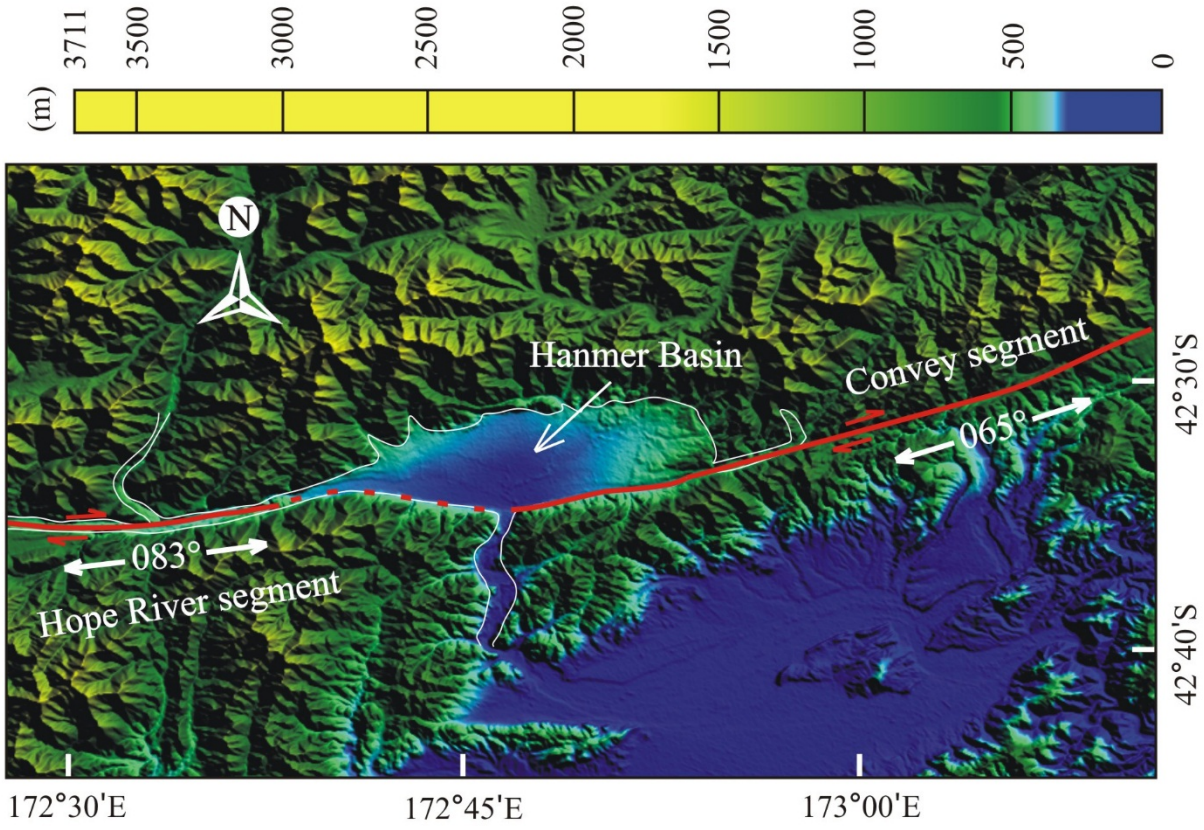

Figure 5.15 Simplified structural map of Hanmer basin in New Zealand based on SRTM digital elevation model (from http://srtm.csi.cgiar.org/index.asp).

The trend of the Hope Fault changes across Hanmer basin from 83°±10° along the Hope River segment to around 65°±5° along the Conway segment east of the basin (Figure 5.15). The two master strike-slip faults are not parallel but converge across the basin [*Freund*, 1971]. The strike of the Hope River segment (83°±10°) is parallel to the azimuth of the relative

plate motion vector (264°±10°). The Conway segment of the Hope Fault strikes in a more northward (65°±5°) direction than the relative plate motion vector (by 10-20°), which leads to convergent strike-slip.

A simplified numerical model based on Hanmer basin (Figure 5.13b) is set up to simulate crack development and basin evolution. Figure 5.16 shows the pull-apart basin development observed in the transpressional model based on Hanmer basin. Crack propagation starts at the tips of the master faults. Later on, oblique-extensional cracks form between the Riedel-shears. With further transpressional offset, the Riedel-shears coalesce with the oblique-extensional cracks, resulting in the formation of a diagonal fault (cross-basin fault) which connects the two master faults (Stage c, Figure 5.16). Then, the first subsidence area forms along the cross-basin fault. With more offset, the basin lengthens and the depocenter is orientated along the cross-basin fault (Stage d, Figure 5.16). The fault pattern, depocenter, and basin geometry of the transpressional model based on Hanmer basin show great similarities to the fault and basin features of Hanmer basin in New Zealand.

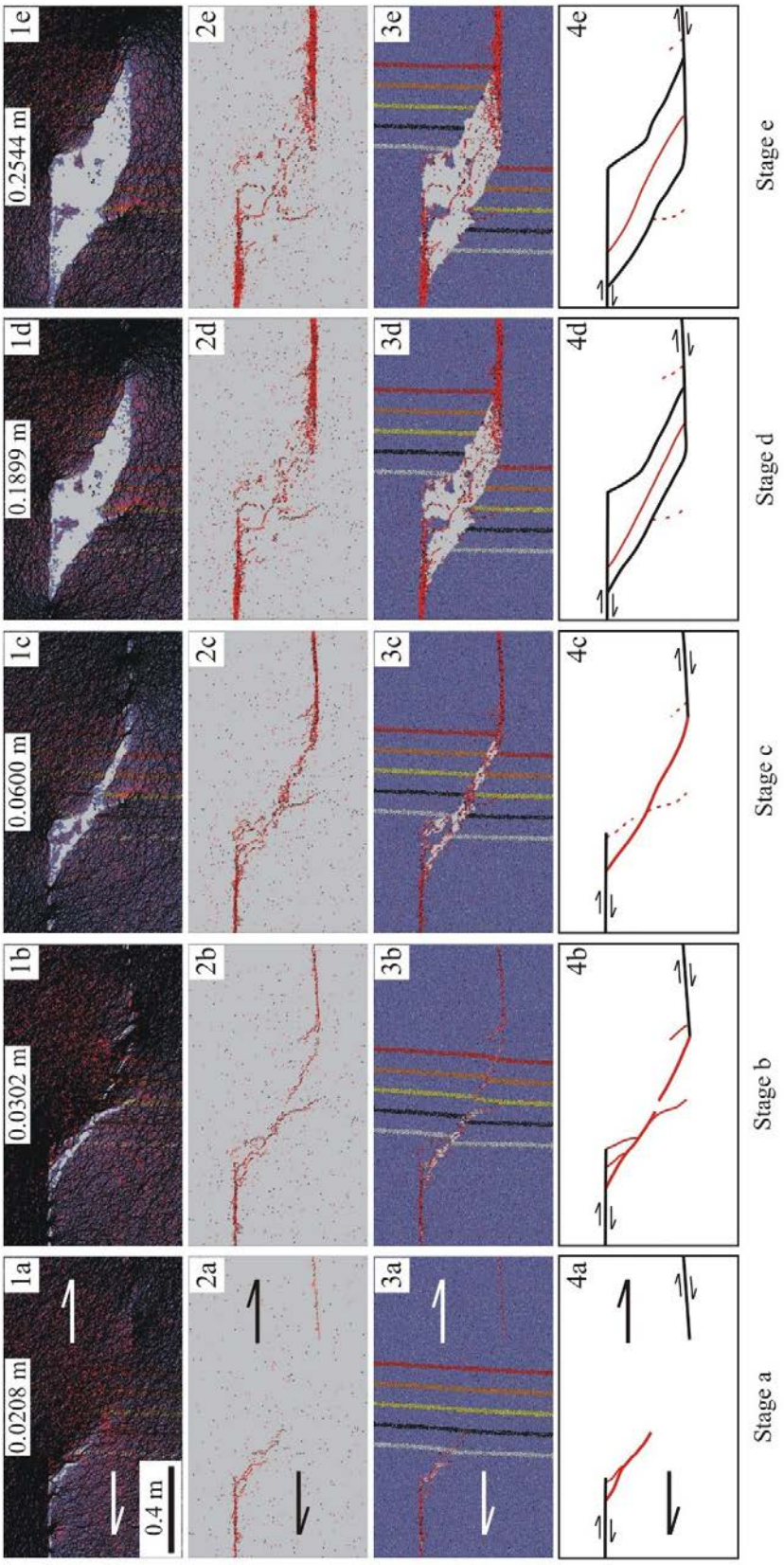

Figure 5.16 Evolution of the transpressional model based on Hanmer basin in New Zealand. 1a-1e: contact force distribution; 2a-2e: crack propagation; 3a-3e: particle distribution with crack propagation; 4a-4e: crack interpretation and basin geometry evolution.

Models for pull-apart basin development

A pull-apart basin could evolve from different initial fault geometries (underlapping, non-overlapping, and overlapping releasing sidesteps). It can also develop from various fault kinematics such as pure strike-slip, transtension, and transpression. Figure 5.17 summarizes the models of pull-apart basin development with different initial conditions.

Pure strike-slip

For pure strike-slip releasing sidestep, pull-apart basins do not suddenly come into existence. They evolve through a sequence of closely related states. In underlapping model, first cracks (Riedel-shears) begin to occur at the tips of master faults when peak stress is reached. Then, the Riedel-shears propagate and coalesce with the master faults, bounding a spindle-shaped depression. The underlapping model produces pull-apart basins that evolve from spindle-shaped through lazy-Z-shaped to the rhomboidal and stretched rhomboidal basin (Figure 5.17a). Non-overlapping and overlapping releasing sidestep generate rhomboidal basins without evolving through spindle and lazy-Z-shaped stages (Figure 5.17b, 5.17c) [*Liu and Konietzky*, 2018].

Transtension

Based on our modeling, the transtensional model with two parallel master faults produces a depression with two depocenters. The basin forming in this transtensional system is wider than the basin in pure strike-slip system. For the transtensional system with two parallel faults, the Riedel-shears occur at the beginning. Then, oblique-extensional cracks connecting the Riedel-shears form. The Riedel-shears propagate continuously and coalesce with the master faults, creating an oblique, lazy-Z-shaped depression. Meanwhile, the oblique-extensional cracks inside of the depression propagate and coalesce with the master faults and Riedel-shears, forming a cross-basin dip-slip fault (Figure 5.17e).

The model based on Central basin is another type of transtensional model where one master fault is parallel to the displacement vector while the other master fault has a minor component of oblique and divergent motion. The Riedel-shears also form at the tips of the master faults at the initial stage. Later on, new Riedel-shears begin to occur. The new Riedel-shears coalesce with each other, bounding an oblique, inner depression. As the transtensional displacement increases, the Riedel-shears which form at the beginning develop as boundary faults of the outer depression, forming an oblique, rhomboidal basin (Figure 5.17d). The basin evolves from an oblique, inner depression to an oblique, wider depression with outer boundary faults. Fault geometry and basin shape of the modeling display close similarities to the rhombic-shaped Central basin in the Sea of Marmara. This transtensional model produces an oblique, wider, rhomboidal basin.

Different from pure strike-slip system, the basins in transtensional system not only lengthen, but also widen because of the increase of fault separation away from the tips of the master faults. Therefore, with the same offset, the basin forming in transtensional system is wider than the basin in pure strike-slip system.

Transpression

Sandbox modeling and numerical simulations of transpressional systems concentrating on crack propagation and basin evolution have not yet been reported. This study incorporates two transpressional models. The transpressional model with two parallel master faults produces a cross-basin fault connecting the tips of the two master faults. Another transpressional model based on Hanmer basin also form a diagonal fault coalescing the tips of the two master faults. In transpressional system, Riedel-shears also propagate at the tips of the master faults. Then, oblique-extensional cracks form between the Riedel-shears. With further offset, the Riedel-shears coalesce with the oblique cracks, forming a diagonal fault which coalesces the tips of the two master faults (Figure 5.17f, 5.17g). As offset increases, the first subsidence area forms along the diagonal fault. Basin sidewalls also develop, bounding an oblique, asymmetric pull-apart basin. With more transpressional offset, the basin lengthens. The depocenter of the basin is along the diagonal fault which is consistent with the Hanmer basin.

The disadvantage of our DEM modeling is lack of subsidence and uplift information in vertical direction because of the limitations of two-dimensional models in general. So, it is not so clear whether the depocenter has migrated or not. However, the cracks and empty areas in our 2D models can represent the opening of the basins. The crack propagation and basin geometry in the transpressional system are quite different from those in pure strike-slip and transtensional systems. The crack pattern and depocenter distribution show great similarities to the Hanmer basin. Modeling results show that a cross-basin fault which connects the tips of the two master faults could develop in transpressional systems and the diagonal fault does not lead to the extinction of the basin.

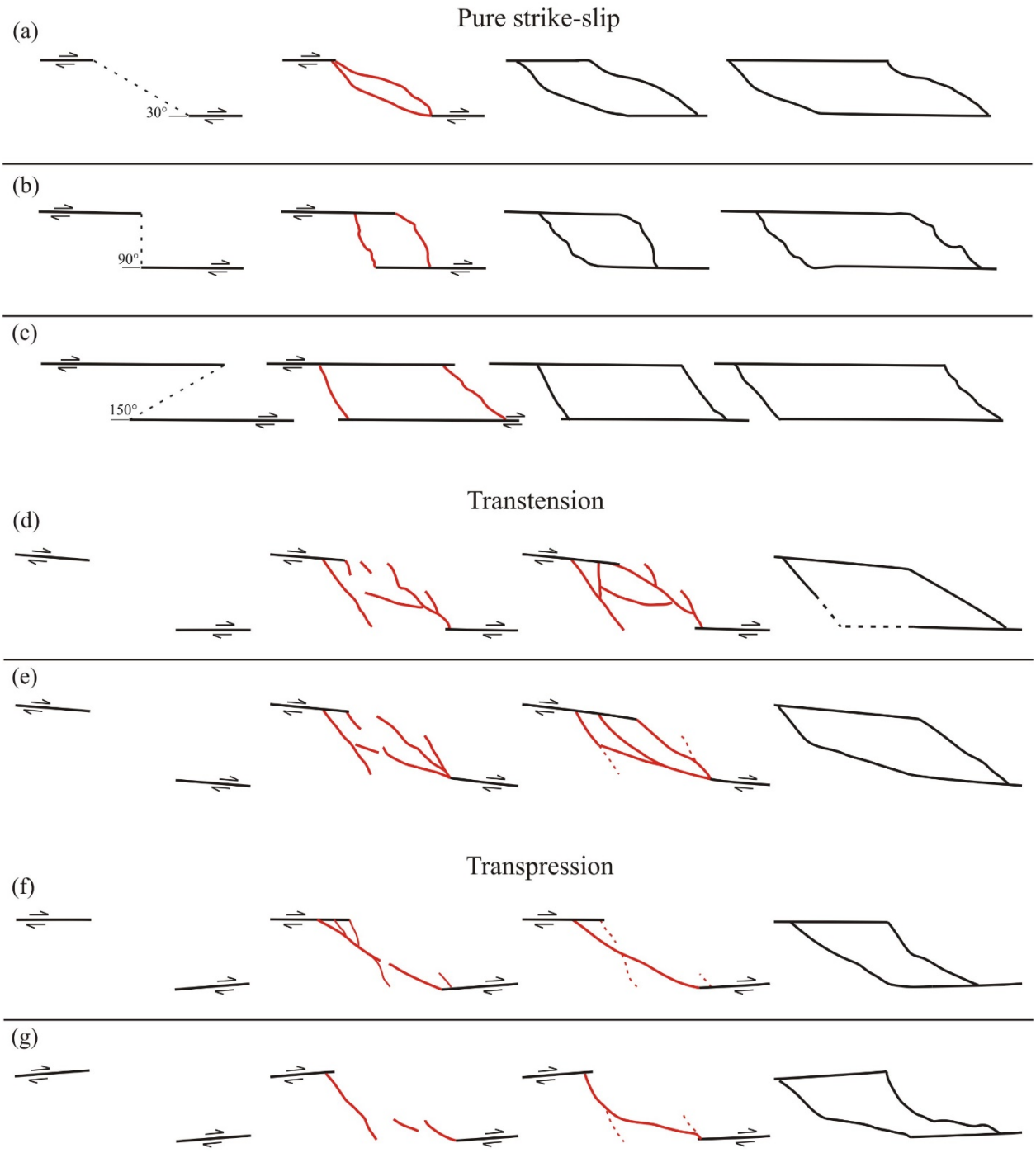

Figure 5.17 Summary of models for pull-apart basin development

5.7 Estimating displacement and age of pull-apart basins

As mentioned above, the amount of motion along the strike-slip system is sometimes difficult to infer from surface geology. The minimum offset to form a pull-apart basin can be deduced based on our modeling results. The three pull-apart basin models (30°, 90° and 150° releasing sidestep) exhibit similar trends in terms of the σ_1-ε_x^*curves. At point P, the peak stress (identical with onset of crack growth) is reached at relative extension (ε_x^*) of about 0.035 (Figure 5.18a and 5.18b). Even for quite different fault separations and different overlapping constellations, when the value of ε_x^* reaches about 0.035, first cracks (Riedel-shears) begin to occur. With more strike-slip displacement, the Riedel-shears continue to propagate. Point M ($\varepsilon_x^* \approx 0.054$) is an example of this stage. When the value of ε_x^* is around 0.155 (point Q), the Riedel-shears link with the master faults (Figure 5.18a), a depression area bounded by master faults and Riedel-shears forms. Although we cannot specify at which exact evolution stage a pull-apart basin in nature is, the evolution stage of this basin is definitely later than the stage of point Q when a depression area begins to form. Therefore, the relative extension (ε_x^*) for a pull-apart basin in nature is larger than 0.155. Applying these data to the pull-apart basins in nature, the following conclusions can be drawn:

- El Paraiso basin exhibits spindle shape with fault separation of 1.5 km (Figure 5.1a). To form Riedel-shears, the value of ε_x^* is about 0.035, and 52.5 m displacement is needed to form Riedel-shears. When the ε_x^* is about 0.155 (point Q), a depression area begins to form, and about 232.5 m offset is needed (Figure 5.18c). Of course, more offset is needed to form the spindle-shaped pull-apart basin. Therefore, the displacement which is needed to evolve to point Q is called minimum displacement to form a pull-apart basin (U_x^{min}). The displacement needed to form first cracks (U_x^c) and the minimum displacement to form a pull-apart basin (U_x^{min}) can be deduced (Table 5.1).
- Algeciras basin is a lazy-Z-shaped pull-apart basin with fault separation of 3 km (Figure 5.1a). As calculated above, 105 m displacement is needed to form the first cracks and at least 465 m displacement is needed to produce this pull-apart basin.
- 20°N basin is a rhomboidal pull-apart basin (90 km long and 35 km wide). 1225 m offset is needed to form the first cracks and at least 5425 m displacement is needed to generate this pull-apart basin.

If the ages of these pull-apart basins are known, the minimum slip rates of the related strike-slip faults can be deduced according to the minimum displacements (U_x^{min}) calculated above. However, because of the technological limitation of geologic chronology of the quaternary sediments and the difficulties to get the depths of these basins which still experience ongoing sedimentations, the exact ages of these pull-apart basins are sometimes

not clear. On the other hand, if we know the slip rates of the strike-slip faults, the minimum ages of initiation for the pull-apart basins can be deduced from the minimum displacements and the slip rates of the faults. Many researchers have used different methods to measure the slip rate of the strike-slip faults. According to measurements of geomorphic displacements such as alluvial fans and sag ponds, right lateral sense of shear of the AFS and displacement of about 3 km with a rate of 1.5 $mm \cdot a^{-1}$ during the past 2 Ma were given by *Chorowicz et al*. [1996]. Based on the displacements calculated from the modeling results and the fault slip rate of 1.5 $mm \cdot a^{-1}$ of the AFS, the time to form the first cracks (T_c) and the time to form a depression area (T_{min}) during the pull-apart basin development along the AFS can be deduced. The time to form a depression area is of course the minimum starting age of the pull-apart basin and is dated as shown in Table 5.1. All the deduced values of time are in agreement with geologic evidences (Table 5.1). Estimated from geodetic and geologic data, a slip rate of 3 ± 1 $mm \cdot a^{-1}$ between Arabian plate and Indian plate was obtained. The minimum starting age of 1.8 Ma for the 20° basin is calculated, which is in accordance with the 3 Ma inferred from *Rodriguez et al*. [2013]. The proposed method to calculate the points in time when first cracks form and when a depression area occurs during pull-apart basin development is recommended for basins which are still active.

Numerical models used in this study are time-independent. However, if we consider the simple viscous assumptions already mentioned in chapter 3.4.3, the corresponding time to form the first cracks can be determined to be in the order of 10^4 to 10^6 years, this means the minimum starting ages of the pull-apart basins are in the order of 10^4 to 10^6 years. The so determined age is quite similar to the one deduced from the minimum displacements calculated from relative extension (ε_x^*), and is again in close agreement with the geologic evidences (Table 5.1).

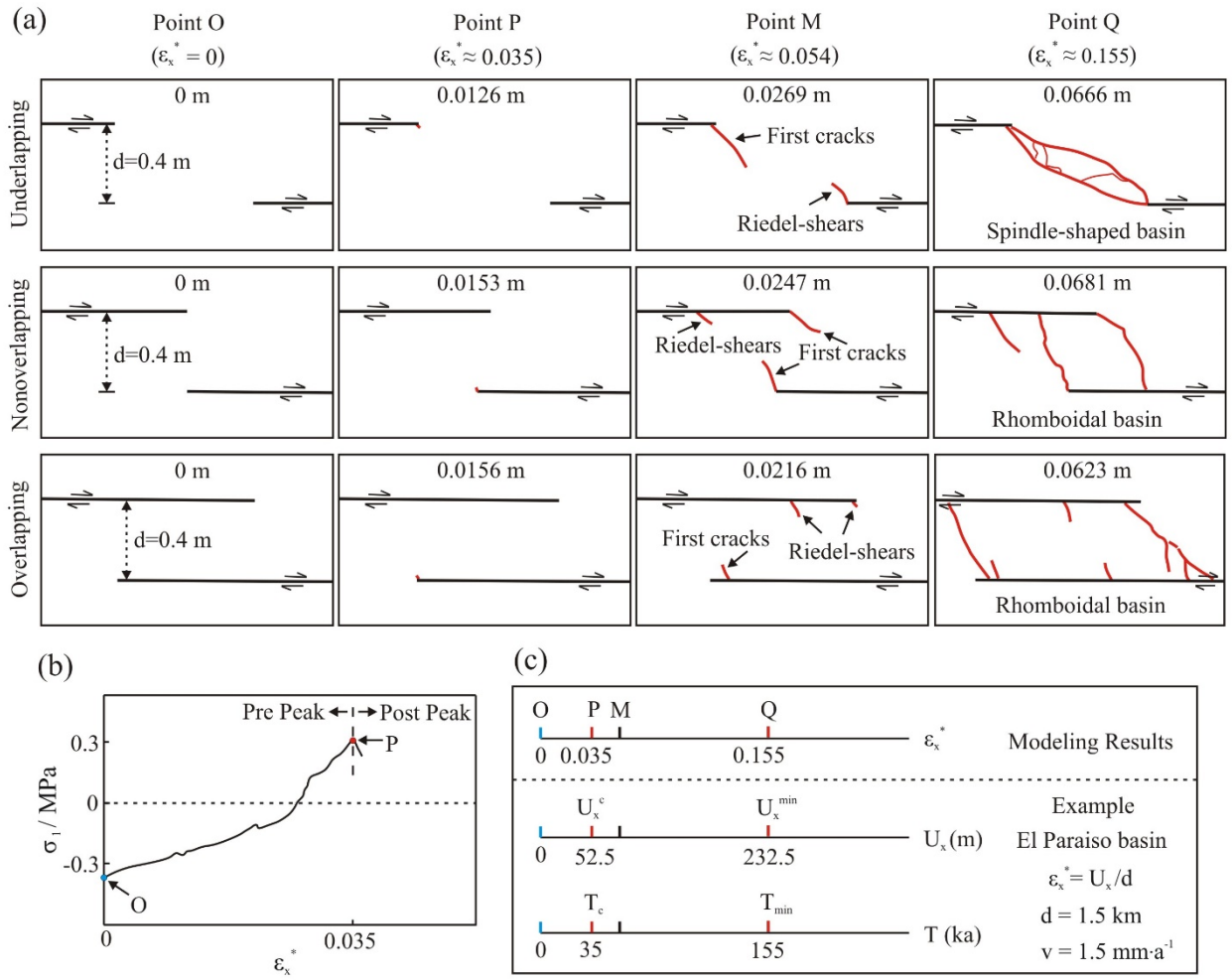

Figure 5.18 Representative evolution points during pull-apart basin development. (a) Point O: at the beginning, no strike-slip displacement. Point P: point when the peak stress is reached, first cracks (Riedel-shears) begin to form. Relative extension (ε_x^*) is about 0.035. Point M: with further offset, cracks propagate. Point Q: When the value of ε_x^* is around 0.155, the Riedel-shears link with the master faults, and first depression area bounded by master faults and Riedel-shears forms. (b) Major principal stress versus relative extension. P is the point when the peak stress is reached. (c) Simplified sketch of the representative evolution points during pull-apart basin development, including relative extension from modeling and corresponding displacement and time for the El Paraiso basin (see Figure 11a) calculated from the modeling results. Minimum displacement (U_x^{min}) is displacement calculated when relative extension (ε_x^*) is 0.155. The corresponding minimum time (T_{min}) is calculated based on the minimum displacement and fault slip rate (v).

Table 5.1 Pull-apart basins characteristics compiled from published references and related data calculated from the modeling results

Basin Name	Basin type	Master faults, Country	Age of activity	Fault separation	Average fault slip rate	References	U_x^c	T_c	U_x^{min}	T_{min}
							a	b	c	e
				d (km)	v ($mm \cdot a^{-1}$)		(m)	(ka)	(m)	(ka)
El Paraiso	Spindle-shaped	Algeciras, Colombia	L.Q.	1.5	1.5	*Velandia et al*., 2005	52.5	35	232.5	155
Ararat	Spindle-shaped	f	L.Q.	20-35	~4	*Karakhanian et al*., 2004	700-1225	175- 306	3100-5425	775-1356
San Juan de Villalobos	Lazy-S	Yunguillo, Colombia	Q.	5	1.5	*Velandia et al*., 2005	175	117	775	517
Algeciras	Lazy-Z	Algeciras, Colombia	L.Q.	3	1.5	*Velandia et al*., 2005	105	70	465	310
Secretary	Lazy-Z	Alpine, New Zealand	L.P.-Q.	~2.5	4-35	*Barnes et al*., 2001; *Barnes et al*., 2005	87.5	21.9-2.5	387.5	96.9-11
Dagg	Lazy-Z	Alpine, New Zealand	L.P.-Q.	~4	4-35	*Barnes et al*., 2001; *Barnes et al*., 2005	140	35- 4	620	155-17.7
Karakoram	Lazy-Z	Karakoram, China	L.Q.	~0.65	~10.7	*Chevalier et al*., 2005; *Murphy and Burgess*, 2006;	22.8	2.1	100.8	9.4
Five Fingers	Lazy-Z	Alpine, New Zealand	L.P.-Q.	2.5	4-35	*Barnes et al*., 2001; *Barnes et al*., 2005	87.5	21.9- 2.5	387.5	96.9-11
Niksar	Lazy-Z	North Anatolian, Turkey	E.P.-L.Q.	~12	5-10	*Barka*, 1992; *Barka et al*., 2000	420	84-42	1860	372-186
George	Lazy-Z	Alpine, New Zealand	L.P.-Q.	1.9	4-35	*Barnes et al*., 2001; *Barnes et al*., 2005	66.5	16.6-1.9	294.5	73.6-8.4

Cariaco (stage 3)	Lazy-Z	Offshore Venezuela	E. P.-Recent	~30	20	*Escalona et al*., 2011	1050	52.5	4650	232.5
Sibundoy	Rhomboidal	San Francisco, Colombia	Q.	~9	1.5	*Velandia et al*. 2005;	315	210	1395	930
Pitalito	Rhomboidal	El Cedro; Oitalito, Colombia	L.Q.	~10	1.5	*Velandia et al*. 2005; *Chorowicz et al*., 1996	350	233	1550	1033
Nancy	Rhomboidal	Alpine, New Zealand	L.P.-Q.	~4.5	4-35	*Barnes et al*., 2001; *Bernes et al*., 2005	157.5	39.4- 4.5	697.5	174.4-19.9
Laohuyaoxian	Rhomboidal	Xiaokou, China	Q.	2	5	*Zhang et al*., 1989	70	14	310	62
Tabriz	Rhomboidal	North Tabriz, Iran	L.Q.	5	>1.5-2	*Karakhanian et al*., 2004	175	117-87.5	775	516.7-387.5
Hanmer	rhomboidal	Hope, New Zealand	L.Q.	~7	~20	*Wood et al*., 1994	245	12.3	1085	54.3
20°N	rhomboidal	Owen, NW Indian Ocean	Q.	35	3±1	*Rodriguez et al*., 2013	1225	408.3	5425	1808.3
Dead Sea	rhomboidal	Dead Sea, Jordan	E. M-L.Q	~10	4-6	*Freund et al*., 1970	350	87.5-58.3	1550	387.5-258.3

Displacement (U_x) = fault separation (d) * relative extension (ε_x^*).

[a]Displacement (U_x^c) calculated when relative extension (ε_x^*) is 0.035. It refers to displacement needed to form the first cracks.

[b]Time needed to form the first cracks (T_c). $T_c = U_x^c$ / Average fault slip rate (v)

[c]Minimum displacement (U_x^{min}) is displacement calculated when relative extension (ε_x^*) is 0.155. It refers to minimum displacement to form the first depression area bounded by master faults and Riedel-shears.

[e]Minimum age (T_{min})=Minimum displacement (U_x^{min}) / Average fault slip rate (v).

[f]Sardarapat- Nakhichevan; Dogubayazit; Maku, Turkey; Armenia; Iran; Azerbaijan

E. M. is Early Miocene, L.P. represents Late Pliocene (P.), E.P. is Early Pliocene, and L.Q. stands for Late Quaternary (Q.).

5.8 Conclusions

Numerical modeling shows that the shape of a pull-apart basin in nature is the consequence of both the initial strike-slip geometry and its various evolution stages. The spindle-shaped depression is the incipient evolutionary stage of a pull-apart basin, developing from the underlapping releasing sidestep, such as El Paraiso basin in SW Colombia. The lazy-Z-shaped basin evolves from the underlapping system through spindle-shaped state. Algeciras basin is a lazy-Z-shaped depression and the master faults are linked by the cross-basin faults.

A rhomboidal basin could evolve through spindle-shaped and lazy-Z-shaped depression, with initial fault geometry of underlapping. There are also rhomboidal basins that don't go through the spindle and lazy-Z-shaped states, but instead form from an initial fault geometry of non-overlapping or overlapping. Pitalito basin in SW Colombia, is a rhomboidal pull-apart basin. This rhomboidal basin might evolve from an overlapping, non-overlapping, or underlapping system with larger displacement. To identify whether a rhomboidal basin has gone through the spindle-shaped and lazy-Z-shaped stages or not, the basin length and the total strike-slip displacement obtained from matching the strata or basement rocks across the pull-apart are compared. The length of the Dead Sea basin is larger than the total amount of left-lateral slip along the Dead Sea rifts. Therefore, the elongated rhomboidal Dead Sea pull-apart basin evolved directly from overlapping releasing sidestep. In other words, the Dead Sea basin didn't evolve through spindle-shaped and lazy-Z-shaped stages.

A pull-apart basin can evolve from different initial fault geometries (underlapping, non-overlapping, and overlapping releasing sidestep). It can also develop from various fault kinematics such as pure strike-slip, transtension, and transpression. This study summarizes the models of pull-apart basin development with different initial conditions.

Combining DEM modeling results with natural examples, physical modeling, and continuum numerical simulations, the existence of deeps or depocenters, the number of depocenters, and whether the depocenter has migrated or not during pull-apart basin development have been discussed.

The numerical modeling indicates that cross-basin faults which connect two tips of the master faults cannot form in non-overlapping and overlapping systems, but cross-basin faults could form in underlapping systems because of the underlap of the master faults. The formation of the cross-basin fault might not lead to the extinction of the basin. Instead, the first depression form along the cross-basin fault and the depocenter is later orientated along the cross-basin fault.

Finally, based on the stress-deformation behavior, the displacement and time needed to form the first cracks and depression area can be estimated from the corresponding relative extension (ε_x^*) and the slip rate of the strike-slip faults. The time needed to form the first depression can be considered as the minimum age of initiation for the pull-apart basin.

6 Numerical simulation of tectonic deformation of Ordos Block under present tectonic stress regime

6.1 Introduction

In this chapter, UDEC models based on Ordos Block and adjacent areas have been established. According to the present tectonic stress regime inferred from geologic evidences, boundary conditions and initial stress states were selected and applied. Modeling results show block rotations as well as shear stress and shear displacement on faults. In addition, a slip tendency analysis (T_s), which represents the potential for slip on individual faults, is predicted under the present tectonic stress regime. This reflects the earthquake-prone of the faults in the study area.

6.2 Geologic setting

Ordos Block is a large and stable crustal segment in the western North China Craton (NCC) (Figure 6.1). The Ordos Block is surrounded by sedimentary basins and grabens. Several convex-to-the-northeast oroclinal structures with strike of NW-SE are situated in the southwest region of the Ordos Block. This region is located at the northeastern margin of the Tibetan Plateau and has gone through a complex intracontinental deformation during the Cenozoic because of the uplift of the Tibetan Plateau. Today, it is still a really active region driven by the coupled effects of the Indian, Eurasian, and Pacific Oceanic plates [e.g., *Deng et al*., 1989; *IG and SBNHAP*, 1990; *Burchfiel et al*., 1991; *Shi et al*., 2015].

Basins around Ordos Block

Shanxi rift (SXR) is an important Cenozoic tectonic belt. It is 40 - 120 km wide and extends about 1000 km along the east margin of the Ordos Block. The SXR has undergone multi-stage extensional deformations during the late Cenozoic [*Shi et al*, 2015]. The graben basins are controlled by several NE- and NW-trending faults (Figure 6.2). The basins around Ordos Block such as Weihe basin, Hetao basin, Jilantai basin, and Yinchuan basin, have also undergone extensional evolution during late Cenozoic.

Convex-to-the-northeast oroclinal faults in southwest margin of Ordos Block

Several NW-striking arcuate faults at the southwest margin of Ordos Block are of great tectonic importance. There are Haiyuan fault (HYF), Xiangshan-Tianjing Shan fault (XTF), Yantong Shan fault (YSF), and Luo Shan- Niushou Shan fault (LNF), from southeast to northwest (Figure 6.2). These faults are situated at the northeastern margin of the Tibetan Plateau in north central China. Among these faults, Haiyuan fault (HYF), a

convex-to-the-northeast oroclinal structure, is not only the nearest fault to Tibetan Plateau, but also the longest and the most active fault. Haiyuan fault consists of many secondary faults, and the trend of the secondary faults change from N30 - 45W to N75 - 90W, from southeast to northwest. Large-scale mapping has found eleven en-echelon faults with huge left-lateral strike-slip movement since late Quaternary and eight pull-apart basins along the Haiyuan fault [e.g., *Deng et al*., 1989; *Burchfiel et al*., 1991; *IG and SBNHAP*, 1990].

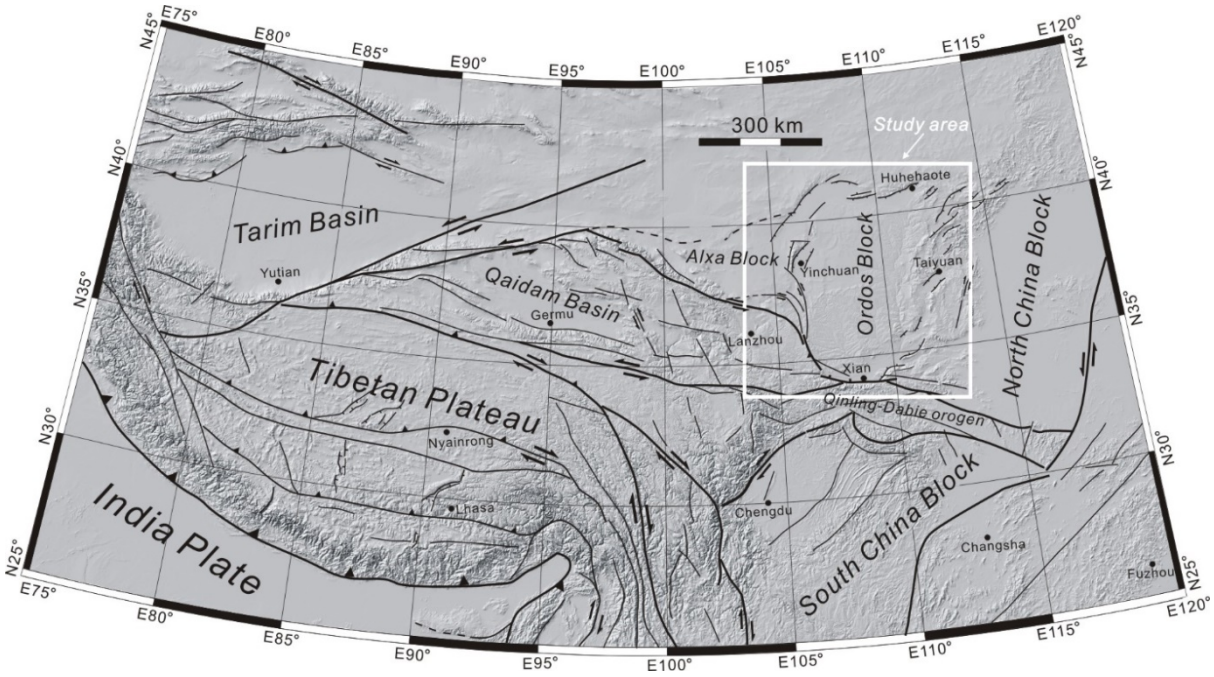

Figure 6.1 Simplified structural map of the Tibetan Plateau and adjacent areas based on SRTM digital elevation model topography (from https://wist.echo.nasa.gov; modified from *Shi et al*., 2015). Study area is shown in white frame.

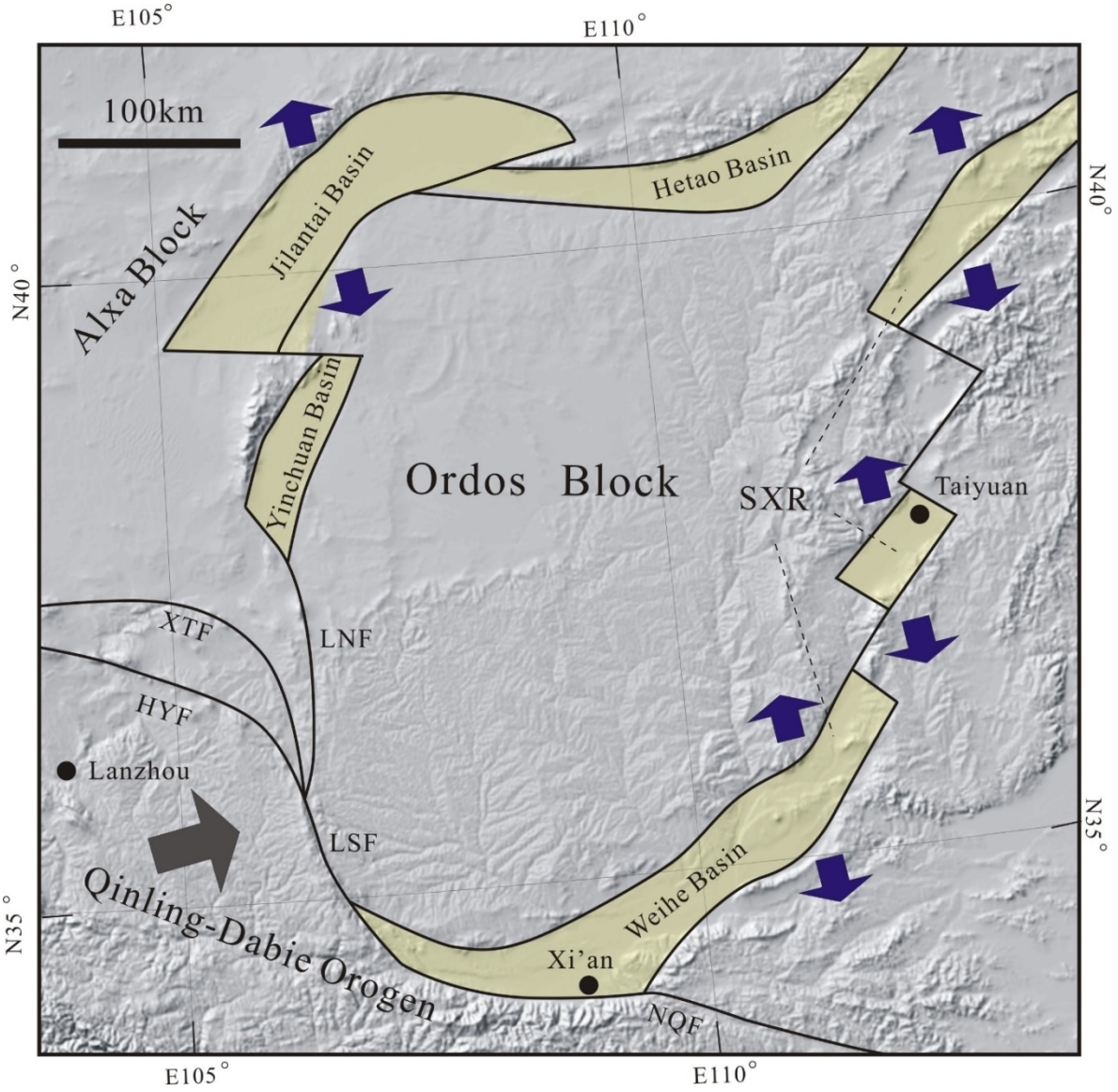

Figure 6.2 Simplified structural map of Ordos Block and adjacent areas based on SRTM digital elevation model topography (from https://wist.echo.nasa.gov).

6.3 Numerical simulation

6.3.1 Principle of UDEC

The Universal Distinct Element Code (UDEC), based on the Discrete Element Method (DEM), is widely used to simulate the rock mass as an assembly of discrete blocks (rigid or deformable). The discontinuities (faults or joints) are represented as contact surfaces between two block edges (Figure 6.3). This program can model the movements of the discontinuous material caused by either static or dynamic loading. The Newton's second law is applied to

all blocks. The deformable elastic blocks used in our model are divided into triangular constant-strain finite-difference zones, and each zone obeys the pre-defined stress-strain law. Large deformations and block rotations are allowed.

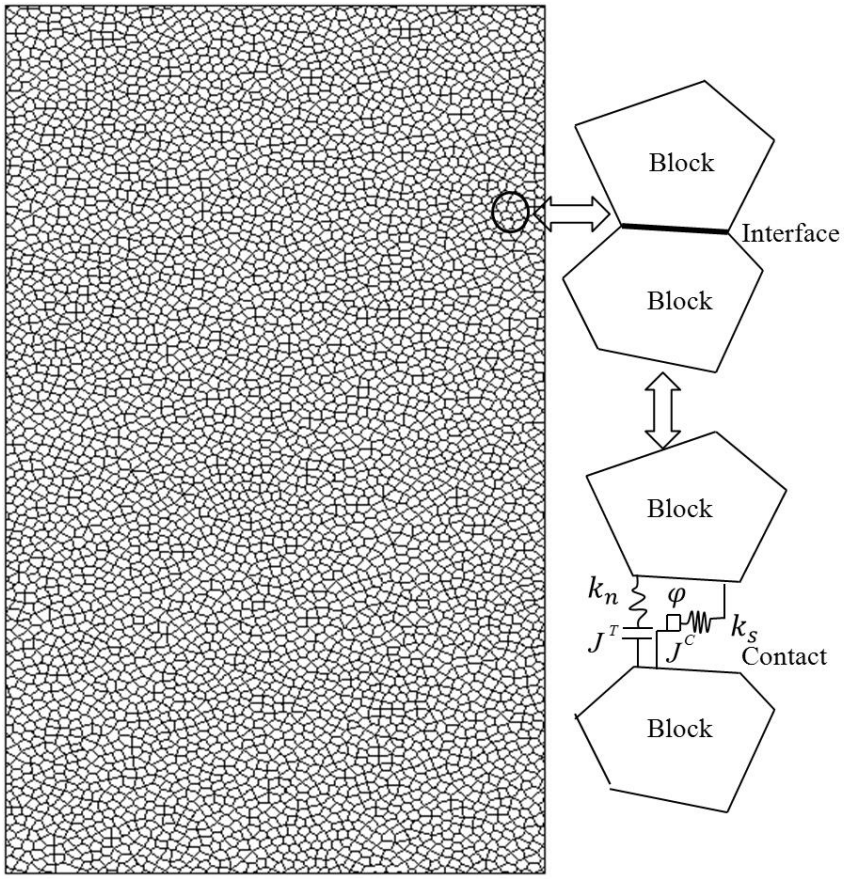

Figure 6.3 Voronoi based UDEC model illustrating blocks and contacts [*Chen et al*., 2015].

Calculation of block displacements

For each block, Newton's second law of motion is applied:

$$\frac{d\dot{u}}{dt} = \frac{F(t)}{m} \tag{6.1}$$

Where u' is velocity of the block centroid, t represents time and m is the mass of the block. Resultant force F(t) includes external boundary forces applied to the block edges, contact forces between blocks, and gravity when introduced by the user.

The time required to reach static equilibrium is divided into incremental time steps Δt. The Δt need to be small enough to avoid information propagating into neighboring blocks so that the finite-difference method can be used. For each time step Δt, acceleration (u'') is deduced by

Eq. (6.1), and is considered to be constant using the finite difference technique during a time step. The central difference for the left-hand side of Eq. (6.1) at time t can be written as

$$\frac{d\dot{u}}{dt} = \frac{\dot{u}(t + \Delta t/2) - \dot{u}(t - \Delta t/2)}{\Delta t} \tag{6.2}$$

Substituting Eq. (6.2) in Eq. (6.1) and rearranging gets

$$\dot{u}(t + \Delta t/2) - \dot{u}(t - \Delta t/2) = \frac{F(t)}{m}\Delta t \tag{6.3}$$

According to velocities stored at the half-timestep point, displacement can be expressed as follows

$$u(t + \Delta t) = u(t) + \dot{u}(t + \Delta t/2)\Delta t \tag{6.4}$$

The new position of the block induces new contact forces. The central difference scheme introduced above is repeated until equilibrium is obtained for each block.

Constitutive laws of contacts and failure criterion

At contact points, the force-displacement relation is defined as spring slider systems. The constitutive laws applied to the contacts are

$$\Delta\sigma_n = k_n \Delta u_n \tag{6.5}$$

$$\Delta\sigma_s = k_s \Delta u_s \tag{6.6}$$

Where k_n and k_s are the normal and shear stiffness of the contact, $\Delta\sigma_n$ and $\Delta\sigma_n$ are the normal and shear stress increments, and Δu_n and Δu_s are the normal and shear displacement increments, respectively.

Moreover, stresses calculated at contact points are submitted to the selected failure criterion:

$$|\sigma_s| \leq c + \sigma_n \tan(\Phi) \tag{6.7}$$

Where c is the cohesion, and Φ is the angle of friction.

In addition to the shear failure criterion, a tensile failure criterion is applied. If tensile stress exceeds tensile strength, the contact breaks and the tensile strength is set to zero.

Block deformability

Blocks may be rigid or deformable. The basic formulation for rigid blocks is given by *Cundall et al*. [1971]. For many cases, the internal deformation of blocks should be taken into consideration. Therefore, deformable blocks are internally discretized into finite-difference triangular elements. The block deformability depends on the number of elements into which

the blocks are divided. Then, Newton's second law is applied at each grid point. Later on, the central difference scheme introduced above is used again to calculate velocity and strain at each grid point.

The constitutive law for the blocks is applied to determine stresses at each zone. For the models in this study, pure elastic conditions are applied. The relationship between stress and strain is given by

$$\Delta\sigma_{ij} = \frac{\gamma E}{(\gamma+1)(1-2\gamma)} \cdot \Delta\varepsilon_{\gamma}\delta_{ij} + \frac{E}{\gamma+1} \cdot \Delta\varepsilon_{ij} \tag{6.8}$$

Where E is the Young's modulus and γ is the Poisson's ratio. $\Delta\sigma_{ij}$ and $\Delta\varepsilon_{ij}$ are the stress and strain increments, $\Delta\varepsilon_{\gamma}$ is the increment of volumetric strain and δ_{ij} is the Kronecker symbol.

Faults and joints are viewed as interfaces between distinct bodies. The motions along the faults or joints are governed by force-displacement law in both the normal and shear directions. Large displacements are allowed along the faults or joints. Therefore, the UDEC program is suitable to solve geologic problems involving faulted and fractured rocks or blocks.

6.3.2 Model set-up

A two-dimensional UDEC model involving Ordos Block and adjacent areas (Figure 6.2) is set up. Linear elastic behavior for the interior of the blocks is assumed for the study area. The numerical models consist of blocks and sedimentary basins (Figure 6.4). Therefore, two domains with different rheological parameters are defined (Figure 6.4; Table 6.1): (1) the competent basement with Young's modulus of 70 GPa (Ordos Block and the other areas), (2) the Cenozoic basins surrounding Ordos Block with low Young's modulus (E = 40 GPa). The values of Young's modulus selected for each domain are referred to *Carmichael* [1989].

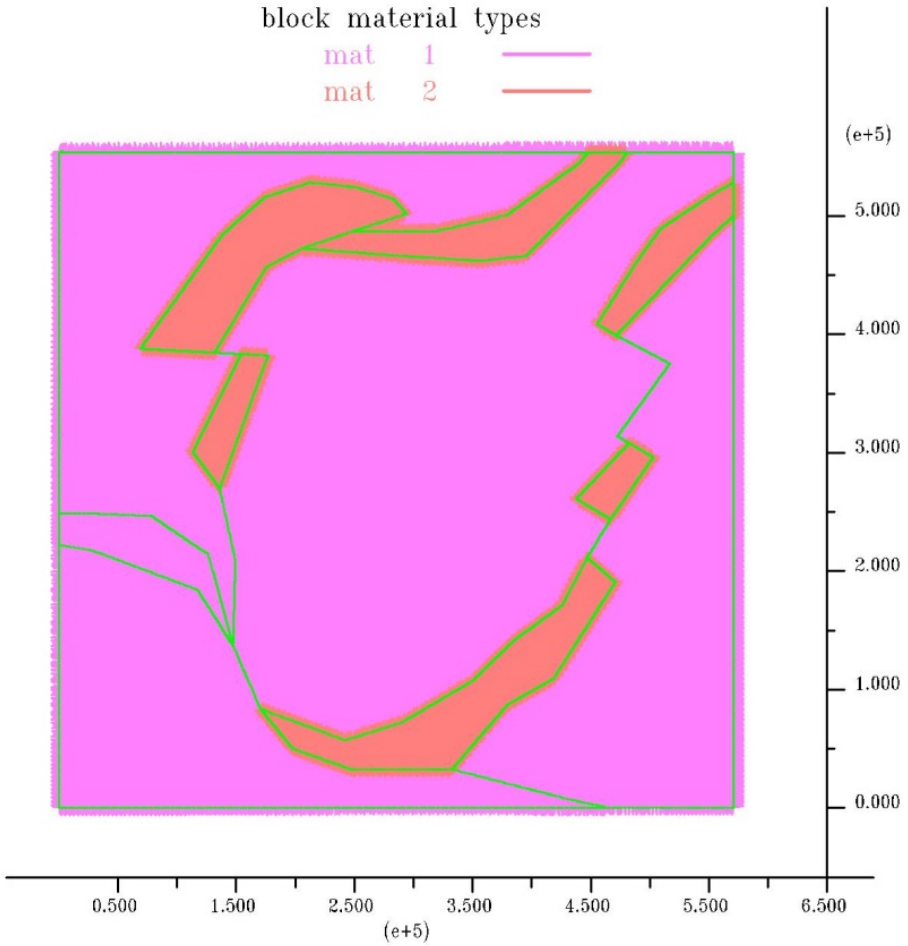

Figure 6.4 The two-dimensional UDEC model of the study area. Two domains with different rheological parameters (two material types) are defined.

Table 6.1 Mechanical parameters of the geologic bodies

	Density ρ/g*cm^{-3}	Young's Modulus E/GPa	Bulk Modulus K/GPa	Shear Modulus G/GPa
Ordos Block and the other areas	2700	70	46.67	28
Basins surrounding Ordos Block	2700	40	26.67	16

Table 6.2 Mechanical parameters of the major faults

	Normal Stiffness Jk_n/GPa*m^{-1}	Shear Stiffness Jk_s/GPa*m^{-1}	Friction angle /°	Cohesion c/MPa	Tension Strength /MPa	Residual friction angle /°
Major faults	0.1	0.1	40	10	1	20

The boundaries of these geologic bodies are faults. These faults are viewed as interfaces between the different geologic bodies. Only major faults of the study area are considered in the models. These major faults are mainly associated with borders of the sedimentary basins around Ordos Block. They also include HYF, XTF, and LNF fault at southwestern margin of Ordos Block, and North Qinling fault (NQF) (Figure 6.2 and Figure 6.4). The parameters for the faults are listed in Table 6.2. The cohesion of the major joints is set to zero. The same holds for the dilation angle.

The two-dimensional model shown in Figure 6.4 represents a present layer of the brittle upper crust situated at a depth of about 5 km. All structures such as the faults and basins described in the modeling are referred to this depth. It is worth mentioning that this simple two-dimensional model is not able to simulate the accurate magnitudes of stress and displacement, but it can reveal general trends and patterns.

6.3.3 Boundary conditions

The most important boundary conditions for the models are those which represent the present tectonic regime. Based on fault kinematic analyses, *Shi et al*. [2015] proposed that the tectonic regime in this area was changed at the end of the Late Pleistocene (ca. 18 ka) from NE-SW extension into a tectonic transpression with subhorizontal maximum principal stress axes (σ_1) trending ENE-direction. This tectonic stress regime has dominated this area and last to present day, which is consistent with the focal mechanisms of earthquakes [*IG and SBNHAP*, 1990; *He et al*., 2003], GPS measurements [*Wang et al*., 2001; *Zheng et al*., 2013], and geo-stresses based on basic database compilation of crustal stress environment in China [*Xie et al*., 2004].

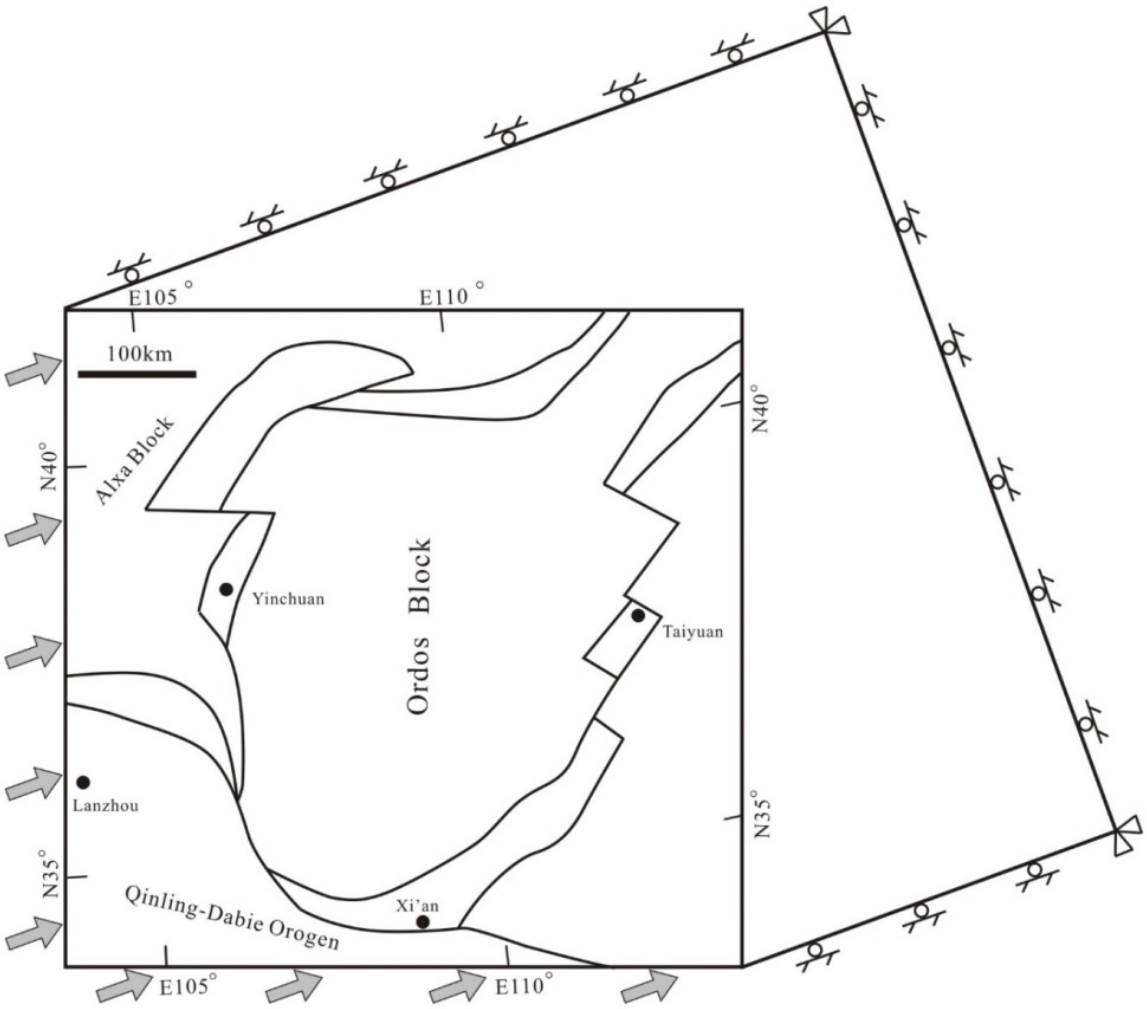

Figure 6.5 Boundary conditions (1) for the two-dimensional UDEC model. ENE-trending (070°) velocities are applied to the left and lower boundaries. The right lower boundary, above boundary, and right boundary are fixed with respect to displacements in normal direction.

This study considers two kinds of boundary conditions: (1) constant velocities are applied to the left and lower boundaries of the model. A constant ENE-trending (070°) of the "push" is assumed. The right lower boundary and above boundary of the model are fixed with respect to displacements in normal direction. The displacements in normal direction of the right boundary are also fixed (Figure 6.5), (2) constant ENE-trending (070°) velocities are assumed to the left and lower boundaries of the model while NNW-trending (340°) velocities are given to the right lower boundary and above boundary. The right boundary of the model is fixed with respect to displacements in normal direction (Figure 6.6).

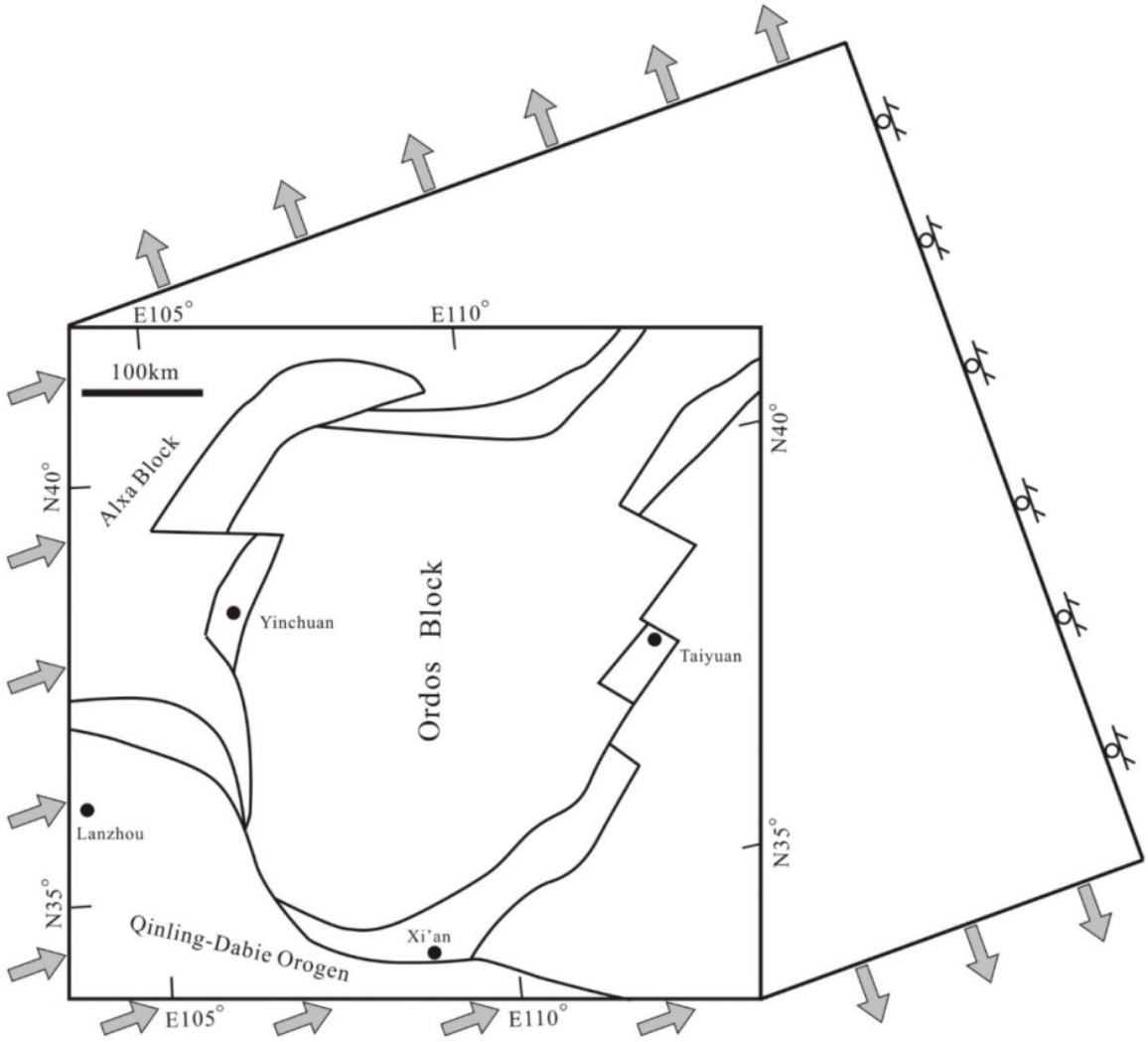

Figure 6.6 Boundary conditions (2) for the two-dimensional UDEC model. ENE-trending (070°) velocities are assumed to the left and lower boundaries while NNW-trending (340°) velocities are given to the right lower boundary and above boundary. The right boundary is fixed with respect to displacements in normal direction.

6.3.4 **Modeling Results**

The models are initialized with in situ stress at the beginning. Two different in situ stress ratios of ENE compression are assumed: (1) a ratio of 1 (isotropic), (2) a ratio of 2 (anisotropic).

Several models with different boundary conditions and in situ stresses are tested within this study. The general trends are quite similar although magnitudes are different. Therefore, only the models with boundary condition (2) and in situ stress ratio of 2 are chosen to illustrate the most important findings.

Block rotations

Strike-slip movement occurs when critical shear stresses act on the block boundaries. The block will rotate and uplift if it is obstructed by the others. In the two-dimensional model, block uplift cannot be observed, but block rotation can be seen and recorded. Figure 6.7 shows the direction of block rotations. According to the modeling results, Ordos Block shows almost no rotation compared with the other geologic bodies, which is consistent with other geologic evidences.

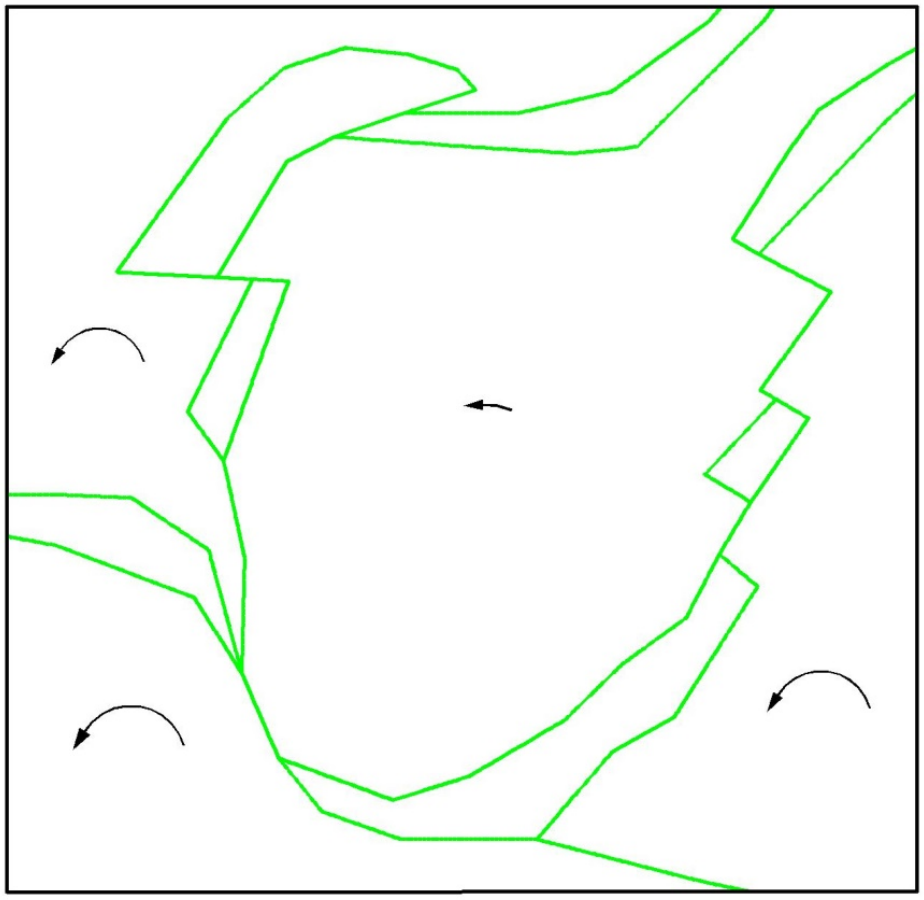

Figure 6.7 Block rotations simulated by UDEC.

Shear stress and shear displacement on faults

Figure 6.8 shows the values of shear stress on faults. The magnitudes of the shear stress may not be accurate because of the limitations of the simplified two-dimensional models. However, the relative value and differences of the shear stresses on each fault are meaningful. Based on the modeling results, the largest shear stresses are located in the transition zones between NE-trending and NW-trending faults (red points in Figure 6.8). In general, the shear stresses on the boundary faults of the sedimentary basins east and west of the Ordos Block are larger than those south and north of the Ordos Block. For Haiyuan fault (HYF), the shear

stress on the middle segment is larger than that of the segments near the junction of the three arcuate faults. For North Qinling fault (NQF), the shear displacement of the eastern segment is larger.

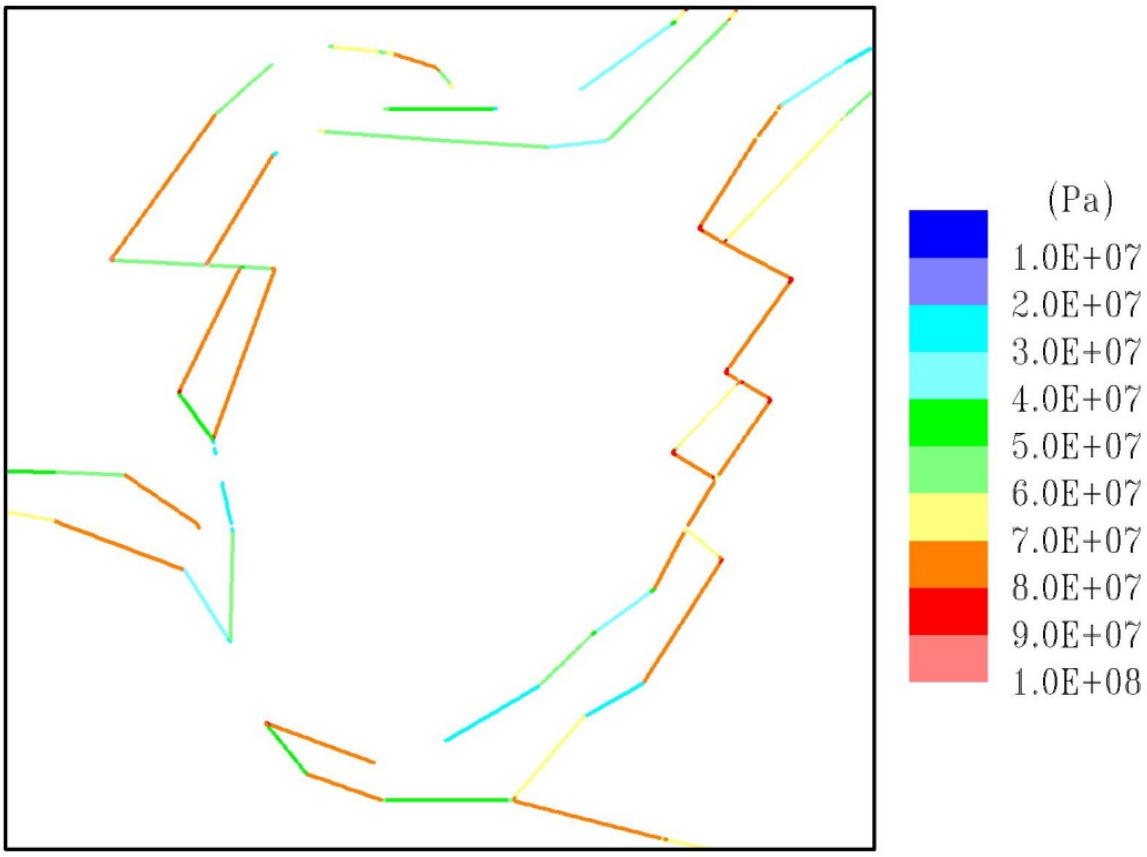

Figure 6.8 Shear stress on faults simulated by UDEC.

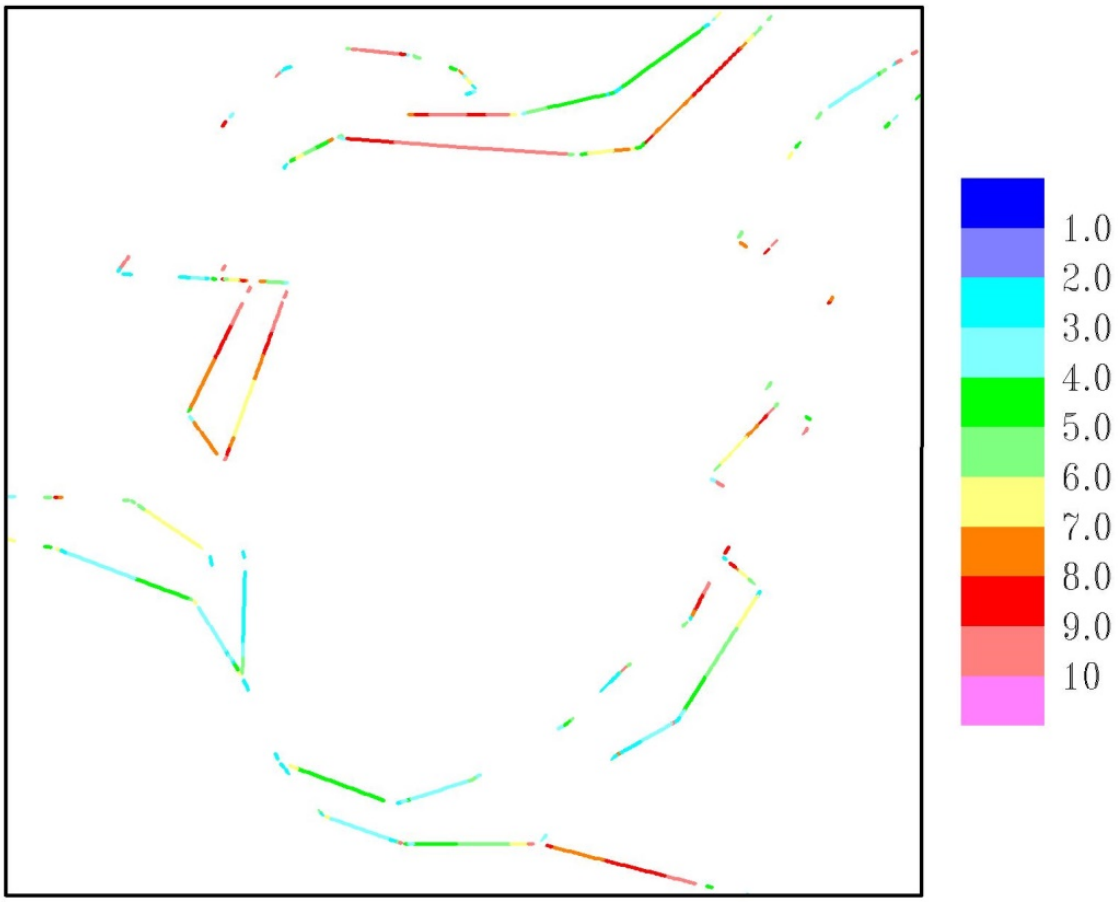

Figure 6.9 Scaled shear displacement on faults simulated by UDEC.

Figure 6.9 displays scaled shear displacement on the faults. The relative value of the shear displacement on the faults is consistent with the shear stress described above. Generally speaking, the NE-trending faults east and west of Ordos Block have larger shear displacements. Similarly, the middle segment of the HYF and the eastern segment the NQF exhibit larger shear displacements.

Slip tendency

Based on *Morris et al*. [1996], the tendency of a surface to experience slip in a given stress field depends on its frictional features which are mainly controlled by rock type and the ratio of shear to normal stress acting on the surface. This ratio is defined as slip tendency. Eq. 6.9 shows the relationship between the slip tendency (T_s), shear stress, and normal stress.

$$T_s = \frac{\sigma_s}{\sigma_n} \tag{6.9}$$

Where σ_s represents shear stress and σ_n is normal stress.

The slip tendency depends on the stress field (stress tensor) and the orientation of the surface.

The coefficient of static friction (μ), is the limit value of T_s which will lead to slip on a cohesionless surface. Therefore, the analysis of slip tendency (T_s) represents the potential for slip on individual faults.

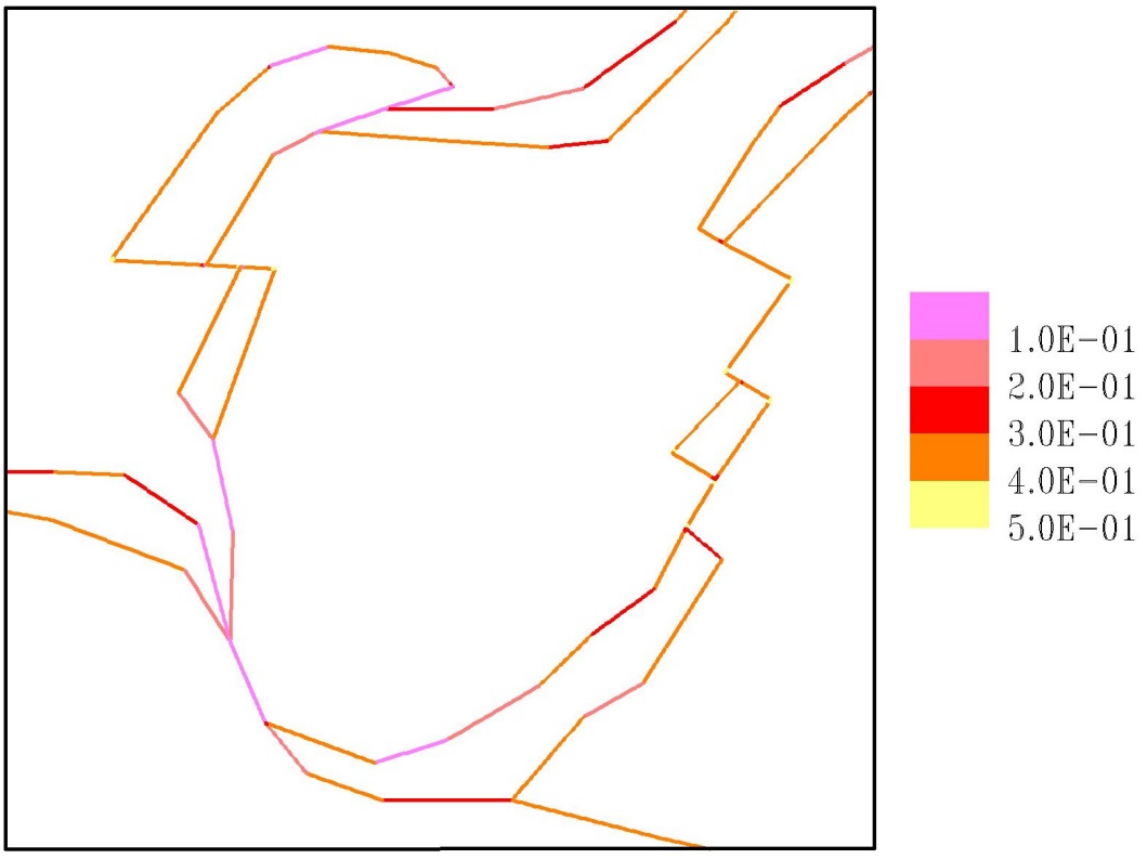

Figure 6.10 Ratio of shear to normal force for each contact (slip tendency) simulated by UDEC.

Figure 6.10 shows the ratio of shear to normal force for each contact defined as slip tendency in this study. Modeling results reveal that the most potential slip zones are located in the transition zones between NE-trending and NW-trending faults (yellow points in Figure 6.10), which is in agreement with the simulation results based on continuum methods by [*Dai et al*., 2015]. Among the convex-to-the-northeast oroclinal faults in southwestern margin of Ordos Block, larger earthquakes tend to occur along Haiyuan fault (HYF). Consistently, the epicenter of the 1920 Haiyuan earthquake (M=8.7) was in Ganyanchi basin on Haiyuan fault. Moreover, Liupan Shan fault (LSF), the southern segment of XTF, and LNF are potentially inactive. For NQF, the middle segment of the NQF (the southern margin fault of the Weihe basin) is more active, which is consistent with the geologic evidences [IG and SBNHAP, 1990; Zhang et al., 2003]

6.4 Conclusions

A two-dimensional UDEC model involving Ordos Block and adjacent areas is built. Boundary conditions based on present tectonic regime are assumed. This study presents modeling results with boundary condition (2) and in situ stress ratio of 2. Block rotations, shear stress and displacement on faults, ratio of shear to normal force (slip tendency) are simulated. Modeling results are applied to the study area and compared with geologic evidences.

7 Conclusions and outlook

7.1 Conclusions

This study presents numerical simulation of geologic processes based on DEM, including modeling of pull-apart basin development based on Particle Flow Code (PFC) and simulation of deformation and earthquake potential of Ordos Block under present tectonic stress regime.

Particle based modeling of pull-apart basin development

Firstly, particle based modeling has been established to simulate the development of pull-apart basins. This study considers the effect of model scale and particle size on the modeling results and shows that proposed modeling approach is scale-independent and robust. Then, micro-scale PFC models are used to investigate crack formation and propagation, and basin development of pull-aparts formed in releasing sidesteps systems with pure strike-slip, transtensional, and transpressional master faults, respectively. In each system, three typical initial strike-slip geometries, i.e., 30° underlapping, 90° non-overlapping, and 150° overlapping releasing sidesteps are selected to simulate the pull-apart basin formation and evolution at natural scale including a parameter study and robustness analyses. The modeling mainly focuses on crack propagation and coalescence, pull-apart basin development, stress-deformation behavior, and relative extension. Finally, the modeling results are compared with natural pull-apart basins worldwide. The origin of rhomboidal pull-apart basins, depocenters of pull-apart basins, cross-basin faults and their significances, models for pull-apart basin development, and minimum displacements and ages to form pull-apart basins are discussed. The main findings are summarized as follows:

(1) For pure strike-slip, 30° underlapping model produces pull-apart basins that evolve through a sequence of closely related states, from spindle-shaped through lazy-Z-shaped to the rhomboidal and stretched rhomboidal basin. 90° non-overlapping and 150° overlapping models directly generate rhomboidal and stretched rhomboidal basins, without going through spindle-shaped and lazy-Z-shaped stages. The shape of a pull-apart basin in nature is the consequence of both the initial fault geometry and its various evolution stages.

(2) A pull-apart basin could evolve from different initial fault geometries (underlapping, non-overlapping, and overlapping releasing sidestep). It can also originate from various fault kinematics such as pure strike-slip, transtension, and transpression. This study summarizes the models of pull-apart basin development with different initial conditions.

(3) 30° underlapping transtensional model with two parallel master faults produces a depression with two depocenters. The basin forming in this transtensional system is wider than the basin in pure strike-slip system. Another type of transtensional model where one master fault is parallel to the displacement vector while the other master fault has a minor component of oblique and divergent motion, forms a basin evolving from an oblique, inner depression to an oblique, wider depression with outer boundary faults. Fault geometry and basin shape of the modeling display close similarities to the rhombic-shaped Central basin in the Sea of Marmara.

(4) 30° underlapping transpressional model with two parallel master faults produces a cross-basin fault connecting the tips of the two master faults. As offset increases, the first subsidence area forms along the diagonal fault. Basin sidewalls develop, bounding an oblique, asymmetric pull-apart basin. The transpressional model based on Hanmer basin also evolves in this way.

(5) 90° non-overlapping and 150° overlapping systems with pure strike-slip, transtensional, and transpressional master faults all directly generate rhomboidal and stretched rhomboidal pull-apart basins, without evolving through spindle and lazy-Z-shaped stages. Basin width does not change significantly and is governed by the separation of the master strike-slip faults. Basin length increases with increasing strike-slip displacements. The shape of a pull-apart basin in 90° non-overlapping and 150° overlapping systems is the consequence of the initial overlap of master faults and its various evolution stages.

(6) Basin length and the amount of motion along the master faults are compared to identify the origin of rhomboidal basins. Rhomboidal basins which have larger basin length than the amount of motion formed in an overlapping system have not gone through the spindle-shaped and lazy-Z-shaped stages, such as the Dead Sea basin and 20°N basin. Rhomboidal basins with cross-basin faults generally formed in underlapping system and have gone through the spindle and lazy-Z-shaped stages, for instance Dayingshui basin and Pitalito basin.

(7) Modeling results indicate that cross-basin faults which connect two tips of the master faults cannot form in non-overlapping and overlapping systems, but cross-basin faults can form in underlapping systems because of the underlap of the master faults. The formation of the cross-basin fault does may not lead to the extinction of the basin. Instead, the first depression forms along the cross-basin fault and the depocenter is later orientated along the cross-basin fault.

(8) All three typical models show nearly the same behavior in respect to the σ_1-ε_x*curve.

Peak stress and onset of crack propagation are observed for ε_x* of approximately 0.035. Then, the first cracks (Riedel-shears) propagate and link with master strike-slip faults, forming a depression area. The relative extension to form the first depression area is about 0.155.

(9) For a pull-apart basin in nature, the displacement and time needed to form the first cracks and depression area can be estimated based on the corresponding ε_x* and the slip rate of the strike-slip faults. The time to form the first depression can be considered as the minimum age of initiation for the pull-apart basin. This method is recommended for the pull-apart basins which are still active.

Simulation of deformation and earthquakes of Ordos Block under present tectonic regime

A two-dimensional UDEC model involving Ordos Block and adjacent areas is established. Boundary conditions based on present tectonic regime are assumed. Main findings are listed below.

(1) Ordos Block shows almost no rotation compared with the other geologic bodies, which is consistent with geologic evidences.

(2) The shear stresses and shear displacement on the boundary faults of the sedimentary basins east and west of the Ordos Block are larger than those south and north of the Ordos Block. For Haiyuan fault (HYF), the shear stress on the middle segment is larger than those of the segments near the junction of the three arcuate faults. For North Qinling fault (NQF), the shear displacement of the eastern segment is larger.

(3) Most of the potential slip zones are located in the transition zones between NE-trending and NW-trending faults. Among the convex-to-the-northeast oroclinal faults in southwestern margin of Ordos Block, larger earthquakes tend to occur along Haiyuan fault (HYF). Liupan Shan fault (LSF), the southern segment of XTF, and LNF are potentially inactive. For NQF, the middle segment of the NQF (the southern margin fault of the Weihe basin) is more active.

7.2 Main contributions

- Particle based modeling has been established to simulate the development of pull-apart basins. A scale-independent modeling approach based on the Discrete Element Method is proposed.

- This study firstly presents the process that a pull-apart basin evolves from spindle-shaped through lazy-Z-shaped to rhomboidal and stretched rhomboidal basin, with discontinuum methods which can intuitively illustrate crack formation and propagation on a fracture mechanical basis.

- Proposal for a method to identify the origin of a rhomboidal pull-apart basin in nature. The rhomboidal Dead Sea basin did not evolve through the spindle-shaped and lazy-Z-shaped stages.

- Comparison of crack propagation and basin development in pure strike-slip, transtensional, and transpressional systems. The modeling results are similar to the well-studied natural examples such as Central basin in the Sea of Marmara and Hanmer basin in New Zealand.

- Summarizing the pull-apart basin development under different initial conditions including different initial fault geometries and various initial fault kinematics.

- Proposal for a method to estimate minimum displacements to form pull-apart basins and minimum ages of initiation of pull-apart basins. This method to deduce the starting age of pull-apart basin development is recommended for basins which are still active.

- A two-dimensional UDEC model involving Ordos Block and adjacent areas is set up. Slip tendency which represents the assessment of the potential for causing slip on individual faults and earthquake-prone of the faults is predicted and compared with geologic and geophysical evidences.

7.3 Recommendations for future research

Compared with the continuum methods, the advantage of DEM modeling is that one can intuitively see the crack propagation and coalescence during the pull-apart basin development. The disadvantage is lack of subsidence and uplift in vertical direction because of the limitations of two-dimensional models. Therefore, three-dimensional DEM models should be built in future to see the subsidence and uplift in vertical direction intuitively. This could reflect the distribution and migration of the basin depocenter and rift flank uplift. Also, the viscous nature of the process should be considered in more detail by introducing visco-elasto-plastic contact models.

More UDEC models which consider different parameters for the major faults should be built. Three-dimensional models of the Ordos Block and adjacent areas as well as the viscous behavior should be considered in future.

References

Armijo, R., B. Meyer, S. Navarro, G. King, and A. Barka (2002), Asymmetric slip partitioning in the Sea of Marmara pull-apart: A clue to propagation processes of the North Anatolian fault? *Terra Nova*, *14*, 80-86.

Aydin, A., and A. Nur (1982), Evolution of pull-apart basins and their scale independence, *Tectonics, 1(1)*, 91-105.

Bahat, D. (1983), New aspects of rhomb structures, *Journal of Structural Geology, 5(6)*, 591-601.

Bandel, K., and H. Khouri (1981), Lithostratigraphy of the Triassic of Jordan, *Facies, 4*, 1-23.

Barka, A. (1992), The North Anatolian fault zone, *Annalae Tectonicae*, *6*, 164-195.

Barka, A., H. S. Akyüz, H. A. Cohen, and F. Watchorn (2000), Tectonic evolution of the Niksar and Tasova-Erbaa pull-apart basins, North Anatolian fault zone: Their significance for the motion of the Anatolian block, *Tectonophysics, 322*, 243-264.

Barnes, P. M., R. Sutherland, B. Davy and J. Delteil (2001), Rapid creation and destruction of sedimentary basins on mature strike-slip faults: an example from the offshore Alpine Fault, New Zealand, *Journal of Structural Geology, 23*, 1727-1739.

Barnes, P. M., R. Sutherland and J. Delteil (2005), Strike-slip structure and sedimentary basins of the southern Alpine Fault, Fiordland, New Zealand, *Geological Society of America Bulletin, 117*, 411-435.

Ben-Avraham, Z. (1985), Structural framework of the Gulf of Elat (Aqaba), Northern Red Sea. *J. Geophys. Res. 90 (B1)*, 703-726.

Ben-Avraham, Z. (1992), Development of asymmetric basins along continental transform faults, *Tectonophysics, 215*, 209-220.

Ben-Avraham, Z., G. Almagor, and Z. Garfunkel (1979), Sediments and structure of the Gulf of Elat (Aqaba)-northern Red Sea, *Sedimentary Geology, 23(1-4)*, 239-267.

Ben-Avraham, Z., and M. D. Zoback (1992), Transform-normal extension and asymmetric basins: an alternative to pull-apart models, *Geology, 20 (5)*, 423-426.

Benesh, C. J., A. Plesch, J. H. Shaw, and E. K. Frost (2007), Investigation of growth fault bend folding using discrete element modeling: implications for signatures of active folding above blind thrust faults, *J. Geophys. Res., 112*, B03S04.

Bertoluzza, L., and C. R. Perotti (1997), A finite-element model of the stress field in strike-slip basin: implication for the Permian tectonics of the Southern Alps (Italy), *Tectonophysics, 280*, 185-197.

Burbidge, D. R., and J. Braun (2002), Numerical models of the evolution of accretionary wedges and fold-and-thrust belts using the distinct-element method, *Geophysical Journal International, 148(3)*, 542-561.

ten Brink, U. S. and Z. Ben-Avraham (1989), The anatomy of a pull-apart basin: seismic reflec- tion observations of the Dead Sea Basin, *Tectonics*, *8*, 333-350.

ten Brink, U. S. and M. Rybakov (1999), Anatomy of the Dead Sea transform; does it reflect continuous changes in plate motion?, *Geology, 27*, 887-890.

ten Brink, U. S., Z. Ben-Avraham, R. E. Bell, M. Hassouneh, D. F. Coleman, G. Andreasen, G. Tibor, and B. Coakley (1993), Structure of the Dead Sea Pull-apart basin from gravity analyses, *Journal of Geophysical Research, 98*, 21877-21894.

Burbidge DR, Braun J (2002), Numerical models of the evolution of accretionary wedges and fold-and-thrust belts using the distinct-element method, *Geophys J Int 148*, 542-561.

Burchfiel, B. C., and J. H. Stewart (1966), “pull-apart” origin of the central segment of death valley, california, *Geological Society of America Bulletin, 77*, 439-442.

Burchfiel, B. C., P. Zhang, Y. Wang, W. Zhang, F. Song, Q. Deng, P. Molnar, and L. Royden (1991), Geology of the Haiyuan fault zone, Ningxia-Hui Autonomous region, China, and its relation to the evolution of the northeastern margin of the Tibetan Plateau, *Tectonics, 10(6)*, 1091-1110.

Bürgmann, R., and G. Dresen (2008), Rheology of the Lower Crust and Upper Mantle: Evidence from Rock Mechanics, Geodesy, and Field Observations, *Annu. Rev. Earth Planet. Sci, 36*, 531-567.

Cardozo, N., R. W. Allmendinger, J. K. Morgan (2005), Influence of mechanical stratigraphy and initial stress state on the formation of two fault propagation folds, *Journal of Structural Geology, 27*, 1954-1972.

Carmichael, R.S. (1989), Practical Handbook of Physical Properties of Rocks and Minerals, CRC Press, Boca Raton, Florida.

Chevalier, M.-L., F. J. Ryerson, P. Tapponnier, R.C. Finkel, J. Van Der Woerd, H. Li, and Q. Liu (2005), Slip-rate measurements on the Karakoram fault may imply secular variations in fault motion, *Science, 307*, 411-414.

Chen, W., H. Konietzky, and S. M. Abbas (2015), Numerical simulation of time-independent and -dependent fracturing in sandstone, *Engineering Geology, 193*, 118-131.

Chorowicz, J., P. Chotin, and R. Guillande (1996), The Garzon fault: active southwestern boundary of the Caribbean plate in Colombia, *Geologische Rundschau*, *85*, 172-179.

Chu, S.-S., M.-L. Lin, W.-C. Huang, W.-T. Nien, H.-C. Liu, and P.-C. Chan (2015), Simulation of growth normal fault sandbox tests using the 2D discrete element method, *Computers & Geosciences, 74*, 1-12.

Corti, G and T. P. Dooley (2015), Lithospheric-scale centrifuge models of pull-apart basins, *Tectonophysics, 664*, 154-163.

Crowell, J. C., (1974), Origin of late Cenozoic basins in southern California, in Dott, R. H., and Shaver, R. H., eds., *Modern and ancient geosynclinal sedimentation*, SEPM Spec. Pub. 19, pp. 292-303.

Crowell, J. C., (1982), The tectonics of Ridge Basin, southern California. *In: Crowell, J.C., Link, M.H. (Eds.), Geologic History of Ridge Basin, Southern California, PacificSection, Soci- ety of Economic Paleontologists and Mineralogists*, pp. 25-42.

Cundall, P.A. (1971), A computer model for simulating progressive, large scale movement in blocky rock systems, in *International Symposium on Rock Mechanics*. International Society of Rock Mechanics, Nancy, France, 129-136.

Dai, L., Q. Li, S. Li, L. Guo, I. D. Somerville, L. Xu, X. Cao, Y. Suo (2015), Numerical modelling of stress fields and earthquake jointly controlled by NE- and NW-trending fault zones in the Central North China Block, *Journal of Asian Earth Sciences, 114*, 28-40.

Dean, S. L., J. K. Morgan, and T. Fournier (2013), Geometries of frontal fold and thrust belts: Insights from discrete element simulations, *Journal of Structural Geology, 53*, 43-53.

DeMets, C., R. G. Gordon, and D. F. Argus (2010), Geologically current plate motions, *Geophysical Journal International, 181(1)*, 1-80.

Deng, Q., D. Wu, P. Zhang, and S. Chen (1986), Structure and deformational character of strike-slip fault zones, *Pure and Applied Geophysics, 124*, 201-223.

Deng, Q., W. Zhang, P. Zhang, D. Jiao, F. Song, Y. Wang, B. C. Burchfiel, P. Molnar, L. Royden, S. Chen, S. Zhu, and Z. Chai (1989), Haiyuan strike-slip fault zone and its compressional structures of the end, *Seismology and Geology, 11(1)*, 1-14.

Dewey, J. F. (1978), Origin of long transform-short ridge systems, *Geol. Soc. America, 10*, 388.

Dewey, J. F., R. E. Holdsworth, and R.A. Strachan (1998), Transpression and transtension zones, in *Continental transpressional and transtensional tectonics* edited by R.E. Holdsworth et al., pp. 1-14, Geological Society, Special Publication, London.

Ding, X., L. Zhang, H. Zhu, and Q. Zhang (2014), Effect of Model Scale and Particle Size Distribution on PFC3D Simulation Results, *Rock Mechanics and Rock Engineering, 47*, 2139-2156.

Dooley, T., and K. McClay (1997), Analog modeling of pull-apart Basins, *AAPG Bulletin, 81*, 1804-1826.

Dooley, T., and G. Schreurs (2012), Analogue modelling of intraplate strike-slip tectonics: A review and new experimental results, *Tectonophysics, 574*, 1-71.

Escalona, A., P. Mann, and M. Jaimes (2011), Miocene to recent Cariaco basin, offshore Venezuela: Structure, tectonosequences, and basin-forming mechanisms, *Marine and Petroleum Geology*, *28*, 177-199.

Fan, J., J. Ma, and W. Gan (2003), Movement of Ordos Block and alternation of activity along its boundaries, *Sci. China (Series D) 46*, 168-180.

Finch, E., S. Hardy, and R. Gawthorpe (2003), Discrete element modelling of contractional fault-propagation folding above rigid basement faults blocks, *Journal of Structural Geology, 25*, 515-528.

Flerit, F., R. Armijo, G. C. P. King, B. Meyer, and A. Barka (2003), Slip partitioning in the Sea of Marmara pull-apart determined from GPS velocity vectors, *Geophys. J. Int., 154*, 1-7.

Fossen, H. (2016), *Structural geology*, Cambridge University Press, New York.

Fossen, H., and B. Tikoff (1998), Extended models of transpression and transtension, and application to tectonic settings, *Geological Society, London, Special Publications, 135(1)*, 15-33.

Freund, R. (1971), The Hope fault: a strike-slip fault in New Zealand, *New Zealand Geological Survey Bulletin, 86*, 1-49.

Freund, R., Z. Garfunkel, I. Zak, M. Goldberg, T. Weissbrod, and B. Derin (1970), The shear along the Dead Sea rift, *Philosophical Transaction of the Royal Society of London*, *Series A 267*, 107-130.

Garfunkel, Z., (1981). Internal structure of the Dead Sea leaky transform (rift) in relation to plate kinematics, *Tectonophysics, 80*, 81-108.

Garfunkel, Z., and Z. Ben-Avraham (1996), The structure of the Dead Sea basin, *Tectonophysics, 266*, 155-176.

Gerya, T. V., R. J. Stern, M. Baes, S. V. Sobolev, and S. A. Whattam (2015), Plate tectonics on the Earth triggered by plume-induced subduction initiation, *Nature, 527 (7577)*, 221.

Gölke, M., S. Cloetingh, and K. Fuchs (1994), Finite-element modeling of pull-apart basin formation, *Tectonophysics, 240*, 45-57.

Groh, U., H. Konietzky, K. Walter, and M. Herbst (2011), Damage simulation of brittle heterogeneous materials at the grain size level, *Theoretical and Applied Fracture Mechanics, 55*, 31-38.

Gürbüz, A. (2010), Geometric characteristics of pull-apart basins, *Lithosphere, 2(3)*, 199-206.

Hardy, S. (2008), Structural evolution of calderas: insights from two-dimensional discrete element simulations, *Geology, 36*, 927-930.

He, J.K., M. Liu, Y. X. Li (2003), Is the Shanxi rift of northern China extending? *Geophys. Res. Lett., 30*, 2213.

Hilley, G. E., R. Bürgmann, P. Z. Zhang, and P. Molnar (2005), Bayesian inference of plastosphere viscosities near the Kunlun Fault, northern Tibet, *Geophysical Research Letters, 32*, L01302.

Hurwitz, S., Z. Garfunkel, Y. Ben-Gai, M. Reznikov, Y. Rotstein, and H. Gvirtzman (2002), The tectonic framework of a complex pull-apart basin: Seismic reflection observations in the Sea of Galilee, Dead Sea transform, *Tectonophysics, 359*, 289-306.

Imber, J., G. W. Tuckwell, C. Childs, J. J. Walsh, T. Manzocchi, A. E. Heath, C. G. Bonson, and J. Strand (2004), Three-dimensional distinct element modelling of relay growth and breaching along normal faults, *Journal of Structural Geology, 26*, 1897-1911.

Institute of Geology, State Seismological Bureau (IG), and Seismological Bureau of Ningxia Hui Autonomous Province (SBNHAP) (1990), *Haiyuan Active Fault*. Seismological Press, Beijing.

Itasca (2004), *PFC^{2D} (particle flow code in 2 dimensions) manual*. Version 4.0 edition. ICG. Minneapolis, Minnesota.

Itô, H. (1979), Rheology of the crust based on long-term creep tests if rocks, *Tectonophysics, 52*, 629-641.

Itoh, Y. (2001), A Miocene pull-apart deformation zone at the western margin of the Japan Sea back-arc basin: implications for the back-arc opening mode, *Tectonophysics, 334*, 235-244.

Karakhanian, A. S., V. G. Trifonov, H. Philip, A. Avagyan, K. Hessami, F. Jamali, M. S. Bayraktutan, H. Bagdassarian, S. Arakelian, V. Davtian, and A. Adilkhanyan (2004), Active faulting and natural hazads in Armenia, eastern Turkey and northwestern Iran, *Tectonophysics, 380*, 189-219.

Katzman, R., U. Brink, and J. Lin (1995), Three-dimensional modeling of pull-apart basins: Implication for the tectonics of the Dead Sea Basin, *Journal of Geophysical Research, 100*, 6295-6312.

Kaufmann, G., and F. Amelung (2000), Reservoir-induced deformation and continental rheology in vicinity of Lake Mead, Nevada, *Journal of Geophysical Research, 105*, 16 341-16 358.

Kim, Y.-S., D. C. P. Peacock, and D. J. Sanderson (2004), Fault damage zones, *Journal of Structural Geology, 26*, 503-517.

Koide, H., and S. Bhattacharji (1977), Geometric patterns of active strike-slip faults and their significance as indicators for areas of energy release, in *Energetic of geological processes*, edited by S.K. Saxena, et al., pp. 46-66, Spinger Verlag, New York.

Lallemand, S., and L. Jolivet (1986), Japan Sea: a pull-apart basin?, *Earth and Planetary Science Letters, 76*, 375-389.

Lazar, M., Z. Ben-Avraham, and U. Schattner (2006), Formation of sequential basins along a strike-slip fault-geophysical observations from the Dead Sea basin, *Tectonophysics, 421*, 53-69.

Lee, C., Y. Park, and S. Kwon (2004), Simulation of a two-dimensional 'thin-skinned' orogenic wedge using PFC, in *Numerical Modeling in Micromechanics via Particle Methods*, Kyoto, Japan.

Liu, M., and Y. Yang (2003), Extensional collapse of the Tibetan Plateau: Results of three-dimensional finite element modeling, *Journal of Geophysical Research, 108 (B8)*, 2361, doi: 10.1029/2002JB002248.

Liu, Y., and H. Konietzky (2018), Particle based modeling of pull-apart basin development, *Tectonics*, 37, 343-358.

Mann, P. (2007), Global catalogue, classification and tectonic origins of restraining and

releasing bends on active and ancient strike-slip fault systems, in *Tectonics of Strike-Slip Restraining and Releasing Bends*, edited by W. D. Cunningham and P. Mann, *Geological Society, London, Special Publications, 290*, 13-142.

Mann, P., M. R. Hempton, D. C. Bradley, and K. Burke (1983), Development of Pull-Apart Basins, *The Journal of Geology, 91*, 529-554.

McClay, K., and T. Dooley (1995), Analogue models of pull-apart basins, *Geology, 23*, 711-714.

Morgan J. K., and M. S. Boettcher (1999), Numerical simulations of granular shear zones using distinct element method 1, Shear zone kinematics and the micromechanics of localization, *J Geophys Res 104*, 2703-2719.

Morris, A., D.A. Ferrill, and D.B. Henderson (1996), Slip-tendency analysis and fault reactivation, *Geology, 24(3)*, 275-278.

Murphy, M. A., and W. P. Burgess (2006), Geometry, kinematics, and landscape characteristics of an active transtension zone, Karakoram fault system, southwest Tibet, *Journal of Structural Geology, 28*, 268-283.

Noda, A., and S. Toshimitsu (2009), Backward stacking of submarine channel-fan successions controlled by strike-slip faulting: the Izumi Group (Cretaceous), *southwest Japan, Lithosphere 1*, 41-59.

Norris, R. J., and A. F. Cooper (2001), Late Quaternary slip rates and slip partitioning on the Alpine Fault, New Zealand, *Journal of Structural Geology, 23*, 507-520.

Naylor, M., and H. D. Sinclair (2005), A discrete element model for orogenesis and accretionary wedge growth, *Journal of Geophysical Research, 110*, 1-16.

Okay, A. I., A. Kaşlilar-Özcan, C. Imren, A. Boztepe-Güney, E. Demirbag, and I. Kuşçu (2000), Active faults and evolving strike-slip basins in the Marmara Sea, northwest Turkey: a multichannel seismic reflection study, *Tectonophysics, 321*, 189-218.

Peacock, D. C. P., and Z. Xing (1994), Field examples and numerical modelling of oversteps and bends along normal faults in cross-section, *Tectonophysics, 234*, 147-167.

Petrunin, A., and S. V. Sobolev (2006), What controls thickness of sediments and lithospheric deformation at a pull-apart basin?, *Geology, 34*, 389-392.

Petrunin, A., and S. V. Sobolev (2008), Three-dimensional numerical models of the evolution of pull-apart basins, *Physics of the Earth and Planetary Interiors, 171*, 387-399.

Potyondy, D. O., and P. A. Cundall (2004), A bonded-particle model for rock, *International Journal of Rock Mechanics and Mining Sciences, 41*, 1329-1364.

Quennell, A. M. (1959), Tectonics of the Dead Sea rift, in *Proceedings of the 20th International Geological Congress*, Mexico, pp. 385-403.

Quennell, A. M. (1958), The structural and geomorphic evolution of the Dead Sea rift, *Quarterly Journal of the Geological Society,114(1-4)*, 1-24.

Rahe, B., D. A. Ferrill, and A. P. Morris (1998), Physical analog modeling of pull-apart basin evolution, *Tectonophysics, 285*, 21-40.

Reilinger, R., S. McClusky, P. Vernant, S. Lawrence, S. Ergintav, R. Cakmak, ... and M. Nadariya (2006), GPS constraints on continental deformation in the Africa-Arabia-Eurasia continental collision zone and implications for the dynamics of plate interactions, *Journal of Geophysical Research: Solid Earth, 111(B5)*.

Rodriguez, M., N. Chamot-Rooke, M. Fournier, P. Huchon, and M. Delescluse (2013), Mode of opening of an oceanic pull-apart: The 20°N Basin along the Owen Fracture Zone (NW Indian Ocean), *Tectonics, 32*, 1343-1357.

Rogers, D. A. (1980), Analysis of pull-apart basin development produced by en echelon strike-slip faults, in *Sedimentation in Oblique-Slip Mobile Zones*, edited by P. F. Ballance and H. G. Reading, pp. 27-41, International Association of Sedimentologists Special Publication.

Rosenberg, C. L. (2001), Deformation of partially molten granite: a review and comparison of experimental and natural case studies, *International Journal Earth Sciences, 90*, 60-76.

Rousset, B., S. Barbot, J. P. Avouac, and Y. J. Hsu (2012), Postseismic deformation following the 199 Chi-Chi earthquake, Taiwan: Implication for lower-crust rheology, *Journal of Geophysical Research, 117*, B12405.

Sanderson, D. J., and W. R. D. Marchini (1984), Transpression, *Journal of structural Geology, 6(5)*, 449-458.

Sarfarazi, V., A. Ghazvinian, W. Schubert, M. Blumel, and H. R. Nejati (2014), Numerical Simulation of the Process of Fracture of Echelon Rock Joints, *Rock Mechanics and Rock Engineering, 47*, 1355-1371.

Schattner, U., and R. Weinberger (2008), A mid‐Pleistocene deformation transition in the Hula basin, northern Israel: Implications for the tectonic evolution of the Dead Sea Fault, *Geochemistry, Geophysics, Geosystem*s, *9(7)*, 1-18.

Schöpfer, M. P. J., C. Childs, and J. J. Walsh (2006), Localisation of normal faults in multilayer sequences, *Journal of Structural Geology, 28*, 816-833.

Schöpfer, M. P. J., C. Childs, and J. J. Walsh (2007a), Two-dimensional distinct element modeling of the structure and growth of normal faults in multilayer sequences: 1. Model calibration, boundary conditions, and selected results, *Journal of Geophysical Research, 112*, B10401.

Schöpfer, M. P. J., C. Childs, and J. J. Walsh (2007b), Two-dimensional distinct element modeling of the structure and growth of normal faults in multilayer sequences: 2. Impact of confining pressure and strength contrast on fault zone geometry and growth, *Journal of Geophysical Research, 112*, B10404.

Segall, P., and D. D. Pollard (1980), Mechanics of discontinuous faults, *Journal of Geophysical Research: Solid Earth, 85(B8)*, 4337-4350.

Shi, W., S. Dong, Y. Liu, J. Hu, X. Chen, and P. Chen (2015), Cenozoic tectonic evolution of the South Ningxia region, northeastern Tibetan Plateau inferred from new structural investigations and fault kinematic analyses, *Tectonophysics, 649*, 139-164.

Sims, D., D. A. Ferrill, and J. A. Stamatakos (1999), Role of a ductile decollement in the development of pull-apart basins: Experimental results and natural examples, *Journal of Structural Geology, 21*, 533-554.

Stahl, M., and H. Konietzky (2011), Discrete element simulation of ballast and gravel under special consideration of grain-shape, grain size and relatively density, *Granular Matter, 4*, 417-428.

Sutherland, R., and R. J. Norris (1995), Late Quaternary displacement rate, paleoseismicity, and geomorphic evolution of the Alpine Fault: Evidence from Hokuri Creek, South Westland, New Zealand, *New Zealand Journal of Geology and Geophysics, 38*, 419-430.

Sylvester, A. G. (1988), Strike-slip faults, *Geological Society of America Bulletin, 100(11),* 1666-1703.

Theuerkauf, J., S. Dhodapkar, K. Manjunath, K. Jacob, and T. Steinmetz (2003), Applying the Discrete Element Method in Process Engineering, *Chemical Engineering & Technology, 26*, 157-162.

Tian, X., J. Teng, H. Zhang, Z. Zhang, Y. Zhang, H. Yang, and K. Zhang (2011), Structure of crust and upper mantle beneath the Ordos Block and the Yinshan Mountains revealed by receiver function analysis, *Physics of the Earth and Planetary Interiors, 184(3)*, 186-193.

Ting, J., B. Corkum, C. Kauffman, and C. Greco (1989), Discrete numerical model for soil mechanics, *Journal of Geotechnical Engineering, 115*, 379-398.

Velandia, F., J. Acosta, R. Terraza, and H. Villegas (2005), The current tectonic motion of the Northern Andes along the Algeciras Fault System in SW Colombia, *Tectonophysics, 399*, 313-329.

Vergnolle, M., F. Pollitz, and E. Calais (2003), Constraints on the viscosity of the continental crust and mantle from GPS measurements and postseismic deformation models in western Mongolia, *Journal of Geophysical Research, 108(B10),* B05411.

Wakabayashi, J., J. V. Hengesh, and T. L. Sawyer (2004), Four-dimensional transform fault processes: progressive evolution of step-overs and bends, *Tectonophysics, 392*, 279-301.

Wang, C., D. D. Tannant, and P. A. Lilly (2003), Numerical analysis of the stability of heavily jointed rock slopes using PFC2D, *International Journal of Rock Mechanics and Mining Sciences, 40*, 415-424.

Wang, Q., P. Z. Zhang, J. Freymueller, R. Bilham, K. M. Larson, X. A. Lai, X. Z. You, Z. J. Niu, J.C. Wu, Y. X. Li, J. N. Liu, Z. Q. Yang, Q. Z. Chen (2001), Present-day crustal deformation of China constrained by global positioning system measurements, *Science, 294*, 574-577.

van Wijk, J., G. Axen, and R. Abera (2017), Initiation, evolution and extinction of pull-apart basins: Implications for opening of the Gulf of California, *Tectonophysics*, 719-720: 37-50.

Wood, R., J. R. Pettinga, S. Bannister, G. Lamarche, and T. McMorran (1994), Structure of the Hanmer strike-slip basin, Hope fault, New Zealand, *Geological Society of America Bulletin, 106*, 1459-1473.

Woodcock, N. H., and M. Fischer (1986), Strike-slip duplexes, *Journal of structural geology, 8(7)*, 725-735.

Wright, L. A., J. K. Otton, and B. W. Troxel (1974), Turtleback Surfaces of Death Valley Viewed as Phenomena of Extensional Tectonics, *Geology, 2*, 53-54.

Wu, J. E., K. McClay, P. Whitehouse, and T. Dooley (2009), 4D analogue modelling of transtensional pull-apart basins, *Marine and Petroleum Geology, 26*, 1608-1623.

Xie, F. R., X. F. Cui, J. T. Zhao, J. C. Chen, H. Li (2004), Regional division of the recent tectonic stress field in China and adjacent areas, *Chin. J. Geophys. 47*, 654-662.

Zak, I., and R. Freund (1981), Asymmetry and basin migration in the Dead Sea rift, *Tectonophysics, 80*, 27-38.

Zhang, P., B. C. Burchfiel, S. Chen, and Q. Deng (1989), Extinction of pull-apart basins, *Geology, 17*, 814-817.

Zhang, Y.Q., Y.S. Ma, N. Yang, W. Shi, S.W. Dong (2003), Cenozoic extensional stress evolution in North China. *J. Geodyn. 36*, 591-613.

Zheng,W.J., P.Z. Zhang, W. G. He, D.Y. Yuan, Y.X. Shao, D.W. Zhen, W. P. Ge, W. M. (2013), Transformation of displacement between strike-slip and crustal shortening in the northern margin of the Tibetan Plateau: evidence from decadal GPS measurements and late Quaternary slip rates on faults. *Tectonophysics, 584*, 267-280.

Zhao, W. L., and W. J. Morgan (1987), Injection of Indian crust into Tibetan lower crust : a two-dimensional finite element model study, *Tectonics, 6*, 489-504.